On Atmospheric Particulate Deposition in Gas Turbines



Nikul Vadgama

University of Oxford

A thesis submitted for the degree of
Doctor of Philosophy

February 2021

On Atmospheric Particulate Deposition in Gas Turbines

Nikul Vadgama, University of Oxford

Particulate deposition has become increasingly concerning for jet engine manufacturers, it can lead to a variety of problems, from stress corrosion cracking and the blocking of cooling holes in the turbine, to reduced stall margins for the engine. This thesis describes the development and validation of quantitative design tools that will enable manufacturers to make engines particulate tolerant. These tools are needed to allow: engines to fly in high concentrations of dust for a limited time; manufacturers to operate a cost of ownership model by predicting damage; and most importantly the safe certification of engines against these risks.

The key capabilities required are the prediction of particulate trajectories through the engine, and their likelihood of adhering to engine components on contact. This thesis focusses on the robust prediction of turbulent particle transport in the context of the highly complex flows encountered in gas turbines. The tools developed are applicable to engine design because of their compatibility with existing design techniques, commercial flow solvers, and their computational efficiency.

A stochastic model of turbophoresis (a Continuous Random Walk, CRW) is developed and a methodology for its application detailed. A model from literature provides the basis of the current transport model. While accurate modelling of turbophoresis has previously been shown to change the likelihood of small particles sticking by several orders of magnitude, compared to the exclusion or inadequate inclusion of turbophoretic effects, these results could only be reliably replicated in simple pipe flows as the models required turbulent flow characteristics determined from Direct Numerical Simulation or experiment. These characteristics are impossible to replicate for complex geometries. Thus, the thesis identifies robust methods to calculate instantaneous turbulent flow fluctuations, seen by the particle in the Lagrangian frame of reference, from Reynolds Averaged Navier Stokes computational fluid dynamic solutions. The model is shown to be equally accurate in simple flows when compared to previous implementations, and requires neither external data nor any a priori assumptions regarding the structure of the turbulence.

The choice of the turbulence model, formulation of the particulate tracking time step, a local cell co-ordinate system to describe the turbulence, and modification of the near-wall Lagrangian timescale are all shown to be critical to the generation of accurate spatially resolved particulate deposition. The method is implemented to interface with a commercial flow solver.

To ensure reliable deposition distribution maps are produced, while maintaining computational efficiency, convergence criteria are developed as well as a methodology to minimise the number of particulate tracking events required in a computational simulation. Here, convergence of particulate tracking based on the well known integral deposition fraction is shown to be insufficient as a measure of convergence of the spatial distribution. Well established metrics for describing variation in multidimensional distributions are compared, and a suitable technique to generate a converged distribution in a computationally efficient way is established.

The revised CRW model has been validated both against existing data in the literature, and further experiments. A difficulty here is the very limited spatially resolved deposition data for which sufficient boundary conditions are available. For more complex, gas turbine relevant flows, no data of sufficient resolution were available in the open literature. A new rig was developed to generate spatially resolved distributions of deposition in accelerating flows, at representative temperatures and flow speeds. The range of tests conducted investigated the effects of geometry curvature, flow speed, and metal temperature.

Finally, the revised CRW model is run according to the methodology developed, which ensures convergence, and these results are compared to the experimental data. As bounce-stick models are still unreliable, to reduce the number of variables considered, both all-stick and all-bounce conditions were simulated and compared. The chosen geometries allowed the effects of curvature and flow speed to be further investigated, with experimental trends well replicated. The mechanisms responsible for these trends were inferred from these simulations. It was found that modelling of turbophoresis was critical to capturing a number of features of deposition that were seen in experiments. The transport model is seen to provide a robust basis for accurate modelling, however, more quantitative comparison requires a similar improvement in the modelling of bounce-stick behaviour.

Acknowledgements

This research would not have been possible without both my primary supervisor Professor David Gillespie and secondary supervisor Professor Matthew McGilvray. They have both been a big part of my journey since starting at Oxford, as an undergraduate, and I have greatly enjoyed working with them over the last 8 years. Their trust has enabled me to conduct research I have truly enjoyed. Further, their consistent support and guidance has shaped me to be better, both professionally and personally.

I would also like to thank Rolls-Royce for their sponsorship during my DPhil, as well as the experience they provided in the year prior to me starting university, which enabled me to attend Oxford in the first place. Specifically, thanks go to Rory Clarkson and Ben Littley for the freedom of direction they enabled in my research, and the industrial insights they provided which confirmed the work to be of real world value.

Finally, I would like to thank my friends and family who have been incredibly supportive throughout my journey (regardless of their familiarity of what a PhD involves!). These include those I met at Catz, Univ, Osney, and my long-standing friends from school. I have depended on their support throughout what have been four challenging and transformative years. I look forward to the future with the continuing support of these people.

Contents

1. Introduction 1

1.1 Jet Engines 1
1.2 Problems Caused by Particulates 2
1.3 Modelling Atmospheric Particles 4
1.4 Motivation 4
1.5 Strategy and Outline 6
1.5.1 Key Aim 6
1.5.2 Objective 1 7
1.5.3 Objective 2 7
1.5.4 Objective 3 7
1.5.5 Further work 8

2 Literature Review 9

2.1 Contaminant Particle Matter 9
2.1.1 Composition and Material Properties 9
2.1.2 Size and Shape 11
2.1.3 Concentration 11
2.2 Particle Transport 12
2.2.1 Drag 14
2.2.2 Pressure Gradient 15
2.2.3 Added Mass 15
2.2.4 Basset Force 16
2.2.5 Magnus Lift 16
2.2.6 Saffman Lift 16
2.2.7 Thermophoresis 17
2.2.8 Brownian Motion 18
2.2.9 Turbophoresis 18
2.2.10 Summary 19
2.3 Regimes of Particle Deposition 19
2.4 Particle Bounce, Stick, and Erosion 21
2.4.1 Particle-Wall Interaction Modelling 24
2.4.2 Erosion Modelling 30
2.5 Numerical Methods and Investigations 32
2.5.1 Fluid Phase 34
2.5.2 Discrete Phase 35
2.5.3 Numerical Studies 42

2.6 Experimental Methods and Investigations 48
2.7 Summary 51

3 Continuous Random Walk Development 53

3.1 Paper: Development and Validation of a Continuous Random Walk Model for Particle Tracking in Accelerating Flows 55
3.2 Summary 86

4 High Temperature Experiments with Acceleration 87

4.1 Experimental Facility 89
4.1.1 Mass Flow Controllers 90
4.1.2 Heater 91
4.1.3 Particle Aerosol Generator 91
4.1.4 Mixing Chamber 91
4.1.5 Particle Material 95
4.1.6 Oven 96
4.1.7 Test Piece 96
4.1.8 Orifice Plates 96
4.1.9 HEPA Filter 97
4.1.10 Weighing Scale 97
4.1.11 Spatially Resolved Measurement 97

4.2 Paper: Experimental Deposition of Particulates in Accelerating Flows at Engine Representative Conditions 98
4.3 Further Results from the Experiments 127

5 Spatial Convergence of Numerical Simulations 129

5.1 Paper: Convergence of Spatially Resolved Particle Deposition 129

6 Deposition in Flow with Acceleration 145

6.1 Fluid Phase 145
6.1.1 Set-up and Solution 145
6.1.2 Mesh Sensitivity and Convergence 146
6.1.3 Fluid Phase Description 147

6.2 Discrete Phase Solution Set-Up 151
6.3 Results and Discussion 154
6.3.1 Baseline Case 154
6.3.2 Ratio of Curvature 159
6.3.3 Flow Rate 162

6.4 Summary and Conclusions 164

7 Conclusions and Further Work 165

7.1 Conclusions 165

Further Work 167

7.2 167

7.2.1 Short-term 167

7.2.2 Long-term 169

8 Appendices 171

8.1 Appendix A: Derivation of the Continuous Random Walk 171

8.2 Appendix B: Experimental Facility 175

8.2.1 Orifice Plates 175

8.2.2 Packing density calibration 176

8.2.3 Experimental Method 176

8.3 Appendix C: Validation of Size Distribution used for Numerical Simulation of Experiments . 178

9 References 179

Nomenclature

Latin Variables

a	Acceleration (ms^{-2})
A_{proj}	Projected area (m^2)
c	Speed of sound (ms^{-1})
C_{c}	Cunningham correction factor
C_{d}	Drag coefficient
C_{L}	Lift coefficients
CoR	Coefficient of restitution
d_{p}	Particle diameter (m)
E	Young's modulus (GPa)
E_{visc}	Viscous energy dissipation (J)
ER	Erosion rate (mg/g)
F	Force (N)
g	Gravity (ms^{-2})
h	Heat transfer coefficient
J	Particle mass flux ($kg\ m^{-2}\ s^{-1}$)
k	Thermal conductivity ($W\ m^{-1}\ K^{-1}$)
l	Length scale (m)
M	Mass distribution
MLF	Mass loading fraction
m	Mass (kg)
N	Number of cells
P	Distribution
PVF	Particle volume fraction
R	Radius (m)
S	Shear stress propagation speed (ms^{-1})
S	Surface area (m^2)
$\mathbf{S}$	Strain rate tensor (m^2s^{-2})
t	Time (s)
T	Temperature (K)
u	Speed (ms^{-1})
u^*	Friction velocity (ms^{-1})

$\overline{u_i u_i}$	Reynolds stress (m^2s^{-2})
v	Velocity (ms^{-1})
$\overline{v_i v_i}$	Particle Reynolds stress (m^2s^{-2})
W	Work (J)
Z_0	Equilibrium separation (m)

Greek Variables

α	Impact angle (degrees)
β	Spread parameter
γ	Surface free energy (Jm^{-2})
ξ	Gaussian random number
η_{k}	Kolmogorov speed (ms^{-1})
Λ	Thermal conductivity ratio
μ	Pneumatic viscosity (Pa s)
ν	Kinematic viscosity (m^2s^{-1})
ν_t	Turbulent kinematic viscosity (m^2s^{-1})
ρ	Density ($Kg\ m^{-3}$)
τ_{e}	Eddy time scale (s)
τ_{k}	Kolmogorov time scale (s)
τ_{p}	Particle time scale (s)
τ_{w}	Wall shear stress (Pa)
ω	rotational speed ($rad\ s^{-1}$)

Non-Dimensional Groups

Bi	Biot number $(= hd_{\mathrm{p}}k_{\mathrm{p}}/6)$
Kn	Knudsen number $(= 2l_{\mathrm{g}}/d_{\mathrm{p}})$
Nu	Nusselt number $(= hl/k)$
R_0	Ratio of curvature $(= 2R_{\mathrm{bend}}/D_{\mathrm{h}})$
Re	Reynolds number $(= \rho ul/\mu)$
$\mathrm{Re_g}$	Gradient Reynolds number
Re_γ	Shear Reynolds number
$\mathrm{Re_p}$	Particle Reynolds Number $(= \rho_{\mathrm{g}}u_{\mathrm{rel}}d_{\mathrm{p}}/\mu)$
Stk	Stokes $(= C_{\mathrm{c}}\rho_{\mathrm{p}}U_{\mathrm{g}}d_{\mathrm{p}}^2/18\mu_{\mathrm{g}}D_{\mathrm{h}}$)
τ^+_p	Non-dimensional particle relaxation time $(= C_{\mathrm{c}}\rho_{\mathrm{p}}\rho_{\mathrm{f}}d_{\mathrm{p}}^2(u^*)^2/18\mu_{\mathrm{g}})$
V_d^+	Non-dimensional deposition velocity $(= J/C_0u^*)$

Y^+	Y plus (= $\rho_f u^* y/\mu_g$)

Subscripts

A	Adhesion
brown	Brownian
c	curvature
Cross	Crossing time
e	Eddy
f	Fluid
h	Hydraulic
i	i-th direction
L	Lagrangian
N	Normal
p	Particle
Pipe	Pipe
rel	Relative
T	Tangential
t	Turbulent
visc	Viscous
y	Yield
turbo	Turbophoretic
thermo	Thermophoretic
Wall	Wall
*	Equivalent

Acronyms

CRW	Continuous random walk
DNS	Direct numerical simulation
DRW	Discrete random walk
GLM	Generalised Langevin model
JKR	Johnson-Kendell-Roberts
LES	Large eddy simulation
RANS	Reynolds averaged Navier-Stokes

Publications

A total of five papers have resulted from this DPhil, four of these are first author publications that directly relate to the thesis and the others are co-authored papers which are related to the subject of this thesis. The most recent three first author publications are reformatted and included as Chapters 3-5 of this thesis.

First author publications

N. Vadgama, P. Forsyth, M. McGilvray, and D. R. H. Gillespie, "Numerical Simulation of Spatially Resolved Particle Deposition in Accelerating flows" AIAA Aviation 2019 Forum, no. AIAA 2019-3720, pp. 1–18, 2019.

N. Vadgama, P. Forsyth, M. McGilvray, and D. R. H. Gillespie, "Development and Validation of a Continuous Random Walk For Particle Tracking In Accelerating Flows" ASME Turbo Expo 2020, Turbomachinery Technical Conference and Exposition, no. GT2020-16026, pp. 1–14, 2020.

N. Vadgama, S. Beal, P. Forsyth, M. McGilvray, D. R. H. Gillespie, and R. Clarkson, "Experimental Deposition of Particulates in Accelerating Flows at Engine Representative Conditions" AIAA Aviation 2020 Forum, no. AIAA-2020-2836, pp. 1–18, 2020.

N. Vadgama, J. Connolly, M. McGilvray, and D.R.H. Gillespie, "Convergence of Spatially Resolved Particle Deposition" European Turbomachinery Conference 2021, no. ETC-2021-659, pp. 1 – 9, 2021.

Other Publications

J. Gaskell, N. Vadgama, M. McGilvray, and D. R. H. Gillespie, "Collision-Induced Rotation and the Magnus Force on Particulates" AIAA Aviation 2020, no. AIAA- 2020-2820, pp. 1–14, 2020

1. Introduction

1.1 Jet Engines

Reciprocating steam engines may have powered the industrial revolution, but it is gas turbines that are essential for power and transport in today's globalised world. They exist in many configurations with each being designed for a specific application, most commonly they are used for flight and power generation. In order to meet the specific demands of different applications engineers have had to optimise each configuration independently.

The engineering of the Jet Engine has resulted in fuel efficiency savings of ~7 percent per decade since the 1970s, with current overall efficiencies of ~40% [1][2]. This has been an essential improvement for their continued adoption. In order to achieve this, aero-engines operate at high pressure ratios (currently up to 58:1) [3] and turbine entry temperatures (~2000 K) [4], [5]. For these conditions to be realised, a key innovation was the introduction of active cooling techniques. This uses air diverted from the main gas path (pre-combustion) and reintroduces it into the turbine to: manage the loads and temperature of turbine blades, discs, and shafts; eliminate ingestion between static and rotating components (sealant flows); and prevent oil leakage. As there are significant efficiency penalties in diverting this air much effort has been put into using it effectively, leading to the use of complex cooling geometries. Currently, these include impinging jets, rib and pin-turbulated cooling passages, and effusion cooling systems [5]. The intricate nature of these means they are susceptible to particulate damage and blockage [6]. Furthermore, the aforementioned high pressure ratios mean that coolant temperatures in the engine may reach 950 K, increasing the likelihood of particles sticking to and fusing within cooling passages due to diminishing yield strength [7]. This sort of damage is a concern given the broader drive for more efficient engines that have longer life-spans [8]. The Advisory Council for Aeronautics Research in Europe's FlightPath 2050 targets set the ambitious goal of 75% reduction in CO_2 emissions per passenger kilometre, relative to new aircraft in 2000 [8]. Efficiency of specific power improvements are still available

from increased pressures ratios/turbine inlet temperatures, and the introduction of new materials [2], for which particulate deposition will continue to be a concern.

1.2 Problems Caused by Particulates

Recent one-off high concentration events such as Eyjafjallajökull's eruption in 2010 [9] and the Doha sand storm in 2015 [10] have highlighted the clear susceptibility of jet-engines to particulate damage. These have a simple, although costly, remedy - not flying for the duration of the event. What is more difficult to mitigate are the constant background levels of particulate matter that engines experience day-to-day [11]. This problem is persistent and will likely get worse, with an increasing number of flights passing through airspace with consistently higher levels of particulate matter, Figure 1. Furthermore, annual dust emissions may have increased 25-50% in the last century according to simulations, and studies predict that climate change could increase dust emissions up to 200% [12].

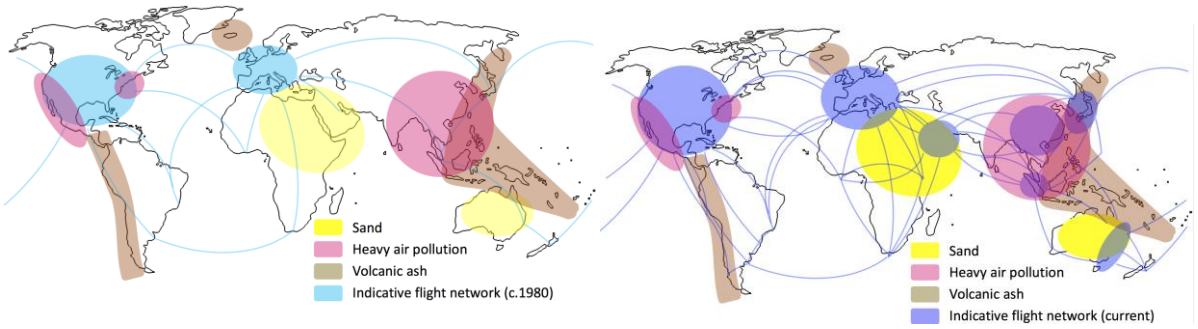

(a) 1980 *(b) 2010*

Figure 1 Comparison of common flight paths in 1980 and 2010 on a world map showing regions of high atmospheric particulate concentration by type [13]

Particulates are able to cause damage through both erosion and deposition onto components. Figure 2 shows common sites for these processes in a jet engine, with Figure 3 showing examples of the most relevant forms of damage (turbine deposition) in a large civil engine. At best, erosion causes degradation of a component's individual aerodynamic optimisation, and at worst has consequences for whole engine operability by, for example, reducing stall margins. Deposition can cause blockages, in the main gas path or the secondary air system, and in some cases chemical reactions occur on the surfaces such that the material is corroded and weakened.

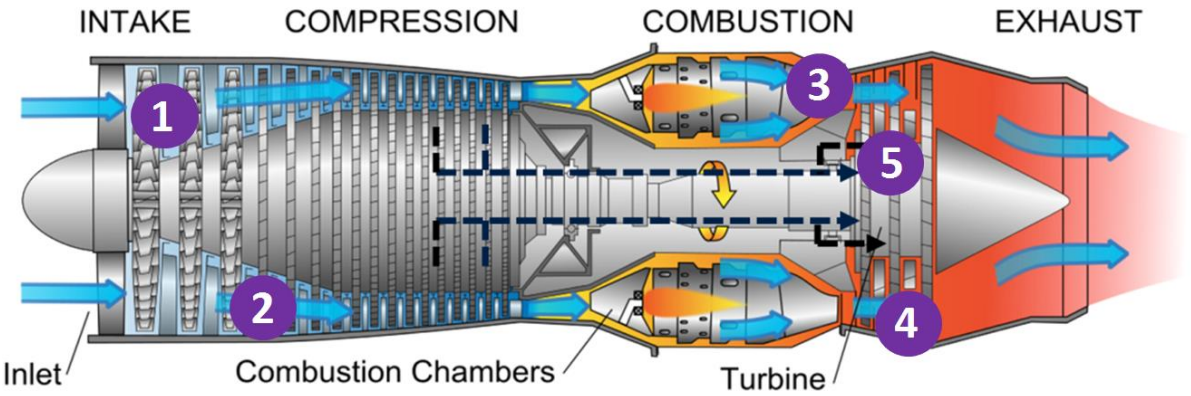

Figure 2 Deposition locations of particulate matter within a gas turbine (turbojet). Dashed lines show secondary air system. 1. Fouling and erosion of compressor, 2. Ice accretion on stators, 3. Deposition on nozzle guide vanes, 4. Deposition on high pressure turbine blades, 5. Deposition within secondary air system.[13]

Both one-off events and consistent exposure have previously had significant effects on jet engines. In 2010 Eyjafjallajökull's eruption filled airspace with volcanic ash, closing European airspace for 5 days and costing an estimated $1.7 bn [14]. Persistent exposure to particulates containing salts and sulphur is thought to have been the root cause of stress corrosion of the Rolls-Royce Trent 1000 engine's intermediate pressure turbine blades. This single problem was reported with an accounting cost of £450 m in 2017, and Rolls-Royce's Chief Customer Officer of Civil Aerospace said that it was "the single most important issue" facing the company [15].

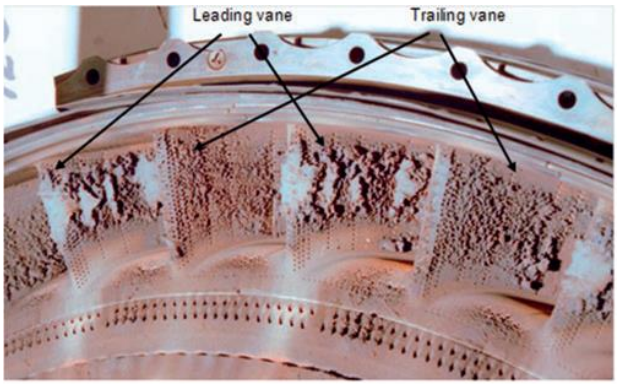

a) Ash on NGVs[9]

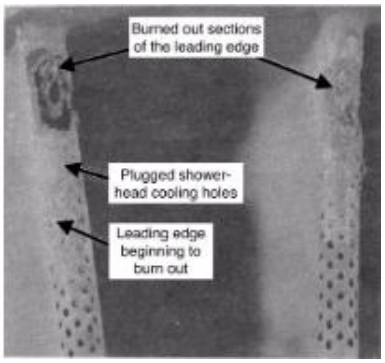

b) Coolant hole blockage[16]

Figure 3 Examples of external and internal particulate deposition

1.3 Challenges Modelling Particulates Across Applications

For aerosols, it is important to consider the transport of particles (forces, interactions, and shape effects), the physicochemical process of particle-wall interactions (bounce, stick, shatter, erosion etc.), and chemical reactions once the deposition has occurred.

Applications range from understanding the effectiveness of face coverings against virus particles (50-200 nm in diameter), to designing accurate ink-jet printers (~100 μm diameter), to predicting the transport of volcanic eruptions in the atmosphere (mm scale) along with particle ingestion in jet engines (0 – 200 μm). The very wide range of the parameter space makes generalised modelling particularly challenging. Even for a particular application the variation in input parameters remains large. Extrapolation from experiments is therefore difficult, and for high temperature applications in a rotating environment complex, both to design and interpret. There is a lack of high resolution data at representative conditions, which is required for pre-existing research to find application in the real world. Therefore, a high resolution modelling approach is favoured, which can be applied across a range of particle shapes, sizes, and chemical compositions, allowing precise solution control.

1.4 Motivation

Previous particle modelling research at the OTI was motivated by the sulphidation of the Rolls-Royce Trent 900 intermediate pressure turbine shank-pocket/root. The shank pocket sits between the blade platform and disk (Figure 4), and cooling air taken from the compressor is delivered to the shank in order to seal the gas platform and provide air to the blades' internal cooling passages. The presence of corrosion in this section of the engine indicates the presence and adhesion of particles. Whilst this sulphidation problem was isolated to specific engines, the 2010 eruption of Eyjafjallajökull highlighted the challenges of understanding any jet engine's susceptibility to particle damage. At the time preventative measures were taken based on particulate matter concentration alone. After this event a 'safe to fly' chart [11], Figure 6, was generated to provide more robust insight in the case of another similar event. This chart is based on known incidents and

experiments, and the method is not robust as it is limited, thankfully, by the number of recorded events available regarding modern engines.

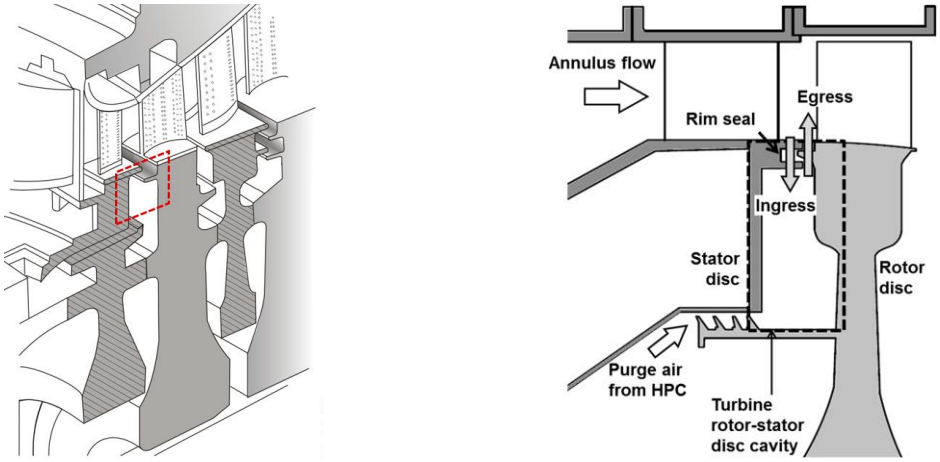

Figure 4 Location of shank cavity shown on a cross section of a realistic engine (left [17]) and a simplified diagram of the in and outflows of the rotor-stator cavity (right [18]).

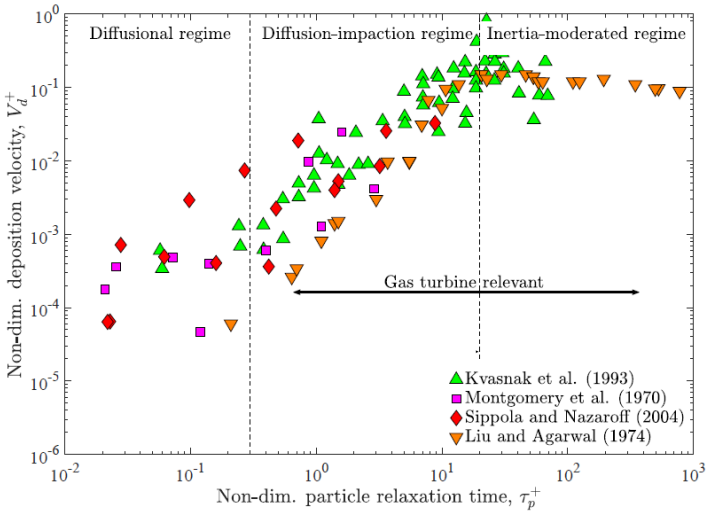

Figure 5 Relevant particle size range in shank cavity based on indicative engine operating conditions [13]

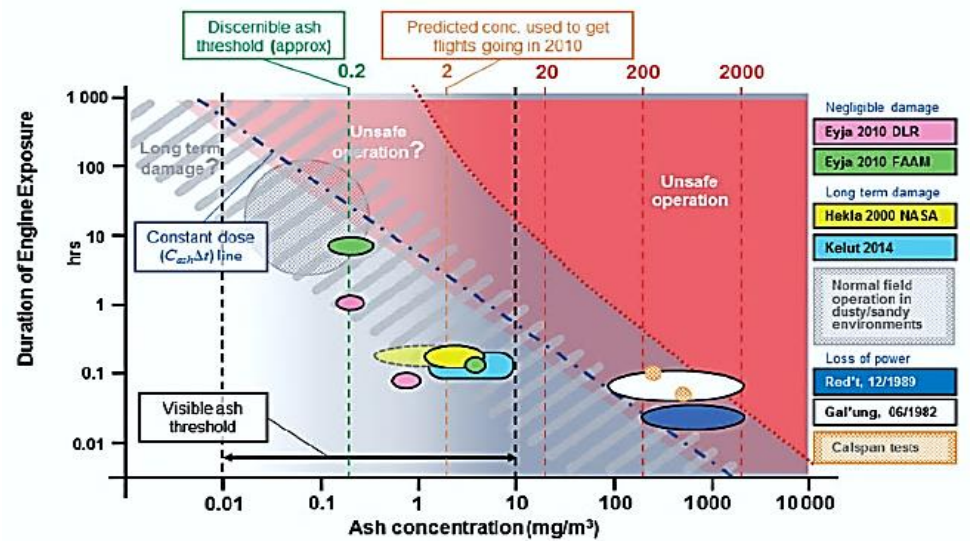

Figure 6 Safe-to-fly chart developed after the 2010 volcanic eruption [11]

The particular engine features that instigate susceptibility to particulate damage are similarly poorly understood. Simple scaling of previously successful engines' architecture, that have experienced comparable flight profiles, does not necessarily lead to a robust design. Here then lies the key motivation of the research, and defines its primary objective: to generate quantitative tools that make engines' particle tolerant. Initially, tools will likely either inform damage mitigation strategies, or a predictive maintenance approach. Further in the future, the tools can be incorporated into design tools to design more robust engines. The aims are to allow engines to fly in high concentrations of dust for a limited time; enable damage to be predicted such that a robust cost of ownership model and be developed; and most importantly allow engines to be safely certified against these risks.

1.5 Strategy and Outline

1.5.1 Key Aim

The key aim of this thesis is to improve the modelling of turbulent particle transport through passages by particles typically encountered in gas turbines. The likelihood of particle stick is subject to separate research, however, a conservative estimate of deposition can be made by assuming all particles which collide with a surface stick, provided the model of particle transport is accurate. For the improvements in modelling to be valuable, to both scientific and industrial users, the model must be applicable to computational fluid dynamics models which can be run over short time periods (i.e. RANS) with known accuracy. Further, the model should enable the prediction of spatially resolved deposit on a component such that likely hotspots can be identified. In the future, once combined with design tools, it is intended that these quantitative tools will enable the danger associated with these hotspots to be analysed, and appropriate action (e.g. component re-design) to be taken. In the short term, such models will enable damage mitigation and predictive maintenance strategies to be employed. This will enable engines to better coper with the particulate matter that resides in the atmosphere, this will be increasingly concerning in the future as concentrations increase as a result of climate change.

1.5.2 Objective 1

The first objective was to improve on a current model of turbophoresis, previously identified as promising at Oxford, such that it can be applied to complex flows. The range of turbulent transport models is reported in the literature review, Chapter 2. Here there is a particular emphasis on the development of the continuous random walk (CRW) model which is chosen as the baseline model for further development. A full derivation of the CRW is included in Appendix A. The current work develops the CRW implementation of Dehbi et al [19] and this is reported in Chapter 3, along with a reproduction of the author's ASME paper GT2020-16026. Here the limiting assumptions of this model are identified, and major refinements are proposed to address them. Importantly, the necessity for appropriate geometry specific training data is eliminated allowing application to real engine geometries in the future. The revised model was shown to result in equivalent accuracy for simple pipe flow: the basis for the selection of the original, tuned, model. Comparison was made with further validation data available from the literature, showing accuracy sufficient for deposition design studies.

1.5.3 Objective 2

The second objective was to design, build, and run a new experimental rig to provide data to validate the model proposed in Chapter 3. Chapter 3 highlighted that existing models may predict the overall deposition fraction of incoming particles well, but the local deposition distribution very poorly. A test rig was designed, built, and operated (Chapter 4). It provides spatially resolved deposition data in an S-bend geometry with flow conditions chosen to represent some key features of internal cooling passages in a high pressure turbine blade. The results are reported in Chapter 4, a reproduction of AIAA-2020-2836.

1.5.4 Objective 3

The third objective of the research was to provide rules for the application of the CRW model, such that a representative spatially resolved deposition map is produced at minimal computational cost. This requires robust means of identifying convergence, achieved here by assessing the changing spatially resolved deposition (rather than the integral deposition fraction). Alternative measures of

convergence were investigated, and an appropriate measure chosen. A methodology, capable of accounting for the stochastic nature of deposition was determined.

1.5.5 Further work

Using these tools Chapter 6 demonstrates experimental data and numerical simulations of deposition using the revised CRW model and appropriate bounce-stick models to demonstrate the outcomes of modelling now possible. The model is demonstrated to capture the key features of the spatial distribution, allowing likely in-service hot spots to be identified.

Chapter 7 concludes the work, with a summary of the findings, a discussion of directions of remaining research questions, and future work that would complement that already undertaken.

2 Literature Review

The multi-physics nature of this research makes the relevant literature extensive. To ensure sufficient context and detail, the literature review first articulates the background theory to provide context (Sections 2.1 - 2.3), before a more critical discussion of the most relevant literature (Sections 2.5 - 2.6) is presented. The critical discussion makes apparent the need for the work conducted in relation to the Aim and Objectives (Section 1.5).

2.1 Contaminant Particle Matter

Often "sand and dust" is used to describe a variety of particle matter that deposits and causes problems in gas turbines. It is important to understand the manner in which these particles enter (concentration etc.) as well as their physico-chemical properties (Young's modulus, melting temperature etc.) to develop deposition modelling tools suitable for real gas turbine flows, and hence allow for the design of suitable prevention methods. Both the atmosphere and fuel are sources of particle matter in jet engines [20], this project focuses on the former. The source of atmospheric particles is diverse (e.g. volcanic eruptions, bursting of bubbles at sea, and anthropogenic activities [21]) and so classifying and characterising particles is challenging. Relevant open literature is limited and primarily from outside the aeronautical industry.

2.1.1 Composition and Material Properties

Particle composition is important in dictating whether the engine will last thousands or a few hours [22]. Atmospheric particles are often categorised using the categories in Table 1, the first three categories are of primary concern [22], [23]. Open literature has focused on documenting and understanding mineral dust [22]. Mineral and industrial dust is the most abundant aerosol with annual contribution estimates of 1500-1800 Tg/yr [24], [25]. The salts found in engines fall under the categories of “Sea Salts” and “Secondary Inorganic Particles”, these play an important role in processes such as sulphidation [26].

Category	Description
Sea Salt Particles (ionic composition)	e.g. Cl^- , Na^+, SO_4^{2-}, Mg^{2+}
Mineral/Industrial Dust and Volcanic Ash	Silicates, Oxides, Sulfates, Carbonates etc.
Secondary Inorganic Compounds	Salts e.g. NO^{3-} and NH^{4+}
Primary Biogenic Aerosol Particles	Biological materials
Combustion Derived Carbonaceous Particles	Organic matter and elemental carbon
Secondary Organic Aerosols	Light elements

Table 1 Categorisation of particle matter used by mineralogists/geochemists [27]

The composition of mineral dust varies significantly, but generally oxides of silicon, aluminium, iron and calcium, as well as carbonates dominate composition [20]. Table 2 shows the approximate oxide composition of a representative dust from the Middle East, however other region's particles cannot be assumed similar in composition [22]. Whilst the chemical composition in terms of oxides can be a useful way to compare samples, the compounds exist as minerals. The mineral forms that exist control the phyisco-chemical properties which are important for deposition modelling, these include density, shape, and melting temperature. A relevant example is the comparison of volcanic ash and test dust properties. These samples contain comparable, and high levels, of silicon dioxide. But the properties differ significantly because it exists as an amorphous glass in volcanic ash, and in crystalline form in sand. For example the melting temperatures of each form are approximately 1000 K and 2000 K respectively [28], [29]. The most common minerals include quartz, feldspar, mica, calcites, gypsum, dolomites, and halites [22]. The composition of a sample is affected by its distance from source, the proportion of large particles falling with distance, due to settling. Examples of large particles include quartz, and feldspars [20]. The size of particles affects the mechanical properties as large particles are more likely to contain faults [30]. Due to the lack of data available, the rule of mixtures is often used with temperature sensitivity disregarded [31].

	% by Mass		
Oxide	Example Sand	Volcanic Ash	Arizona Road Dust
CO_3	22.2	-	-
$Si0_2$	20.3	66.4	69-7
CaO	17.4	2.78	2.5-5.5
Al_2O_3	11.4	15.6	8-15
H_2O	8.8	-	-
MgO	5.9	0.62	1-2
Na_2O	5.2	5.26	1-4
ClO_2	4.5	-	-
SO_4	2.2	-	-
K_20	15	2.61	2-5
Fe_2O_3	0.6	-	4-7
FeO	-	4.81	-
TiO_2	-	0.7	-

Table 2 Comparison of particle samples and test dust

2.1.2 Size and Shape

Atmospheric particles range in size from a few nanometres, to tens of micrometres. Generally, dust (<0.01 mm) is considered to be smaller than sand (0.01-1 mm) [20], [22], [27]. Ground samples of mineral dust and sand have shown both Gaussian and log-normal distributions [20], [29], [32].

Most modern literature models particles as spherical, and reported diameters are equivalent diameters [27]. Particles are not spherical and their shape is critical in determining forces acting on them (Section 2.2) and can also affect the heat transfer to a particle depositing [28]. For irregular particles it is common to specify two of the following parameters; volume, surface area, projected area, or projected perimeter [33]. Based on these parameters shape factors can be calculated (e.g. volumetric shape factor, sphericity, and circularity) each of which are useful in different situations [33] (Section 2.2). The median aspect ratio of mineral and industrial dust samples is ~1.4 to 1.7 regardless of particle size, with a log-normal distribution [25], [34]. It has been shown, in DNS studies of channel flow, that aspect ratios of 3 can result in the near wall ($Y+ < 5$) concentration of particles changing by orders of magnitude [28].

2.1.3 Concentration

Recently guidance for 'safe' flight conditions has been based on the DEvAC chart, Figure 6. In this, ash concentration is plotted against the duration of exposure, and real-world data suggests that the total dosage (dust concentration × duration) is an indicator of likely damage. Useful comparative

points of reference for assessing concentration are that at 0.6-0.7 mg/m^3 visibility through the dust is very limited, and at 1.5 mg/m^3 visibility through the dust is non-existent [35]. Concentrations are <1 mg/m^3 in most operating environments, although as Figure 7 shows this is by no means an upper limit with local events such as sand storms and helicopter landings increasing levels significantly. The concentration is highly dependent on the local factors such as surface geology, geography, and weather conditions. Hence the distribution changes with both location and time [22]. Work will focus on inlet concentrations <1 mg/m^3 as this covers the majority of situations. Developing tools to allow effective engine modification to allow prolonged flight in these situations will have maximum impact on aircraft operability.

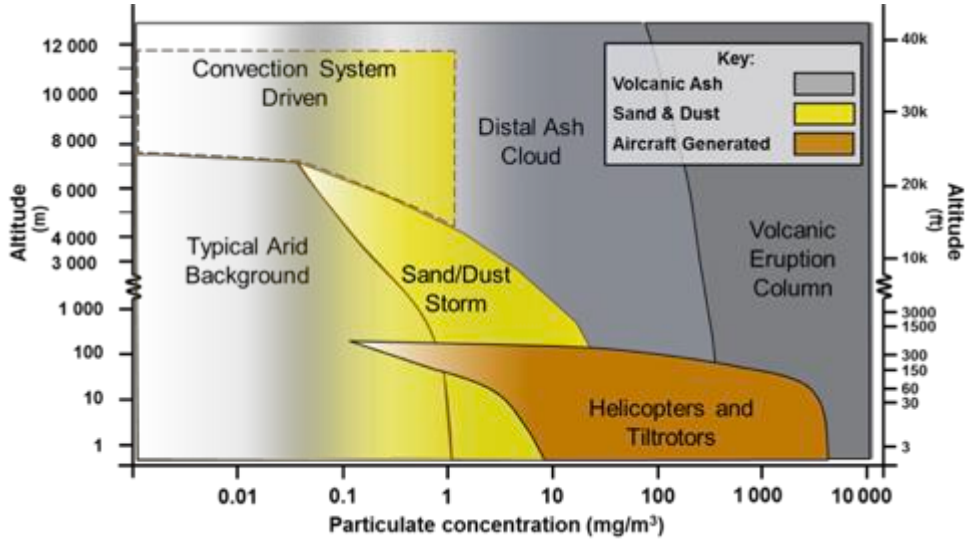

Figure 7 Approximate global sand and dust concentration distribution across altitudes categorised by cause [22].

2.2 Particle Transport

Studying particles requires an understanding of both their transport to the surface and their interaction with surfaces (bounce, stick, shatter, erosion etc.). This section describes the transport of particles, a critical discussion of numerical modelling methods is presented in Section 2.5.2. Direct numerical simulation of a particle laden flow field may be conducted using the Navier-Stokes equations but solution of these is iterative, difficult, very lengthy, and requires discrete boundary conditions. The derivation of approximate ordinary differential equations of particles helps the modelling and understanding of dynamics, but is not simple. Some of the most commonly applied strategies are described below.

The Basset-Boussinesq-Oseen equation (Equation 1) describes spherical particle motion in a still quiescent flow, with a low particle Reynolds number ($\mathrm{Re_p} = d_\mathrm{p} v_\mathrm{Rel}/\nu_\mathrm{f}$), $\mathrm{Re_p}$<<1 [36]. There are four forces: drag (2.2.1), gravity & buoyancy, added mass (Section 2.2.3), and Basset history (Section 2.2.4). A further development is the Maxey-Riley-Gatignol equation, this accounts for unsteady and non-uniform flow effects. Equation 2 is the Maxey-Riley-Gatignol equation with an additional term for lift, where τ is a dummy variable for time and D represents the derivative along the particle path. In order to account for the unsteadiness of a flow an additional term must be added to the added mass term and Basset force, further an additional force as a result of the pressure gradient appears (Section 0) [37]. The Faxen correction accounts for the non-uniform flow, the particle velocity (v_p) is surface averaged for the drag and basset history forces, and volume averaged for the added mass and pressure gradient terms. A particle's acceleration is calculated as the sum of six terms (from left to right): drag, gravity & buoyancy, pressure gradient, added mass, Basset history, and lift. For this whole equation to be valid the particle shear Reynolds numbers ($\mathrm{Re_\Gamma} = r_\mathrm{p}^2 \Gamma/\nu$) should much less than one [38].

$$\frac{d\, m_\mathrm{p} v_\mathrm{p}}{dt} = \underbrace{-3\pi d_\mathrm{p}\mu\left(v_\mathrm{p} - v_\mathrm{f}\right)}_{\text{Stokes Drag}} + \underbrace{\left(m_\mathrm{p} - m_\mathrm{f}\right)g}_{\text{Gravity \& Buoyancy}} - \underbrace{\frac{1}{2} m_\mathrm{f}\left(\frac{\mathrm{d}v_\mathrm{p}}{\mathrm{d}t}\right)}_{\text{Added Mass}} \underbrace{- \frac{3}{2}\pi d_\mathrm{p}^2 \mu \int_0^t \left(\frac{\mathrm{d}v_\mathrm{p}}{\mathrm{d}\tau}\right) \frac{1}{\sqrt{\pi\nu(t-\tau)}}\mathrm{d}\tau}_{\text{Basset History}} \qquad 1$$

$$\frac{d\, m_\mathrm{p} v_\mathrm{p}}{dt} = \underbrace{-3\pi d_\mathrm{p}\mu\left(v_\mathrm{p} - v_\mathrm{f}\right)}_{\text{Stokes Drag}} + \underbrace{\left(m_\mathrm{p} - m_\mathrm{f}\right)g}_{\text{Gravity \& Buoyancy}} + \underbrace{m_\mathrm{f}\frac{\mathrm{D}v}{\mathrm{D}t}}_{\text{Pressure Gradient}} \qquad 2$$

$$\underbrace{- \frac{1}{2} m_\mathrm{f}\left(\frac{\mathrm{d}v_\mathrm{p}}{\mathrm{d}t} - \frac{\mathrm{D}v_\mathrm{f}}{\mathrm{D}t}\right)}_{\text{Added Mass}} \underbrace{- \frac{3}{2}\pi d_\mathrm{p}^2 \mu \int_0^t \left(\frac{\mathrm{d}v_\mathrm{p}}{\mathrm{d}\tau} - \frac{\mathrm{d}v_\mathrm{f}}{\mathrm{d}\tau}\right) \frac{1}{\sqrt{\pi\nu(t-\tau)}}\mathrm{d}\tau}_{\text{Basset History}}$$

$$\underbrace{+ m_\mathrm{f} C_\mathrm{l}\left(V_\mathrm{f} - V_\mathrm{p}\right) \times \boldsymbol{\omega}}_{\text{Lift}}$$

In addition to these forces there can also be Saffman lift, thermophoresis, Brownian motion, electrostatic, and magnetic forces. Most often the above equation is simplified based on assumptions of the conditions such that it is more easily used.

2.2.1 Drag

In practice the skin drag and pressure drag are thought of together and are often the dominant force. Drag is calculated via formulae and correlations based on a drag coefficient (Equation 3). Figure 8 shows the existence of 3 distinct drag regimes over a sphere: Stokes, Sub-critical, and Super-critical. These regimes exist due primarily to the structure of the wake changing. At the lowest Reynolds numbers ($\mathrm{Re_p} < \sim 10^1$) a stable set of vortices form on the rear of the sphere and result in high drag (Figure 9b). As $\mathrm{Re_p}$ ($\sim 10^1 < \mathrm{Re_p} < \sim 10^3$) increases the vortices begin to shed and von Karman vortex streets start to form and the increased mixing on the rear reduces the drag (Figure 9c). Between a $\mathrm{Re_p}$ of 10^3 and 10^5 the periodic nature of the von Karman vortex street breaks down and a turbulent wake forms, while the flow on the flow facing side remains laminar (Figure 9d). After a critical Reynolds number, the drag reduces significantly due to the transition to turbulent flow which results in the separation points moving further downstream on the sphere's surface (Figure 9e). As the critical point is a function of transition it is not well defined and is affected by factors such as particle roughness, and turbulence intensity [39], [40].

$$C_\mathrm{d} = \frac{F_\mathrm{d}}{\frac{1}{2}\rho_\mathrm{f} A_\mathrm{proj}^2 \nu_\mathrm{f}} \qquad 3$$

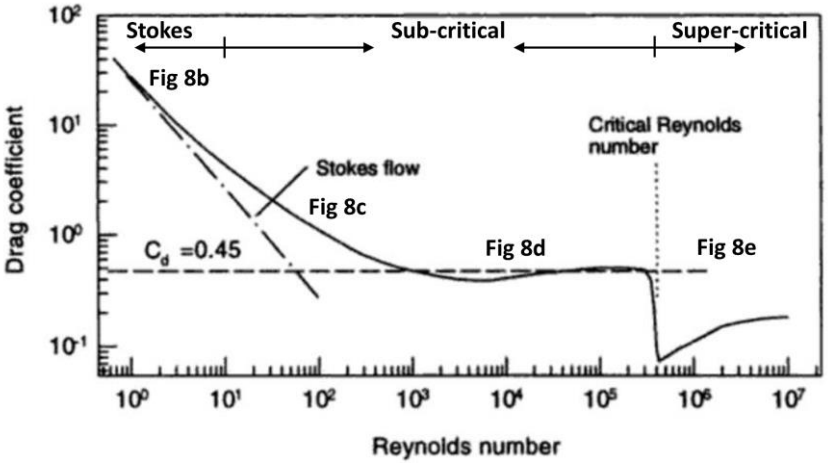

Figure 8 Drag coefficient of a sphere as function of particle Reynolds number [41]

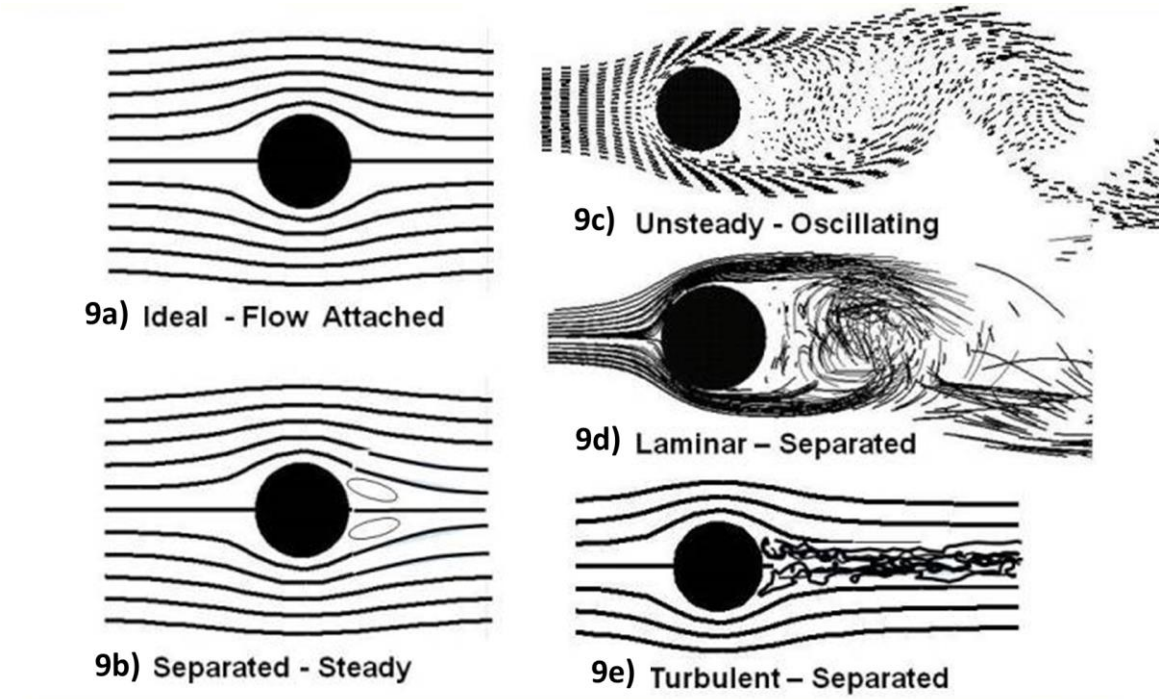

Figure 9 Flow regimes which result in different drag behaviours. Regimes marked on Figure 8 [42]

2.2.2 Pressure Gradient

This term accounts for forces due to local pressure gradient across the particle and shear stresses in flow. The magnitude of this force is of the order (ρ_f/ρ_p). Borello et al. argue that this force is not negligible in the case of compressible flows when modelling a power plant gas path, which typically achieve lower pressure ratios than large civil aeronautical engines, as the fluid density becomes significantly large enough. [39], [40], [43]

2.2.3 Added Mass

The added mass force term is an unsteady force that considers the force required to move the fluid surrounding the particle as it is accelerated. The shape of the particle has a direct effect on this result as it changes the volume of fluid around the shape that must be accelerated [39]. This force is of order ρ_f/ρ_p.

2.2.4 Basset Force

The second of two unsteady forces due to acceleration is called the Basset force, also referred to as the history force, and it accounts for the delay in development of the boundary layer as the particle's relative velocity changes [39] . This force is of order $\sqrt{\rho_f/\rho_p}$.

2.2.5 Magnus Lift

Magnus lift is the force generated by particle rotation due to the pressure difference as a result of differing velocities on either side of the particle [44]. This results in the oncoming flow being accelerated on one side and decelerating on the other side, creating a pressure difference and resultant force towards the side on which flow is being accelerated. As the force is proportional to the fluid density in the bulk flow this force can be regarded as small if $\rho_p/\rho_f \gg 1$ [45]. However, it is not always negligible near surfaces where particles rebound with large velocities and in regions of strong shear stresses. The direction of the Magnus force may change on successive impacts if there is significant sticking, and therefore change in particle rotation. Gaskell et al. showed that this force should be modelled when particle-wall interactions are considered [46].

$$F_M = \pi\rho_f \left(\frac{d_p}{2}\right)^3 \boldsymbol{\omega_p} \times U_p \qquad 4$$

2.2.6 Saffman Lift

The Saffman force is lift due to shear in the fluid, and hence a velocity gradient in the flow, [39], [45]. It is considered large if the particle is much smaller than the Kolmogorov length scale ($d_p/\eta_k < 1$) [45]. For highly turbulent flows the Saffman force can be important even in the bulk flow [45]. In Equation 5 it is assumed that $Re_p << Re_G << 1$, where Re_G is based on the velocity gradient (Equation 6), if this is not the case the force is much smaller than that predicted by Equation 5. Similar to the Magnus force, this cannot always be disregarded near surfaces where particles rebound with large angular velocities and near regions of strong shear. The extent of the Saffman force's effects are a function of the shear layer thickness [45].

$$F_{\text{saff}} = 1.61\mu_{\text{f}} D\, V_{\text{rel}}\sqrt{\text{Re}_{\text{G}}} \qquad 5$$

$$\text{Re}_{\text{G}} = \frac{d_p^2}{V_{\text{f}}}\frac{\text{d}u}{\text{d}y} \qquad 6$$

2.2.7 Thermophoresis

Thermophorisis is the force a particle feels due to temperature gradients [47].The force results from unequal interchange of momentum between the fluid molecule and particle, around the particle's surface, as the hotter fluid imparts more energy the particle moves away from the hotter region and toward the colder fluid [48]. This means for hot surfaces in gas turbines that are being cooled by a cooling flow, particles in the cooling flow are less likely to deposit. At the same time cooling the surface increases the thermophoretic effects on particles in the hot path, increasing their deposition onto the surface.

Thermophoresis can also act in the opposite direction, the particles experience a force towards the hot gas, this is called 'reverse' thermophoresis [13]. This is possible when the particles' thermal conductivity ratio (Equation 7) is much greater than 1. The particle is effectively uniformly heated, meaning that the thermal creep flow (gas in the thin interfacial layer moving along a solid surface in the direction of the surface's temperature gradient) is negligible as there is no substantial temperature difference along the surface and thermal stress slip flow (flow around the sphere from the hotter to colder region, moving the particle towards the hotter region) dominates [49], [50].

The thermophoretic force depends on a multitude of parameters (Section 2.5.2.5) this means there is no simple scaling that enables an estimation of its magnitude in flows that have temperature gradients.

$$\Lambda = \frac{k_{\text{p}}}{k_{\text{g}}} \qquad 7$$

2.2.8 Brownian Motion

Famously studied by Einstein, Brownian motion is the random motion of particles due to their collision with atoms of the fluid. In isothermal conditions it is only relevant to particles well under a micron in effective diameter [44].

2.2.9 Turbophoresis

In the case that RANS solutions are used, a model must be used to take into consideration the effect of turbulence on the particles. Turbophoresis is the effective force experienced by particles due to gradients of fluid turbulence. This force results in the net movement of particles from regions of high turbulence to regions low turbulence.

The effective acceleration due to fluid fluctuations can be derived analytically in terms of the particle's Reynolds stress ($\overline{v_i v_i}$), Equation 8. Here $E_{\mathrm{visc},i}$ is the viscous energy dissipated by a particle in the i-th direction, where τ_p response time of the particle (= $\rho_\mathrm{f}\rho_\mathrm{p} d_p^2/18\mu$) and the force is determined using the Stokes equation. This is used to determine the force acting on it ($F_{\mathrm{Turbo},i}$), and acceleration it experiences ($a_{\mathrm{Turbo},i}$).

$$E_{\mathrm{visc},i} = F_{\mathrm{D},i} V_i \tau_\mathrm{p} = 3\pi\mu_\mathrm{f}\overline{v_i v_i}\tau_\mathrm{p}$$

$$F_{\mathrm{Turbo},i} = m_\mathrm{p} a_{\mathrm{Turbo},i} = \frac{\mathrm{d}E_{\mathrm{visc},i}}{\mathrm{d}x_i} = 3\pi\mu_\mathrm{f}\tau_\mathrm{p}\frac{\mathrm{d}\overline{v_i v_i}}{\mathrm{d}x_i} \qquad 8$$

$$a_{\mathrm{Turbo},i} = -\frac{\mathrm{d}\overline{v_i v_i}}{\mathrm{d}x_i}$$

Turbophoretic deposition is controlled by the particles' interactions with near wall coherent turbulent structures, such as low-speed streaks, stream-wise vortices, ejections, and in-sweeps. Figure 10 shows how particles aggregate near the wall as they interact with two counter-rotating vortices which result from a low speed streak of turbulence. Figure 11 shows the overall process by which particles can deposit. Particles accumulate in the buffer layer and then are brought into an accumulation region (corresponding to the turbulent peak) by in-sweeps. Particles that follow the

turbulent structure as it becomes an ejection are re-entrained into the flow, however if they become decoupled from that structure there is deposition. [51]

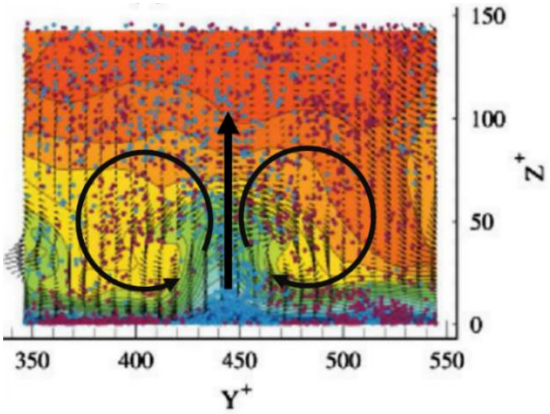

Figure 10 Motion of particles near wall calculated in a DNS study of channel flow. Flow is coming out of the page and there are two dominant counter-rotating vortices. Blue particles are moving away from the wall, purple particles are moving towards the wall. Vectors show the in-plane velocity vectors [51]

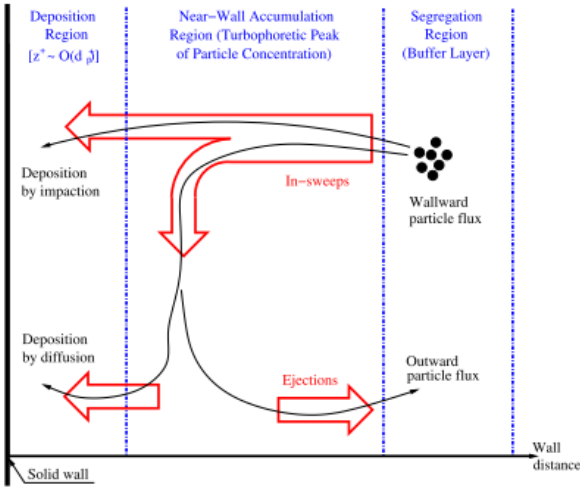

Figure 11 Process of particles interacting with near wall coherent turbulent structures[51]

2.2.10 Summary

As reasoned above, for small and relatively heavy ($\rho_p/\rho_f \gg 1$) particles [52], the largest forces acting on particles are drag and gravity forces. As per Section 2.1 this is true for the situations we are interested in and the studies carried out in this thesis, the particles are multiple orders of magnitude denser than the fluid and micron sized. Many studies have introduced combinations of other forces which affect motion at small scales, and in turbomachinery flows it is clear that thermophoretic forces are important. The numerical methods for modelling these forces are discussed in Section 2.5.2.

2.3 Regimes of Particle Deposition

A particle's responsiveness to a flow is most commonly thought of in terms of a bulk Stokes number (Equation 11), a non-dimensional parameter that compares the time scale of a particle (Equation 9) to the time scale of the fluid domain (Equation 10).

$$\tau_p = C_C \rho_p D_p^2 / 18\mu \qquad 9$$

$$\tau_{\mathrm{f}} = \frac{l_{\mathrm{f}}}{u_{\mathrm{f}}} = D_{\mathrm{h}}/\bar{U}_{\mathrm{f}} \quad (10)$$

$$\mathrm{Stk} = \tau_{\mathrm{p}}/\tau_f = C_{\mathrm{C}}\frac{\rho_{\mathrm{p}}\bar{U}_{\mathrm{f}}d_{\mathrm{p}}^2}{18\mu D_{\mathrm{h}}} \quad (11)$$

In simple flows particle deposition is reported as a non-dimensional deposition velocity (V_{d}^+, Equation 12). This is the wall-normal volume flux of particles per unit area ($J_{\mathrm{w}}/\rho_{\mathrm{p}}$) normalized by wall shear velocity (Equation 13) [53]. V_{d}^+ is a function of the non-dimensional particle relaxation time τ_{p}^+ (Equation 14). This is defined as the ratio of the particle relaxation time (τ_{p}) compared to the turbulent length scale near the wall ($\nu/(u^*)^2$).

Figure 12 shows three particle deposition regimes; *diffusional*, *diffusion-impaction*, and *inertia-moderated* [53]. In the *diffusional* deposition regime V_{d}^+ decreases with τ_{p}^+ [53]. There is also a dependence on Schmidt number which quantifies the ratio of momentum diffusivity to the particle Brownian diffusion coefficient ($\mathrm{Sc} = \nu/D_p$). A gradient diffusion model predicts deposition well in this regime [53]. In the *diffusion-impaction* regime V_{d}^+ increases due to eddies imparting the particles with energy [53], [54]. In this regime $V_{\mathrm{d}}^+ \propto (\tau_{\mathrm{p}}^+)^2$ and there is a wide spread of data, in addition to experimental uncertainty, factors such as roughness have an impact on results and are hard to control. This is the type of deposition that predominantly occurs at gas turbine conditions, and modelling is unsatisfactory [54]. In the *inertia-moderated* regime turbulent eddies are responsible for deposition, with increasing inertia associated with increasing τ_{p}^+ reducing the response of particles and explaining the reduction in V_{d}^+ [53].

$$V_{\mathrm{d}}^+ = \frac{J_{\mathrm{w}}}{\rho_{\mathrm{p}}u^*} \quad (12)$$

$$u^* = \sqrt{\frac{\tau_{\mathrm{w}}}{\rho_{\mathrm{f}}}} \quad (13)$$

$$\tau_{\mathrm{p}}^+ = \frac{\tau_{\mathrm{p}}u^{*2}}{\nu_{\mathrm{f}}} \quad (14)$$

This approach of classification is not applicable to more complex flows, although Wu and Young [55] attempted to extend use of these parameters to a rectangular cross section bend. In these more complex flows the impact fraction is more commonly reported than the dimensionless deposition time, and often this is reported as a function of the Stokes number.

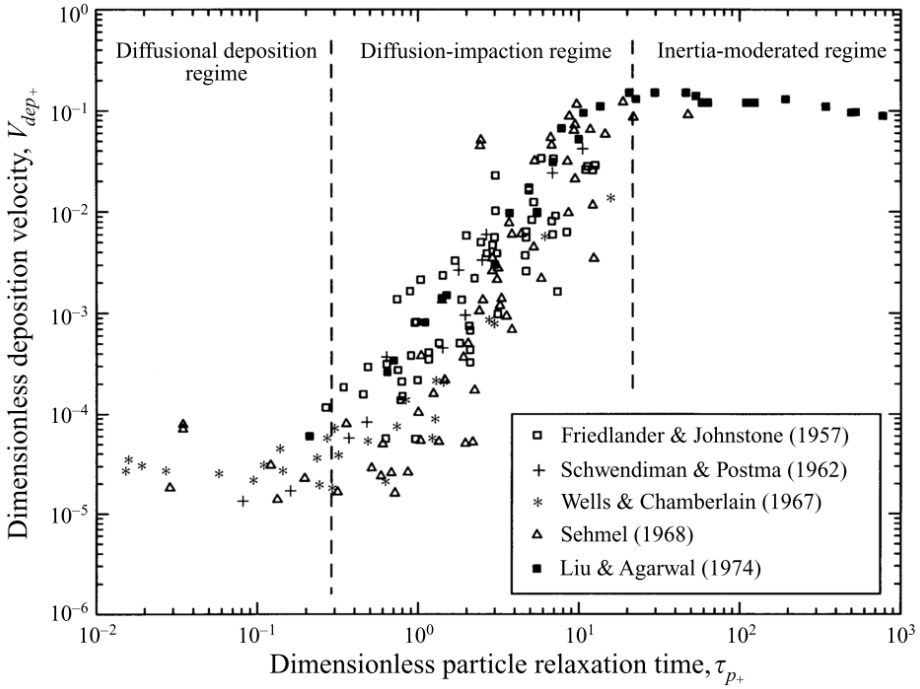

Figure 12 Dimensionless deposition velocity compared to dimensionless particle relaxation time[53]

2.4 Particle Bounce, Stick, and Erosion

Models of particle deposition must predict whether a particle sticks to the surface on impact or bounces off that surface. In the latter case the coefficient of restitution of the particles (CoRs) and particle spin are important for further flow trajectory model. A further complication is that the particle may shatter at impact or act to erode other material off the substrate surface. Ultimately, outputs of particle trajectory models are inputs to particle-wall interaction models. For this reason, an understanding of particle-wall interaction models should inform the aims of particle trajectory models. Modelling particle-wall interactions is a vast area of research, this section discusses the key considerations and some common modelling approaches to provide context.

There are a number of forces generated during the contact, which can make models complicated, especially for small particles [56]. For small particles (1 -100 μm) and low velocities

(1 -10 m/s), which are common in a gas turbine, electrostatic and van der Waals forces can become influential, resulting in a reduction of the CoRs [56]. The van der Waals force is many magnitudes larger than electrostatic forces that can be imparted as the particle moves through the engine at these particle sizes. If there is moisture present then liquid bridges form, these result in forces a magnitude larger than those of the van der Waals forces.

There have been many fundamental theories of adhesion suggested, all of which have different assumptions and hence create models that require different bespoke parameters. To understand when best to apply each theory an adhesion force theory applicability map has been constructed, Figure 13. The horizontal axis is a function of the Tabor parameter (μ_T, Equation 16 - 18) compares the elastic deformation from adhesion to the effective range of surface forces. The Johnson-Kendall-Roberts (JKR) theory is best suited to compliant solids of large radius with large adhesion energy ($\mu_{\mathrm{T}} \gg 1$) [57]. This model focuses on the development of van der Waals adhesion forces as the particle and surface come into contact, it is the basis of many subsequent adhesion theories [58]. Equation 15 is used to calculate the adhesion energy, in this γ is the surface free energy and is usually of order unity [31], [59]. The alternative Derjaguin-Muller-Toporov (DMT) theory applies well to small stiff solids with weak adhesion energy ($\mu_{\mathrm{T}} \ll 1$) and hence appears on the opposite side of Figure 13 [60]. The vertical axis is the ratio of the load to adhesive force. When the loading is high adhesive forces can be considered negligible and hence Hertz theory, which assumes no adhesive forces, becomes more relevant [60]. Nonetheless, it has been argued that none of these models are insufficient for particles of size 100 nm - 500 um as they do not describe the interaction forces on the microscale [61].

There are further considerations when modelling adhesion, for example the adhesion parameter given by Equation 19 which describes the ratio of the compressive forces (caused by peaking asperities) and adhesive forces (from lower asperities), and hence can be important in capturing surface roughness effects.

Furthermore, every approach ultimately requires material properties which tend to be unknown for the materials studied. These are often determined by fitting the required parameters to validation datasets, with notable deviation between these effective properties and those populated

from well-conditioned material testing. This suggests some oversimplification in the modelling strategies, and although accurate for calibrated materials, makes them difficult to apply generally.

$$W_{\mathrm{a}} = A_{\mathrm{contact}}\gamma \quad 15$$

$$\mu_{\mathrm{T}} = \left(\frac{R^{*}\Delta\gamma^{2}}{E^{*2}Z_{0}^{3}}\right)^{\frac{1}{3}} \quad 16$$

$$R^{*} = \frac{R_1 R_2}{R_1 + R_2} \quad 17$$

$$E^{*} = \left(\frac{1-\nu_1^2}{E_1} + \frac{1-\nu_2^2}{E_2}\right)^{-1} \quad 18$$

$$\theta = \frac{E\,\sigma^{\frac{3}{2}} r^{\frac{1}{2}}}{r_{\mathrm{w}} A} \quad 19$$

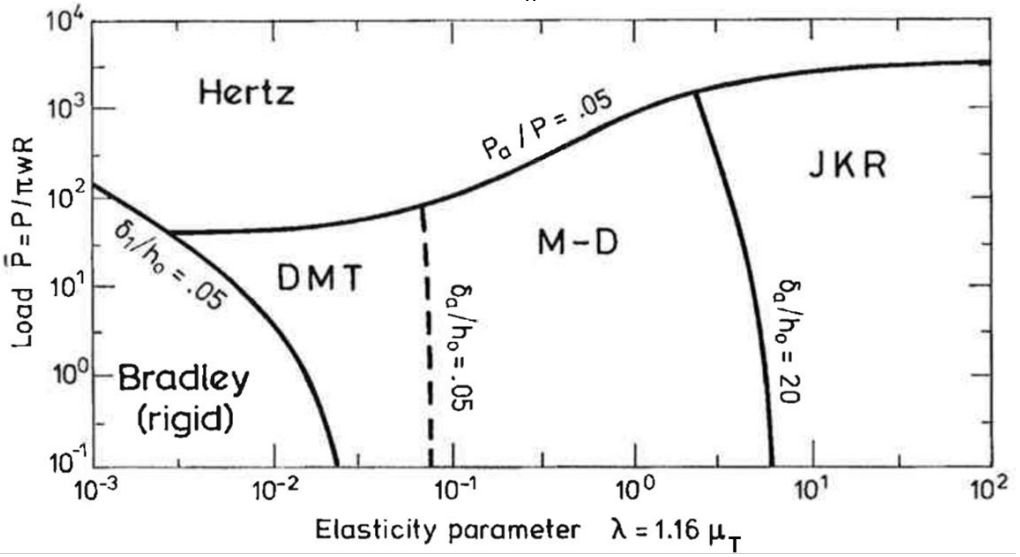

Figure 13 Map of suggested adhesion theory. The horizontal axis is the transition parameter (λ) which is a measure of elastic deformation to surface forces and proportional to the tabor parameter (μ_T). The vertical axis is the ratio of the load (P) to adhesive force (πwR), in this w is the surface free energy. The cut-off lines are based on the ratio of compressive force (δ_a) to the maximum separation distance, between the particle surface and adhesion surface, where adhesive stresses are present (h_0). The values used for these lines are indicative rather than absolute. [60]

Calculating if a particle is likely to stick is dependent on many parameters and there are various classification systems for impacts. One such system helps to determine the important variables for predicting deposition based on a comparison of the impact velocity and the speed of sound (c) in the material. Equation 20 shows how this can be calculated in cases where the stress wave propagates in the elastic regime, under the assumption that S is the gradient of the stress strain curve and therefore given by the elastic modulus [31], [62]. The general findings are as follows:

- Low-velocity ($V \ll c$) - Geometry and material properties dominate,
- High-velocity ($V \sim c$) - Inertia and material failure dominate,

- Hyper-velocity ($V \gg c$) - Material behaves like a fluid, hydrodynamic pressure dominates.

$$c = \sqrt{\frac{S}{\rho}} = \sqrt{\frac{E}{\rho}} \qquad 20$$

2.4.1 Particle-Wall Bounce and Stick Modelling

Particle-wall interaction models are required to understand if particles stick, and if not, how they rebound (their velocity, angle, and rotation). In some cases the models include break-up of the impacting particle and erosion of the surface.

Much progress has been made since early work where a constant COR was assumed, but further work is still required to accurately model particle-wall interaction [63]. Choice, and existence, of an appropriate model is a primary issue when conducting studies [58].

The general idea is that there are adhesion forces that must be overcome, after the dissipation of energy through various mechanisms, for the particle to not stick. The most common dissipative routes are hysteresis, visco-elasticity, and plastic deformation [56].

There are two main approaches; first-principle models that derive exact equations for idealised cases, and phenomenological models that consider the physical processes and potentially appropriate equations to model them. The factors considered, in the models discussed, range from velocity and angle of impaction to material properties. Material properties considered appropriate vary greatly between models and include: viscosity, Young's modulus, yield stress, roughness, and their temperature dependence.

Finally, some of these models only predict stick or bounce, whilst others predict the angles, velocities, and accelerations of rebounding particles. Popular methods in each category are described briefly such that an appreciation of the important factors can be understood. It has been argued that a phenomenological model may allow for clearer representation of the decisive factors and hence better insight [64].

2.4.1.1 First Principle Models

As described in Section 2.4 there are various models that aim to exactly describe the physics of adhesion. These are the basis of first-principle models of particle bounce-stick.

The Brach and Dunn model uses classical impact theory, Hertizan mechanics, and JKR adhesion theory to model deposition. It attempts to include particle deformation, adhesion force, adhesion induced rolling, various material types (visco-elastic, elastic-plastic etc.), and tangential and rotational motions. Even this careful treatment of forces, and well developed theory, led to the unrealistic and unexpected result that the surface free energy is proportional to$\sqrt{\gamma}$. This is unlikely, and indicates an error in the assumptions or theory used [56], [65].

Kim and Dunn [66] expanded the model to include elastic-plastic effects, and surface roughness. The inclusion of elastic-plastic effects results in a lengthy, applicable, analytical description for exact analysis, e.g. Equation 21. Nonetheless these appear insufficient to fully describe these effects.

Another attempt to include elastic-plastic deformation on the basis of the Branch and Dunn model was by Singh and Tafti that built on Jackson and Green's work [67]. Surface roughness effects are taken into account by assuming a Gaussian distribution and use of a linear scaling factor of adhesion force, based on the adhesion parameter, with the most appropriate adhesion model chosen using the Tabor parameter (Section 2.4) [66]. Ai and Fletcher expanded the model to include particle re-entrainment due to shear drag using critical momentum theory, resulting in a critical wall shear velocity above which particles are re-entrained [68].

Another popular model is that proposed by Thornton and Ning, which models the impact of two spheres and considers only plastic spheres with adhesion, this also results in a critical velocity criterion for adhesion [63]. A limitation of these models is that they require the particle to be almost spherical for equations to hold, and it is unclear how shape effects would influence the results.

$$F_{\max} = \frac{1}{4}\left(A_1^2 + \frac{1}{2}\sqrt{\frac{1}{4}\left(\frac{(1+\mathrm{B})\delta_1 F_1^{-\frac{1}{2}}/6}{(1-\beta)\delta_1 F_1^{-1}/4}\right) - \frac{4}{3}\frac{\frac{\delta_1 F_1(5\beta-1)}{60} - \frac{mv^2}{2}}{(1-\beta)\delta_1 F_1^{-1}/4}} \dots\dots \right) \qquad 21$$

2.4.1.2 Phenomenological Models

Equation 22describes a popular model that takes into account changing material properties, using the idea of sticking probability, based on viscosity. Viscosity was deemed to be the important parameter as it was thought to control the shape and hence contact area of the impact. Viscosity is calculated as a function of only temperature according to the Frenkel expression, Equation 23. The reference viscosity can be calculated by examining the distribution of particles at exit, or taken as the softening temperature of the material [69]. It has been shown that whilst this model can be tuned to predict the correct volume of deposition, the spatial distribution is not consistent with experiments [64]. Other probability based models exist which include velocity, temperature, and size as parameters [58].

$$p(T) = \begin{cases} \frac{\mu_{\mathrm{ref}}}{\mu}, & \mu > \mu_{\mathrm{ref}} \\ 1, & \mu < \mu_{\mathrm{ref}} \end{cases} \qquad 22$$

$$\mu = Ae^{B/T} \qquad 23$$

Bons et al. created a model based on the principle that the particle could be considered a cylinder impacting end-on [64]. The aim of this model is to offer insight into the macroscopic processes without considering and calculating the exact response of the particle. The model assumes that any kinetic energy from motion normal to the surface that cannot be stored elastically (in that it causes stresses above the yield stress) is lost to plastic deformation. The maximum elastic energy the particle can store is given by Equation 24. The particle rebounds with a normal CoR (CoR_{N}) of 1 if no plastic deformation occurs, otherwise it is given by Equation 25.The adhesion force is modelled in which the contact area is given by Equation 26 and reduces CoR_{N}. The model incorporates the rolling induced by boundary layer shear by increasing W_{crit},although the effects have been found to be small in the case of turbo-machinery applications and can be ignored [31]. To predict the tangential *CoR* (CoR_{T}) Bons et al. modified Equation 27 derived by Branch and Dunn to Equation 28. In Equations 27 and 28, μ_{imp} is the impulse ratio not the friction coefficient although they are equal when in sliding, a value of 0.3 is common [64]. In Equation 28 the inclusion of a cosine term

makes the impulse ratio sensitive to impingement angle. Bons et al. effectively use this as a tuning parameter along with the nominal yield stress. [31], [64]

$$E_{\mathrm{crit}} = \frac{E A_{\mathrm{cross}}}{l} \frac{w_{\mathrm{crit}}^2}{2} \tag{24}$$

$$CoR_{\mathrm{n}} = \frac{V_{\mathrm{n}2i}}{V_{\mathrm{n}1}} = \frac{1}{V_{n1}} \sqrt{\frac{2\, E_{\mathrm{crit}}}{\rho_1 \mathrm{Vol}}} = \frac{1}{V_{\mathrm{n}1}} \sqrt{\frac{\sigma_{\mathrm{y}}^2}{\rho_1 E_{\mathrm{c}}}} \tag{25}$$

$$\frac{A_{\mathrm{cont}}}{A} = a + b \left(\frac{W_{\mathrm{max}}}{W_{\mathrm{crit}}} \right)^c \tag{26}$$

$$V_{\mathrm{t}2} = V_{\mathrm{t}1} - \mu_{\mathrm{imp}} (V_{\mathrm{n}1} + V_{\mathrm{n}2i}) \frac{V_{\mathrm{n}2}}{V_{\mathrm{n}2i}} \tag{27}$$

$$V_{\mathrm{t}2} = \left(V_{\mathrm{t}1} - \mu_{\mathrm{imp}} (V_{\mathrm{n}1} + V_{\mathrm{n}2i}) \frac{V_{\mathrm{n}2}}{V_{\mathrm{n}2i}} \right) \cos^2 \alpha_1 \tag{28}$$

Comparison of the predicted *CoR*, normal *CoR* (CoR_{N}), and tangential *CoR* (CoR_{T}) were made to experimental data (Figure 14a - Figure 14c). The model over predicts the reduction in CoR_{N} caused by both the impingement angle and velocity (Figure 14b), but the general trend is well replicated [31]. The CoR_{T} is over-predicted and the trend is not fully replicated as shown in Figure 14c, the experimental data shows the presence of two minima whilst only one is predicted by the model. While the cosine term used to correct CoR_{T} by Bons et al. is valuable, it does not have a rigorous physical justification and appears to compromise the models accuracy in the sliding regime. The physical reasoning given is that particles with a high normal velocity would act to crush surface asperities, while particles with a low normal velocity would be more effected by the asperities and rebound with a lower tangential velocity. However, there does not appear to be an obvious alternative formulation, and more thought is required on how best to model CoR_{T}.

Using a model proposed by Maw [70] , Chow [31] considers the impact of two spheres and identifies that the model suggested by Bons matches FEM simulations and experiments in the sliding regime predicted by the Maw model. He suggests that this could be improved by modifying the model for relevant effects in the slip-stick and sticking regimes which occur at higher impact angles. He notes that the Maw model does not consider the size of the sphere, but nonetheless

particle size is important: moment of inertia scales with d_{p}^4, whereas frictional forces scale with d_{p}^3. A consequence is, the thresholds of regimes in Maw's model change with particle diameter. This would have the effect of changing the boundary of the sticking regime [31]. Figure 15 shows how the application of an empirical refinement function that transfers energy from the tangential direction into rotation of the particle, with the required energy budget accounted for in a lossy translation to the normal direction. This is intended to capture the physics of particles sliding and sticking on the surface, resulting in a closer match to experimental data.

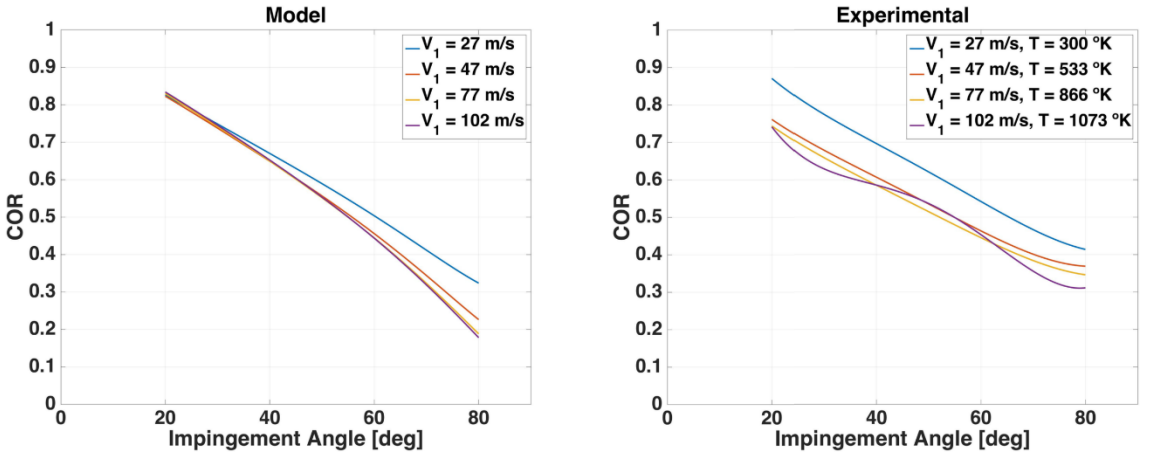

a) CoR

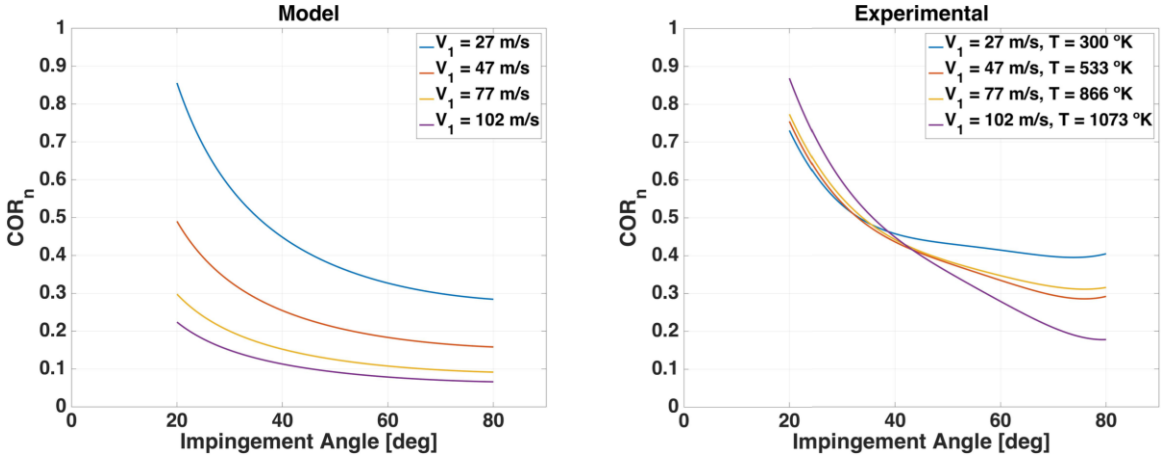

b) CoR_{N}

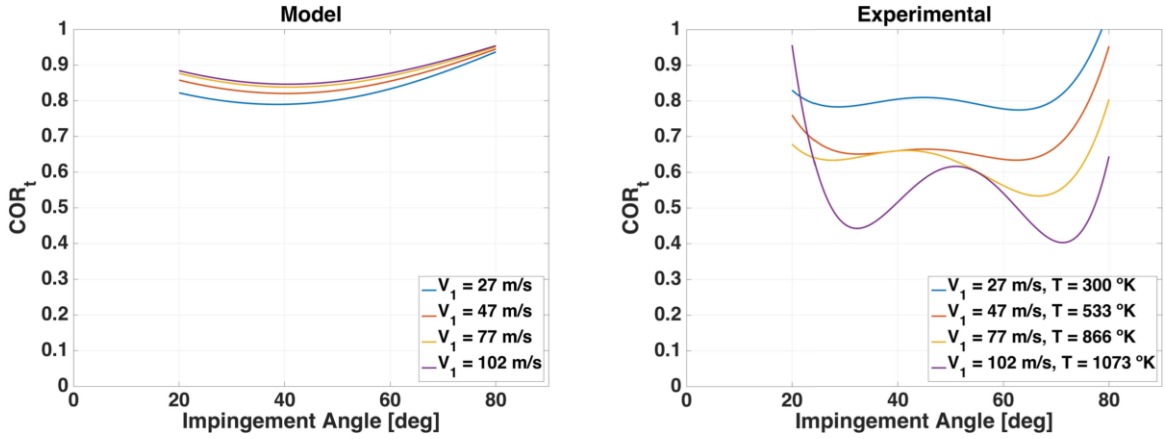

c) CoR_T

Figure 14 Comparison of Bons model predictions and experimental data[31]

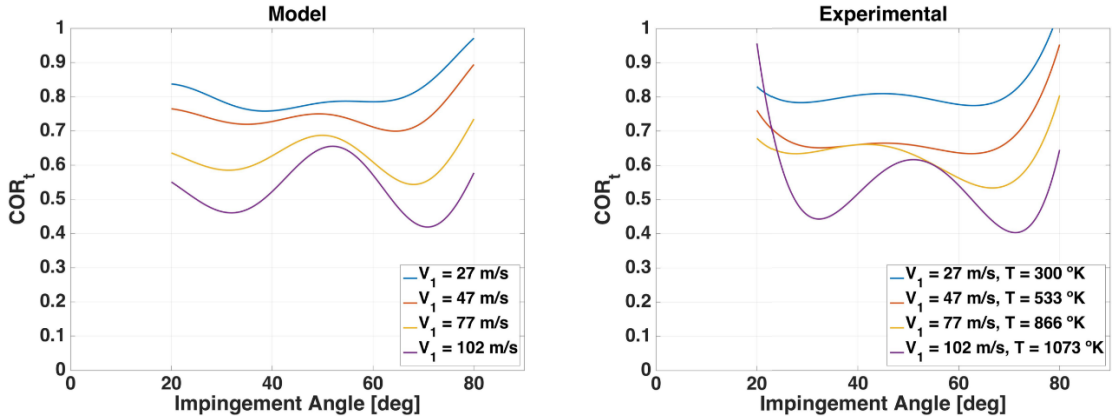

Figure 15 Comparison of Bons model predicted and experimentally measured COR_T with a posteriori empirical correction by Chow [31]

More recently an energy based model has been suggested that includes both temperature and velocity considerations, Equation 29 [71]. This assigns a probability of sticking for each impact and assumes a portion of each particle sticks, this is often employed by other workers rather than setting a critical probability that determines if the whole particle arriving at a surface sticks.

$$p = Ae^{\frac{C_1}{\frac{1}{2}m_p v_p n^2 (1+C_2\frac{T}{T^*})}} \qquad 29$$

2.4.1.3 Other Factors

Roughness - A particle is not able to impact on concave sections of the surface whose angle (γ) is steeper than the particle's own trajectory (α_1, Figure 16). This means particles have a higher probability of hitting the luff side of roughness elements, called the shadow effect, and it effectively

increases the particle's impingement angle. The extent of this effect also depends on the particle size and roughness height (Figure 17). Sommerfeld showed that altering the impingement angle by a random value, according to a Gaussian distribution (ξ), was a good approach to simulate roughness (Equation 30) [65], [72].

$$\alpha = \alpha_1 + \Delta\gamma\xi \qquad 30$$

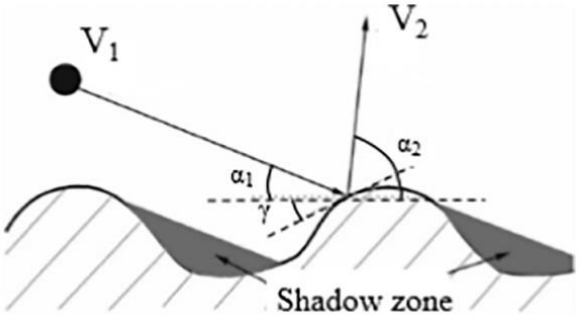

Figure 16 Diagrammatic explanation of the shadow effect [73]

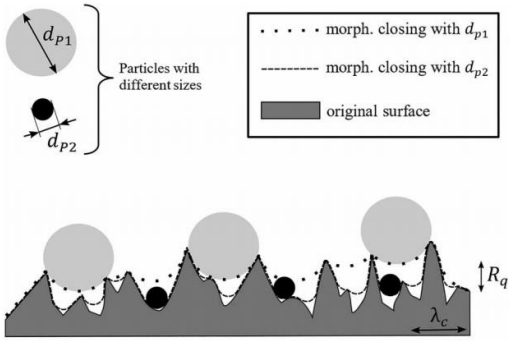

Figure 17 Effect of particle size and roughness height on the effective surface roughness. Dotted line represents the effective surface seen by the large particles, dashed line represents the effective size seen by the small particles. [72]

Temperature – This is an important factor as it effects the particle viscosity and yield stress [36]. Material properties have been altered in some simulations according to the rule of mixtures, as per Equation 31, in an attempt to make the model temperature sensitive [58], [74].

$$X_1 = \sum_{i=1}^{N} X_i V_i \qquad 31$$

2.4.2 Erosion Modelling

In order to model deposition accurately it is also necessary to take into account erosion, such that realistic deposits are formed, it is sensible to imagine that deposits would reach a steady state or their formation would be cyclical. Deposits can be removed if the particle-particle or particle-wall adhesion/sticking force is overcome, either by aerodynamic forces or by forces exerted by incoming particles. It has been found, by two separate studies, that spherical particles are released from surfaces by a rolling action rather than sliding or lifting [75]. Another process that leads to the

reduction in the mass deposited is the cooling of formations which can cause the deposits to crack [76].

A model that accounts for erosion due to further incoming particles is that developed by Tabakoff et al. who worked in this area for more than forty years starting in the 1970s [77]. The model, given by Equations 32 - 35, predicts the erosion rate (ER, mg) per unit mass of impacting particles on a surface (g). K_1, K_2, K_{12}, and K_C are material dependent constants.

$$ER = K_1 f_a |V|^2 \cos^2 \alpha \left(1 - R_T^2\right) + f_i \quad 32$$

$$R_T = 1 - 0.0061\,|V| \sin \alpha \quad 33$$

$$f_a = \left(1 + K_c \left[K_{p,s}\, \sin \frac{90\,\alpha}{\alpha_0}\right]^2\right) \quad 34$$

$$f_i = K_s (|V| \sin \alpha)^4 \quad 35$$

Erosion due to aerodynamic forces on deposits can be modelled using critical moment theory. This approach predicts a critical wall shear velocity at which a particle will detach from a surface (u_{rc}), resulting in Equation 36 [68], [78]. Figure 22 lays out the basis for the model, in which the force applied must generate a sufficient moment around point O to detach the particle. This model assumes a spherical particle, and would likely change significantly for otherwise shaped particles, especially as the derivation uses a relation for the contact area. Further this approach requires the work of sticking (W_A) which is not readily available, this is further complicated as it depends on both the particle and surface material.

$$u_{rc}^2 = \frac{C_c\, W_A}{\rho_f\, d_p} \left(\frac{W_A}{d_p K_{c1}}\right)^{\frac{1}{3}} \quad 36$$

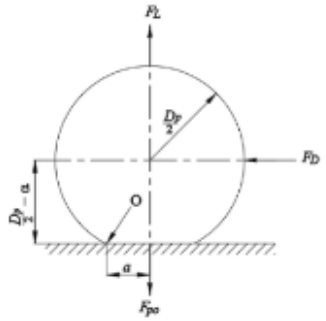

Figure 20 Free-body force diagram used to predict the critical momentum at which particles are re-entrained [41]

2.5 Numerical Methods and Investigations

Equations for a particle's motion can be put into either the Lagrangian or Eulerian form, with each having its own advantages. The Lagrangian form requires equations to be solved for each particle so they are individually tracked, it implies a discrete phase. This method is easy to implement, results in a more detailed and easily understood description of the particle phase, is more stable for large particle velocity gradients, and less prone to numerical diffusion errors. The Eulerian form treats particles as a second continuum phase for which ensemble averaged field quantity equations (continuity, momentum, and energy) are solved. In this form boundary conditions become harder to model, as do particle-density discontinuities. Another challenge is defining the exchange rates and closure laws of the interaction between the two phases. While Eulerian approaches would allow the effect of large numbers of particles to be determined in a single calculation, for the aforementioned reasons, in discrete phase flows concerning deposition, the Lagrangian formation is favoured and detailed further below. Figure 18 provides an overview of the couplings that can exist and the typical naming convention. Figure 19 provides a good starting point to understand which of these are important, whilst it is recognised mass loading fraction is important little information is available on how [71, 19, 42, 27].

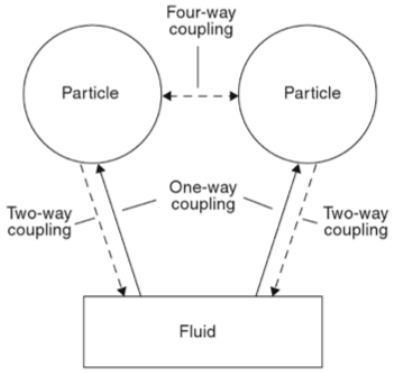

Figure 18 Fluid Particle coupling conventional naming convention [41]

From the data in Section 2.1.3, conditions typical of an extremely high particle loading can be determined. If a concentration of 1 mg/m^3 with a density of 1000 kg/m^3 the particle volume fraction (*PVF,* Equation 37) is 10^{-9} at the inlet. Assuming compression through the engine increases

this by an order of magnitude, the PVF remains bellows 10^{-6}, and hence the situations we are interested in can be modelled with one-way coupling based on Figure 19. This is true regardless of mass loading fraction *(MLF,* Equation 38*)*, particle relaxation time (τ_{p}), and the Kolmogorov time scale (τ_{K}, Equation 39). This is beneficial and time efficient as the Lagrangian method can be used as a post-processing step using a converged fluid solution, rather than requiring a coupled solution [35]. Although this assumption may need investigation if there is significant increase in local particle volume fraction, due to effects such as turbophoresis (Section 2.2.3), this is not usually considered. Higher order coupling requires a Eulerian approach, not only because there is a lack of understanding of the fluid process at high *PVF* making it hard to model all forces in the Lagrangian method, but also because a Lagrangian approach would require unfeasible memory resource and would be too timely to implement as an engine design tool [35].

$$PVF = V_{\mathrm{p}}/V_{\mathrm{Tot}} \qquad 37$$

$$MLF = M_{\mathrm{p}}/M_{\mathrm{Tot}} \qquad 38$$

$$\tau_k = \frac{l_{\mathrm{k}}}{\eta_{\mathrm{k}}} \qquad 39$$

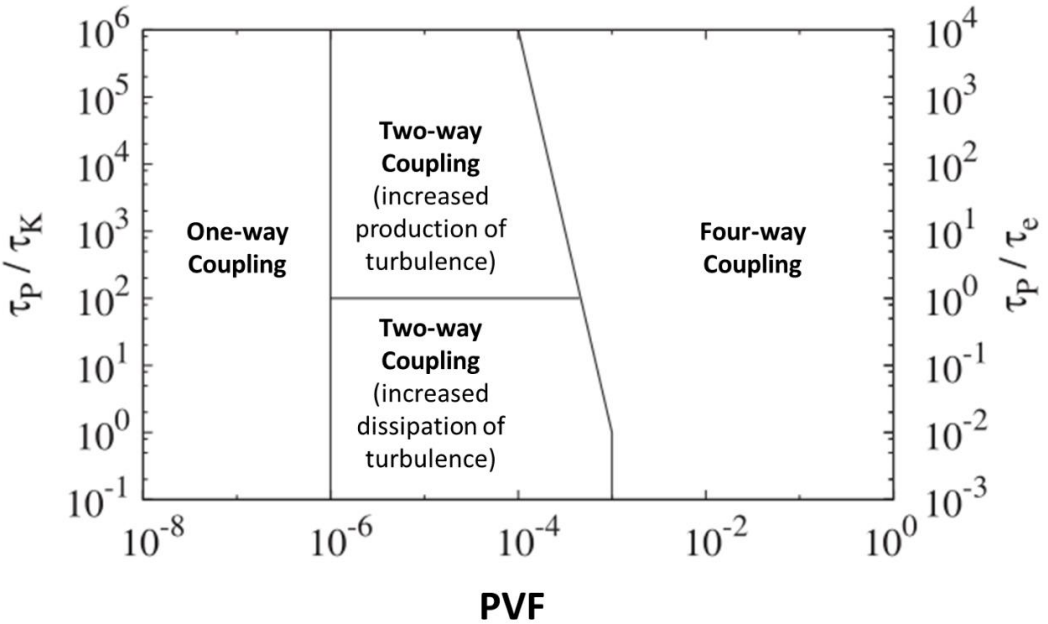

Figure 19 Suggested coupling requirements for two phase discrete systems as a function of particle relaxation time, fluid time scales, and particle volume fraction [79].

2.5.1 Fluid Phase

The method used to model particle motion is highly dependent on the approach for solving the continuous medium. The most commonly used methods for solving the continuous medium (in order of reducing computational expense) are Direct Numerical Simulation (DNS), Large Eddy Simulation (LES), and Reynolds Averaged Numerical Simulation (RANS).

DNS resolves every scale of turbulence and is unsteady. As the number of cells scales with the Reynolds number to the power of 3.6, these simulations remain limited to low Reynolds numbers and very simple geometries such as pipes and channels [52]. When this approach is used there is the choice between treating the particle as a point mass, or fully resolving the particle using a moving boundary in the mesh. Fully-resolving the particles can perhaps be considered the most precise and pure approach, there is direct coupling between the particle motion and fluid flow. This approach requires particles to be bigger than the grid and resolves hydrodynamic forces to calculate particle motion, but in practice only $O(10^4)$ particle can reasonably be simulated [52]. Treating particles as a point mass enables four orders of magnitude more particles to be modelled, under the constraint that the particles must be much smaller than the DNS grid spacing [52]. This approach means that the flow around particles is not resolved and it also requires the particle to be moved around by calculated forces such as lift and drag. A particular difficulty, recently observed, is that many DNS codes require quiescent conditions as an inlet boundary condition, limiting their applicability in problems dominated by turbulent deposition.

LES models large scale eddies, but averages over the smaller scales of turbulence closer to the wall, and provides a time varying solution. The number of cells scales with $Re^{2.4}$ and as such these simulations are most often used for intermediate Reynolds number flows in geometries that are more realistic of the real world [52]. The applicability of such codes in a timely manner to real engine problems is much more mature than DNS. Although LES studies are gaining traction, they remain impracticable for the most complex regions of the engine and in design studies where a large number of solutions are explored. Further, work completed in complement to this thesis found LES were very sensitive to the specification of turbulence at the inlet.

RANS models all scales of turbulence with a variety of models available and effecting the computational requirements. Most often two-equation models such as k-epsilon and k-omega are used, the specific choice is heuristic. These models make the assumption of isotropy which is particularly limiting for modelling turbulent transport in wall bounded flows, as anisotropy near the wall is known to be influential. The Reynolds stress model provides the complete Reynolds stress tensor from a RANS solution. Other turbulence models e.g. v^2-f and EARSM synthetically predict anisotropy of the Reynolds stresses providing wall normal fluctuations in velocity. These models have shown improvements in the modelling of separated and rotating flows. This is particularly important in the case of gas turbines and particle motion.

RANS simulations remain dominant, and frequently the only timely way of modelling complicated real gas turbine geometries. As they lose certain aspects of flow unsteadiness the first fundamental challenge of this research is to develop modelling capabilities for particle-turbulent interaction using high quality RANS flow solutions. The models must be capable of capturing effects driven by particle turbophoresis, and the accuracy is evaluated to determine if it provides a route for engine component design and particle damage risk assessment.

2.5.2 Discrete Phase

Section 2.2 described the forces acting on a particle, here methods for their calculation in RANS simulations are discussed. In addition to the forces described the modelling of Turbophoresis, the process by which particles preferentially migrate from regions of high turbulence to regions of low turbulence, is discussed. As turbulence is modelled in RANS this modelling must be extended to the discrete phase. LES fluid solutions require different models of Turbophoresis which account only for the effect of sub grid scales of turbulence on particles. Hence there is no clear advantage over RANS fluid solutions which remain industry standard.

2.5.2.1 Drag

In the simplest of cases over a sphere (sub-sonic uniform continuum flow) the linear region of the Stokes regime is modelled using Equation 40. As the relationship becomes non-linear correction

factors are included, Equation 41 was proposed by Oseen and 42 by Ingebo [39]. In the Sub-critical regime ($100 < \mathrm{Re_p} < 3 \times 10^5$) a constant value of 0.445 is used, known as Newton's drag law [39].

$$C_\mathrm{d} = \frac{24}{Re_\mathrm{p}} \qquad \text{for } Re_p < 1 \qquad 40$$

$$C_\mathrm{d} = \frac{24}{\mathrm{Re_p}}\left(1 + \frac{3}{16}\mathrm{Re_p}\right) \qquad \text{for } Re_p < 5 \qquad 41$$

$$C_\mathrm{d} = \frac{27}{\mathrm{Re_p^{0.84}}} \qquad for\ 6 < Re_p < 400 \qquad 42$$

In order to model the effects of gas rarefaction the Cunningham correction (C_C) factor is used. The drag is reduced as the gas becomes further rarefied (Figure 20) as the no-slip condition is no longer valid [80] [75].

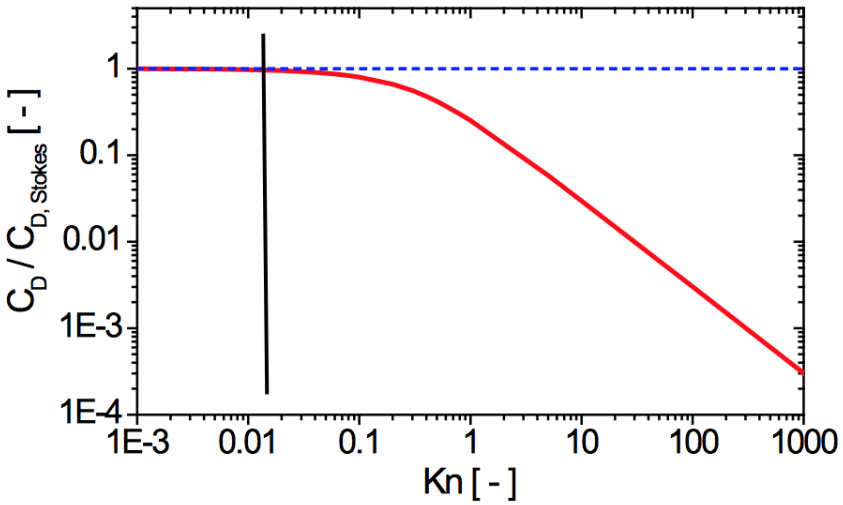

Figure 20 Reduction in drag coefficient due to rarefaction of the fluid [40]

These methods are not valid at high Mach numbers [39], Mach number effects become significant above Mach 0.6, when sonic flow first occurs on a spheres surface. Above this Mach number empirical correlations are used [81], ANSYS FLUENT (which is employed in the remainder of this thesis for numerical solution) expresses the drag coefficient as a function of the particle Reynolds number using a second order polynomial.

For non-spherical particles shape factors are used to modify spherical drag laws. There are various formulations, FLUENT uses Equation 43 developed by Haider and Levenspiel [82]. In this equation each constant (A, B, C, and D) is a function of the shape factor $\frac{s_\mathrm{eqv}}{s}$ and $\mathrm{Re_p}$ is the Reynolds

number based on an equivalent sphere diameter [81]. This approach has not been confirmed to be accurate for all flows and particle shapes.

$$C_{\mathrm{D}} = \frac{24}{\mathrm{Re_p}}\left(1 + A\,\mathrm{Re_p^B}\right) + \frac{C\,\mathrm{Re_p}}{D + \mathrm{Re_p}} \qquad 43$$

2.5.2.2 Magnus Lift

The theoretical calculations of lift coefficient at a low Reynolds number result in Equation 44, while an experimental investigation at higher Reynolds numbers (10-140) showed a particle Reynolds number dependency, Equation 45 [83].

$$C_{\mathrm{L}} = 2 \qquad 44$$

$$C_{\mathrm{L}} \cong 0.45 + (2\omega - 0.45)\exp(-0.075\omega^{0.4}\mathrm{Re_p^{0.7}}) \qquad 45$$

2.5.2.3 Saffman Lift

Equation 46, from Li and Ahmadi, can be used to model the Saffman lift (Section 2.2.6). In this equation the constant C_1 is found to be 2.59 and s is the strain rate tensor. This equation is only valid where $\mathrm{Re_p} < \sqrt{\mathrm{Re_\Gamma}}$.

$$F_{\mathrm{Saff},ij} = \frac{2C_1\nu^{1/2}\rho_{\mathrm{f}}s_{ij}}{\rho_{\mathrm{p}}d_{\mathrm{p}}(s_{lk}s_{kl})^{\frac{1}{4}}}V_{\mathrm{rel}} \qquad 46$$

2.5.2.4 Brownian Motion

Brownian motion is often modelled as a Gaussian white noise process using Equation 47, where ζ is a normally distributed random number. $S_0$is defined by Equation 48 [84], where k_{B} is the Boltzmann constant.

$$F_{\mathrm{brown,i}} = \zeta_{\mathrm{i}}\sqrt{\frac{\pi S_0}{\Delta t}} \qquad 47$$

$$S_0 = \frac{216\nu_{\mathrm{f}}\mathrm{k_B}\mathrm{T_f}}{\pi^2\rho_{\mathrm{f}}d_{\mathrm{p}}^5\left(\rho_{\mathrm{p}}/\rho_{\mathrm{f}}\right)^2 C_{\mathrm{C}}} \qquad 48$$

2.5.2.5 Thermophoresis

There are multiple models of thermophoresis, Fluent uses that suggested by Talbot [85] (Equation 49). It has been noted that this commonly used model of thermophoresis does not hold well at high values of thermal conductivity [47][86].

$$F_{\text{thermo, x}} = -K_{\text{thermo}} \frac{1}{m_{\text{p}} T_{\text{f}}} \frac{\partial \text{T}_{\text{f}}}{\partial \text{x}} \qquad 49$$

$$K_{\text{thermo}} = \frac{6\,\pi\,\text{d}_{\text{p}}\mu_{\text{f}}^2 1.17(\frac{\kappa_{\text{f}}}{\kappa_{\text{p}}} + 2.18\text{Kn})}{\rho_{\text{f}}(1 + 3.42\text{Kn})(1 + 2\frac{\kappa_{\text{f}}}{\kappa_{\text{p}}} + 4.36\text{Kn})} \qquad 50$$

2.5.2.6 Turbophoresis

The challenge of modelling turbophoresis lies in coupling the particle Reynolds stresses ($\overline{v_i v_i}$) to the fluid Reynolds stresses ($u_i u_i$) and modelling these instantaneous fluctuations (Equation 8). Young and Leeming suggested the approach in Equation 51, where Γ is the ratio of particle and fluid time scales [53]. In this the eddy timescale (τ_e) is defined as $\overline{v_i v_i}/\nu_{\text{t}}$ where ν_t is the turbulent kinematic viscosity. This is neither equivalent to the Eularian nor Lagrangian integral timescales, which makes this approach difficult to use [53].

$$\frac{\text{d}\overline{v_i v_i}}{\text{d}x_i} = \frac{\text{d}\Gamma\overline{u_i u_i}}{\text{d}x_i}$$

$$\Gamma \approx \frac{\tau_{\text{e}}}{\tau_{\text{e}} + \tau_{\text{p}}} \qquad 51$$

In practice it is difficult to accurately couple the particle and fluid fluctuating velocities, rather an instantaneous fluid fluctuation is modelled over many successive particle injections. There have been many attempts to model turbulent fluctuations using stochastic approaches, the most popular models are the Discrete Random Walk (DRW), Continuous Random Walk (CRW), and Generalised Langevin Model (GLM). Additionally Jin and Reeks [87] suggest a model based on the physical understanding that near wall coherent structures (turbulent sweeps and ejections) are critical to deposition (Figure 11). With the exception of the Generalised Langevin Model (GLM) these are non-exact equations that are designed only to capture the most important features of turbulence (i.e. they do not derive from the Navier Stokes equation).

Models that predict the unsteady velocities in the fluid field, and the turbophoretic forces resulting on particles, are typically described as a random walk. The development of modelling where the unsteady velocity a particle experiences changes during its interaction with a single eddy, called a Continuous Random Walk, is described below (for a more comprehensive derivation see Appendix A). In 1908 Langevin proposed that Brownian motion could be modelled using Markov chains. These are models in which the next state is only dependent on the current state i.e. they are without "memory". In Equation 52 the transported quantity is the velocity (u), and this is expressed as the sum of a damping like term and a stochastic acceleration term. Often in this area references to the Fokker-Planck equation are made, this is the Eulerian equivalent of the Langevin equation [88].

It is important to note that these equations are Markov sequences, not processes, meaning that they are only well defined at discrete times. In practice this means that $dt \to 0$ is not the solution.

$$\frac{du}{dt} = -\alpha u + \beta\, \xi(t) \qquad 52$$

To the author's knowledge Taylor was the first to apply this thinking to turbulent diffusion in 1921 [89][88]. Under this use the first term is not related to viscous dissipation but the decoupling of the previous velocity fluctuation; the second term is the acceleration from the turbulence. When the Lagrangian time scale is defined by Equation 53, the coefficients α and β are then given by Equations 54 and 55 respectively [90].

$$t_{\mathrm{L}} = \frac{1}{U'(0)} \int_0^{\infty} \overline{w'(0) w'(t)}\, \mathrm{d}t \qquad 53$$

$$\alpha = 1/t_{\mathrm{L}} \qquad 54$$

$$\beta = \sigma \sqrt{\frac{2}{t_{\mathrm{L}}}} \qquad 55$$

Various workers replicated this approach, and found that simulations predicted a non-physical accumulation of particles in regions of low-turbulence [90], [91]. This is due to the mean pressure gradient that particles experience in an inhomogeneous flow [90]. This led to multiple

suggestions for a third, drift correction, term. Equation 56 incorporates the suggestion by Legg and Raupach [90]. Wilson et al. suggested a drift correction half the size based on a different Markov chain which came to be referenced as the normalized continuous random walk (Equation 57) [92][93]. The normalized Langevin equation uses a different transported quantity, the velocity over the RMS fluctuating velocity (u/σ). This has been found to better predict velocities when large gradients in turbulence are present [93] [94]. Both of these suggestions were initially ad-hoc responses to observed phenomena [88]

$$\frac{\mathrm{d}u}{\mathrm{d}t} = -\frac{1}{t_\mathrm{L}}u + \sigma\sqrt{\frac{2}{t_\mathrm{L}}}\,\xi(t) + \frac{\partial\sigma^2}{\partial x} \qquad 56$$

$$\frac{\mathrm{d}\frac{u}{\sigma}}{\mathrm{d}t} = -\frac{1}{t_\mathrm{L}}\frac{u}{\sigma} + \sqrt{\frac{2}{t_\mathrm{L}}}\,\xi(t) + \frac{\partial\sigma}{\partial x} \qquad 57$$

Finally, in 2006 Bocksell and Loth re-derived the drift correction to account for the finite mass of particles [94]. They were able to more rigorously derive the finite drift correction by considering the total derivative of the change in fluid velocity along the path, making the distinction between the finite inertia and zero-inertia cases more apparent. In the case of a fluid tracer (no inertia), Equation 58 gives the change in fluid velocity along a particle's path, but for a finite mass particle which decouples from the fluid this becomes Equation 59. In simulations the first term is accounted for by sampling the fluid velocity along the trajectory. Using a particles equation of motion Bocksell and Loth showed the second term of Equation 59 is equal to Equation 60.

$$\overline{\frac{\mathrm{D}u_\mathrm{f}}{\mathrm{D}t}} = \overline{\frac{\partial\bar{u}_\mathrm{f}}{\partial t}} + \overline{u'_\mathrm{f}\frac{\partial u'_\mathrm{f}}{\partial x}} \qquad 58$$

$$\overline{\frac{\mathrm{D}u_\mathrm{f}}{\mathrm{D}t}} = \overline{\frac{\partial\bar{u}_\mathrm{f}}{\partial t}} + \overline{u'_\mathrm{p}\frac{\partial u'_\mathrm{f}}{\partial x}} \qquad 59$$

$$\overline{u'_\mathrm{p}\frac{\partial(\frac{u'_\mathrm{f}}{\sigma})}{\partial x}} = \overline{u_\mathrm{f}\frac{\partial(\frac{u'_\mathrm{f}}{\sigma})}{\partial x}}\frac{1}{1+\mathrm{Stk}} \qquad 60$$

In recent studies the most commonly used model is Equation 61, which incorporates the normalized transport term and finite drift correction. Research more recently has focussed on the practicalities of using this equation.

$$\frac{\mathrm{d}\left(\frac{u}{\sigma}\right)}{\mathrm{d}t} = -\frac{1}{t_{\mathrm{L}}}\left(\frac{u}{\sigma}\right) + \sqrt{\frac{2}{t_{\mathrm{L}}}}\ \xi(t) + \overline{u_{\mathrm{f}}\frac{\partial\left(\frac{u_{\mathrm{f}}'}{\sigma}\right)}{\partial x}\frac{1}{1+\mathrm{Stk}}} \qquad 61$$

Pope derived a different stochastic model which was consistent with the Navier-Stokes equations, Equation 62. This approach led to the natural occurrence of a drift correction type term [95]. In this the G_{ij} and B_{ij} are drift and diffusion-like parameters. Taniere and Arcen note that this model is less tractable than the normalized CRW model [95] and no deposition predictions have been made in real flows using this approach.

$$\mathrm{d}u_i = \left[-\frac{1}{\rho}\frac{\partial\langle p\rangle}{\partial x_i} + \nu\nabla^2\langle U_i\rangle\right]dt + G_{ij}\left[u_j - \langle u_j\rangle\right]\mathrm{d}t + B_{ij}\mathrm{d}W_j \qquad 62$$

Unlike the above models the Discrete Random Walk (DRW) assumes that the velocity fluctuation a particle sees is constant over the length of any eddy the particle encounters. This model is also referred to as the eddy interaction model (EIM), as it models a sequence of eddy interactions. This leads to different behaviour, Figure 21. Each eddy has a velocity (taken from a Gaussian probability based on the Reynolds stresses) and an eddy lifetime (τ_{e}). The time for a particle to cross this eddy is given by Equation 65. The eddy lifetime is either calculated to be twice the local Lagrangian timescale (Equation 63) or a proportion of this using a stochastic term (Equation 64) where the Lagrangian time scale is multiplied by the log of a uniform random number (r) between 0 and 1. The particle experiences the eddy velocity for the shorter of the eddy lifetime and crossing time. The DRW/EIM is very simple to model but has shown to over predict deposition in confined flows within the diffusion-impaction and diffusion regimes by several orders of magnitude [54].

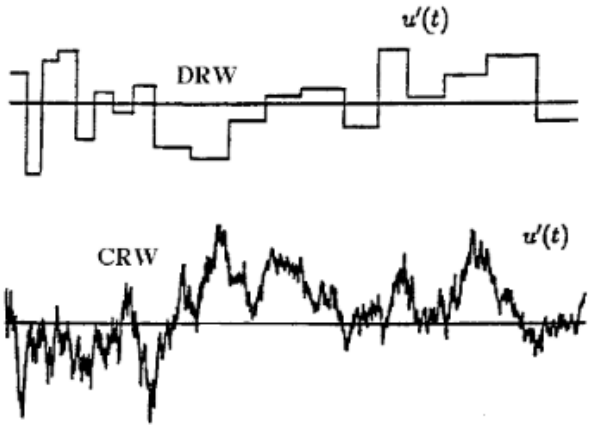

Figure 21 Comparison of the velocity fluctuations predicted by a DRW and CRW model[91]

$$\tau_{\mathrm{e}} = 2T_{\mathrm{L}} \quad 63$$

$$\tau_{\mathrm{e}} = -T_L \log(r) \quad 64$$

$$t_{\mathrm{cross}} = -\tau_{\mathrm{e}}\, ln\left[1 - \left(\frac{L_{\mathrm{e}}}{\tau_{\mathrm{p}} u_{\mathrm{rel}}}\right)\right] \quad 65$$

2.5.3 Numerical Studies

2.5.3.1 Idealistic Simulations

There have been extensive studies on simple flows in order to develop particle tracking models as the experimental data are most consistent and comparable in these flows. The studies are usually high fidelity simulations (DNS) where the aim is to understand additional complexities such as non-spherical or flexible particles better, or lower fidelity (LES/RANS) that look to match results of DNS or experiments.

There have been a number of studies using DNS. Examples of the more theoretical studies include Soldati and Marchioli [51] use of a point-based particle approach and DNS of a channel flow to conduct a thorough examination of the near wall structures responsible for turbulent deposition, confirming the importance of coherent near wall turbulent structures. On the other hand Ouchene et al. used an immersed boundary method and DNS to derive a better correlation for drag of ellipsoid particles in the Stokes regime, as well as understanding the effect of these particles clustering [96]. In an attempt to verify the potential of stochastic methods for modelling turbophoresis Mito and Hanratty used a DNS solution alongside a stochastic particle model, the idea being that the DNS solution would remove the additional hurdles that come with modelling turbulence. They found that the use of a joint Gaussian distribution to calculate the fluctuation in the normal and stream wise directions improved predictions of deposition [97]. More recently Taniere et al. further scrutinised the ability for these empirical stochastic models to accurately model deposition. They compared the Generalized Langevin Model (GLM) and Normalized Continuous Random Walk (CRW) using a DNS simulation. The implementation of the Normalized Langevin equation neglected eddy crossing effects and certain Reynolds stress terms. Their conclusion was

that the CRW satisfactorily predicted the RMS of longitudinal and wall normal particle velocities, but the kinetic stresses and off diagonal fluid-particle covariances calculate, with their implementation, were not realistic. Their conclusion was that the Normalised CRW model is more tractable in engineering situations, compared to the GLM's intractable nature [95].

In cases where the authors have put this approach to the test in simple flows the results have been promising. A commonly referenced study, conducted by Kallio and Reeks, investigates duct flow using a stochastic model informed by theoretical knowledge of the flow-field such as the law-of-the-wall relations for fluctuating velocities [98]. This study found good agreement to the experimental data available [98]. Tian and Ahmadi investigated the potential for such models to be informed by a RANS solutions using a 2D channel. They found that the use of a specific (two-layer zonal) model combined with a correction to Reynolds stresses in the wall normal direction (such that the known law-of-the-wall was replicated) achieved the best predictions [99]. Their work did not include any modelling of the drift correction terms later found to be important for finite inertia particles, despite studying particles for which this effect is important [99][94]. Bocksell and Loth re-derived the most commonly used form of the drift correction, for finite-inertia particles, in their 2006 study [94]. In this, they used a DNS fluid solution to compare the effects of assuming turbulence was isotropic, that only the diagonal terms of the Reynolds stress tensor matter, and additionally including R_{uv}. They found that the latter was required for the best predictions, indicating the benefits of enhanced fidelity turbulent statistics. Further, they compared stochastic models where the transport term was the instantaneous velocity to that where the instantaneous velocity is normalized by the Reynolds stress, finding the latter was needed to prevent non-physical diffusion near walls [94]. They commented that the predictions may be improved with the use of non-Gaussian statistics or a better description of the near wall flow field [94]. In an attempt to extend this approach to non-duct flows and improve the accuracy Dehbi et al. suggested a formulation that used DNS statistics near the wall and could be applied to any flow using a body-fitted coordinate system [19], [100]. This paper showed that this model also satisfied the well-mixed criterion successfully [61]. Stochastic methods have shown promise in basic flows, but even in these turbulence's anisotropy and near wall complexity must be accounted for to produce accurate results.

2.5.3.2 Flows with acceleration

There are numerous numerical studies which consider deposition in bends of circular and rectangular cross sections. These studies tend to use RANS solutions not least due to researchers' computational resource limitations, as discussed in Section 2.5.1. For example complementary to the current research reported in this thesis, the University of Surrey undertook a DNS study of flow around a 90 degree bend (Figure 22). It took more than four months to successfully simulate a system, at a Reynolds number of 10000, and required major domain restrictions and simplification of the inlet conditions (no inlet turbulence), using some of the most experienced users of DNS codes in the UK.

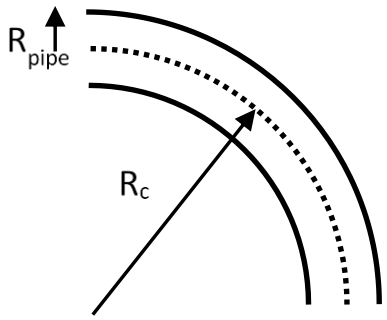

Figure 22 Key dimension of a 90 degree pipe. The ratio of curvature (R_0) is defined as the square root of the radius of curvature (R_c) divided by the radius of the pipe (R_{pipe}).

Nonetheless, there have been some DNS studies of particle deposition in accelerating flows. Noorani et al. [101] investigated the effect of minor curvature (R_0=0-0.1) on deposition at a Reynolds number of 11,700, they noted that even slight curvature changed particle distribution significantly. It was also found that the side-wall boundary layer that formed was critical in determining the path of particles, Figure 23. Specific observations included that the centre of the Dean vortices were deplete of particles, Figure 24, and that both weak and strong secondary motions affect particle trajectory via turbophoresis. Furthermore, particular balances of centrifugal and turbophoresis forces, seen in Figure 25, can, unexpectedly lead to the highest deposition concentration being at the inner side of the bend.

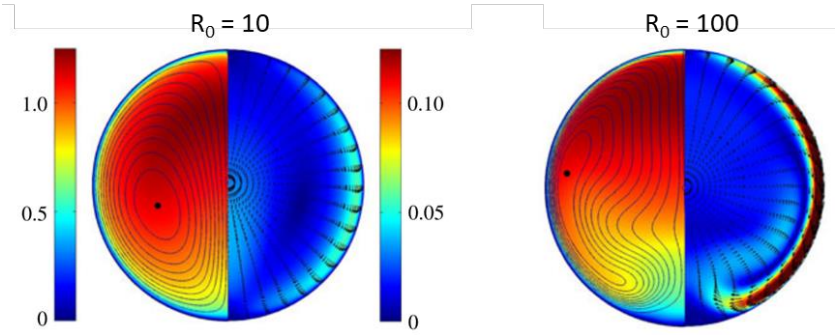

Figure 23 Flow structure in a mildly curved (left, R_c=10) and strongly curved (left, R_c=100) pipe. The left shows stream-wise velocity and the right in-plane motion. The centres of the vortices are marked.

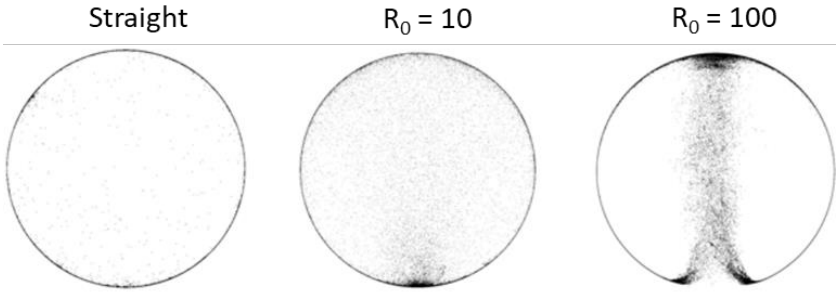

Figure 24 Position of particles, projected onto front view, with Stk = 2.26 in a straight pipe, mildly curved (left, R_c=10) pipe, and strongly curved (left, R_c=100)pipe (left to right) .[101]

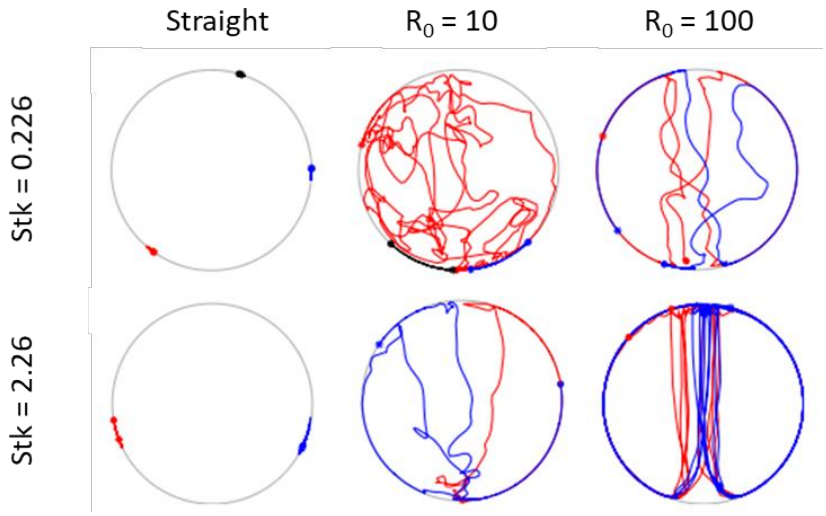

Figure 25 Particle trajectories of small (top, Stk *= 0.226) and larger (bottom,* Stk*=2.26) particles in a straight pip (left, R_c= 0), mildly curved pipe (left, R_c=10), and strongly curved pipe (left, R_c=100). Tracks run from the solid dot to the asterisk.*

Huang and Durbin [102] studied deposition in a serpentine duct, with U-bend, at Stokes number of 0.125-0.6 at a Reynolds number of 2,800. They investigated the particle dynamics extensively and suggested there was a "reflection layer" in which particles concentrate around the bend. Their studies also showed a concentration of particles before the separation that forms around the inner bend. Neither of these studies compared their work to experimental data.

The experimental work of Pui et al. [103] has been the subject of multiple numerical studies. The most computationally intense approach was that of Breuer et al. [104], fully-resolved LES was used with a point particle approach. The main development of this study was an efficient particle tracking approach which made the work feasible. Usefully, spatially resolved results of particle deposition in the stream-wise and circumferential directions was given. Berrouk et al. [105] used LES that did not fully resolve the turbulence, coupled with a stochastic sub-grid model, and reported the deposition as a function of the particles' the initial position. Dehbi et al. applied their implementation of the CRW with a $k-\omega$ turbulence model and found satisfactory agreement looking at the penetration fraction, although the CRW model made little difference when compared to the default in-built FLUENT model that does not account for turbulent fluctuations.

Wilson and Matida [89] attempted to match their own experimental results using a RANS solution and SST turbulence model for the fluid phase, and the FLUENT DRW model for particle tracking. They found satisfactory matching above a Stokes number of 0.4. They also stated there was a Reynolds number effect which it did not capture, decreasing deposition fraction with increasing Re for particles with a Stokes number of 0.2. They argued this was driven by different dominant eddy frequencies at each Reynolds number. [89]

There have also been attempts to use RANS simulations in design focused studies of bends. Arsalanoo [106] used FLUENT's in built tracking, neglecting turbulent fluctuations, to study the effect of imposing swirl on the flow before it entered the 90 degree bend on the deposition around the bend. Multiple spiral vane configurations were considered, varying the height of the vanes and their pitch. It was found that increasing swirl increased, then decreased, the deposition for smaller particles. For larger particles any additional swirl decreased deposition.

Whilst there have been numerous studies of deposition in flows with acceleration the findings beyond integral deposition fractions are largely qualitative, and there is no validation data beyond this fidelity.

2.5.3.3 Modelling of Applied Deposition Problems

A number of numerical studies have been published where particle deposition models are used to model real world deposition problems, they are more often focused on comparing deposition models, with limited comparison to experimental data.

Both Dehbi and Ghahramani [100], [107] applied the CRW model to an upper airway tract and compared the results to experimental data. The geometry used by Dehbi was simpler than the realistic model used by Ghahramani [100], [107]. In both cases trends in deposition fraction were well replicated by the CRW, but the deposition of larger particles was under predicted [100], [107]. Ghahramani, who also applied the DRW model, found that this was unable to match those trends. In a separate study using Lagrangian tracking of an LES solution (i.e. ignoring sub-grid scale fluctuations) Ghahramani found similar results to those predicted by the CRW, but with particles depositing on different sites. No experimental data of this fidelity was presented, so it is impossible to know which model is most accurate [107].

In gas turbines, there have been studies of particle deposition/erosion across most engine parts. At the front of the engine Suman et al. used the DRW model to predict spatially resolved deposition on subsonic compressor blades and presented the results in a spatially resolved manner [108], [109]. In this work they developed a probabilistic sticking model but no comparison to experimental data were made.

In the turbine more extensive studies of deposition have been conducted: due to the temperatures, the arrival of particles at a surface is more likely to result in their sticking here. The majority of the studies focus on the main gas path.

A group, led by Prof. Bons, at The Ohio State University has completed a number of studies in this area. Whitaker et al. studied the effect of freestream turbulence on predicted deposition and found the DRW model to be insufficient to capture the increase in deposition as a function of particle size and turbulence intensity [110]. Prenter et al. compared the use of steady and unsteady RANS solutions, neglecting turbophoresis [111]. They found that there were significant differences in the results, but as there was no comparison to experimental data it was not possible to conclude the precise deficiencies in each of the approaches [111]. Borello et al. completed a wide ranging study

of erosion and deposition throughout the hot path, but validation was limited to side-by-side pictures with significant differences apparent [43].

The Ohio State group has also completed studies related to internal cooling passages, Casaday et al [112] looked at the formation of conical depositions under impinging jets in these passages.

Other research in this area includes that by Sreedharan and Tafti [113], who investigated the deposition and erosion of syngas ash, transported by the hot gas path, into the cooling holes using LES. They reported that for each particle size there was an optimum blowing ratio that minimised deposition but no validation in a comparable flow was undertaken [113]. Wylie et al. looked at deposition in cooling holes, cause by particles transported in the secondary air system, using the numerical results to explain their experimental findings [114]. Forsyth et al applied the CRW and DRW models to a shank cavity finding that the CRW had much higher sensitivity to particle size, especially for smaller particles, in this flow [54].

For applied deposition problems numerical studies have attempted to go beyond the analysis of integral deposition fractions, with a focus on exploring likely deposition rather than validating models. Further, these studies have been largely qualitative and limited by their dependence on particle-wall interaction models (Section 2.4.1), and lack of equal fidelity experimental data (Section 2.6). This makes apparent the need to validate models in such flows quantitatively beyond integral deposition fractions. This requires a validated particle-wall interaction model or, if this is not available, comparison without reliance on particle-wall interaction models. Further, higher fidelity experimental data of representative experiments is required for more robust validation.

2.6 Experimental Methods and Investigations

The most commonly studied geometry is a straight pipe. There have been multiple experimental campaigns that look at particle motion in these, the most commonly referenced data has come to be that of Liu and Agarwal [115]. The experiments studied deposition of olive oil droplets, tagged with Uranine - a florescent tracer, in a vertical pipe at two Reynolds numbers (10,000 and 50,000). The wide range of particle sizes (τ_p^+ = 0.21 to 774) and lack of Reynolds dependency make this dataset

appealing. Other commonly referenced data include that of Friedlander & Johnstone, Sehmel, Wells & Chamberlain, and Schwendiman & Postma, shown in Figure 12. These data, varying by magnitudes, indicate the difficulties of experimentally measuring deposition, even in simple flows. But they show that the influence of turbophoresis is critical to capturing the correct trend in the diffusion-impact regime. Forsyth et al. were able to conduct an investigation into thermophoresis using NaCl particles and a straight horizontal pipe, using a swabbing technique to measure the total deposit [116].

There have been other studies on simple flows where the main intent is to study the effect of other forces such as electrostatic and thermophoresis. Montgomery and Corn [117] looked at deposition of methylthioninium chloride, tagged with Uranine, in horizontal pipe flow at Reynolds numbers ranging from 48,000-360,000. They were able to show that particle charge had a significant effect but within the spread of data seen in experiments of this kind. The most referenced study regarding thermophoresis was conducted by Healy and Young [86]. Here, simple pipe flow was modified to use two concentric tubes so that a well-defined temperature gradient could be imposed. Liquid droplets of Oleic acid with a solid core of Uranine were used. They found that the expression derived by Beresnev and Chernyak for thermophoretic force was most accurate for this study [86].

The second most commonly studied geometry is a 90 degree bend, with the most referenced study for this type of geometry being that by Pui et al [103], all known tests use liquid droplets to mimic an all stick boundary condition. Pui et al. conducted forty-four tests investigating the effect of Reynolds number and Stokes number on the penetration fraction. An exponential relationship between penetration fraction and Stokes number was found, with no dependence on Reynolds number, having tested for $Re \leq 10{,}000$ [103]. Wilson et al. [89] carried out experiments with $10{,}250 \leq Re \leq 30{,}750$, finding a significant relationship between Reynolds number and deposition fraction for particles with Stokes numbers between 0.1 and 0.4. Deposition was found to increase 2.6 times between the lowest and highest Reynolds number. Although their simulations using a Discrete Random Walk model (Section 2.5.2.6) were not able to capture this dependency, some analytical work indicated that the interaction between particles and turbulence was a likely driver. Wu and Young [55] conducted similar experiments in a bend with a rectangular cross section, specifically

setting the conditions such that centrifugal and turbophoretic forces were comparable. This is the only study to report spatial deposition, but there was variation of almost an order of magnitude between repeated experiments [55] making them of limited value. Sippola and Nazaroff [118] looked at the effect of duct material on deposition, although they reported deposition on different surfaces, the recycling of particles in the system made it difficult to simulate and use as validation.

Wylie et al. [114] investigated the deposition of volcanic ash in cooling holes at turbine relevant gas and metal temperatures. There have been multiple relevant experimental campaigns run at the Osney Thermofluids Institute, these initial attempts struggled to control conditions and generate well-conditioned particles. The data presented is a combination of integral statistics and pictures of the deposition [114]. In contrast to many other papers the magnitude of deposition was measured in terms of the reduction in flow parameter. These experiments showed that the cooling holes' orientation were significant in the formation of deposit, and reported the existence of a metal temperature at which deposition increases rapidly for these materials and geometry. The aforementioned work by Forsyth et al. was conducted using iterations of this experiment having been developed further to gain control of the conditions and particle delivery system [13].

Another investigation into deposition in cooling arrangements was conducted by Clum et al. [112], who investigated impinging jets. Whilst this campaign was carried out at a much lower temperature than that seen in a jet engine, it is unique in its capture of the spatially-resolved transient build up. This granularity of data has shown its usefulness, being used as a validation data-set in numerous instances.

The most engine representative experiments carried out in a lab are likely those carried out in the turbine reacting flow rig (TuRFR) at The Ohio State university [119]. This rig allows for deposition on NGVs at the correct metal temperatures, cooled by representative cooling gas, to be investigated. All papers that use this rig thus far have been limited to quantifying deposit via an integral mass, and photographic evidence.

In addition to studying particle-wall impacts experimentally, Bons et al. provided a review of the key methods used, differentiating between discrete particle tracking and field averaging techniques. The former tracks each particle independently whereas the latter averages across all

particles, unsurprisingly tracking each particle is more accurate coming at the cost of computational power [120]. There are a number of papers which apply these techniques in order to measure the coefficient of restitution or develop sticking models, but all of these are essentially curve-fits where the experiment serves to inform arbitrary coefficients. This is a problem as it means no generalizable model is formed. Moreover, the experiments are done on larger than realistic particles to aid imaging techniques, this is a problem as the physics does not scale completely, and hence these models will be less accurate for smaller particles [64], [121]–[124].

The majority of experimental studies limit any quantifiable data reported to the integral deposition fraction and aim to investigate the effect of operating conditions, whilst keeping experiments easy to run, on this result. This means there is a lack of spatially resolved deposition data at gas turbine in gas turbine representative flows, as these make experiments more challenging to conduct.

2.7 Summary

The literature review has made clear that jet engines experience a wide range of particle matter which is capable of causing concerning damage throughout the engine. In particular the deposition of particles is problematic. Further, while there has been significant progress in our understanding of this area, numerical tools require significant further development in order to realise a tool to assist with design and certification. This applies to both particle transport and bounce-stick models, this thesis is focused on the former. For this, the continuous random walk (CRW) model provides a good foundation, but it is currently too dependent on turbulent quantities from sources external to the fluid solution. The focus of the next chapter is to develop a generalised version of the CRW which does not require tuning, or use of external statistics, for each application. This is critical as current methods cannot be tuned for cases of interest. To enable validation of this model in conditions of interest, Chapter 4 presents quantitative spatially resolved deposition data from experiments at representative of gas turbine conditions. To ensure robust validation (Chapter 6), a methodology to ensure convergence of spatially resolved quantities is presented in Chapter 5.

3 Continuous Random Walk Development

This chapter discusses the specific challenges of using the continuous random walk (CRW) model, described in Section 2.5.2.6, to characterise turbulent fluctuations in accelerating flows. The outcome of the research, and a comparison of the model's performance to the best existing alternatives, was presented as a paper at IGTI2020 which is included as Section 3.1 of this chapter.

The resulting CRW has highly generalised applicability to complex flow fields for which time averaged solutions are available. The flows may exhibit substantial acceleration (typically induced in rotational and complex passage flows), but the revised CRW does not require external DNS data and is seen to achieve results of equal accuracy to existing best practice in simple flows for which DNS data are available.

First, the need for development of the previous 'best' CRW model is explained, and a high level comparison is made between the features of that and the newly proposed model. A full derivation of the CRW is provided as Appendix A of this thesis. Details of the new model development, including the rationale for the approached chosen, are then presented in the paper included in this chapter. While model development was considered the key output from this paper, it usefully also presents an application of the revised model to an accelerating flow in a 90 degree pipe bend, exploring the effects of changes made.

There are four main considerations in using the CRW model turbophoresis: the method used to solve the stochastic differential equation; the integration time-step; the co-ordinate frames required; and the turbulent statistics used. Prior to the current research the CRW, when applied to RANS fluid solutions, has only been validated rigorously in simple flows (channels and pipes). Hence its implementation has been focused on being sufficient for these cases. Specifically, for the original implementation, the domain must be split into an isotropic bulk and anisotropic near-wall region. In the anisotropic region there is a reliance on external statistics, taken from higher fidelity sources, which are only applicable for simple flows. Further, in this implementation, only

orthogonal Reynolds Stresses (in a geometry dependent co-ordinate system) are considered in the near wall region.

If this model is to be applied to a gas turbine engine its implementation needs to reflect the added complexities of the flows seen in these situations. A region of a jet engine of particular interest is the rotor-stator cavity feeding the shank cavity pocket under a turbine blade. Here particles are considered the likely cause of the onset of corrosive behaviour, and previous workers have attempted to model deposition, see Forsyth et al [13] who presented a study of deposition in this region for a Rolls-Royce Trent 900 engine. Interestingly they observed that realistic deposition was not possible with the industry standard DRW model, but the CRW model's accuracy could not be determined. Such flows involve acceleration and anisotropic turbulence. The external statistics used in existing CRW models are not applicable to these flows. Hence, the approach taken thus far is not sufficient for application to real flows. The CRW must be implemented and validated in a way that does not have these assumptions or dependencies.

Table 3 compares the original and the newly developed models, the key difference being that anisotropic turbulence is considered, fully informed by the fluid solution using a Reynolds stress model. The implementation of this approach requires more than simply changing the turbulence model used for the fluid solution. First, using geometries for which experimental solution data are available, and LES data were generated, Reynolds stress models are compared to select that which gives the most accurate match in several important quantities, namely: the Reynolds stresses (particularly near the wall); and the Lagrangian time scales. Then an implementation which allows for full anisotropic stresses to be considered in a domain of any complexity is formulated. Finally, a method of computing the Lagrangian time scales is proposed, noting that this is only a well-defined quantity for homogenous turbulence, and that even using the most suitable Reynolds stress model a critically important feature of the Lagrangian time scales near the wall must still be estimated.

	Original CRW	Developed CRW
Governing equation solution	- Implicit finite difference	- Exact solution (via integration)
Integration timestep	- Geometric mean of Lagrangian and Kolmogorov time scale	- Geometric mean of Lagrangian and Kolmogorov time scale
Co-ordinate frames	- Segregation between the near-wall and bulk region arbitrarily defined at Y^+=100 - Principle Reynolds Stresses aligned with flow direction in near wall region (Y^+≤100)	- A local co-ordinate frame for each cell, as calculated by diagonalising the Reynolds Stresses
Source of Turbulent statistics	- RANS fluid solution for Y^+>100 -Fit to high fidelity unsteady solutions of idealised flow geometries for $Y^+ \leq 100$	- RANS fluid solution, with no flow segregation
Reynolds Stresses	- Isotropic for Y^+>100 - Ignores cross terms for Y^+≤100	- Anisotropic, with all terms of the Reynolds Stress tensor accounted for throughout the domain
Lagrangian timescale	- Isotropic everywhere	- Anisotropic, no simplifications

Table 3 Comparison of the pre-existing and newly developed CRW implementations

3.1 Paper: Development and Validation of a Continuous Random Walk Model for Particle Tracking in Accelerating Flows

The included paper demonstrates the development of the CRW model as described above. In this paper, the thesis author is the primary author. Professors McGilvray and Gillespie are the principal investigators on the project, Dr Forsyth was responsible for the implementation of the original CRW model in an ANSYS Fluent UDF, and Dr Kapsis generated the LES flow solutions used to compare turbulent statistics, to RANS solutions, and choose the most appropriate RSM. The development and implementation of the developed CRW model, application of all models, and the post-processing of results were all conducted by the thesis author.

DEVELOPMENT AND VALIDATION OF A CONTINUOUS RANDOM WALK MODEL FOR PARTICLE TRACKING IN ACCELERATING FLOWS

N. Vadgama, M. Kapsis, P.Forsyth, M. McGilvray, D. R. H. Gillespie

Department of Engineering Science, University of Oxford, Oxford, OX1 3UJ

ABSTRACT

Stochastic particle tracking models coupled to RANS fluid simulations are frequently used to simulate particulate transport and hence predict component damage in gas turbines. In simple flows the Continuous Random Walk (CRW) model has been shown to model particulate motion in the diffusion-impaction regime significantly more accurately than Discrete Random Walk implementations. To date, the CRW model has used turbulent flow statistics determined from DNS in channels and experiments in pipes. Robust extension of the CRW model to accelerating flows modelled using RANS is important to enable its use in design studies of rotating engine-realistic geometries of complex curvature.

This paper builds on previous work by the authors to use turbulent statistics in the CRW model directly from Reynolds Stress Models (RSM) in RANS simulations. Further improvements are made to this technique to account for strong gradients in Reynolds Stresses in all directions; improve the robustness of the model to the chosen time-step; and to eliminate the need for DNS/experimentally derived statistical flow properties. The effect of these changes were studied using a commercial CFD solver for a simple pipe flow, for which integral deposition prediction accuracy equal to that using the original CRW was achieved. These changes enable the CRW to be applied to more complex flow cases.

To demonstrate why this development is important, in a more complex flow case with acceleration, deposition in a turbulent 90° bend was investigated. Critical differences in the predicted deposition are apparent when the results are compared to the alternative tracking models suitable for RANS solutions. The modified CRW model was the only model which captured the more complex deposition distribution, as predicted by published LES studies. Particle tracking models need to be accurate in the spatial distribution of deposition they predict in order to enable more sophisticated engineering design studies.

NOMENCLATURE

Latin

A_i	Drift Correction
C	Concentration (km m^{-3}), Cunningham correction
D	Diameter (m)
t	Time (s)
L	Length (m)
N	Number of Particles
R	Radius (m)
R_c	Radius of curvature (m)
S	Arc Length (m)
u^*	Friction velocity (m/s)
u_i	Instantaneous velocity fluctuation (m/s)
$\overline{U}_g$	Mean flow velocity (m/s)

Greek

σ	Root mean square velocity fluctuation (m/s)
μ	Dynamic Viscosity (Pa s)
ρ	Density (kg/m^3)
τ_L	Lagrangian time scale (s)
τ_K	Kolmogorov time scale (s)
ξ	Normally distributed random number, dt variance
Δt	Time-step

Subscripts

1	Stream-wise
2	Wall-normal
3	Span-wise

p	Particle
f	Fluid
CCS	Cartesian Co-ordinate System
BFCS	Body Fitted Co-ordinate System

Non-dimensional Groups

C	Curvature Ratio ($= 2R_c/D$)
C_f	Skin friction coefficient
De	Dean Number ($= \mathrm{Re}\sqrt{D/2\mathrm{R_c}}$)
R_c	Curvature Ratio ($= R_{\mathrm{bend}}/R_{\mathrm{pipe}}$)
Re	Reynolds number ($= \rho_{\mathrm{g}}\overline{U}_{\mathrm{g}}\, D_{\mathrm{h}}/\mu_{\mathrm{g}}$)
Re_p	Particle Reynolds number ($= \rho_{\mathrm{g}}V_{\mathrm{rel}}d_{\mathrm{p}}/\mu_{\mathrm{g}}$)
Stk	Stokes number ($= \rho_{\mathrm{p}}d_{\mathrm{p}}^2\overline{U}_{\mathrm{g}}/18\,\mu_{\mathrm{g}}D_{\mathrm{h}}$)
V_d^+	Non-dimensional deposition velocity
y^+	Non-dimensional wall distance
τ_L^+	Non-dimensional Lagrangian time scale
τ_p^+	Non-dimensional particle relaxation time
σ^+	Root mean square velocity fluctuation normalised by friction velocity

Acronyms

CRW	Continuous Random Walk
DNS	Direct Numerical Simulation
LES	Large Eddy Simulation
NWR	No Wall Reflections
RANS	Reynolds-Averaged Naiver Stokes
RMS	Root Mean Square
RS	Reynolds Stress
SIMPLEC	Semi-Implicit Method for Pressure Linked Equations-Consistent

RSM	Reynolds Stress Model
WWR	With Wall Reflections

I. INTRODUCTION

The ingestion of particle matter into aircraft engines is known to cause significant damage to turbine and compressor components [1]. Particulates may damage the engine through erosion, accretion and corrosion [1]. The particulates that reach the turbine tend to be less than 10 μm and they deposit on external surfaces of the main gas path [1] and on internal surfaces fed by the secondary cooling air [2].

A combination of more frequent flights in regions known for highly dust laden and polluted environments, and higher engine compression ratios and turbine entry temperatures, have increased the likelihood of particulate deposition in hot stages of the engine. Thus, it is timely to develop a practicable and validated method of predicting particle deposition, applicable to fully featured engine flow simulations, in which extreme flow acceleration is a key component.

To date, high fidelity fundamental deposition studies have mostly focused on simple turbulent pipe flows [3]. These experiments most often consider pipes in vertical orientation to eliminate the effects of gravity in the wall-normal direction. To uncouple the transport problem from that of stick and bounce, liquid droplet particulates are used which provide an all-stick boundary condition at the wall [3, 4]. Transport of particles towards the wall may be described by the non-dimensional deposition velocity (Eq 1). This provides a fully scalable parameter in the case of fully developed fluid and particle distributions, and disregards possible change in particle distribution as a result of deposition. Here V_d^+ is the ratio of the particle mass flux (J) towards the wall to the local mean concentration (C_0) normalized by u^*, and C_{in} and C_{out} are local mean concentrations at the inlet and outlet of the pipe.

$$V_{\mathrm{d}}^{+} = \frac{J}{C_o u^*} = \frac{1}{4}\frac{D}{L}\frac{U}{u^*} ln\left(\frac{C_{\mathrm{in}}}{C_{\mathrm{out}}}\right) \tag{1}$$

Previous work has shown that V_{d}^{+} is strongly dependent on the non-dimensional particle relaxation time (Eq. 2,Fig. 1). This parameter gives an indication of a particle's response to changing flow conditions and is the product of the particle Stokes number and the ratio of wall to gas viscous forces.

$$\tau_{\mathrm{p}}^{+} = \frac{\tau_p (u^*)^2}{\nu} = \frac{C_{\mathrm{c}} \rho_{\mathrm{p}} \rho_{\mathrm{f}} D_{\mathrm{p}}^2 (u^*)^2}{18\,\mu} = 2\,Stk\,Re\,C_{\mathrm{f}} \tag{2}$$

Thus, particles of low τ_{p}^{+} are highly diffusive while those with high τ_{p}^{+} follow ballistic trajectories as shown in Fig. 1. Particles of interest in the gas turbine secondary air system are in the diffusion-impaction regime, a regime where the deposition is heavily dependent on the particles' interaction with turbulent eddies (in the absence of significant body-forces) [5].

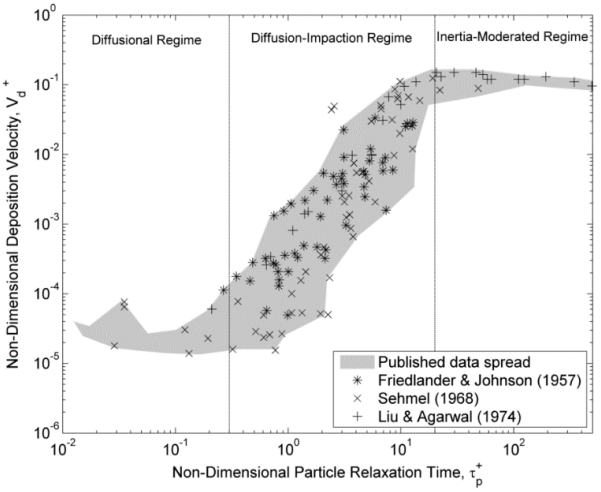

Figure 1 Experimentally measured particle deposition in a vertical turbulent pipe ***[3, 5]***

For more complex geometries (bends, nasal passages, rooms etc.), deposition is often reported as a bulk deposition or penetration efficiency through the full geometry.

$$\eta_{\mathrm{deposition}} = 1 - \eta_{\mathrm{penetration}} = \frac{N_{\mathrm{deposited}}}{N_{\mathrm{entered}}} \tag{3}$$

Pui et al. [4] reported the bulk deposition of particles with *Stk* = 0.03–1.35 (noting that here the length scale used was the radius), at *Re* = 6,000 and 10,000 in a bend with a radius of curvature of 5.6 - 5.7 [4]. In addition to bulk values, spatially resolved deposition data were computed for this case using LES [7].

Industrial design investigations of particle deposition frequently use Reynolds Averaged Navier-Stokes (RANS) fluid simulations. Here, stochastic models are required to predict the transport of particles when influenced by fluid turbulent fluctuations. The commonly used Discrete Random Walk (DRW) has been shown to be inaccurate for particles in the diffusion and diffusion-impaction regime [3, 7, 9]. Better agreement with experimental data is achieved using Continuous Random Walk (CRW) models, using fluid statistics from DNS or experiments [3, 10, 12]. In the CRW bulk flow data from two-equation RANS simulations have been employed [3, 9]. The CRW requires anisotropic Reynolds Stresses and the Lagrangian time scale in the near-wall layer region ($y^+ < 100$), and to date these have been populated using data from experimental and DNS studies. While matching experimental pipe flow data well, it is impossible to apply these data to more complex flow fields, and unfeasible to generate bespoke DNS solutions.

The authors' previous work [12] showed that it was possible to correct unsteady fluid property statistics of a complex flow extracted from a RANS solutions of the flow field employing a Reynolds Stress turbulence Model (RSM), based on the discrepancy between DNS and RSM statistics of simple flows, to noticeably improve the predicted deposition distribution in a 90° bend. The authors recognized that while providing, in part, an engineering solution, the physical arguments underlying the correction were unclear. Underlying this approach was the continued use of a body fitted co-ordinate system in the near-wall region limiting its validity in complex geometries where the boundary layer is highly disrupted. The need for a correction factor means that the reliance on DNS statistics was not eliminated with that approach.

In this paper Reynolds Stress distributions and time scales acquired from a RANS RSM simulation of the flow field are used without a scaling correction to increase the applicability of the model to complex flows. Two variants of the Reynolds Stress turbulence models are compared to higher fidelity data (LES/experiment) to determine which is likely to provide the most representative time-averaged solution, as the CRW's success is dependent on an accurate fluid phase solution [11]. While literature has shown fluids modelled using an RSM turbulence model provide a sound basis for the implementation of the CRW [13], in this paper we implement

modifications that make it independent from any external (DNS/experimental) data. Further improvements are made to account for anisotropic turbulence and more robust calculation of an accurate local time-step. The updates are progressively applied to a straight vertical pipe, to asses validity. Then the final model, with all alterations, is applied to a turbulent 90° pipe bend (where more complex flow features exist and the application of external statistics is less appropriate) to demonstrate the effect of these changes.

II. COMPUTATIONAL MODELLING APPROACH

The geometries chosen for the current study are a straight pipe and a 90° bend, both of circular cross-section and diameter *D*. The geometries used are shown schematically in Fig. 2 with dimensions in Table 1.

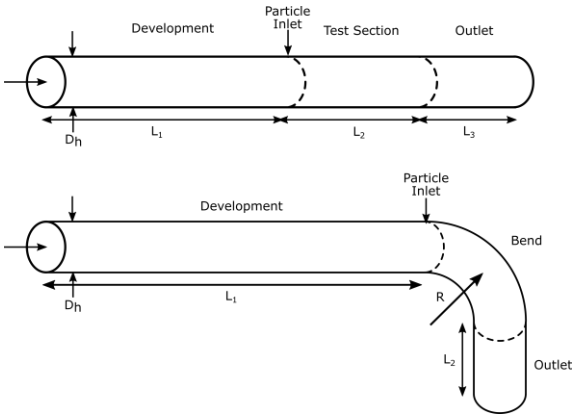

Figure 2 Domain structure used, see Table 1 for dimensions of each simulation. "Particle Inlet" labels show where the number of particles ($N_{entered}$) is measured.

Table 1 Dimensions of unstructured meshes used for particle injection in RANS simulations

Case	D (mm)	L_1 (mm)	L_2 (mm)	L_3 or R (mm)	R_c
Straight, L&A [14]	12.7	254	764	1020	N/A
Bend, Pui [4]	8.51	255	17	24.3	5.7

A Reynolds number of 10,000 is used based on the bulk velocity U_b, and the diameter *D*. RANS simulations using RSM are used to simulate the fluid phase through which particles are tracked. In order to choose the most suitable available RSM model the resulting solutions are compared to higher fidelity LES and experimental data. For all solutions commercial software Fluent 19.2 and ICEM 19.2 were used for the flow solution and the mesh generation respectively.

As the Mach number is much lower than 0.3 (0.05), incompressible flow was assumed. Consequently, the dynamic viscosity was constant and the pressure-based SIMPLEC numerical scheme was employed, with second order spatial discretisation. The LES solutions were calculated on smaller, but equivalent, domains to reduce computational cost. A comparison of meshes can be seen in Fig. 3.

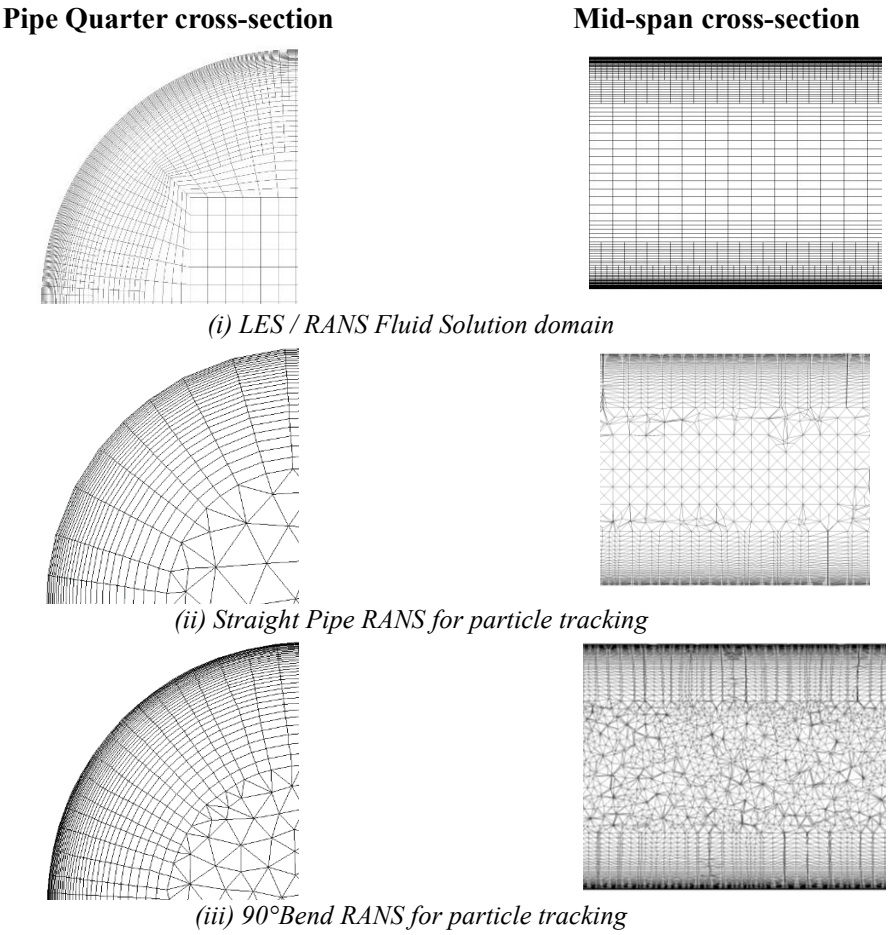

(i) LES / RANS Fluid Solution domain

(ii) Straight Pipe RANS for particle tracking

(iii) 90°Bend RANS for particle tracking

Figure 3 Detail of meshing used in simulations

The meshes used for the RANS fluid solution and particle tracking are those previously validated as providing mesh independent solution as reported in [3] and [12]. For the RANS solutions two implementations of the RSM turbulence model were employed: in these the pressure-strain term linear model was calculated a) with wall reflections (WWR) and b) with no wall

reflections (NWR). For both cases the same boundary conditions were adopted. The walls of the pipes were adiabatic with no-slip conditions and the exit was set at constant static pressure.

In each case the particles are injected uniformly, distributed in an equally spaced grid, at the inlet with the initial velocity of the fluid in the nearest cell. The number of particles was adequate for the bulk deposition value to be converged. The deposition efficiency is calculated as $\eta_{\text{deposition}} = N_{\text{deposited}}/N_{\text{entered}}$. $N_{entered}$ is calculated at either the inlet of the straight test section or the bend inlet (Fig. 2). An all-stick condition is used, so $N_{\text{deposited}}$ is equal to the number of particles that impact the relevant wall sections, i.e. the bend, and the full test section in the straight pipe. [10]

For the LES simulation bounded second order implicit time integration was applied for dual-time stepping of transient simulations. At each physical time-step, the normalised residuals drop by four orders before reaching a plateau. The dynamic Smagorinsky-Lilly model was used for the modelling of the sub-grid scale flow structures. A structured multiblock approach was adopted, with local refinement near the walls as shown in Fig. 3(i). Where LES and RANS fluid solutions properties are compared the same structured mesh is employed. However, where particle tracking is investigated, the mesh is unstructured, as used in industrial applications (Fig. 3 (iii)).

When setting up the inlet conditions for the LES, a preliminary steady solution using RANS with the realisable k-ε turbulence model was initially performed for a long straight pipe (L/D=20). At the inlet a uniform velocity profile equal to U_b was applied. The purpose of the preliminary simulation was to obtain the fully developed profile at the exit plane of the velocity components, the turbulence kinetic energy and the turbulence dissipation rate. These profiles were then applied to the inlet of the main cases. These profiles were used to generate realistic turbulence at the inlet by employing the vortex method [16].

III. CRW MODEL

For particles in the diffusion-impaction region, including a turbulent transport model to capture fluctuating fluid momentum is essential. We choose to use the CRW for this.

There are several different formulations of the CRW; but here that of Dehbi et al. [9] is employed due to its demonstrated accuracy in prior applications [3, 7]. At the core of the model is the normalised Langevin equation (Eq. 4)

$$d\left(\frac{\mathrm{u}_i}{\sigma_i}\right) = -\left(\frac{\mathrm{u}_i}{\sigma_i}\right)\frac{d\mathrm{t}}{\tau_L} + \sqrt{\frac{2}{\tau_L}}d\zeta_\mathrm{i} + A_i d\mathrm{t} \tag{4}$$

Here the LHS, the transported quantity, is the instantaneous velocity fluctuation normalised by the RMS velocity fluctuation. This form provides a decorrelation in the time history where the gradients are large, which is essential for accuracy in the near-wall regions and areas of high acceleration [10] . The first RHS term is a damping term, after time $\mathrm{d}t$ the particle loses $\mathrm{d}t\ /\tau_L$ of the imparted velocity. The second RHS term imparts a velocity to the particle. In this, $\mathrm{d}\zeta_i$ is a Gaussian random number with zero mean and $\mathrm{d}t$ variance [1]. The drift correction $\mathrm{A_i}$ accounts for the decorrelation of the particle and fluid (i.e. that the particles have finite-inertia). This is essential for the model to fulfil the well-mixed criterion and its exact formulation varies [22, 23]. Equation 5 is the linearised solution of Eq. 4 used to calculate the fluid fluctuation velocity that the particle experiences [10].

$$\frac{u_{\mathrm{i},t+\Delta t}}{\sigma_{\mathrm{i},t+\Delta t}} = \frac{1}{1+\frac{\Delta t}{\tau_\mathrm{L}}}\left(\frac{u_{i,t}}{\sigma_{i,t}} + \sqrt{\frac{2\,\Delta t}{\tau_\mathrm{L}}}\xi + A_i\Delta t\right) \tag{5}$$

$$A_i = \overline{u'_{\mathrm{f,j}}\frac{\partial u'_{\mathrm{f,i}}}{\partial x_\mathrm{j}}} \tag{6}$$

The model requires the RMS turbulent fluctuations ($\boldsymbol{\sigma}$), drift correction term ($\mathrm{A_i}$), and time-step (Δt). The model is calculated in two layers, as shown in Fig. 4. For both layers the time-step is a function of the Lagrangian (τ_L) and Kolmogorov (τ_K) time scales (Eq. 7). Apart from the Kolmogorov time scale the turbulent statistics are differently defined for the Bulk and Near-wall region, due to assumptions of isotropy and anisotropy, respectively [9].

[1] Eq.4 and this sentence have been updated to correct a typographical error

$$\Delta t = \sqrt{\tau_K \tau_L} \tag{7}$$

In the bulk region the turbulent fluctuations are assumed isotropic and are calculated using Eq. 8. This assumption likely only has merit along the centre of a pipe, but extension to the whole 'bulk' region avoids the need for anisotropic statistics. The Lagrangian time scale is calculated using Eq. 9. The Kolmogorov time scale is approximated by Eq. 10, which is used in both regions. In the bulk flow the drift correction is expressed as per Eq. 11. In this Stk_p is a local Stokes number defined as τ_p/τ_L [9].

$$\sigma = \sigma_{11} = \sigma_{22} = \sigma_{33} = \sqrt{\frac{2}{3}k} \tag{8}$$

$$\tau_L = 0.3 \frac{\kappa}{\varepsilon} \tag{9}$$

$$\tau_K = \frac{\tau_L}{Re^{\frac{1}{2}}} \tag{10}$$

$$A_i = \frac{1}{3\sigma} \frac{\partial k}{\partial x_i} \frac{dt}{1 + Stk_p} \tag{11}$$

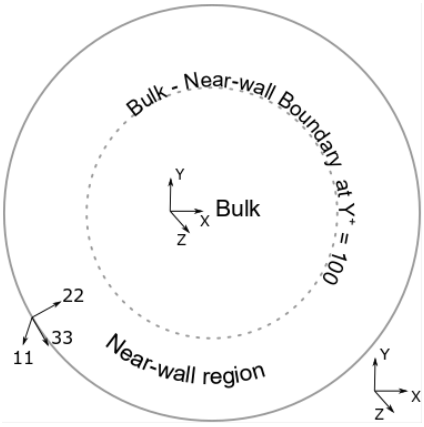

Figure 4 The CRW model defines turbulent statistics and principal axes differently in the bulk and boundary layer. The regions are split at a y^+*=100. Both co-ordinate systems are Cartesian. In the bulk the principal axes align with the global co-ordinate system. In the near-wall region the axes are defined with respect to the wall and flow. Direction 11 is aligned with the flow, 22 is wall-normal, and 33 is taken to be the cross product of these.* ***[9]***

This model has previously been applied to two-equation turbulence models flow solutions. To predict anisotropy DNS data has been used to provide correlations of the fluctuating velocities, Lagrangian time scales, and drift correction factor. It is important to note that *only orthogonal Reynolds Stresses* along the principal axes of the local co-ordinate frames are used [9]. Using an

anisotropic drift correction, assuming that the cross terms are negligible, and that the wall-normal direction is most important results in a different drift correction term for each direction (Eq. 12) [9].

$$A_{11} = A_{33} = 0\,, \qquad A_{22} = \frac{1}{2\sigma_i}\frac{\partial \sigma_i^2}{\partial x_i}\frac{dt}{1 + Stk_p} \tag{12}$$

The effect of changing the integration time-step is shown in Fig. 5, where particle tracking is implemented in a straight pipe, using the DNS correlations in the near wall region, but varying Δt. The results show that particles in the diffusion regime are most sensitive to the choice of time-step, but when Eq. 10 is employed all but the smallest particles lie within the range of published experimental data.

Solutions generated with time-steps of $1x10^{-5}$ s and $1x10^{-6}$ s agree closely, though tend to under-predict deposition of small particles. Increasing the time-step to $1x10^{-4}$ s noticeably changes the level of V_d^+ by more than an order of magnitude for all particles except those in the inertia-moderated regime.

A lessening of the time-step to $1x10^{-7}$s, increases deposition of particles in the diffusion and diffusion impaction regimes, by up to one order of magnitude. As described below the shortest time-step should not be less than the time period over which the acceleration is correlated, and a time-step of $1x10^{-7}$s contravenes this. Thus, the good agreement between the experimental data and the prediction has no physical basis. The necessity to fully define the next state from the current state, means that a simple assessment of temporal convergence cannot be made by comparison of other solutions to that with the smallest time-step for which numerical diffusion errors (as opposed to physical modelling errors) are not expected. The presence of temporal convergence is therefore concluded from the close agreement of the time-steps of $1x10^{-6}$ and $1x10^{-5}$s (separated by one order). This is to be expected. For the case modelled, Eq. 10 estimates the time scales τ_L and τ_K to be separated by ~2 orders of magnitude, and we expect accurate time-stepping solutions to use values lying between these limits.

Physically, a small time-step means that further momentum is imparted to the particle before the previously imparted momentum is adequately diminished. For this to be acceptable the model needs to include inputs from more states than just the previous state. The mathematical basis for this is discussed in section 2 of "CRW Model Development". This extra momentum results in higher predicted deposition.

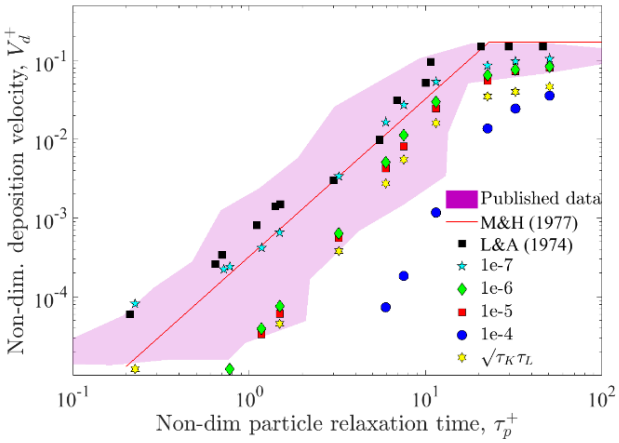

Figure 5 Comparison of different time-steps, for deposition in a straight pipe using the two-layer model, and fitted DNS statistics for fluctuating velocities and local isotropic Lagrangian time scales.

IV. CRW MODEL DEVELOPMENT

To eliminate the need for DNS statistics whilst retaining improved accuracy the following possible improvements were investigated:

1. Identification of the RSM which is most likely to generate representative Reynolds Stresses, by comparison to LES solutions
2. Use of the exact solution of Eq. 4
3. Use of RSM calculated fluctuating velocities
4. Change to a universally defined co-ordinate frame
5. Apply a constant τ_L in the buffer layer (fully informed by fluid solution)
6. Application of anisotropic τ_L

1. Identification of Appropriate RSM Model for Fluid Solution

To understand the limitations of RANS modelling with RSM, comparisons were performed of RANS solutions against those of LES. For validation purposes, two experimental data sets from the open literature were selected. The first, den Toonder and Nieuwstadt [18], provides velocity profile information at Re=10 000. The second, Shivran [19], provides RMS velocities of fully developed flows in both pipes and 90° bends. Turbulence statistics were obtained via single hot-wire measurements, thus for this section the presented RMS velocities reflect the fluctuations perpendicular to the wire i.e. the combined axial and wall-normal velocity components.

1a. Straight Pipe

The straight pipe cases considered were a) 5D-long and b) 20D-long. The nominal time-step, normalised by U_b and D, was equal to 0.035 and the nominal mesh size was 1M cells per 5D-long section. A 5D-long configuration with half the nominal time-step and 30% larger mesh than the nominal is also reported (notated as 'dense').

In Fig. 6 comparisons between experimental data, RANS solutions and LES are presented. LES matches the predicted experimental axial velocity profiles well. The RANS-RSM with wall reflections also shows adequate agreement, contrary to the RSM without wall reflections which produces a velocity profile more akin to laminar flow. This was also observed when the RSM was applied to the 20D-long straight pipe case.

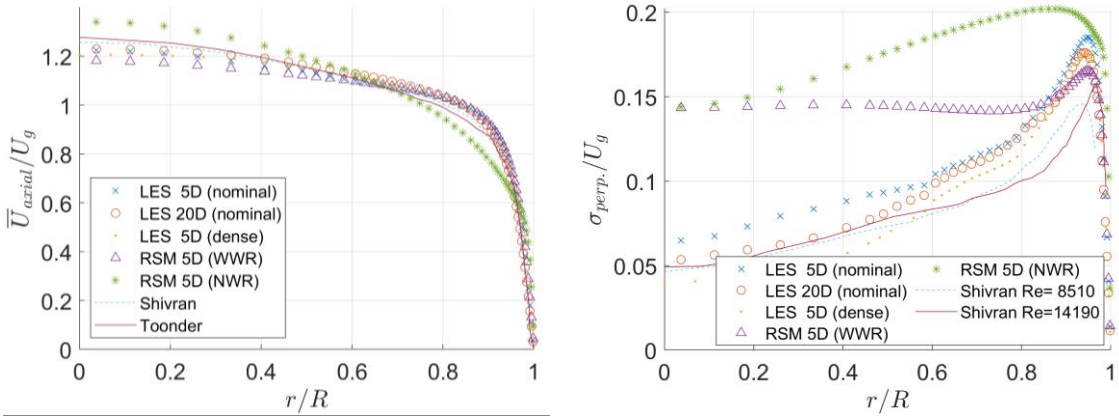

(a) Axial velocity *(b) RMS of the perpendicular velocity*

Figure 6 Fluid solution, Straight pipe: Results of LES (time-averaged) and RANS RSM at the exit plane compared to experimental data [14 , 15]

Regarding the RMS velocity, the LES predict the trends measured by the hot-wire. RANS turbulence models are tuned for higher Re, hence the currently investigated moderate Re introduces challenges. Hence, the Reynolds stresses are significantly over predicted in the bulk region. Still, the RSM with wall reflections seems to capture the peak, at r/R ~ ±0.95, near the wall.

Particle deposition models are highly sensitive to the time-step, hence its distribution with non-dimensional wall distance should be considered. For this analysis non-dimensional time-step, τ_{L}^{+} for the LES in each direction is calculated as:

$$\tau_{\mathrm{L},i}^{+} = C_0 \frac{\sigma_i^2}{\varepsilon_i} \times \frac{\nu}{u^{*2}} \tag{13}$$

The directional turbulent dissipation rate is defined as [20]:

$$\varepsilon_i = \nu \left(\overline{\frac{\partial u_\iota}{\partial x_j} \frac{\partial u_\iota}{\partial x_j}} - \frac{\partial \sigma_i}{\partial x_j} \frac{\partial \sigma_i}{\partial x_j} \right) \tag{14}$$

where the Einstein notation is applied only to the j subscript. For the RSM solutions the ε of turbulence model is used.

It is noted that for the LES simulation, the Lagrangian time scale is not presented for the low y^+ region resolved by the simulations. This is because non-physical values of directional turbulence dissipation rate were calculated near the wall. Specifically, the expected trend [20] near the wall should be flat for y^+<10, and equal to 10 [21]. The LES however predicts a minimum turning point in τ_{L}^{+}, at y^+~10. When a denser mesh is employed (Fig. 7a) a wider plateau in wall-normal τ_{L}^{+} is predicted at value of 10. As the wall-normal term dominates the likelihood of deposition it is perhaps unsurprising that the fit (Laufer) to the experimentally resolved τ_{L}^{+} is best in the wall-normal direction. The values generated by the RSM simulation are clearly not in good agreement. Although they plateau, they drop to zero.

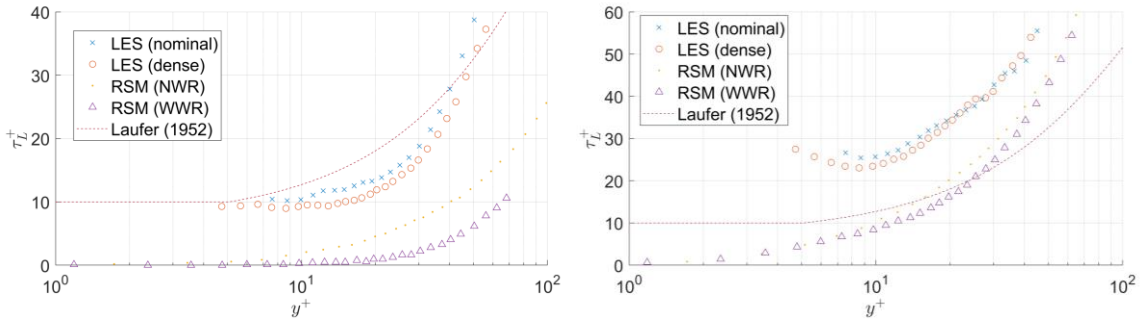

(a) Wall-normal *(b) Total ($\varepsilon=\varepsilon_1+\varepsilon_2+\varepsilon_3$)*

Figure 7 Fluid Solution, Straight pipe: Directional τ_L^+. C_0 is set to 0.3 for the RSM solutions. For the LES the values 2/7 and 2/14 are employed for the axial and the wall-normal directions, respectively, as in [20].

1b. 90° Bend

The bend considered in this paper models the geometry used by Pui et al. [4] operating at *De*=4,225. The computational domain consists of a 1D-long pipe upstream of the bend inlet, the bend, and a 2D-long pipe downstream of the bend. The baseline mesh size was 1.7M cells and the LES time-step, normalised by U_b and D, was conservatively set to 0.004. Using this mesh the maximum values of the instantaneous y^+ in the wall adjacent cells and ratio of SGS viscosity to laminar viscosity were 1.16 and 4.92 respectively. The maximum y^+ based on the time-averaged shear stress was found to be 0.41. The dense mesh configuration was 2.7 times the cell count of the baseline mesh, with 0.5 times the baseline time-step.

Additionally, in Fig. 8 the axial velocity and the Reynolds Stresses downstream of the bend exit are presented and compared to experimental measurements. For this case, the flow field predicted by the RSM without wall reflections seems to match the LES time-averaged solution better than the RSM with wall reflections. The Reynolds stresses predicted using the RSM solutions fail to match the experimental trends (Fig. 8(b)) well. The experimental measurements demonstrate a peak at the centreline where there is a shear layer between the separated and accelerated flow is located. This peak is more pronounced in the LES results *cf.* the RSM solutions. It is noted that the experimental data are acquired over a different range of De = 6 000 – 11 000 and Re = 13 500 – 33 000, however the normalised Reynolds Stresses appear to be insensitive to these variations.

Also, in Fig. 8 a LES solution using the dense mesh with smaller physical time-step is presented, demonstrating that the nominal mesh and time-step adequately resolves the essential integral flow-scales. The RSM was also tested in this configuration, predicting the same profiles as the nominal mesh.

The gradients of the Reynolds Stresses near the wall are vital when modelling the turbulence dispersion in the CRW and can have a strong effect on the predicted particle deposition. Based on the results from these two cases, the RSM *with* wall reflections matches the LES best. Although this model produces less accurate velocity profiles, for the accelerating flow case, its Reynolds Stresses are closer to the experimental data and LES predictions.

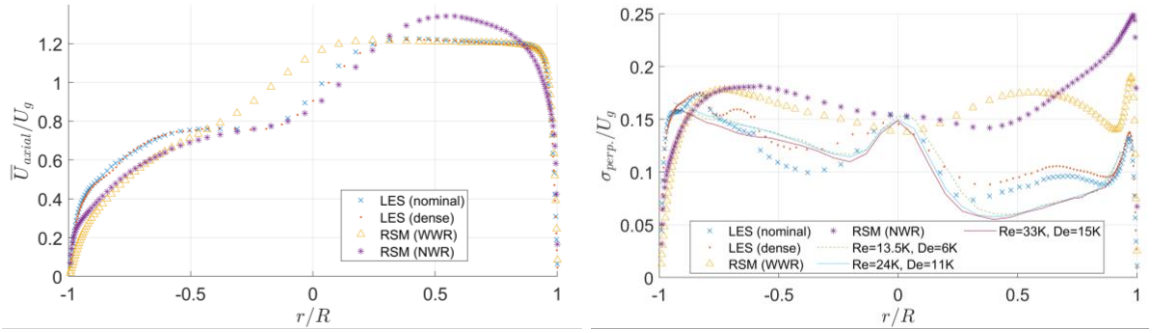

(a) Axial velocity *(b) RMS of the perpendicular velocity*

Figure 8 Fluid Solution, Bend: Results of LES (time-averaged) and RANS RSM compared to experimental data [19]. The plotting line is located 0.5D downstream of the bend's exit, at the symmetry plane between the Dean vortices. Smallest and largest Z/D values denote the inner (left) and the outer (right) bend's radii, respectively.

2. Improved Solution of the Langevin Equation (Eqn 4)

The Langevin equation (Eq. 4) is a Markov sequence, rather than chain, meaning it is only well defined at discrete times [17]. Therefore, the solution does not converge as $\boldsymbol{\Delta t} \rightarrow 0$. A lower limit is set by the requirement that in a Markov chain the next state is completely defined by the current state, meaning $\boldsymbol{\Delta t}$ should be larger than the time scale over which the particle acceleration is correlated [9]. In the open literature this lower limit appears disputed, e.g. Legg and Rupach argue it should be equal to $\boldsymbol{\tau_\lambda}$ [17] while Sawford argues it should be equal to $\boldsymbol{\tau_K}$ [22], and Dehbi [9] uses an absolute minimum value of 10^{-6} s. When RANS is used and these scales need to be estimated, under common assumptions, both $\boldsymbol{\tau_\lambda}$ and $\boldsymbol{\tau_K}$ converge to $(\nu/\varepsilon)^{1/2}$. An upper limit for $\boldsymbol{\Delta t}$ is set by the requirement that turbulence must be resolved accurately, i.e. $\mathbf{d}\boldsymbol{t} \ll \boldsymbol{\tau_L}$. Equation7 ($\boldsymbol{\Delta t} = \sqrt{\boldsymbol{\tau_K \tau_L}}$)

fulfils this criteria as long as the approximation used in Eq. 10 is reasonable. To improve robustness decrease sensitivity of the model the exact solution to Eq. 4 (Eq. 15 [10]) is used rather than the linearised solution (Eq. 5), as this is only valid when $\boldsymbol{\Delta t \ll \tau_L}$.

$$\frac{u_{i,\ t+\Delta t}}{\sigma_{i,\ t+\Delta t}} = \frac{u_{i,\ t}}{\sigma_{i,\ t}} exp\left(\frac{-\Delta t}{\tau_L}\right) + \sqrt{1 - exp\left(\frac{-2\,\Delta t}{\tau_L}\right)}\xi + A_i \Delta t \qquad (15)$$

3. Use of RSMs calculated fluctuating velocity

In the existing model the RANS simulation fully informs the Langevin equation while the particle is in the Bulk region, but in the near-wall region τ_L and σ_i are based on curve fits [9]. These fits are from DNS or experimental data of simple flows (pipes and channels) [23, 30] and are likely not applicable to more complex flows. Using the RSM rather than a two-equation model enables us to source these anisotropic statistics directly from the fluid solution as all Reynolds Stresses are calculated.

4. Universally defined co-ordinate frame

It is noted above that only orthogonal Reynolds Stresses along the principal axes of the local co-ordinate frames are used [9] in the CRW. Furthermore, the current model uses two regions with a body fitted co-ordinate system near the wall (where DNS fitted data are used) and a Cartesian co-ordinate system where y^+>100. This results in two inaccuracies. First a discontinuity at the boundary of the regions and second a discounting of the energy contained in the non-orthogonal stresses. This is illustrated in Fig. 9 where the proportion of energy in the Reynolds Stresses captured by transformation of the Cartesian orthogonal stresses is shown in both co-ordinate systems. These are calculated using Eqs. 16 and 17. Up to ~5% of the stresses are seen to be in off-diagonal terms. On the LHS of Fig. 9 there is clear lack of circumferential symmetry. These data are used in the bulk region. In the near-wall region (RHS), the Reynolds stresses from DNS empirical data actually result in *more* unsteady momentum transfer than the full fluid solution suggests, but the change of co-ordinate frames does create rotational symmetry. Here the bulk appears homogenous (though the scale is much larger than the LHS). It is clear that, the change of frame is important, and for

more complex geometries it would be unlikely that a simple transition between co-ordinate frames will be suitable or possible. A universally defined co-ordinate frame would remove the need to define a boundary.

$$\alpha_{\mathrm{CCS}} = \sqrt{\frac{\mathrm{R}_{\mathrm{UU}}^2 + R_{\mathrm{VV}}^2 + R_{\mathrm{WW}}^2}{\mathrm{R}_{\mathrm{UU}}^2 + R_{\mathrm{VV}}^2 + R_{\mathrm{WW}}^2 + 2(\mathrm{R}_{\mathrm{UV}}^2 + R_{\mathrm{UW}}^2 + R_{\mathrm{VW}}^2)}} \tag{16}$$

$$\alpha_{\mathrm{BFCS}} = \sqrt{\frac{R_{11}^2 + R_{22}^2 + R_{33}^2}{R_{\mathrm{UU}}^2 + R_{\mathrm{VV}}^2 + R_{\mathrm{WW}}^2 + 2(R_{\mathrm{UV}}^2 + R_{\mathrm{UW}}^2 + R_{\mathrm{VW}}^2)}} \tag{17}$$

While there have been implementations of the CRW that use all 9 Reynolds Stresses, these lead to complicated models which are less physically intuitive, so arguments are often made to ignore cross terms [10]. These conflicting requirements can be satisfied through transformation of the full, real, symmetric Reynolds Stress matrix into a diagonal matrix [24]. The diagonal terms are the eigenvalues of the Reynolds stress matrix with eigenvectors defining their principal axes which take unique values in each cell. Figure 10 shows the 1st and 2nd eigenvectors calculated. At the wall it is clear that one of the eigenvectors tends to lie close to the wall-normal direction as in the body fitted co-ordinate system and there is smooth, continuous transition to the centre of the pipe. Whereas the previous model only considered the diagonal terms this new model accounts for all fluctuations. Previous literature studying deposition has found the effect of cross-terms to be weak in simple flows [11], but as more complex flows tend to have higher strain the cross-terms are larger. In addition, the form of the drift correction for the wall-normal direction in Eq. 12 is now fully applicable in all directions.

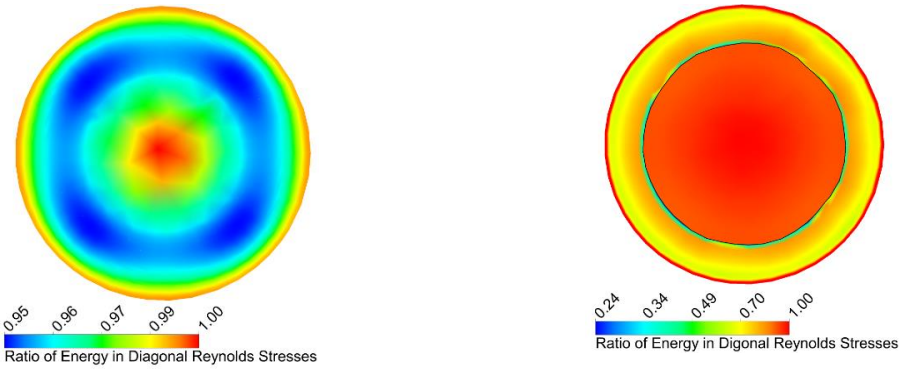

Figure 9 Left - $\boldsymbol{\alpha_{CCS}}$ (Eq. 16) plotted at the outlet of L&A case [14]. Minimum is 0.948 (mid-radius) and the maximum is 0.999. Right - $\boldsymbol{\alpha_{CCS}}$ (Eq. 16) in bulk and $\boldsymbol{\alpha_{BFCS}}$ (Eq. 17) in near-wall region, boundary denoted by black solid line. The minimum is 0.250 (near the boundary) and maximum is 9.18 (in the near-wall region). The color scale is limited to 1 for clarity.

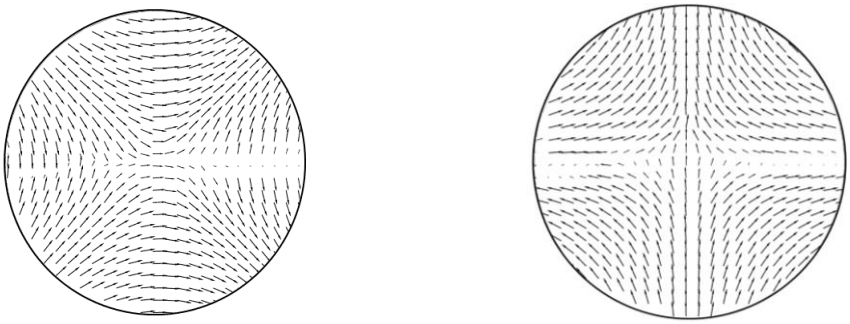

Figure 10 Vector plot of 1st and 2nd eigenvectors. The 1st /2nd eigenvectors along the diagonals align with the wall-normal/span-wise directions respectively. The 1st /2nd eigenvectors along the diagonals align with the span-wise/ wall-normal directions respectively. Magnitudes are not representative; all have magnitude equal to unity.

5. Constant isotropic τ_L in buffer layer

The CRW shows high sensitivity to the Lagrangian time scale. Figure 7 shows the RSM model underpredicts this close to the wall. In order to apply a lower cut-off in τ_L to this region, the value of τ_L calculated using the RSM fluid solution at a chosen location $y^+ = y^+_{lim}$ is assigned to cells with smaller y^+ in close proximity using a search algorithm. This synthetic value of τ_L is referred to as the effective Lagrangian time scale (τ'_L). The scaling of τ_L derived from the raw RSM data near the wall of the straight pipe is shown Fig. 11. The isotropic effective Lagrangian time scale is used in the calculation of the time-step (Eq. 7) and the velocity fluctuation (Eq. 15).

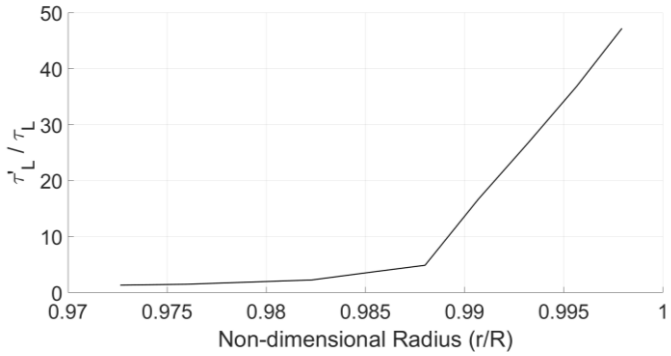

Figure 11 Ratio of Lagrangian time-scale ($\boldsymbol{\tau'_L/\tau_L}$) with $y^+ < y^+_{lim}$ *when* $y^+_{lim} = 10$

6. Anisotropic τ_L

For isotropic flow the Lagrangian time-scale is defined as in Eq. 9. In engine relevant flows the Lagrangian time scale is anisotropic described by Mito and Hanratty [20] using Eq. 14. Unfortunately this definition cannot be used with RANS RSM solutions because unavailable

unsteady terms are required. However in regions where $y^+ > y^+_{\text{lim}}$ the reported isotropic value of ϵ is used, which allows an anisotropic $\tau'_{\text{L}}$to be calculated using anisotropic Reynolds Stresses. As the principal axes directions are now cell specific, in the region where $y^+ < y^+_{\text{lim}}$ the anisotropic time-step, $\tau_{\text{L,i}}{}'$, must be calculated for each cell using the Reynolds Stresses and ε from geometrically closest cell lying at $y^+ \sim y^+_{\text{lim}}$ transformed to the local co-ordinate system. This approach results in cross terms in the time-scale however they are found to be less than 1% in magnitude compared of those in the principal directions, and thus are neglected. The anisotropic Lagrangian time scales are used in Eq. 15 in the local diagonalised directions, however a single time-step, Δt is required and this is set using the effective isotropic Lagrangian time scale as noted above.

V. CRW EVALUATION RESULTS

The effect of time-step on deposition is already noted in Fig. 5 when the original linearly approximated solution to Eq. 4 is used. When using the exact solution to the Langevin equation (Eq. 15) the results (Fig. 12), show the relative levels of deposition with changing time-step definitions remains similar. However it is notable that the use of the exact solution leads to an increase in predicted deposition by more than an order of magnitude compared to a solution using Eq. 8. The physically informed time-step $\Delta t = \sqrt{\tau_{\text{K}}\tau_{\text{L}}}$ matches the experimental data best in the diffusion-impaction regime, thence this is used for all subsequent simulations except where explicitly stated. The original CRW solution and the exact solution with $\Delta t = \sqrt{\tau_{\text{K}}\tau_{\text{L}}}$ as baseline predictions in the graphs below.

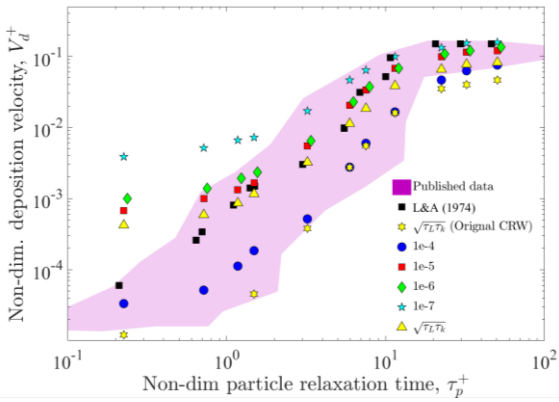

Figure 12 The effect of using the exact solution to the Langevin equation (Eq. 15). (Two-layer model, fitted DNS statistics, local isotropic Lagrangian time scale and time-step).

Figure 13 provides a comparison of different strategies for co-ordinate system transformation. The results show that using the RSM statistics with the two-layer cell model over predicts deposition of smaller particles. By calculating the gradients along the principal axes on a per cell basis (through Reynolds Stress diagonalisation), the total fluctuations and Reynolds Stress gradient experienced by the particle is taken into account. Interestingly this results in deposition distribution very similar to the original two-layer CRW using this time-step, although less accurate than the exact DNS tuned solution for the vertical pipe.

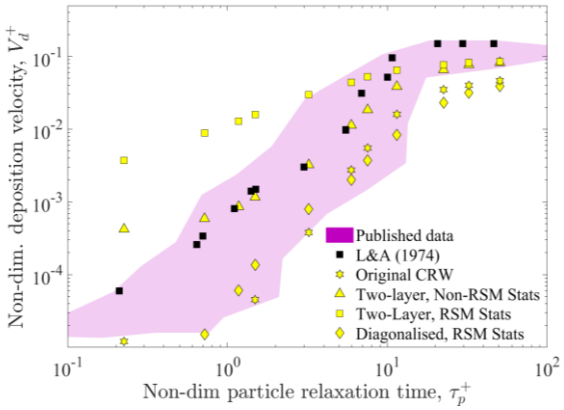

Figure 13 Effect of using RSM RANS predicted fluid statistics and a universally defined co-ordinate frame. All results use the exact solution to the Langevin (Eq. 15) and isotropic τ_L and Δt (which is are unbounded near the wall).

In Fig. 14 the effect of limiting the Lagrangian time-step in the region where $y^+ < y^+_{lim}$ and of using an anisotropic time-step are demonstrated. The definition of a non-zero lower limit of y^+_{lim}, while continuing to assume that τ_L is isotropic, reduced deposition only marginally (labelled 'isotropic τ_L') for $y^+_{lim} = 5$. This is the limit below which a constant time-step is imposed when using experimentally derived statistics. Results for a $y^+_{lim} = 10$ were generated and did not show significant difference compared to the results using $y^+_{lim} = 5$ (these are not shown on Fig. 14 for clarity). Gross anisotropy in τ_L was demonstrated in Fig. 7. Its effect relative to the isotropic case is shown using the same values of y^+_{lim}, remembering that the imposed Reynolds Stresses are assumed constant to generate local anisotropy in τ_L. Interestingly, this resulted in a very substantial increase in deposition, most significantly for smaller particles generating a result very close to the exact DNS tuned solution.

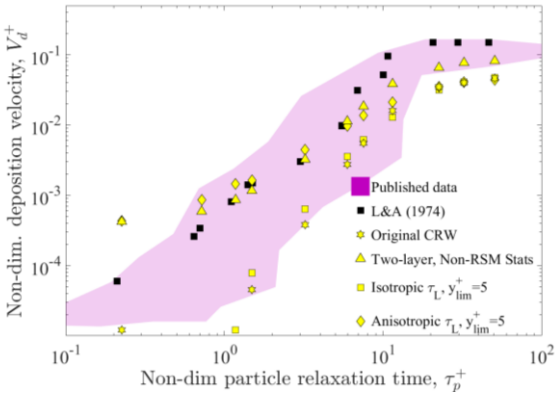

Figure 14 Effect of constant isotropic / anisotropic time scales in the very near-wall region (y^+_{lim}<= 5). All results use a single universal co-ordinate frame and the exact solution to the Langevin Eq 15, and local isotropic time-step.

The above discussion demonstrated the difficultly of developing the CRW based on integral results as there are several parameters over which there is some flexibility. From Fig. 14 we can conclude that: using the exact solution to the Langevin equation, with locally diagonalised Reynolds Stresses, and local anisotropic time-stepping capped for the region where y^+lies below a lower limiting value, it is possible to predict deposition with accuracy equivalent to the CRW model using DNS statistics in simple pipe flows. Also, the CRW continues to show better agreement to experimental data than other random walk models. Importantly, now there is no physical reason that any of the assumptions should be violated when applied to highly accelerating flows.

VI. FULL MODEL DEPOSITION RESULTS IN A 90° BEND

The modified CRW model (as described in the previous paragraph) has been used to model deposition in a 90° bend. This model is less dependent on external correlations, but produced equivalent results in a simple flow. These correlations are sourced from simple flow cases and thus would be less appropriate for the simulated case. Hence, these results demonstrate the effect of considering case-specific turbulent statistics in a situation where they are expected to have an effect.

The geometry and operating conditions are as described in Fig. 2 and Table 1. Here, particle tracking is carried out on the fluid solution modelled using the RSM WWR, as this was shown to most accurately capture the important fluid features, in particular the near-wall Reynolds Stresses, when compared to the LES. Other key features of the flow for deposition modelling, such as a constant Lagrangian time scale near the wall, result from the modifications made to the

implementation of the CRW as described previously. Simulations were carried out using no turbophoresis model, the DRW, the original CRW, and the new CRW model. First, the predicted integral deposition fraction is compared to the experimental results of Pui et al. [4]. Then, the deposition distributions are compared to the LES results of Breuer et al. [7].

Figure 15 shows there are two distinct features of the integral deposition curve: the increase in gradient as *Stk* increases from 0 to 0.3; and the decreasing gradient of curve above *Stk* = 0.3. Further, all models under-predict the deposition from a Stokes number of 0.3 to 0.8. The following analysis is focused on the differences in deposition predicted by the old and new CRW models, contextualised by other data, to understand the effect of case-specific turbulent statistics.

Without turbulent dispersion modelling, the largest absolute disagreements compared to the experimental results are in the intermediate Stokes number regime, as a results of a flatter curve. Further, the results change little when the Original CRW model is used, implying that the original CRW model has little effect. The DRW results are most distinct from the others, it strongly over predicts deposition of small Stokes number particles which is in line with previous results in straight pipe flows. The DRW also predicts a more linear relationship between Stokes number and deposition for *Stk*>0.3. The revised CRW model appears to capture the shape of the curve above *Stk*=0.3 and the curved tail below Stk = 0.3 well. Investigating the spatial distribution of deposition shows differences not apparent when comparison is made at the integral level.

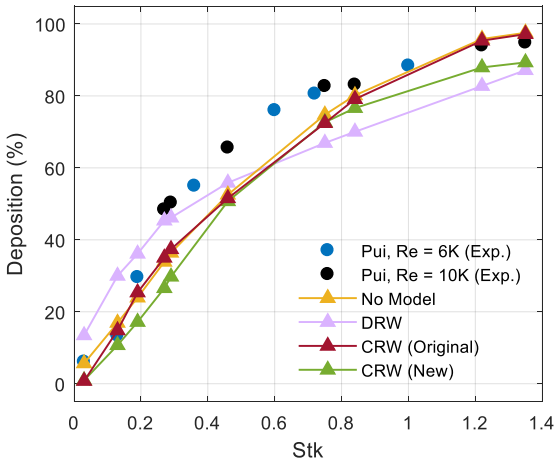

Figure 15 Predicted deposition in the Pui et al. [4] test case using WWR RSM, compared to the experimental results.

The simulated and experimental integral deposition results show the most similarity to one another at Stk = 0.84 (Fig.15), hence the spatial distribution of deposition around the bend is compared at this condition to illustrate why this comparison is particularly important. As one would expect for the particle tracking without a turbulent diffusion model, such that deposition is inertia driven, the particles predominantly hit the outer wall (Fig. 16a). The DRW predicts less deposition, and Fig. 16b shows this is due to fewer particles impinging onto the earlier section of the bend and a lower plateau in the axial direction. Despite Fig. 15 showing little difference, in the predicted integral deposition between models at Stk = 0.84, Fig.16 shows that the original CRW does affect the particle deposition. Both the original and modified CRW create a peak toward the start of the bend. The latter's peak is sharper and further upstream location. Figure 17 shows that the use of the new CRW (reliant on only RSM statistics) has resulted in predictions more similar, in distribution, to the LES results by Breuer et al [7]. The key feature being the presence, position, and sharpness of the peak. The asymmetry in LES spatial results from previous literature [7], where it would otherwise be expected due to a symmetric flow field, indicates the particle tracking from this study may not be reliable at this level of fidelity. The ability to model this peak with a simple RANS fluid solution and stochastic particle tracking model will also allow for its origin to be investigated practicably. This is only possible due to the developments in this paper, and demonstrates the value of the model.

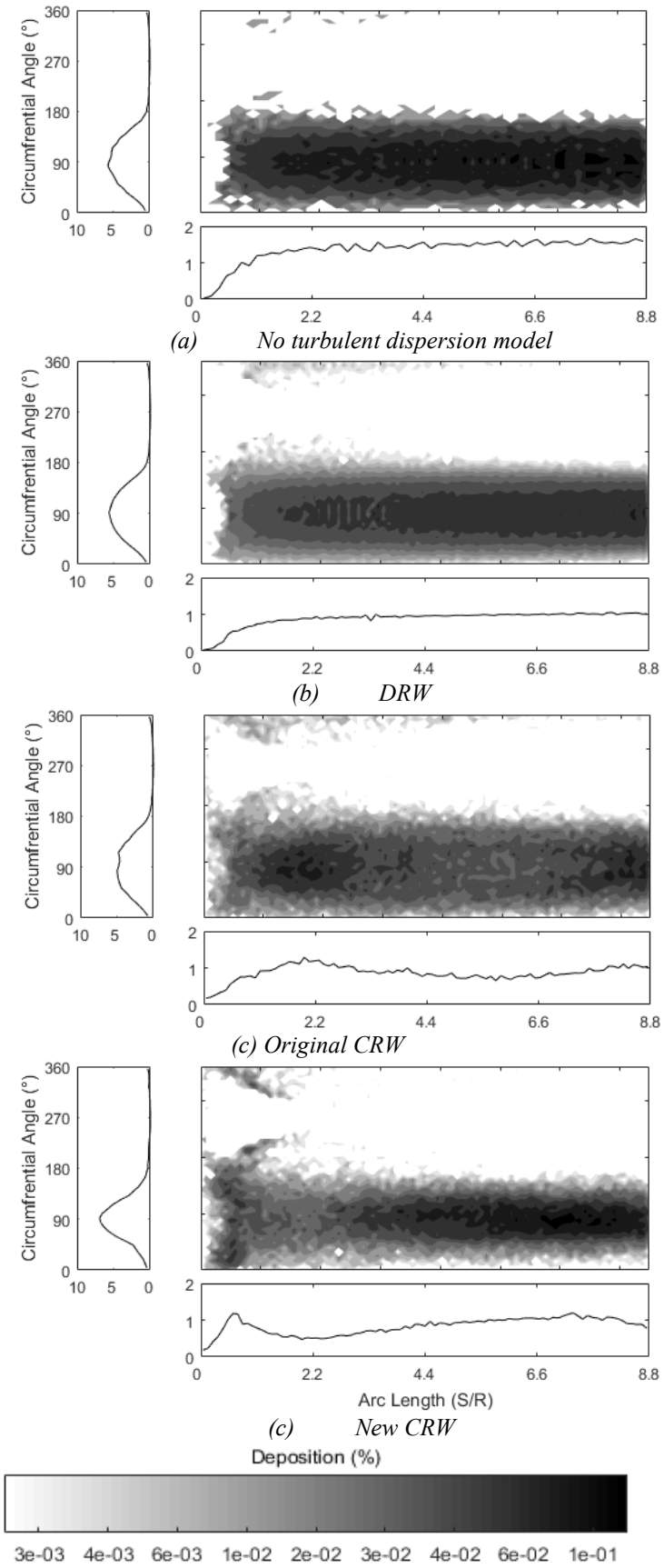

Figure 16 Deposition on bend sections using different Turbophoresis models. RSM WWR fluid solutions used. Outer-bend centerline at 90°. Inner-bend centerline at 270°.

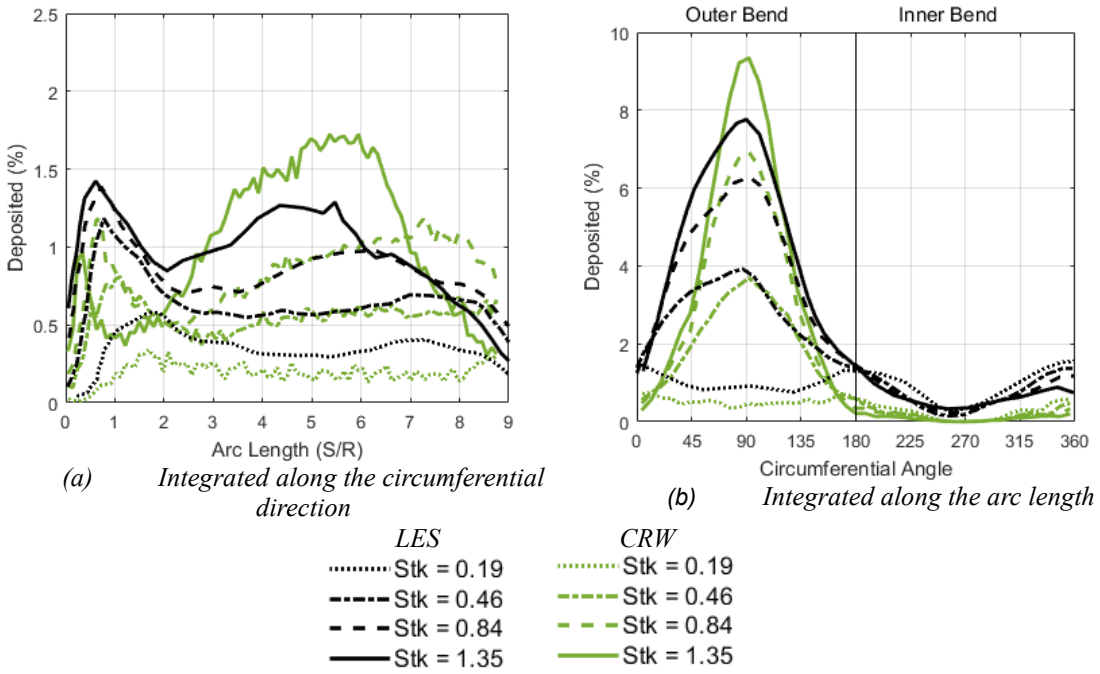

(a) Integrated along the circumferential direction

(b) Integrated along the arc length

Figure 17 Spatially resolved deposition using new CRW and RSM-WWR compared against LES results by Breuer et al. [7]

VII. SUMMARY

Capturing particle-turbulent interaction in complex flows, using RANS simulations, is essential for particulate driven damage to be considered in the design process.

In this paper, a revised CRW model is proposed which can be applied to engineering design CFD solutions by employing essential turbulence properties derived from appropriate RANS solutions. This eliminates any dependence on higher fidelity simulations for turbulent statistics or so called correction factors. The revised model has the additional benefit of being less sensitive to the choice of the time-step making its appropriate use by engine designers more likely.

The model accounts for the cross-terms in the Reynolds Stress tensor, anisotropic time scales, and applies realistic anisotropic time scales within the near-wall region. The model is shown to predict deposition with accuracy equivalent to that of the CRW in idealised flows.

The application of the modified CRW model to a 90° bend has clearly demonstrated that the modifications have notable affect in more complex, accelerating, flows. Although the revised model does not match integral levels of deposition, it does capture important trends across the

Stokes number range tested. Further, the spatial distribution predicted includes features only otherwise seen in LES predictions.

Using this model in a comprehensive study of particle motion and deposition in a 90° bend will allow for the initial peak in deposition and integral deposition trends (with Stokes number) to be explained. This may also uncover the source of the discrepancy compared to experimental data. The model requires further validation in a geometry with engine representative features and particle acceleration.

ACKNOWLEDGMENTS

The authors would like to acknowledge the EPSRC via the Centre for Doctoral Training in Gas Turbine Aerodynamics studentship (EP/L015943/1) and Rory Clarkson at Rolls-Royce PLC for their support.

REFERENCES

[1] Hamed, A., Tabakoff, W. C., and Wenglarz, R. V., "Erosion and Deposition in Turbomachinery," *J. Propuls. Power*, vol. 22, no. 2, pp. 350–360, 2006.

[2] Wylie, S., Bucknell, A., Forsyth, P., McGilvray, M., and Gillespie, D. R. H., "Reduction in Flow Parameter Resulting From Volcanic Ash Deposition in Engine Representative Cooling Passages," *J. Turbomach.*, vol. 139, no. 3, p. 031008, 2016.

[3] Forsyth, P., "High Temperature Particle Deposition with Gas Turbine Applications," University of Oxford, 2017.

[4] Pui, D., Romay-Novas, F., and Liu, B., "Experimental Study of Particle Deposition in Bends of Circular Cross Section," *Aerosol Sci. Technol.*, vol. 7, no. 3, pp. 301–315, 1987.

[5] Forsyth, P., Gillespie, D. R. H., Mcgilvray, M., and Galoul, V., "Validation and Assessment of the Continuous Random Walk Model For Particle Deposition In Gas Turbine Engines," *ASME Turbo Expo 2016 Turbomach. Tech. Conf. Expo.*, vol. GT2016-573, pp. 1–13, 2016.

[6] Young, J. and Leeming, A., "A Theory of Particle Deposition in Turbulent Pipe Flow," *J.*

Fluid Mech., vol. 340, 1997.

[7] Breuer, M., Baytekin, H., and Matida, E., "Prediction of aerosol deposition in 90 degree bends using LES and an efficient Lagrangian tracking method," *J. Aerosol Sci.*, vol. 37, pp. 1407–1428, 2006.

[8] Ghahramani, E., Abouali, O., Emdad, H., and Ahmadi, G., "Numerical analysis of stochastic dispersion of micro-particles in turbulent flows in a realistic model of human nasal/upper airway," *J. Aerosol Sci.*, vol. 67, pp. 188–206, 2014.

[9] Dehbi, A., "Turbulent particle dispersion in arbitrary wall-bounded geometries: A coupled CFD-Langevin-equation based approach," *Int. J. Multiph. Flow*, vol. 34, no. 9, pp. 819–828, Sep. 2008.

[10] Bocksell, T. L. L. and Loth, E., "Stochastic modeling of particle diffusion in a turbulent boundary layer," *Int. J. Multiph. Flow*, vol. 32, no. 10–11, pp. 1234–1253, Oct. 2006.

[11] Bocksell, T. L. and Loth, E., "Random Walk Models for Particle Diffusion in Free-Shear Flows," *AIAA J.*, vol. 39, no. 6, pp. 1086–1096, Jun. 2001.

[12] Vadgama, N., Forsyth, P., McGilvray, M., and Gillespie, D. R. H., "Numerical Simulation of Spatially Resolved Particle Deposition in Accelerating flows," in *AIAA Aviation 2019 Forum*, 2019.

[13] Mofakham, A. A. and Ahmadi, G., "On random walk models for simulation of particle-laden turbulent flows," *Int. J. Multiph. Flow*, vol. 122, p. 103157, Jan. 2020.

[14] Liu, B. Y. . and Agarwal, J. K., "Experimental observation of aerosol deposition in turbulent flow," *J. Aerosol Sci.*, vol. 5, no. 2, pp. 145–155, Mar. 1974.

[15] Berrouk, A. S. and Laurence, D., "Stochastic Modelling of Aerosol Deposition for LES of 90° Bend Turbulent Flow," *Int. J. Heat Fluid Flow*, vol. 29, no. 4, pp. 1010–1028, Aug. 2008.

[16] Mathey, F., Cokljat, D., Bertoglio, J. P., and Sergent, E., "Assessment of the vortex method

for Large Eddy Simulation inlet conditions," *Prog. Comput. Fluid Dyn. An Int. J.*, vol. 6, no. 1/2/3, p. 58, 2006.

[17] Legg, B. J. and Raupach, M. R., "Markov-chain simulation of particle dispersion in inhomogeneous flows: The mean drift velocity induced by a gradient in Eulerian velocity variance," *Boundary-Layer Meteorol.*, vol. 24, no. 1, pp. 3–13, Sep. 1982.

[18] den Toonder, J. M. J. and Nieuwstadt, F. T. M., "Reynolds number effects in a turbulent pipe flow for low to moderate Re," *Phys. Fluids*, vol. 9, no. 11, pp. 3398–3409, Nov. 1997.

[19] Shivran, S., "Experimental study of complex pipe flows," KTH Mechanics, 2011.

[20] Mito, Y. and Hanratty, T. J., "Use of a Modified Langevin Equation to Describe Turbulent Dispersion of Fluid Particles in a Channel Flow," *Flow, Turbul. Combust.*, vol. 68, pp. 1–26, 2002.

[21] Laufer, J., "The Structure of Turbulence in Fully Developed Pipe Flow," 1952.

[22] Sawford, B., "The Basis For, And Some Limitations Of, The Langevin Equation in Atmosphere Relative Dispersion Modelling," *Atmos. Enviroment*, vol. 18, no. 11, pp. 2405–2411, 1984.

[23] Kallio, G. A. and Reeks, M. ., "A Numerical Simulation of Particle Deposition In Turbulent Boundary Layers," vol. 15, no. 3, pp. 433–446, 1989.

[24] Zhou, Q., Leschziner, M. A., Zhou, Q., and Leschziner, M. A., "A time-correlated stochastic model for particle dispersion in anisotropic turbulence," in *Symposium on Turbulent Shear Flows, 8th, Munich, Federal Republic of Germany, Sept. 9-11*, 1991, vol. 1, pp. 1–6.

[25] Dehbi, A., "A CFD Model for Particle Dispersion in Turbulent Boundary Layer Flows," *Nucl. Eng. Des.*, vol. 238, no. 3, pp. 707–715, 2008.

3.2 Summary

The CRW model developed in this chapter is far more generalised and achieves comparable accuracy in simple flows when compared to the original model previously used (Section 3.1, Figure 14). Particularly useful characteristics of this developed model include:

- Independence from external high fidelity data that is not available for geometries of interest in gas turbines. This was possible through careful selection of the Reynolds stress model and physically informed modification of the near the wall Lagrangian time scale.
- A universally defined co-ordinate system via diagonalization of the Reynolds stress tensor. The flow no longer requires segregation into bulk and near-wall zones at an arbitrary Y^+ value. Diagonalisation eliminates the need for inclusion of the cross-terms, maintains computational efficiency, and ensures the assumption of small cross terms in the drift correction term used remains satisfied [19]
- Consideration of all Reynolds stress terms throughout the domain. There is no assumption regarding the directionality of turbulence, or the dominant terms of the Reynolds Stress tensor. It is shown that previous models do not fully describe the magnitude of turbulence, particularly at the interface of the bulk and near wall zones. Moreover, the revised model demonstrates that such modelling is still required in these in these 'bulk-flow' regions.

The model also addresses recent literature which has debated the appropriate definition of the integral time step [54]. Revisiting the fundamental mathematical basis of the model, and re-examining early literature, provided an explanation for the artifices in previous models. A suitable integral time step definition is proposed in the current implementation. The use of an exact solution to the governing stochastic differential equation, and comparison of results using different integration time steps, is used to demonstrate this (Section 3.1, Figure 5).

These developments make the model a feasible tool to predict general turbulent particle transport and allow its application to gas turbine flows.

4 High Temperature Experiments with Acceleration

There are very limited data which illustrate the vulnerability of real engine parts in the gas turbine engine secondary air system to particulate deposition. While deposition does occur in the compressor, it is more concerning where temperatures are higher as hot corrosion can occur (the turbine) and where the air flow is critical to the engine's integrity (the secondary air system). To explore this, experiments were designed that aimed to mimic the internal temperature of cooled turbine components and components directly under the blade platform feeding these cooling systems where particles are known to form deposits. In order to further validate the model presented in Chapter 3, suitable experimental data are also required. The criteria set for useful data are that they should be:

- relevant to gas-turbine flows
    - using particles of appropriate shape, size, and composition
    - using velocity fields and temperatures typical of secondary air and cooling passages
- be sufficiently complex to test the underlying assumptions of the modelling approach
- spatially resolved, rather than merely an integrated total deposition mass

In order to make the test case comparable to the gas-turbine secondary air system, and cooling passage flows, significant acceleration and anisotropic turbulence are needed. To achieve this, a test piece including a double 90 degree bend fed with bulk flow in the turbulent regime was studied. A rectangular cross-section was chosen for its similarity to cooling passages found in the engine. The choice of cross section is significant as it changes the in-plane flow structures significantly compared to a circular cross-section, and introduced additional secondary flows. A double bend was chosen, first to replicate the single bend of Wu and Young [55], but then deliberately changed to better match the pattern of vorticity which may occur in multipass cooling schemes and larger secondary air structures where there is flow turning in confined passages. The test piece provides

some insight as to how deposition is affected in regions of curvature, and downstream thereof in the engine. Physical constraints in the experimental rig supported the adoption of two double -bends running in parallel as this allowed integration into a pre-existing air system in the experimental facility most easily (also designed by the author). The conditions chosen represent engine temperatures which ensure materials, both surface and particle, have appropriate material properties. It is later discussed whether this provides the best conditioned data for validation of the CRW in the absence of a reliable bounce-stick model. Finally, the representative passage velocity ensures similar particle-wall interaction, which resulted in significant sticking.

The primary challenge of conducting experiments for the validation of deposition driven by atmospheric particulates, is to have sufficient particles in the test stream to cause significant measurable deposition, over the duration of the test, without violating the one-way coupling between the flow of air and particles. For validation of one-way coupled simulation, one-way coupling is need in the experiments. This requires low particle concentrations (Section 2.5.2), and hence long run times. Previous experimental campaigns at gas turbine conditions have failed to replicate this, and it has been shown that the non-dimensional deposition rate is affected by it [114]. A new dry particle delivery system was constructed to maintain these low concentrations, and a bespoke inline heater was selected such that conditions could be maintained for the test duration required. Details of the design of the experimental facility, and its commissioning, can be found in Section 4.1.

As identified in the literature review, there is a lack of spatially resolved data, and previous studies have found models to predict similar integral deposition fractions with varying spatial deposition [100], [107]. The comparison of turbulent transport models in Chapter 3 confirmed this pattern. Further, for particle deposition to be considered in component design, models must be spatially accurate as the deposition location determines the associated risk. The test piece was constructed in a way that the spatial deposition could be captured. A high resolution microscope (Alicona InfiniteFocus) was used to generate a point-cloud geometry of the specimen after exposure to the dust. Whilst other studies have used liquid droplets to create near all-stick conditions [89], [103], solid particles were used to ensure deposition could be measured at high resolution.

Furthermore, these data can provide longer term value, as they can be used for validation of all transport, sticking, and erosion models, supporting the wider group's research. In addition to the results reported in the paper included below (Section 4.2), further results are included as Section .4.3.

While there are high quality data for the direct impingement of particles onto heated metal plates, these are the first of their kind in combining these aspects of secondary airflow, making it a valuable resource. Beyond the immediate validation, they can be used by the wider research community for partial validation of both transport and bounce-stick models for particle deposition in gas turbines.

4.1 Experimental Facility

The basic function of the test rig is described in the paper which largely constitutes this chapter (Section 4.2), however more detailed design considerations were conducted than were possible to report there. Figure 26 shows a labelled schematic of the experimental facility, and Figure 27 shows the equivalent schematic. The test gas for this rig is lab air at 7 barg pre-dried (dew point -40 degrees Celsius) and filtered. Hot air is provided by an eight kilowatt in-line heater (Section 4.1.2) and is mixed with cold particulate laden flow using a coaxial jet (Section 0). Flow control is provided by three mass flow controllers (Section 4.1.1) and verified with an orifice plate (Section 4.1.8). Particles are injected using a solid particulate aerosol generator (Section 4.1.3). The test piece (Section 4.1.7) sits with an oven (Section 4.1.5), and metal temperatures <1473 K and gas temperatures <1030 K can be created. At the test-section exit, cold air is mixed in to reduce the temperature so that it can be filtered by HEPA filters (Section 4.1.9).

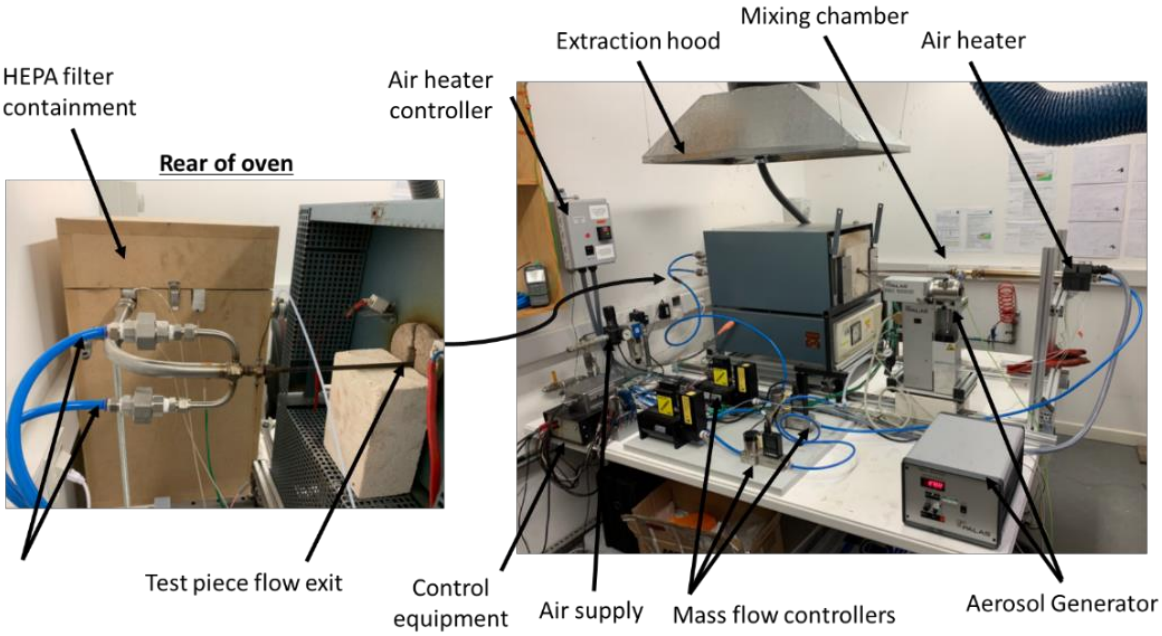

Figure 26 Photograph of the experimental rig with key equipment labelled. Photographs taken by S. Beal.

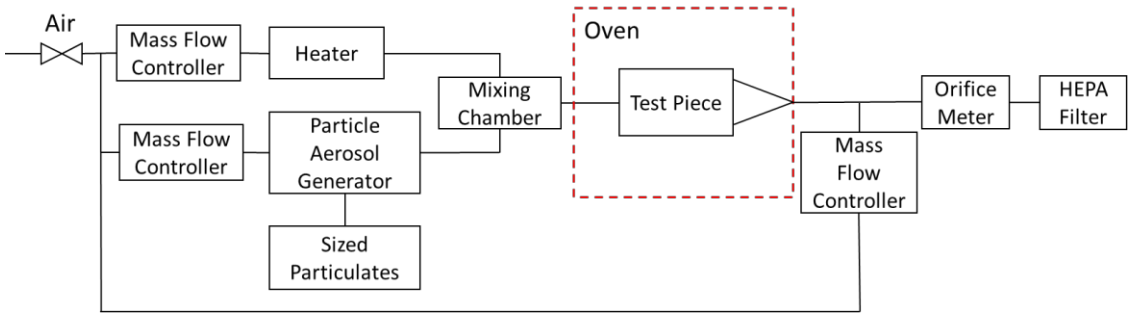

Figure 27 Schematic of air flow through rig, flow from left to right.

4.1.1 Mass Flow Controllers

As per Figure 27, three mass flow controllers were required, that attached to the: particle aerosol generator had a flow range of 0-1.1 g/s (Omega FMA-2609A); heater 0-11 g/s (Omega FMA-2612A); and the exit pipework dilution flow 0-22 g/s (Omega FMA5445). The mass flow controller with the largest capacity was controlled using a voltage output module (NI-9263) in a National Instruments CompactDAQ chassis (cDAQ-9174), while the others were controlled using a serial RS232 connection. All of these were controlled from a bespoke National Instruments LabView Virtual Instrument which was used to capture data for the whole experiment.

4.1.2 Heater

The Tutco SureHeat JET 8 kW heater was chosen for its low minimum mass flow rate requirements and high temperatures. It is capable of heating flow (1.25-7.35 g/s) up to 1033 K, higher than any currently expected gas turbine cooling air flow. This allowed engine flow temperatures to be recreated without the need for further, cumbersome, heating elements (unlike previous rigs at the OTI that used heater tape). Further, the excess temperature range enabled faster heating of the test piece.

4.1.3 Particle Aerosol Generator

The PALAS RBG1000 IGD was chosen for aerosol generation due to the large particle concentration range it can cover, with a minimal (unheated) flow rate required to transport particles (0.17 g/s) to the main flow allowing for higher inlet gas temperatures. Importantly this allows very low dosing of the flow with particles, a minimum of 0.08 g/m^3. These are still substantially higher than engine conditions but balance the need for substantial deposition over the duration of the experiment with the need for the particle laden flow to remain 'one-way coupled' and thus the subsequent deposition to remain representative of engine conditions.

4.1.4 Mixing Chamber

A mixing chamber is required to mix the hot gas with the cold particulate stream. In previous rigs, where the particles were injected perpendicular to the hot gas, the particle stream would penetrate the hot gas stream completely causing particles to impact onto the chamber's walls. Even in less extreme cases numerical simulations showed that this would result in a non-uniform particle injection, and non-axisymmetric deposition in a pipe flow. For this work a co-axial jet was used to ensure this did not happen. The basic premise of these is a primary jet is injected at the centre of the secondary jet. It is reported that confined/recessed systems result in better mixing efficiencies, therefore such a design was adopted [125]. As this work aims to increase understanding of particle transport designing such a system is *à* priori challenging, none the less consideration was given to the design choices.

The first consideration was which stream should be the primary, and which should be the secondary. Multiple studies indicate that the low density stream should be at the centre [126], [127]. It was also reported that a high secondary velocity/momentum ratio is required. For these reasons, as well as to ensure that the shear layer forming resulted in vortices rolling up into the centre the system was designed to achieve higher momentum in the secondary stream with a momentum ratio of 20:1.

The second consideration was the angle at which the incoming secondary stream should be injected, Figure 28 . One study was found in the open literature on non-parallel confined co-axial injection, this suggested that increasing the angle of the secondary stream injection had little effect on when the fully mixed condition is achieved [127]. CFD simulations of inlets from 15° to 45° (in 15° increments) were tested with the first resulting in best particle mixing. It is observed that as the inlet angle is increased the separation becomes larger which results in a lensing effect of the particles (Figure 29 to Figure 31). Further, the secondary inlet from opposing sides begins to penetrate the bulk flow and interact at high injection angles. Whilst this might result in better mixing at design conditions it is unclear if it would lead to similar problems as experienced previously, with particles penetrating the bulk flow and sticking onto the end walls.



Figure 28 CAD of the mixing chamber designed. The larger diameter pipe forms the secondary inlet, carrying the heated gas. The primary inlet is fed by a curved pipe and carries the cold particle-laden flow.

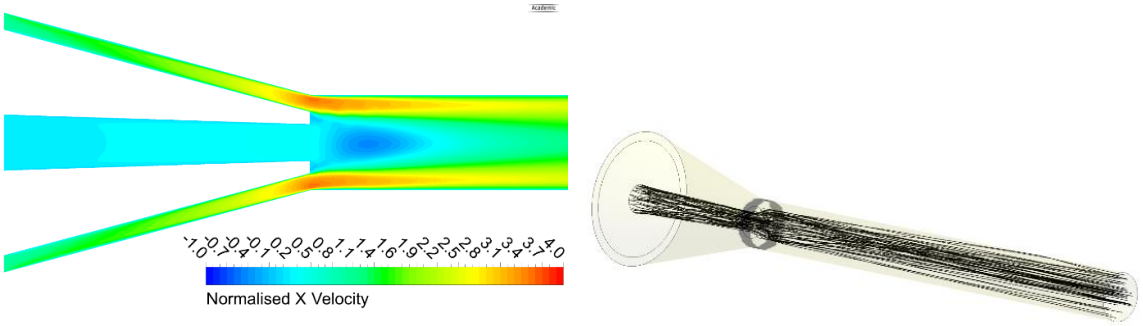

(a) Normalised X-velocity in mid-plane

(b) Negative wall shear stress in grey and 8 µm particle tracks.

Figure 29 Mixing chamber with a 15 degree secondary inlet cone angle

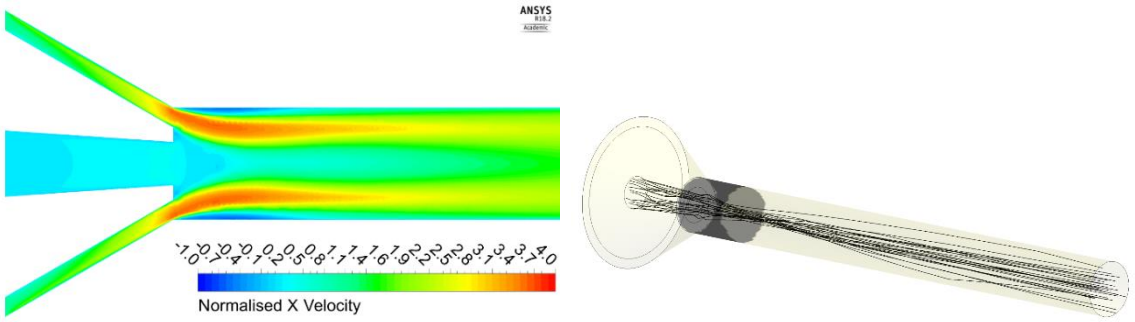

(a) Normalised X-velocity in mid-plane

(b) *Negative wall shear stress in grey and 8 µm particle tracks.*

Figure 30 Mixing chamber with a 30 degree secondary inlet cone angle

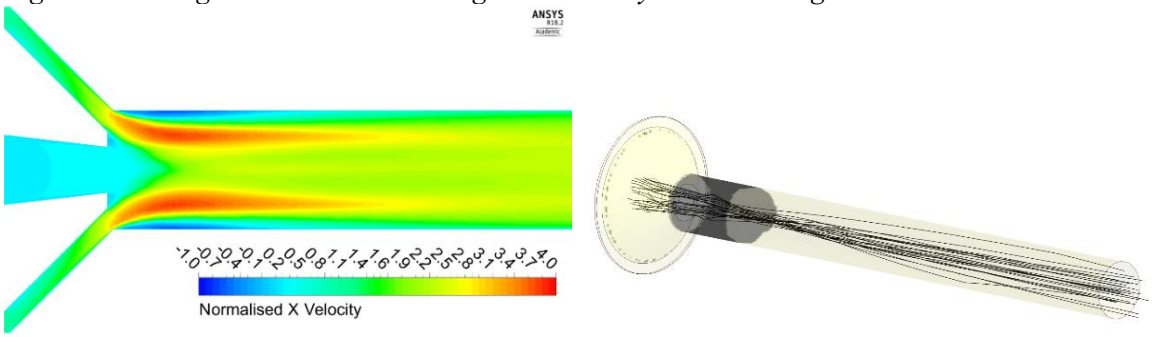

(a) Normalised X-velocity in mid-plane

(b) *Negative wall shear stress in grey and 8 µm particle tracks.*

Figure 31 *Mixing chamber with a 45 degree secondary inlet cone angle*

The final design consideration was the heating of particles. It is critical that the gas and particles arrive at the test section in isothermal equilibrium. Spherical particle with a minimum Nusselt number of 2 were used in a heat transfer analysis as a conservative case scenario, after, Whittaker (Equation 67) [128]. As the maximum Biot number (Equation 66) calculated for the likely particles encountered is ~0.2, a lumped element model can reasonably be used. The temperature response was calculated using an explicit finite difference method with a small time, such that negligible difference is seen in the results ($dt = 1 \times 10^{-6}$ s). Each particle that interacts with the surface is of a particular material and size, both of these affect the particle's heating. The relevant correlations for each mineral's thermal conductivity was estimated from existing data [129], [130]. The conductivity of air at these temperatures is given by Equation 68.

$$\mathrm{Bi} = \frac{h d_\mathrm{p} k_\mathrm{p}}{6} \qquad 66$$

$$\mathrm{Nu} = 2 + \left(0.4\mathrm{Re}^{\frac{1}{2}} + 0.06\mathrm{Re}^{\frac{2}{3}}\right)\mathrm{Pr}^{0.4}\left(\frac{\mu}{\mu_\mathrm{s}}\right)^{\frac{1}{4}} \qquad 67$$

$$k = 1.5207 \times 10^{-11} T_\mathrm{f}^3 - 4.8574 \times 10^{-8} T_\mathrm{f}^2 + 1.0184 \times 10^{-4} T_\mathrm{f} - 3.9333 \times 10^{-4} \qquad 68$$

Figure 32a shows the effect of particle size on heating rate, the largest particle is seen to take 6ms to heat. Table 4 lists common minerals in sand and dust, their heat capacity is calculated using the Kopp-Neumann law (rule of mixtures). Figure 32b shows that material has minimal effect on the required heating time even for the largest particles, with Calcite being the slowest to heat and Mica being the fastest. The piping is designed to provide 6 ms of heating time, which is adequate heating time but not excessive, in order to prevent spurious deposition prior to the test piece. Further, Figure 33 shows that the largest particles will reach velocity equilibrium with the fluid in this time.

Mineral	Chemical Formula	Specific Heat Capacity (J/Kg-K)	Density (kg/m^3)
Quartz	SiO_2	820	2648
Feldspar (Potassium)	$KAlSi_3O_8$	862	2560
Mica (Muscovite)	$KAl_3Si_3O_{10}(OH)_2$	944	2880
Calcite	$CaCO_3$	785	2710
Gypsum	$CaSO_4 \cdot 2H_2O$	1130	2360
Dolomite	$CaMg(CO3)_2$	847	2850
Halite	NaCl	1063	2160

Table 4 Properties of common minerals used to predict their heating. Heat capacity is calculated using the Kopp-Neumann law.

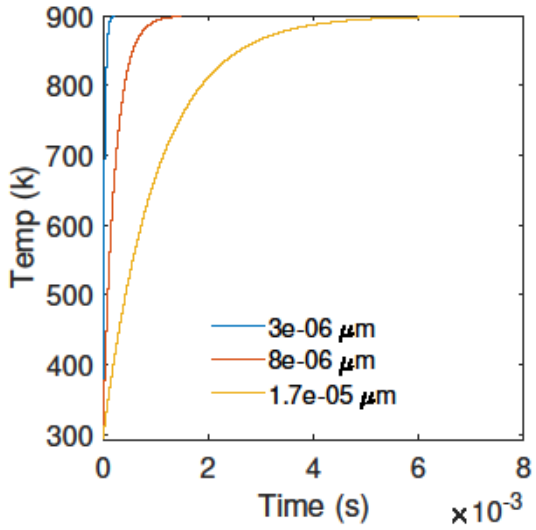

(a) Heating of various sized particles with slowest temperature response (calcite)

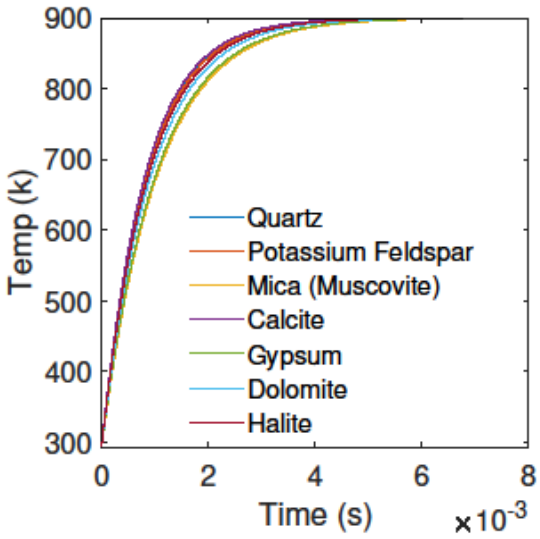

(b) Heating of 17μm particles with the most common mineral compositions at baseline conditions

Figure 32 Worst case (Nu = 2) particle heating time prediction using a finite difference method and various correlations.

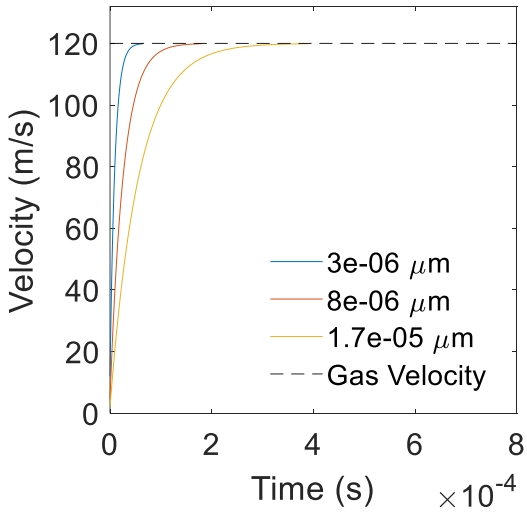

Figure 33Velocity response of a stationary particle in a 120 m/s flow, assuming minimal drag (Cd = 0.4).

4.1.5 Particle Material

Ultra-fine Arizona Road dust is used for the experiments in Section 4.2. This dust was chosen as it is: easily available in large quantities; widely used is turbine deposition studies; previous experiments have shown sticking at the temperature design point [131] ;and it matches the range of particle sizes expected in the engine which makes the experiment's particle impacts representative (as the bulk fluid velocity is matched to the engine).

4.1.6 Oven

A Wild Barfield, 3 kW oven was used to heat the test piece up to representative metal temperatures. This oven could reach 1250 K when sealed. For these experiments the oven was modified so the gas path could exit the rear. This removes the need for any bends before the cold air is mixed in so that sticking in the transfer piping and associated upstream effects are minimised. Further, custom doors were manufactured to reduce heat loss as it was physically impossible to shut the doors provided with the required pipework in place. The slow response of this oven is a limiting factor in the initial heating of the test piece.

4.1.7 Test Piece

Each test article used is assembled from four constituent parts and sits within a test piece holder. An initial design was modified as the first proposed test article was subject to an ongoing patent application making it unsuitable for disclosure in the open literature. The test piece is contained with an upstream cavity and downstream exit plenum, using 316 stainless steel bolts. Three test pieces, with ratio of curvatures (R_0) of 5, 10, and 15 were manufactured. Further details of the test piece are presented in the paper included in Section 4.2.

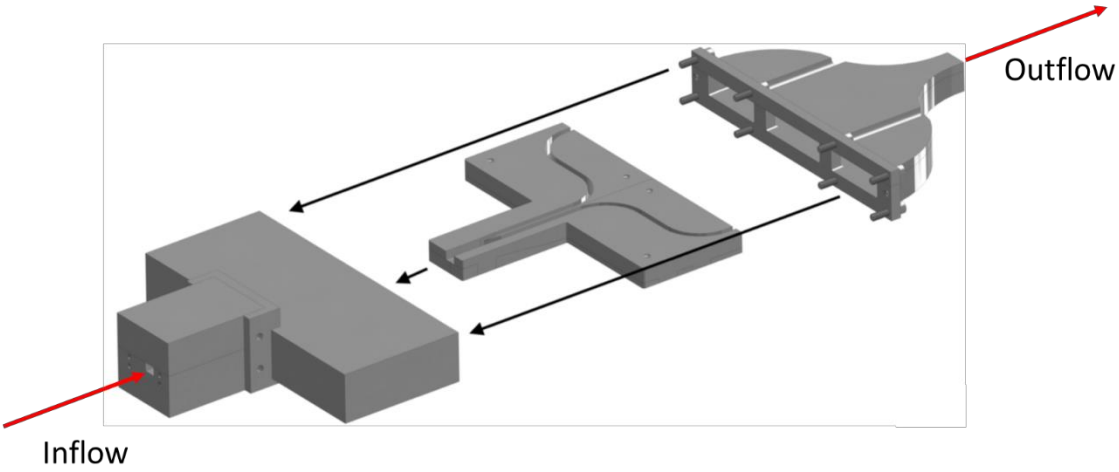

Figure 34 Assembly of the test piece in its holder. Red arrows show the flow direction, black arrows show assembly. Figure 3 of the paper included in Section 4.2 shows a further exploded view of the test piece.

4.1.8 Orifice Plates

An orifice plate was positioned prior to the HEPA filter and after the dilution flow (Figure 27). This was used to check the exit mass flow rate, and through a mass balance with the incoming mass flow

controllers ensure there were no serious leakages. The small pipe size meant that the orifice could not be designed to an international standard, and custom orifice plates were manufactured and calibrated to fit the exit pipework (Appendix B).

4.1.9 HEPA Filter

To ensure particles were not being directly emitted into the room, HEPA filters were attached to the exit (Figure 27). The filters (screw mount glove box HEPA filters by M.C. Air Filtration) had a maximum pressure drop of 90 Pascals when clean and maximum working temperature of 70 degrees Celsius. These weighed 570 g when new, enabling them to be weighed (section 4.1.10). These provide insight into the particle fraction deposited.

4.1.10 Weighing Scale

The Satorious Entris 623i is used to weigh parts before and after runs, to measure deposition. It has a maximum capacity of 620 g and linearity of 2 mg, this enables measurement of small amounts of deposition, enabling lower dosages and/or shorter duration tests.

4.1.11 Spatially Resolved Measurement

The data were also recorded spatially resolved. The process for doing this in a way that enabled quantitative measurement and inclusion in a paper is shown in Figure 35. The specimen with deposit (Figure 35a) is scanned to form a point cloud of the geometry with deposit (Figure 35b). The specimen's underlying geometry is then subtracted to calculate the deposit height normal to the surface (Figure 35c), and this can be represented as a 2D map (Figure 35d).

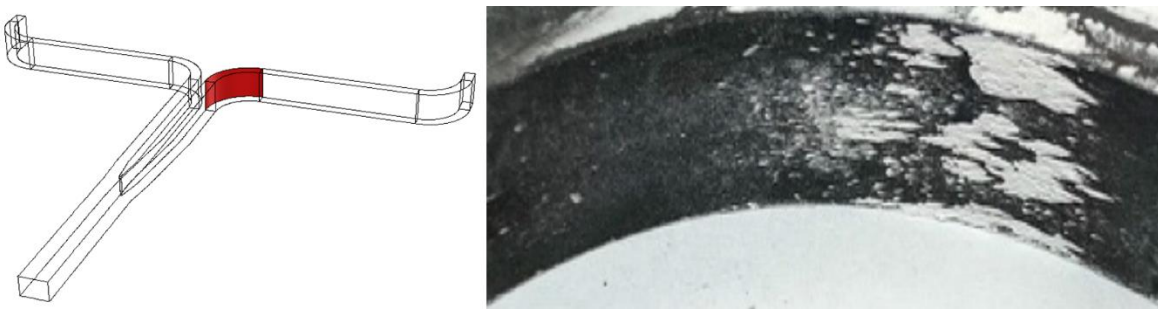

(a)Location of first bend ($R_0 = 5$) shown on CAD model (left), and a zoomed in photo of the deposition from an experiment (right).

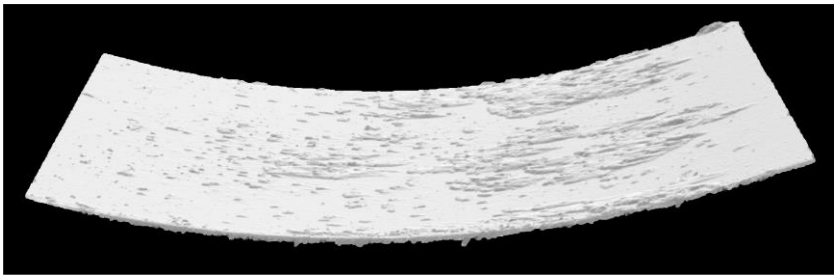

(b) Point cloud generated using an Alicona InfiniteFocus machine to measure deposit

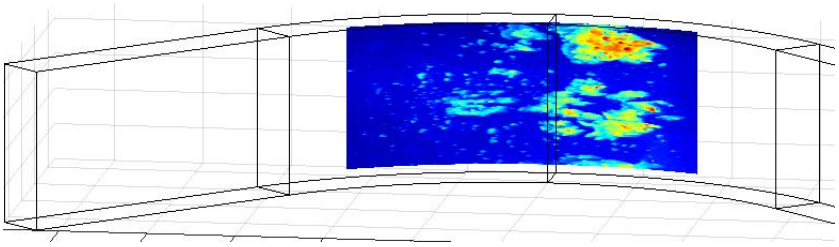

(c) Contour map of deposition height generated from the point cloud, mapped onto a wireframe of the geometry

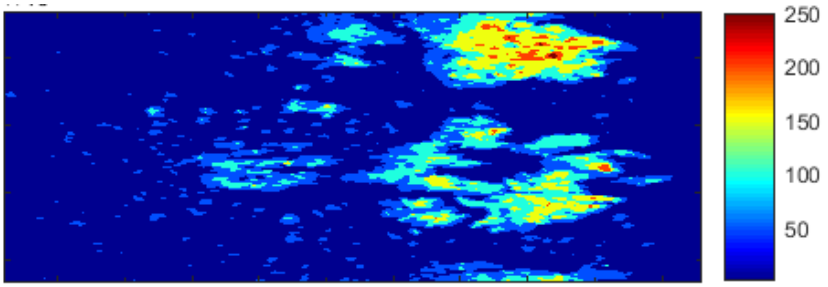

(d) Unwrapped contour map of deposition height (microns), plotted against the channel height and arc-wise position.

Figure 35 Processing of experimental results in order to generate spatially resolved data. Flow is from left to right in all pictures.

4.2 Paper: Experimental Deposition of Particulates in Accelerating Flows at Engine Representative Conditions

The included paper provides further details on the experimental rig, tests conducted, as well as a discussion of the results generated. In this paper, the thesis author is the primary author. Professors. McGilvray and Gillespie are the principal investigators on the project, Mr Simon Beal, an undergraduate, assisted with the manufacture and design of the test article and running of experiments, and Dr Forsyth a Research Assistant within the group supported the work based on previous experimental campaigns he had run at Oxford. The thesis author was responsible for the design and build of the new facility, the specification of the experimental conditions, development of post-processing techniques, and interpretation of experimental results.

Experimental Deposition of Particulates in Accelerating Flows at Engine Representative Conditions

Nikul Vadgama, Simon Beal, Peter R. Forsyth, Matthew McGilvray and David R.H. Gillespie

Department of Engineering Science, University of Oxford, Oxford, OX1 3UJ

ABSTRACT

This paper presents an experimental investigation into the spatial deposition of particles in internal flows relevant to the secondary air system (S-bends) at engine representative temperatures and velocities. The confidence in results from computational deposition models is limited by previous workers use of integral deposition measurements to validate their predictions. Measuring spatially resolved deposition measurements means this data can provide more rigorous test data for the validation of numerical deposition models. In the presented results, Arizona Road Dust is injected into the test piece at engine representative temperatures by mixing cold particle laden flow from a generator with hot particle-free flow. The test pieces are preheated and sit within an oven for the duration of the test, creating near steady state conditions. The tests are conducted at realistic metal temperatures (1230 K) and gas temperatures (830 K). For each test, the integrated deposition fraction and spatial map of deposition height is reported. The effects of bend curvature, Reynolds number, and metal temperature are studied. It was found that tests conducted at engine cooling passage representative temperatures exhibit some different fundamental trends in deposition seen when compared to cold experiments. Further, clear trends in the spatial distribution of deposits were apparent. The experiments provide a promising basis for a local deposition data validation set for numerical work with improved resolution compared to integral deposition fraction results.

NOMENCLATURE

a_c Centripetal acceleration

a_T Turbophoretic acceleration

C_c Cunningham slip correction factor

C_d Discharge coefficient

D_h Hydraulic diameter (m)

d_p Particulate diameter (m)

d_{orifice} Orifice diameter (m)

D_{h} Hydraulic diameter (m)

E Youngs Modulus (N/m^2)

Ep Epstein number ($= d_{\text{p}} \nabla T_{\text{g}}/T_{\text{g}}$)

Kn Knudsen number

P_{Th}^{+} Non-dimensional thermophoretic parameter

Pe Peclet number ($= U D_{\text{h}}/\alpha_{\text{th}}$)

q_m Mass flow rate (kg/s)

R_0 Ratio of Curvature ($= 2R_{\text{bend}}/D_{\text{h}}$)

R_{pipe} Radius of pipe (m)

R_{bend} Radius of bend (m)

Re Reynolds number ($= \rho_{\text{g}}\overline{U}_{\text{g}} D_{\text{h}}/\mu_{\text{g}}$)

Ri Richardson number

s Sample standard deviation

Stk Stokes number ($= C_{\text{c}}\rho_{\text{p}}\overline{U}_{\text{g}}{d_{\text{p}}}^2/18\mu_{\text{g}}D_{\text{h}}$)

t t-multiplier

T_{m} Temperature of metal exterior (K)

T_{w} Temperature of wall (K)

T_{g} Temperature of gas (K)

u^* Friction velocity (m s^{-1})

$u_i u_i$	Reynolds Stress ($m^2\ s^{-2}$)
$\overline{U_g}$	Mean gas velocity ($m\ s^{-1}$)
$\dot{m}$	Mass flow rate (kg/s)
n	number of samples
W	Convective velocity (m/s)
α	Impact angle (°)
α_{th}	Thermal diffusivity (m^2/s)
Γ	Ratio of time-scales
γ	Surface free energy
η	Deposition fraction (%)
Λ	Particulate to fluid thermal conductivity ratio ($= k_p/k_g$)
μ	Dynamic Viscosity (Pa s)
μ_{imp}	Impulse Ratio
ν	Poison Ratio
ξ	Density ratio (ρ_p/ρ_g)
ρ	Density ($kg\ m^{-3}$)
σ_y	Yield Strength (MPa)
τ_g	Gas time constant (s)
τ_p	Particle relaxation time (s) ($= C_c \rho_p d_p^2/18\ \mu^2$)
$\tau_p{}^+$	Non-dimensional particle time relaxation time (s) ($= C_c \rho_p \rho_g d_p^2 (u^*)^2/18\ \mu^2$)
Φ	Thermophoretic coefficient
ARD	Arizona Road Dust
CRW	Continuous Random Walk
MFC	Mass Flow Controller

I. INTRODUCTION

Particulate matter ingested into the engines of aircraft can cause significant damage to both turbine and compressor components [1]. With more flights occurring in regions of highly dust laden environments in the Middle East and Asia, alongside increasing turbine entry temperatures, deposition in hot stages of engines is likely to increase. Particulates can damage the engine through erosion, accretion, and corrosion. Particulates in the turbine section are known to deposit both on external surfaces [1] and internal surfaces, where they are delivered through the secondary air system and are typically of diameter <10 μm [2].

To allow increased turbine entry temperatures and realise efficiency improvements, more complex cooling features are required. However, their design needs to consider the mitigation of likely deposition and blockage. In industrial applications these systems are modelled using RANS CFD simulations due to time and computing power restrictions. For heat transfer, this approach is usually adequate, particularly in comparing the effects of small design changes. Due to low concentrations, one-way Lagrangian tracking has been seen to be an effective and inexpensive method of simulating the particle motion. Previous work has shown that capturing the effect of turbulent particulate motion, turbophoresis, is essential for accurate modelling of particle deposition [3]. The effects of turbophoresis are commonly modelled using Random Walk models. While the Discrete Random Walk model is available in many commercial CFD packages, the Continuous Random Walk model (CRW) has been shown to improve the fidelity of deposition modelling of small particulates which are affected by Turbophoresis [3]. To date, these results are only validated for non-rotating pipe flows at high pressure turbine temperatures and gas to wall temperatures [4]. Modifications to the model have been suggested to enable its generalisation to more complex (accelerating and separated) flows [4], [5]. This revised model has been shown to perform equally well in simple flows and shows promise for accelerating flows. The numerical work revealed noticeable difference between the spatial distributions predicted by the models in the complex flows, but the integral deposition fraction predicted was comparable [4]. This highlighted the need

for spatially resolved experimental data, of deposition in complex flows, to validate the revised model's performance.

This paper details the relevant considerations and build of newly designed rig, including the general flow path and specific test pieces used in this experiment. A dual s-bend test piece was tested using ultrafine ARD at engine relevant flow conditions. Details of the running procedure and post-processing are also provided. To provide context for the results, the operating parameters are outlined and numerical analysis to establish the likely effects of turbophoresis and thermophoresis are presented. The results of the tests are presented in terms of integral and spatial deposition. These are discussed and used to suggest likely physical mechanisms.

II. EXPERIMENTAL CONSIDERATIONS

A test case which is sufficiently simple such that the complete range of relevant physical phenomena can be investigated is required. In real cooling passages, there is significant flow acceleration both from the rotation of the body and because of their torturous flow paths. In addition to sufficient flow complexity, for internal cooling paths it is vital that turbophoresis, thermophoresis, and bounce-stick behaviour are also replicated. In theory for a cooling passage, where the fluid phase is colder than the metal surface temperature, thermophoresis should results in a retarding of deposition.

The use of a simple bend as a validation test piece introduces the additional complexity of flow acceleration and cross passage secondary flow structures such as Dean vortices which are typically encountered. These latter vortices result from the centrifugal force which causes the fluid at the centre of the pipe to accelerate radially outward, and their typical structure is shown in Figure 1 [6], [7]. The Dean number (De), a combination of R_0 and Re, characterises the strength of these vortices. The motivation here is to provide significant flow acceleration without the need for a rotating experiment. Careful choice of the operating conditions and geometry can ensure that turbophoresis and thermophoresis are of importance in experiments. Bounce-stick behaviour can only easily be replicated by generating the correct temperature difference between the wall and the particles and engine representative approach velocities and particle size distributions.

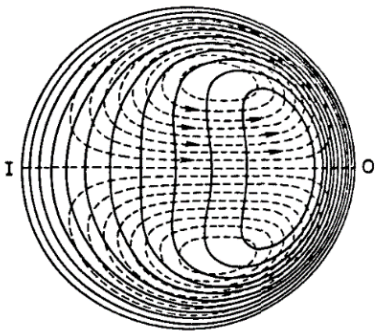

Figure 1 Typical Dean vortices in a circular bend. Flow calculated at De = 77. "I" indicates inside of the bend. "O" indicates outside of the bend. [10]

Particle deposition in simple systems is best described by non-dimensional deposition velocity (V_d^+) which is well correlated with the particles non-dimensional relaxation time (τ_p^+) [3]. In more complex cold flows it is more common for deposition to be reported as a function of Reynolds number (Re*)*, Stokes number (Stk), Density ratio (ξ), Peclet number (Pe), and Richardson number (Ri) [8]. There must also be a description of the geometry, in bends this is the curvature ratio (R_0). Further, when thermophoresis becomes important the particles' motion, and therefore deposition, becomes dependent on Kn, Ep, and Φ [2]. Hence, for a bend with an all-stick condition,

$$\text{Deposition} = \text{fn}(\text{Re}, \text{Stk}, R_0, C_f, \xi, \text{Pe}, \text{Ri}, \text{Kn}, \text{Ep}, \Phi) \quad (1)$$

As this paper's experiments are not all-stick, the sticking probability (*SP*) of particles must also be considered. According to the more comprehensive models of sticking [9],

$$SP = \text{fn}(d_p, \rho_p, E_p, E_s, \upsilon_p, \upsilon_s, \sigma_y, \gamma, \mu_{imp}, V_p, \alpha) \quad (2)$$

Previous experimental campaigns which use elbow geometries and turbulent flow (Re>2300 [8]) are: those of Pui et al [6]; Wilson et al [8] ; McFarland et al [10] ; and Wu et al [11]. All are cold experiments that aimed to create all-stick conditions and use circular geometries apart from Wu et al. who uses a rectangular passage geometry. In these literature, limited spatially resolved data and no fully resolved surface deposition distributions are presented. Experiments suggest that Stokes number is the primary indicator of deposition in a bend with an all stick condition [6], [8], [10]. Pui et al. investigated deposition of particles (Stk = 0.28 - 1.35) in bends with ratio of curvatures of 5.6-5.7 at Reynolds numbers of 6,000 and 10,000. They found that there was little dependency on Reynolds number [6]. In contrast Wilson et al. reported a dependency for

smaller particles in their tests at higher Reynolds numbers [8]. They investigated deposition of particles (Stk = 0.12 - 1.03) in bends with ratio of curvatures of 7.4 at Reynolds numbers of 10,250, 20,500, 30,750. Specifically, dependency on Reynolds number was found for particles with Stokes numbers less than 0.4 [8]. McFarland et al. stated a limited effect of Reynolds number in a Stokes number range of 0.07 to 0.7, a maximum of 5% difference occurred when the Reynolds number increased from 3,200 to 19,800 [10]. McFarland et al. showed that a curvature ratio less than 4-5 resulted in much more deposition but above this it made limited difference [10]. Wu et al. reported 1D spatial deposition in a rectangular duct at Re = 4450, Stk = 0.03-1.84, and R_0 = 17.7 and found Turbophoresis to be important, although their experiment was set up with the intention of comparable Turbophoretic and centrifugal forces [11]. Operating in a similar range to these experiments enables critical comparison and investigation into the additional physical phenomenon present in this set of experiments.

In reality particulate matter can be sea salt particles, mineral dusts, volcanic ash, secondary inorganic compounds, primary biogenic aerosols, combustion derived carbonaceous, or secondary organic compounds [12]. They all have vastly different material properties and shapes, the understanding of each properties variation and effect on deposition is an active area of research. Previous literature found that for a larger grade of ARD (measuring 20 - 40 μm) there was a significant increase in deposition between tests at 1273 K and 1323 K [13], for the smaller dust used here (Ultra-fine) this onset should be at a lower temperature. Previous testing in the facility, not presented here, showed that no deposition was found at 1180 K, but there was measurable deposition at ~1230 K (the desired operating point).

In this paper experiments were conducted with gas turbine secondary air system representative particle size and loading, and coolant gas and component metal temperatures. The Reynolds number is turbulent for all experiments, which were conducted between Re =3400 - 4400. While low for a high pressure turbine, such Re can be found in the low pressure turbine cooling system. The metal temperature (T_m) is varied between low and high operating points (1230 K and 1300 K). Arizona Road Dust (ARD) of a singular particle size distribution (*Ultra-fine,* 0 - 20 μm) was used, this dust is easily available and commonly used in gas turbine particulate studies. This

operating range allows comparison to current literature and the dust is comparable in size to engine conditions if not necessarily composition.

III. EXPERIMENTAL FACILITY AND MEASUREMENTS

A new experimental rig capable of recreating engine representative conditions was built for the experimental campaign, shown schematically in Figure 1. The rig can generate dust concentrations, incoming coolant gas temperature and the internal metal component surface temperature experienced by engine components. Test articles are designed to allow for the deposition height and chemical composition distributions on the components to be obtained during post-processing. Detail of the system design is provided below.

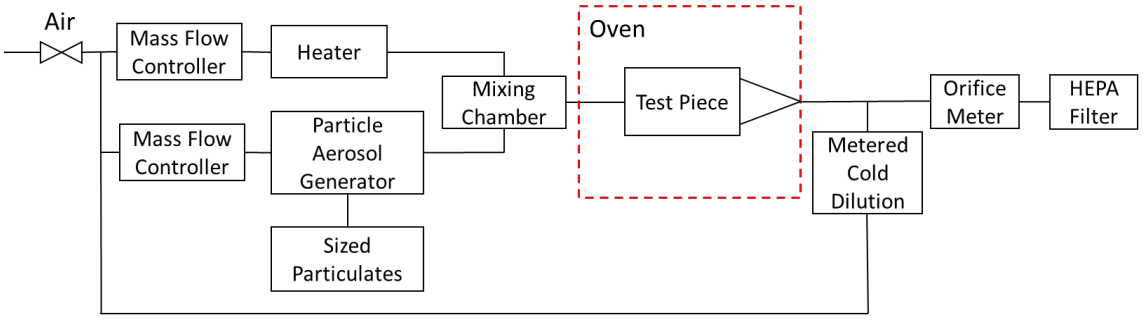

Figure 1 Schematic of air flow in rig. Flow from left to right.

A. The Particulate Laden Flow Path

The rig is supplied with dry compressed air at 7 barg, with all mass flow rates being set using Omega mass flow controllers. The main flow of inlet air is passed through an 8 kW heater capable of reaching temperatures up to 1033 K at 1.25 – 7.35 g/s [14].

The secondary incoming air at ambient temperature air is supplied to a Pallas RGB1000 IGD particle dispersion device at 0.17 – 0.41 g/s. This device uses a linear piston to feed test dust onto a rotating steel wire brush over which air flows. Due to the very low feed rate (1 mm / hr) the system allows a low dose of particulates to be accurately delivered to the coolant stream compared to other dispersion techniques. For the reported experiments, Ultrafine Arizona Road Dust (ARD) was used. Although the mineral composition is not entirely reflective of what is encountered by fleet aero engines, this dust is easily available, has well documented properties, and is commonly

used. By volume 10% of the particles are below 1.5 μm, 50% below 4.4 μm, and 90% below 9.8 μm. The bulk density of ARD is quoted as 2560 kg/m^3 [15].

The fluid stream for delivery to the test piece is then formed by mixing the ambient particle-laden air stream with the main heated flow in a bespoke co-axial mixing chamber. This is necessary both to protect the flow heater and to allow the particulate delivery system to operate at ambient conditions. The chamber is designed to generate an isothermal uniformly laden flow, whilst minimizing likely deposition inside the chamber. The mixing chamber design and delivery system were found to provide a reasonably repeatable dosage of particulates whilst minimising the amount cold gas required, allowing the gas temperature to be engine representative of an HP blade or vane cooling passage (800 – 1000 K). The delivery system allowed the particle volume fraction of the flow to be kept to <1x10^{-7} across all experiments. This importantly ensured that one-way coupling could be assumed in the analysis of all experiments. This feature is important as for the same total particulate dose, a concentration much higher than expected in service has previously been shown to result in more rapid deposition than for the same total dose at atmospheric concentration [2]. This two-way coupling becomes an important consideration at volume fractions of 1x10^{-6} [16].

With both the heater and particle generator operating at maximum flow rate 7.7 g/s are generated at a temperature of 994 K with a particle volume fraction (*PVF*) of 2.2 x10^{-10}. This assumes the slowest piston speed and that the heater is operating at its highest temperature. Reducing the flow rate across the particle generator to its minimum provides a hotter flow (1016 K) with a similar PVF. Operating with both devices at their minimum flow rates, a total of 1.5 g/s, generates a 940 K flow with a PVF of 1.4 x10^{-9}. In reality the experiment is operated at higher *PVF* to ensure a high enough dosage is delivered whilst maintaining a reasonable test time.

The air then passed down a short delivery pipe to the test article which sits in an oven, capable of heating the test piece to approximately 1450 K when no cooling flow is present. Air exiting the test article is diluted to reduce its temperature (to below 333 K) and then passed through a HEPA filter. Secondary sealing and local ventilation prevented particulates from entering the surrounding air in the case of leakage or failure.

B. Test Article

Based on the requirement for a simple test piece which could be operated at high temperature and subsequently measured to determine the particle deposition, the geometry for the flow passage through the working section was first specified. A rectangular passage cross-section was chosen for the test article, typical of many gas turbine cooling passages. The cross-section, of dimension 9 mm x 3 mm (H x W), is swept through 2 x 90 degree bends to form a characteristic *S*-bend used in these experiments to generate significant flow acceleration (Figure 2). The aspect ratio was chosen by Beal [17] who modelled the flow field using RANS CFD. The aim was to generate a passage in which the Dean vortices were centred near the end walls (short-sides) of the cross-section with a near uniform secondary flow across the passage in the mid-height region. Typical secondary flow vectors are shown in Figure 2 half way around the circumference of the first and second bends. It is noticeable that the vortices restricted to a smaller region near the wall around the second bend. The use of an S-bend rather than a single bend introduces further complexity to test particle tracking models, in that the particle density field coming out of the first bend and into the second needs to be accurately modelled, along with any change in the flow temperature over the passage length if generic rules for adhesion are to be obtained. The effects of curvature ratio (R_0) through the bend are investigated by specifying three test channel geometries R_0 =5, 10, 15.

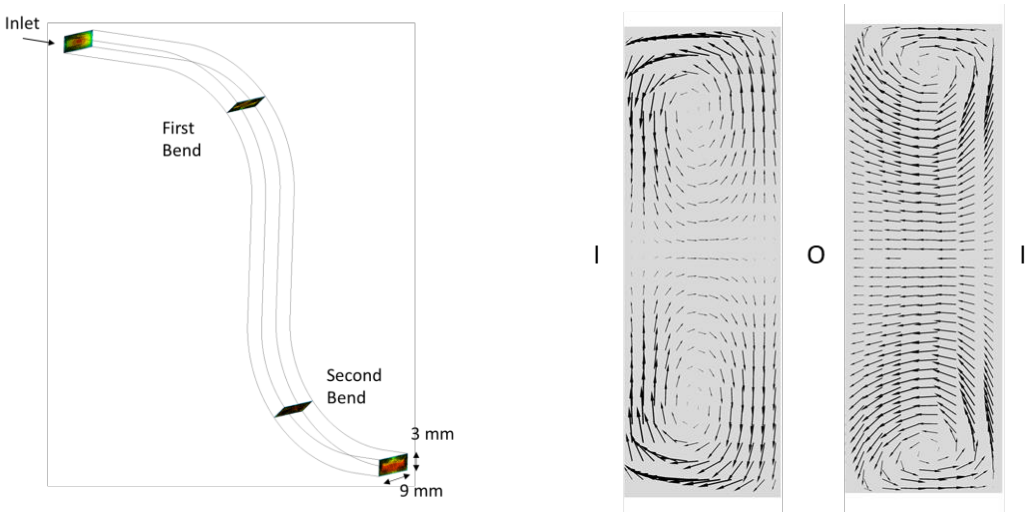

Figure 2 Flow passage through the test section, R_0 = 10. Mid-bend planes (as depicted on left) shown on right with vectors of secondary flow field generated at experimental condition 2 from Table 1 [17]. "O" demarcates outside of the bend and "I" demarcates inside of bend.

To form the channels required, the test-article was manufactured as shown schematically in Figure 3, from stainless steel SS316. This was held in a thick-walled holder which provided sufficient thermal mass such that isothermal conditions were maintained during the test time (~20 minutes). The geometry was designed to create two identical passages for each running condition such that each run produced two sets of results. This was deemed useful as hot-particulate experiments are inherently uncertain. Importantly, each S-bend was made in two parts to allow them to be dissembled after cooling for the measurement of spatially resolved height distributions across the surface (Figure 3). A compromise required for the design is that the deposits on the top wall of the channel cannot be captured in post-processing. After the system is dissembled, and before post-processing, any loose deposits, which were easily differentiable from the adhered deposits were removed from the test piece.

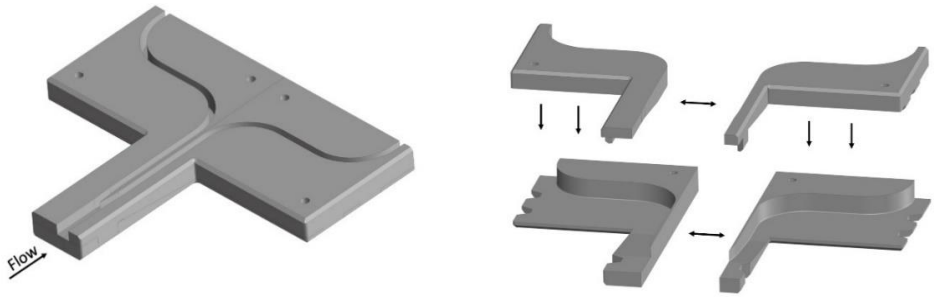

Figure 3 CAD model of the S-bend test piece (R_o = 10) used in experiments. Left picture shows assembled construction and right an exploded view. The left half is sample 1 and right half is sample 2 for each test.

C. Running procedure

Prior to each test, the individual pieces' weights were recorded. The parts were then assembled and heated using both the internal gas flow and oven until the operating conditions for that run were reached at near steady state conditions. This process took up to 6 hours (limited by the oven heating capacity). The particles were then injected for the test time duration (typically 20 minutes). A total mass of 0.250 - 0.272 g of dust entered the test piece during each run. After the experiment the test piece was slowly cooled to maintain adhesion of dissimilar particles on the model surface. After cooling the experiment was dissembled and each part weighed again.

D. Measurements and Post-processing

The temperature of the fluid stream at the inlet and exit of the test section as well as at 8 points within the test-pieces' metal casing were measured using K-type thermocouples except at the exit where N-type thermocouples were used. The local static pressure was also measured at the inlet and exit of the test article using NXP MPX51000 pressure transducers. Atmospheric pressure was measured using a Fortin barometer. The local data were measured at 1 kHz. Mass flow rates of clean air entering the test rig were reported by the mass flow rate controllers (+/- 1 %).

A precision weighing scale (with a linearity of ±2 mg) was used to measure the mass of each component along the gas path before and after each experiment to allow the mass of injected particles to be accurately assessed. This included the brush and casing of the particle dispenser, but not the short 90° bend within the co-axial mixing chamber (which has cold flow passing through and is likely to remain near-clean). The mass of particles leaving the piston of the particle generator was used as a confidence check on the measurement. It was calculated using the measured density of packed powder in the piston of 969 (±56.9) kg / m^3, characterised during commissioning tests (but not for each test conducted). The piston itself was weighed before and after each test and the total mass injected to the working section calculated by subtracting the mass increase of components upstream of the working section from the mass leaving the piston. The test article was weighed whilst fully assembled (accreted deposits attached to both bends) and, subsequently after cleaning the deposited material from one of the two bends constituting the S-bend so that the deposit on each could be calculated. The confidence interval associated with each integral deposition measurement was calculated using equation (3), with number of samples (n) equal to two.

$$\text{Confidence Interval} = t_{90,1}\left(\frac{s}{\sqrt{n}}\right) \quad (3)$$

An Alicona Infinite Focus microscope was used to create a surface scan of deposition on the test piece with ±10 nm vertical and ±400nm horizontal resolution. In order to calculate the deposited height, the underlying clean geometry must subtracted. A perfect arc used to define the manufacturing drawing radius of curvature was assumed in the bend region and matched to the original surface shape on the flat parts of the system where no deposition was detected (further

microscopy services not being available at the time of writing). The images generated in the process are represented in Figure 4. It should be noted that on some test-pieces machining marks were visible and created a discrepancy with this baseline. These were in the order ~0 - 50 μm.

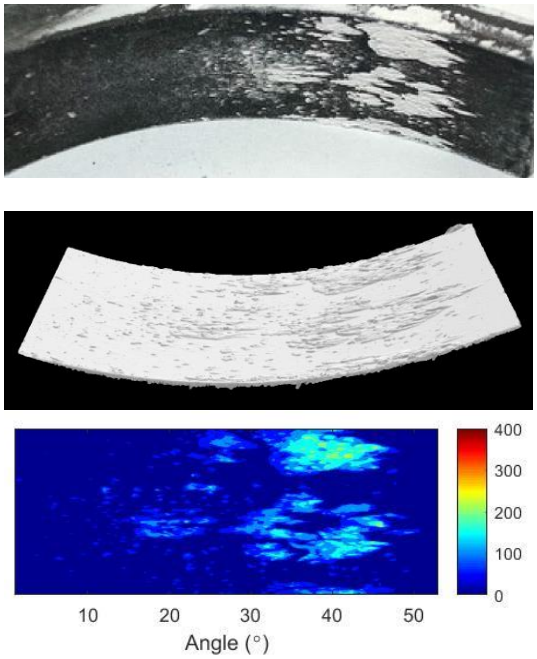

Figure 4 Steps taken to measure the deposit height. First, a sample (top) is scanned and a 3D points cloud (middle) is created, this is then unwrapped such that it can be intuitively represented using a 2D co-ordinate system (bottom). Flow from left to right in all images.

IV. OPERATING PARAMETERS

In this study the intent is to investigate the effect of R_0, Re, and Stk. As dust of a single composition is used Re and Stk could not be varied independently. In addition to the matching well known non-dimensional groups, it is known that turbophoresis and thermophoresis are important drivers of deposition for this geometry. This is confirmed by numerical simulations. Thus, tests are also conducted over at a range of wall to gas temperature ratios. The test matrix employed is shown in Table 1.

Exp	R_0	T_m (K)	T_g (K)	$\dot{m}$ (g/s)
1	5	1230	830	1.6
2	10	1230	830	1.6
3	15	1230	830	1.6
4	5	1230	830	2.1
5	10	1230	830	2.1
6	10	1300	830	1.6

Table 1 Test matrix for experimental campaign. Test 2 can be considered the baseline.

The importance of turbophoresis in simple flows is usually quantified using the non-dimensional relaxation time (τ_p^+), but the definition of this in more complex flows is difficult due to varying friction velocity (u^*). To quantify the significance of turbophoresis, the ratio of turbophoretic to centripetal force, F_{ratio} , is calculated using equations ((4) - ((8) [11]. In these equations a single overbar represents the ensemble-average value and a double overbar the density-weighted ensemble-averaged component. First an intermediate variable is defined as the ratio of the gas time constant to the sum of the particle relaxation time and gas time constant Equation (4). Equation ((5) is a momentum equation. Here the terms within the large brackets on the right hand side represent the turbophoretic force, mean viscous drag, and mean lift per unit mass respectively [11]. For these calculations the convective velocity (W) is approximated as the fluid velocity and the mean streamline curvature of each bend is used throughout the domain. After defining the turbophoretic and centripetal accelerations, Equations (6) and (7), F_{ratio} can be deduced. In contrast to Wu et al. [11] the total turbophoretic force is considered rather than just that in the wall-normal direction, as this force affects particle deposition even if when it is not acting in a wall-normal direction to the flow [18]. For the 90th percentile of particle size (9.8 m) at the median radius of curvature case (R_0 = 10) the volume-averaged value of F_{ratio} = 2.8 . For the smallest 10th percentile of particles in the R_0 = 10 geometry the value is almost 5 times higher, $\mathrm{F_{ratio}} = 13.8$. These values are seen to scale inversely with R_{bend}. It is clear that the force due to turbophoresis is comparable to the centripetal acceleration even in the tightest bends. Although the bend in the current study is much tighter, than that in by Wu et al [11], F_{ratio} is comparable in magnitude. This is because a_{T} is larger as a result of turbophoresis effects in all directions being accounted for.

$$\Gamma = \frac{\tau_g}{\tau_p + \tau_g} \qquad ((4)$$

$$\frac{\partial\left(\overline{\rho_{\mathrm{p}}}\overline{\overline{W_i}}\right)}{\partial t} + \frac{\partial\left(\overline{\rho_{\mathrm{p}}}\overline{\overline{W_i W_k}}\right)}{\partial x_k} \approx \overline{\rho_p}\left[-\frac{\partial\left(\Gamma\overline{u_i' u_k'}\right)}{\partial x_{\mathrm{k}}} + \frac{\overline{U_i} - \overline{\overline{W_i}}}{\tau_{\mathrm{p}}'} + \overline{\overline{F_{\mathrm{l},i}}}\right] \qquad ((5)$$

$$a_{\mathrm{T}} = \sqrt{\left(\left[-\frac{\partial\Gamma u_x u_x}{\partial x} - \frac{\partial\Gamma u_x u_y}{\partial z} - \frac{\partial\Gamma u_x u_z}{\partial z}\right]^2 + \left[-\frac{\partial\Gamma u_y u_x}{\partial x} - \frac{\partial\Gamma u_y u_y}{\partial z} - \frac{\partial\Gamma u_y u_z}{\partial z}\right]^2 + \left[-\frac{\partial\Gamma u_w u_x}{\partial x} - \frac{\partial\Gamma u_w u_y}{\partial z} - \frac{\partial\Gamma u_w u_z}{\partial z}\right]^2\right)} \qquad ((6)$$

$$a_{\mathrm{c}} = \left| \frac{\overline{\overline{W}}^{2}}{r_{\mathrm{bend}}} \right| \qquad ((7)$$

$$F_{\mathrm{ratio}} = \left| \frac{a_{\mathrm{T}}}{a_{\mathrm{C}}} \right| \qquad ((8)$$

In addition to the parameters already listed above, the wall and gas temperatures and their effects are an important consideration. These tests are run at temperatures representative of the surface temperatures within internal cooling passages, with metal temperatures around 1200 K and an internal gas temperature of 830 K, such that the results are relevant to HP turbine engine conditions. The temperature distribution in the fluid and metal were modelled in a conjugate simulation using ANSYS Fluent 2019. Simulations were conducted assuming an isothermal exterior metal temperature equal to that at the intended operating point. The system is near isothermal during the experiment and the rate of heat loss to the coolant seen to match the radiative heating input power of the oven. Furthermore, comparison of the solution to the 8 thermocouples in the working section at each condition showed a maximum error of 4.1% (Appendix, Section A). Table 2 and Table 3 compare the modelled flow and metal temperatures at each bend and each operating condition. As expected a higher Reynolds number in the same geometry results in a lower mean wall temperature and larger difference in temperature between the 1st and 2nd bends because of the enhanced convective heat transfer, and the limited thermal capacity of the coolant through the specimen.

Condition	1	2	3	4	5
1st Bend	962.2	951.9	940.0	952.1	941.7
2nd Bend	1023	1005	995.8	1011	994.7
Difference	60.4	53.3	55.8	59.3	53.0

Table 2 Comparison of area-averaged fluid temperatures (in Kelvin) on entry to 1st and 2nd bends.

Condition	1	2	3	4	5
1st Bend	1166	1174	1211	1152	1161
2nd Bend	1184	1181	1218	1172	1168
Difference	17.2	6.72	7.34	20.80	7.68

Table 3 Comparison of area-averaged wall temperatures (in Kelvin) on 1st and 2nd bends.

Where temperature gradients are large it can also be important to consider thermophoretic forces, as they may become comparable in magnitude to the drag force. Forsyth [19] defined a non-dimensional thermophoretic parameter (P_{Th}^{+}, equation (9)) that is the ratio of the thermophoretic to

(shear) inertial force felt by the particle. P_{Th}^{+} can be calculated from the experimental operating conditions, however, this is dependent on the thermophoretic coefficient $\Phi = \mathrm{fn}(Kn, \text{particle material})$, for which there are many correlation formulae suggested, each with high uncertainty à priori [19] and diverging results. Forsyth showed through back analysis of literature and experiments that for $P_{Th}^{+} = -1 \times 10^{-6} \rightarrow -1 \times 10^{-5}$, a decrease of 10% in deposition could be expected compared to isothermal conditions [19]. To estimate the effects of thermophoresis an upper limit of $\Phi = 2$ is estimated from Healy and Young at a Knudsen number (Kn) of ~0.1 and thermal conductivity (Λ) of ~0.5 [20], and the temperature gradient (∇T_g) is calculated as $2(T_{w,avg} - T_{g,avg})/D_h$. The value of P_{Th}^{+} for each experiment over the expected range of particle sizes is as shown in Figure 5. It is clear that all particle diameters are likely to be influenced by thermophoresis during all tests, justifying varying the metal temperature in the test matrix.

$$P_{Th}^{+} = \frac{Particle\ thermophoretic\ force}{Particle\ (shear)\ intertial\ force} = \frac{\Phi Ep}{6\pi \tau_p^{+}} = \Phi \frac{3\mu^2}{\pi \rho_g \rho_p d_p (u^*)^2} \frac{\nabla T_g}{T_g} \qquad (9)$$

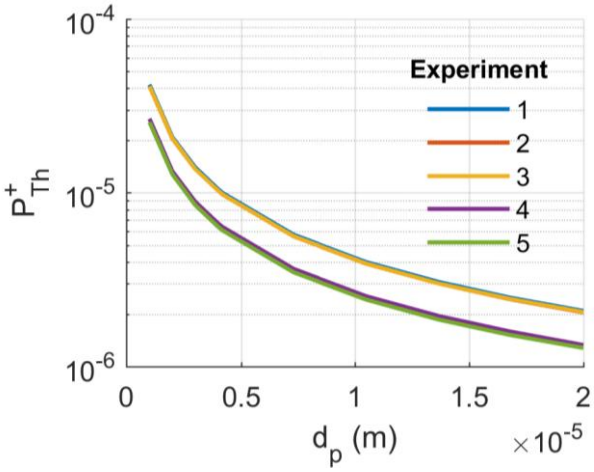

*Figure 5 Calculation of Thermophoretic parameter (**Φ**) for experiments 1-5 using equation (9).*

V. RESULTS AND ANALYSIS

The specified operating conditions were well matched during testing. In all but one test both the inlet gas temperatures and metal temperatures were within 1% of the intended conditions (Table 4). During the highest metal temperature test (exp. 6) it was only possible to achieve a 39 K, rather than the planned 70 K, temperature increase compared to the baseline test (exp. 2). The results show that for the range tested, treating experiment 2 as the baseline, the most dominant parameter was

the ratio of curvature, then wall temperature, and finally mass flow rate (Table 4). For each parameter varied, trends in the integral deposition fraction and spatial deposition are noted, followed by discussion of the likely physical mechanisms responsible in each case. Figure 7 and Figure 8 respectively show the local deposit height (μm) on the outer curved walls of the first and second bends for each of the tests conducted. It should be noted that while there is noticeably more deposition at the bottom of the passage, this is due to the test pieces' construction. The dissemblance of the test piece from its carrier results in the deposit along on the top edge being dislodged. (Notably this is not a gravitational effect in the results.)

Exp	R_0	Re	$T_{gas,in}$ (K)	T_m (K)	η (%)	1st Bend η (%)			2nd Bend η (%)		
						Avg	S_1	S_2	Avg	S_1	S_2
1	5	3442	828±4.2	1239±6.0	26.8	17.0	18.8	15.1	12.1	12.7	11.4
2	10	3429	833±4.3	1237±4.7	10.1	8.6	10.1	7.1	1.65	1.3	2.0
3	15	3442	836±4.8	1238±5.0	9.7	6.6	5.8	7.4	3.35	3.1	3.6
4	5	4415	882±4.6	1225±1.7	17.8	12.9	12.3	13.5	5.7	5.4	6.0
5	10	4569	834±4.2	1230±1.1	16.7	12.6	11.6	13.6	4.8	5.4	4.2
6	10	3427	834±3.5	1276±0.3	21.8	12.4	12.8	12.0	10.9	11.2	10.6

Table 4 Measured experimental conditions and integral deposition fractions. The fraction in each bend is expressed using the local mass of particulates that enter that bend. At the entrance to the test section an equal split between the two flow passages is assumed. The deposit weighed over the surface of the first bend is subtracted from the loading to obtain the mass entering the second bend. S_1 and S_2 refer to sample 1 and 2 respectively. The quoted temperature deviations are the maximum change in temperature recorded from any single thermocouple over the particle injection period.

A. Ratio of Curvature

Experiments 1 to 3 were designed to study the effect of the Ratio of Curvature (R_0). Figure 6 shows the integral percentage of deposition on Bend 1 (upstream) and Bend 2 (downstream). It is clear that increasing the ratio of curvature tends to reduce deposition, as shown previously by Wilson et al [8]. It should be noted that unlike their experiments there is some coupling between the gas and metal temperatures achieved and the bends' radii of curvature. At the same nominal operating conditions, these temperatures vary as detailed in Table 2. For the tighter bends, R_0=5, the fluid is 24.6 K hotter on entry to the bends and the walls are 39.5 K colder which will one would expect to have some effect on the sticking probability. The observed persistence of this trend in experiments of varying wall temperature lead the authors to conclude that that the wall temperature range variation is less important compared to the radius of curvature (within the ranges tested) which strongly affects the particle trajectories.

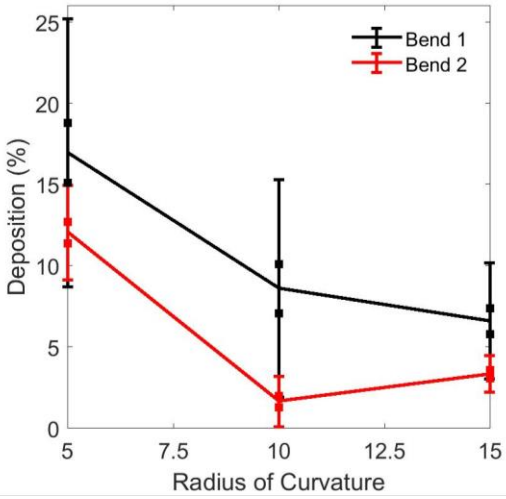

Figure 6 Effect of R_0 on deposition around each bend as a percentage of mass entering that bend. $\dot{m}$ *= 1.6 g/s.* $T_{g,\,in}$ *= 830 K and* T_m *= 1230 K.*

Maps of local deposition along the first bend for experiments 1, 2, and 3 are shown in Figure 7 a, b, c. The angular position is measured relative to the mid-point around the bend. On the first bend increasing R_0 is seen to move the position of deposits further upstream. This is the result of deposition being largely inertial, and for a given particle trajectory coming into the bend this results in deposition occurring further around a tighter bend compared to a gentle bend as the overall arc angle is significantly increased. This may seem counter-intuitive but is a result of the passage having a near uniform distribution of particles in a passage of finite width. Furthermore, the deposition is clearly bi-modal in the axial direction with an initial peak at about ~40º regardless of the value of R_0. This is similar to the trend predicted by Breuer et al. in their numerical study [21], and may be associated with the initial generation of a pair of Dean vortices or simply the initial capture of particles lying close to the wall in the incoming boundary layer.

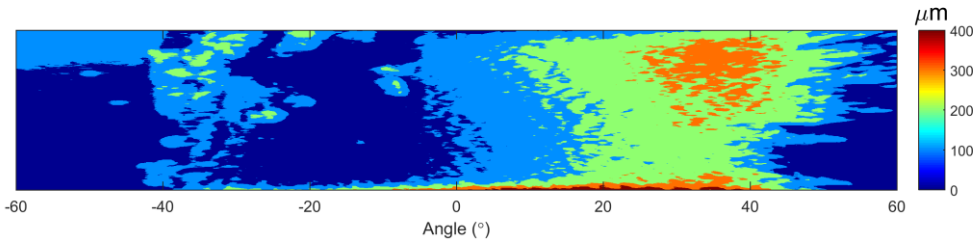

(a) Experiment 1. R_0 = 5, T_m = 1239 K, Re = 3442

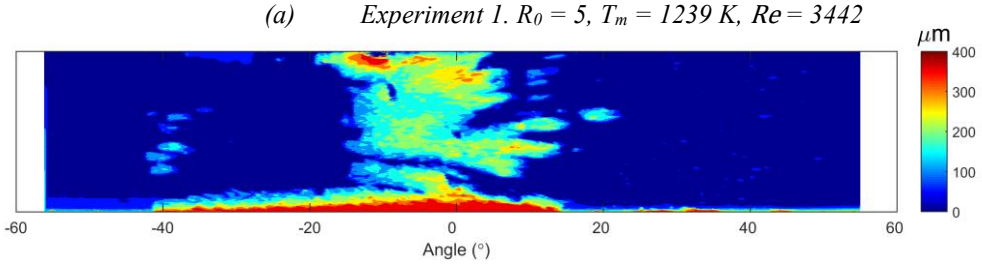

(b) Experiment 2. R_0 = 10, T_m = 1237 K, Re = 3429

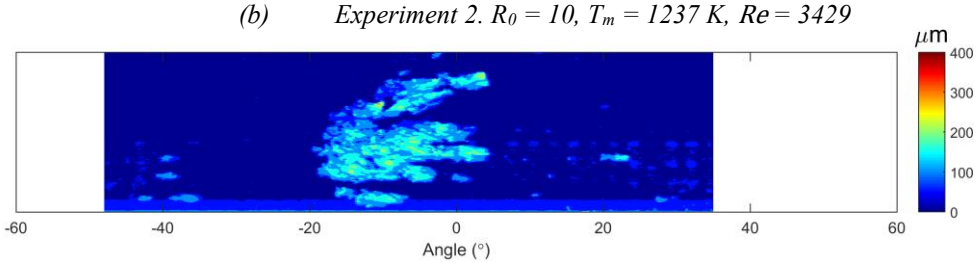

(c) Experiment 3. R_0 = 15, T_m = 1238 K Re = 3442

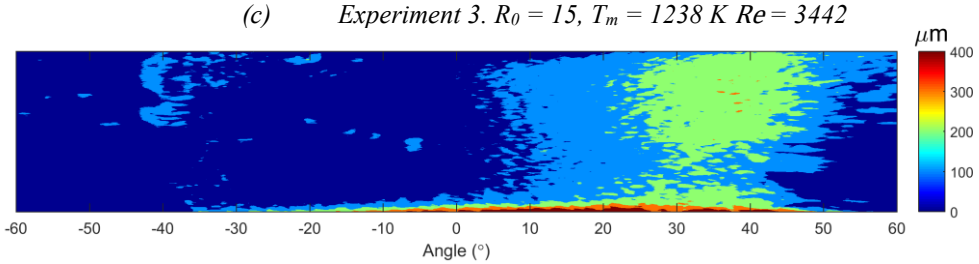

(d) Experiment 4. R_0 = 5, T_m = 1225 K, Re = 4415

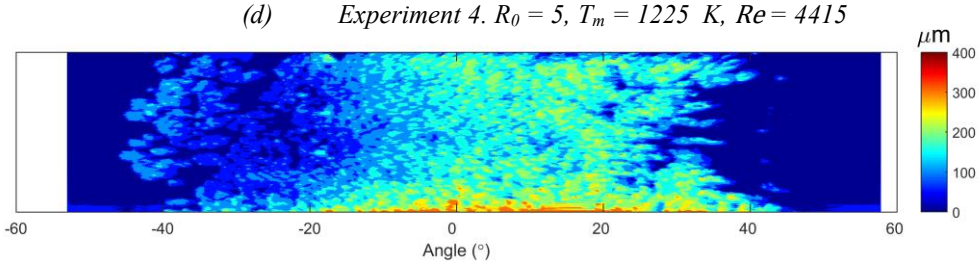

(e) Experiment 5. R_0 = 10, T_m = 1230 K, Re = 4569

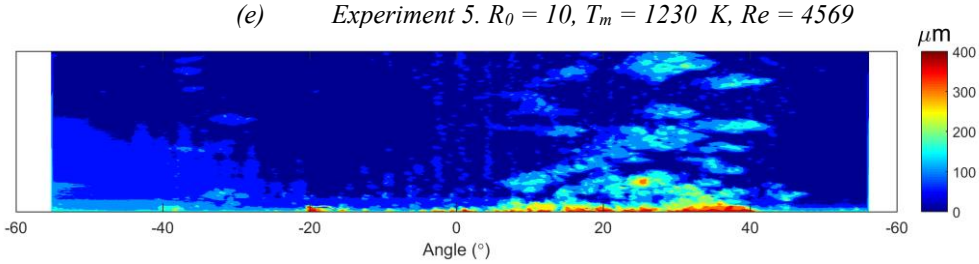

(f) Experiment 6. R_0 = 10, T_m = 1276 K, Re = 3427

Figure 7 Deposition height (μm) on the first bend in experiments 1-6. Flow from left to right, with the middle of the bend corresponding to 0°. Y-axis is height of the wall.

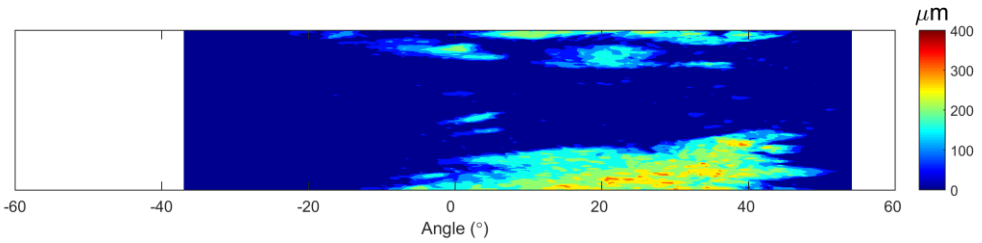

(a) Experiment 1. R_0 = 5, T_m = 1239 K, Re = 3442

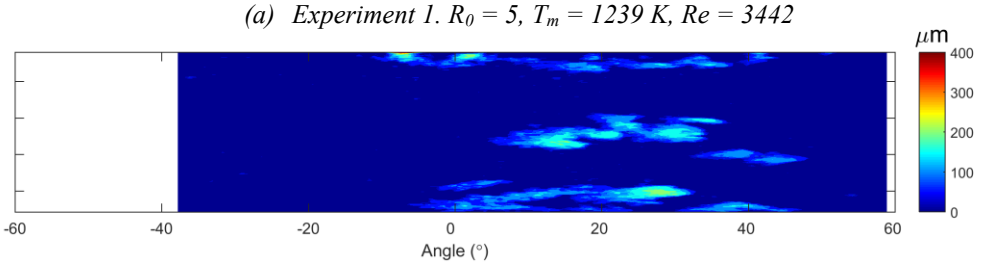

(b) Experiment 2. R_0 = 10, T_m = 1237 K, Re = 3429

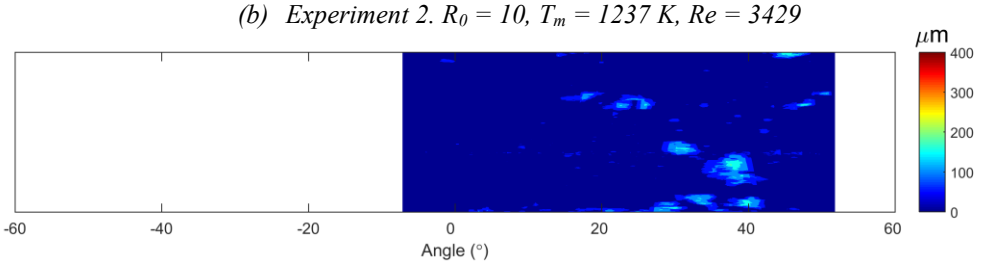

(c) Experiment 3. R_0 = 15, T_m = 1238 K Re = 3442

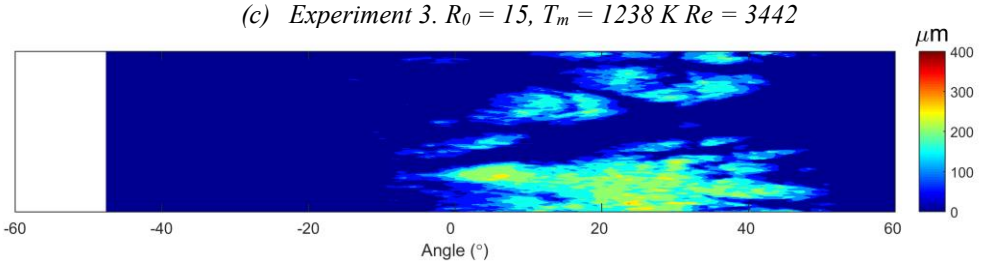

(d) Experiment 4. R_0 = 5, T_m = 1225 K, Re = 4415

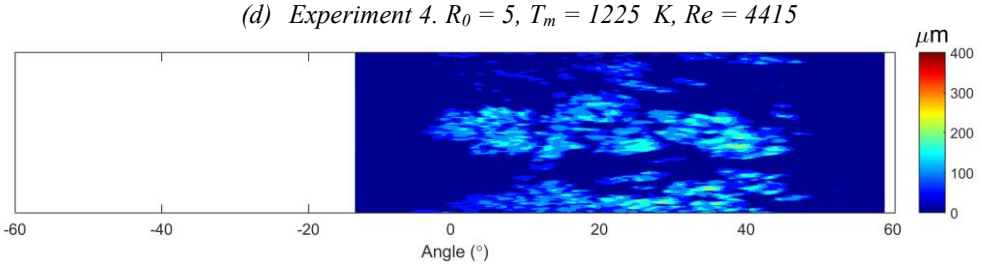

(e) Experiment 5. R_0 = 10, T_m = 1230 K, Re = 4569

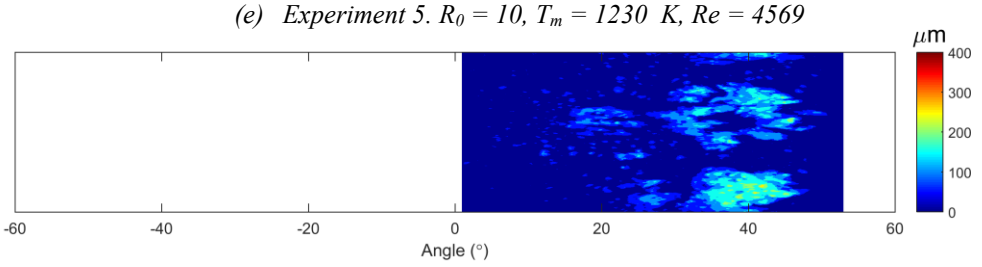

(f) Experiment 6. R_0 = 10 , T_m = 1276 K, Re = 3427

Figure 8 Deposition height (μm) on the second bend in experiments 1-6. Flow from left to right, with the middle of the bend corresponding to 0°. Y-axis is height of the wall.

It is also noticeable that deposition occurs closer towards the mid-height of the passage with increasing R_0. The tendency of particles to deposit more centrally on the outer wall can be linked to the relative strength of the vortices and the apparent centrifugal force. Stronger vortices (low R_0) are able to sweep particles up away from the centreline. The strength of the Dean vortices is inversely related to $\sqrt{R_{bend}}$ whilst centripetal acceleration is inversely related to R_{bend} [6], hence the ratio of acceleration due to the apparent centrifugal action to that of the Dean vortices is inversely proportional to $\sqrt{R_{bend}}$. Therefore, as R_{bend} increases, centripetal forces are less influential and particles tend to follow the streamlines of the vortices more closely. Deposition at mid height could be a result of either the more tangential impacts created by following the Dean vortices (which would reduce the sticking probability), or particles only impacting after they move radially outward along the parallel streamlines where the two Dean vortices meet. Numerical investigation is required to investigate this phenomenon in greater detail. Further, the wider spread in deposition at smaller R_0 is likely due to the dominance of apparent centrifugal forces at lower R_{bend}.

On the second bend (Figure 8 a, b, c) the axial trend is reversed, with increasing R_0 seen to move the position of deposits further downstream; the distribution in the axial direction is also unimodal. It is speculated that particles injected into the second bend of the more gentle bends are constituted from larger particles which are more inertial in their behaviour, and furthermore their distribution within the flow field is dependent on the flow geometry and particle deposition distribution upstream. Due to the same physics described in relation to the first bend more of the deposition occurs at the passage mid-height with increasing R_0. The increased spread of deposition height-wise may be due to the Dean vortices' unsteadiness: the pair tend to oscillate around the channel centroid [7]. This could in effect spray the particles over a broader area, across the height of the passage.

B. Metal Temperature

Comparison of experiments 2 and 6 as shown in Figure 9 demonstrates that the effect of the substrate metal temperature is as expected, with an increase in T_{met} resulting in an increase in deposition. This trend is consistent across both bends, but the increase in deposition is 15x greater for the second bend than the first. This is likely the result of a strong increase in gas temperature around the passage which heats the particles such that they are more likely to stick. Higher temperature experiments showed smaller uncertainty, indicating that the uncertainty is largely a result of the sticking probability or a stronger deposit forming at high temperature. The effects of an increased metal temperature are studied by comparing Figure 7b to Figure 7f (first bend) and Figure 8b to Figure 8f (second bend). The vertical banding on Figure 7f can be attributed to the curvature of the bend not being completely smooth, but very slightly faceted due to manufacturing constraints at such scales. Deposit on the first and second bends occurs further downstream in more axially concentrated locations. Increasing thermophoresis in the hotter experiment would increase the force on particle away from the wall, this could explain the movement of the initial deposition sites downstream. Whereas in the early part of the bend where the particle concentration across the passage is near uniform, the effect of thermophoresis is noticeable, further around the bend the afore mentioned inertial movement of particles towards the outside of the bend occurs, and the increased temperature promoted further sticking of particles.

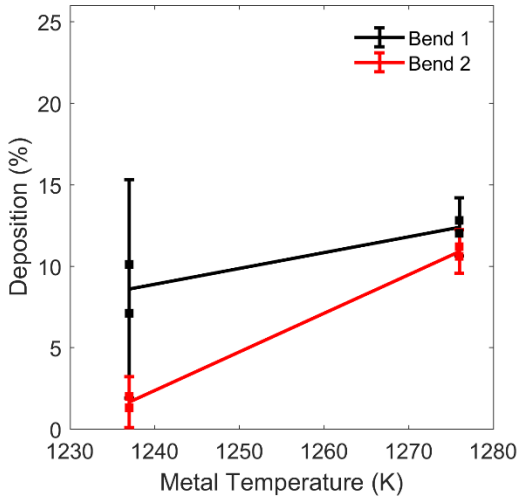

Figure 9 Effect of exterior metal temperature on deposition for $\dot{m}$= 1.6 g/s, R_c = 10, and $T_{g,\,in}$ = 830 K.

The distribution on the second bend is more even across the span. The regions without deposition at a lower metal temperature correspond to the vortices' velocity vector being more parallel to the wall. This makes the impacts likely to be more tangential to the wall normal and hence of lower sticking probability. It appears the increase in metal temperature has increased the probability of sticking in these substantially enough for there to be noticeable deposition in these regions. The increased sticking probability is likely a result of increased particle heating as the fluid will be hotter at the increased wall temperature for the same inlet temperature, although conjugate heat-transfer simulations were not conducted for this case.

C. Mass Flow Rate

Experiments 4 and 5 are similar to cases 1 and 2 respectively, but with the mass flow rate increased by 33%. This results in increased Reynolds, Dean, and Stokes numbers. It also reduced the temperature of the fluid into each bend (due to increased thermal capacity of the flow) and wall temperature along the bends (due to increased convective heat transfer) by ~10K (Table 2 and Table 3). More deposition would be superficially expected as a result of higher Stokes and Reynolds numbers [6]. However, Figure 10 shows a more complicated outcome with deposition reduced in for the sharper bend geometry (R_0 = 5) and increased for the gentler bend (R_0=10). For these cases the temperature changes were dominant over any deposition increasing mechanisms previously seen for the tighter bend.

Comparing Figure 7a and Figure 7d shows there is little change in spatial deposition with an increase in mass flow rate, and hence Stokes number, in first bend of the test piece with R_0 = 5. This is likely due to a dominant apparent centrifugal force, compared to the Dean vortices, which reduced the effect of the fluid motion. On other hand Figure 7b and Figure 7e shows that deposition on the first bend of the sharper curvature test piece (R_0 = 10) is spread over a larger axial region. The increased unsteadiness due to stronger Dean vortices, with the unsteadiness increasing with the strength of the vortices, and/or increased Turbophoresis at this higher Reynolds number could explain this [22]. For the same reasons as in the lower flow rate case deposition on the second bend

of gentler curvature (Figure 8d) is concentrated closer to the outer centreline than the second bend of sharper curvature (Figure 8e). The stronger Dean vortices in the high flow rate case also explain why deposition is more centrally distributed in the higher flow rate cases (Figure 8d and Figure 8e) than lower flow rate cases (Figure 8a and Figure 8b) on the second bend.

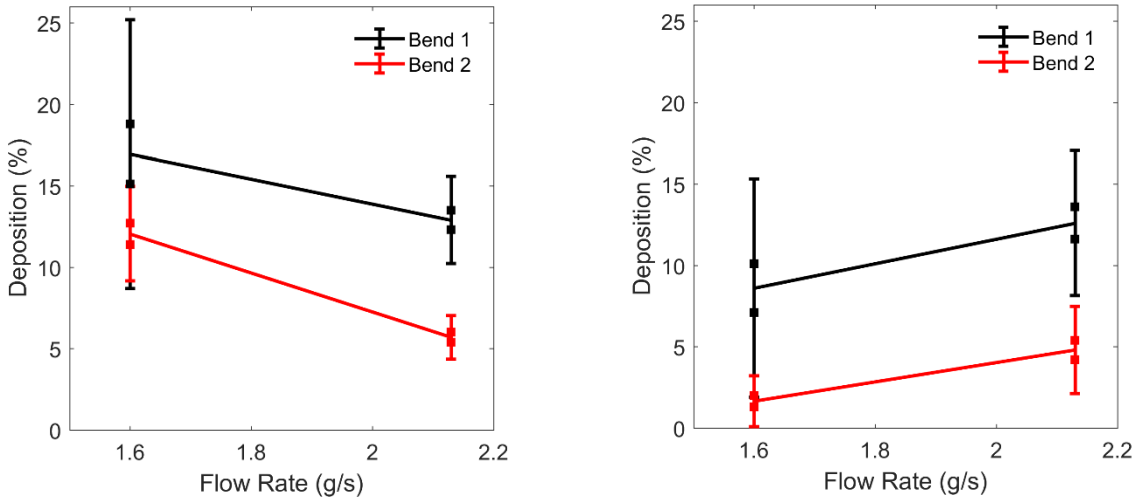

(a) $R_0 = 5$ *(b) $R_0 = 10$*

Figure 10 Deposition fraction as a function of flow rate. T_m = 1230 K and $T_{g,\,in}$ = 830 K.

VI. SUMMARY

A new test rig capable of recreating engine representative conditions was designed and used to study the deposition of Arizona Road Dust in rectangular cross section S-bends. The effects of curvature ratio, mass flow rate, and metal temperature were investigated. Further, numerical analysis indicated that for these conditions both thermophoresis and turbophoresis were likely important considerations.

For the range tested the most dominant parameter was the ratio of curvature, then wall temperature, and finally mass flow rate. Many of the trends that one would expect from cold tests were mirrored in these tests. The one trend that was unexpected was a reduction in deposition at higher mass flow rate, and therefore Re and Stk. The likely reason for this is that in the testing conducted these were associated with both lower flow and lower metal temperatures in the equivalent engine geometries. For these early tests the use of Arizona Road Dust allows comparison to other test facilities, but it is acknowledged that this may not be representative of the material

constituents of other dust and sands encountered by aircraft engines in fleet operation. It has, however, been possible to create air flow and metal surface temperatures typical of those experienced in the cooling systems of high pressure turbine blades, and to vary these from that required to induce the onset of particle sticking to the maximum internal cooling surface temperature expected. Flow temperature is seen to be a very strong driver of deposition at these temperatures.

The temperatures were set to be engine representative but appear to be a key source of uncertainty, with the single test conducted at a higher metal temperature showing lower uncertainty. Whilst a test dust with lower softening temperature or conducting experiments at a higher temperature could alleviate this, in order to remain engine representative the only option is to conduct further repeats. This is difficult in practise as the tests and required post processing take ~1.5 days.

Clear and testable trends were found in the spatially resolved deposition, which make these results promising for validation of particle tracking models. There were several mechanisms suggested to explain these trends. The relative strength of centrifugal acceleration compared to that induced by the dean vortices appeared influential, either altering the impact locations or the sticking probability. The turbulence and unsteadiness of the flow field appeared to affect the spatial spread of deposit. Additionally, there was evidence that accurate modelling of the particle size distribution exiting the first bend would be essential in any models. Numerical investigation that account for the multi-physics effects of aerodynamics and temperature would allow for testing of these suggested mechanisms.

ACKNOWLEDGEMENTS

The authors would like to thank Leo Verling, James Carter, Duncan Blake, and Jason McCluskey of the Oxford Thermofluids Lab who helped to manufacture and maintain the experimental rig. Thanks also go to Dr Rory Clarkson from Rolls-Royce for his support on the project. Finally, the authors would like to acknowledge the EPSRC via the Centre for Doctoral Training in Gas Turbine Aerodynamics studentship (EP/L015943/1) for their support.

APPENDIX

A. Temperature Distribution

Thermocouple	Exp 1	Exp 2	Exp 3	Exp 4	Exp 5
T1	97.3 (958)	95.9 (958)	97.2 (951)	98.1 (944)	96.8 (946)
T2	98.2 (952)	97.2 (951)	98.1 (943)	99.1 (939)	98.8 (940)
T3	99.6 (961)	100.4 (959)	99.6 (955)	1000.9 (945)	100.5 (946)
T4	98.0 (953)	98.1 (948)	97.6 (946)	99.1 (937)	98.3 (932)
T5	99.5 (963)	100.2 (961)	100 (958)	101.0 (945)	101.5 (947)
T6	97.0 (956)	97.8 (953)	97.3 (950)	98.2 (934)	98.2 (937)
T7	99.4 (966)	100.0 (963)	99.66 (961)	101.5 (949)	101.2 (949)
T8	97.8 (962)	98.2 (958)	97.9 (956)	99.2 (946)	99.0 (944)

Table 5 Temperatures at 8 points in the test piece predicted in conjugate simulations as a percentage (%) of the experimental measurements. Experimental measurements in brackets (in Kelvin).

REFERENCES

[1] A. Hamed, W. C. Tabakoff, and R. V. Wenglarz, "Erosion and Deposition in Turbomachinery," *J. Propuls. Power*, vol. 22, no. 2, pp. 350–360, 2006.

[2] S. Wylie, A. Bucknell, P. Forsyth, M. McGilvray, and D. R. H. Gillespie, "Reduction in Flow Parameter Resulting From Volcanic Ash Deposition in Engine Representative Cooling Passages," *J. Turbomach.*, vol. 139, no. 3, p. 031008, 2016.

[3] P. Forsyth, D. Gillespie, M. Mcgilvray, and V. Galoul, "Validation and Assessment of the Continuous Random Walk Model For Particle Deposition In Gas Turbine Engines," *ASME Turbo Expo 2016 Turbomach. Tech. Conf. Expo.*, vol. GT2016-573, pp. 1–13, 2016.

[4] N. Vadgama, P. Forsyth, M. McGilvray, and D. R. H. Gillespie, "Numerical Simulation of Spatially Resolved Particle Deposition in Accelerating flows," in *AIAA Aviation 2019 Forum*, 2019.

[5] N. Vadgama, P. Forsyth, M. Mcgilvray, and D. R. H. Gillespie, "Development and Validation of a Continuous Random Walk For Particle Tracking In Accelerating Flows," *ASME Turbo Expo 2020, Turbomach. Tech. Conf. Expo.*, no. GT2020-16026, pp. 1–14, 2020.

[6] D. Pui, F. Romay-Novas, and B. Liu, "Experimental Study of Particle Deposition in Bends of Circular Cross Section," *Aerosol Sci. Technol.*, vol. 7, no. 3, pp. 301–315, 1987.

[7] A. Kalpakli, R. Örlü, and P. H. Alfredsson, "Dean vortices in turbulent flows: rocking or rolling?," *J. Vis.*, vol. 15, no. 1, pp. 37–38, Feb. 2012.

[8] S. R. Wilson, Y. Liu, E. A. Matida, and M. R. Johnson, "Aerosol Deposition Measurements as a Function of Reynolds Number for Turbulent Flow in a Ninety-Degree Pipe Bend," *Aerosol Sci. Technol.*, vol. 45, no. 3, pp. 364–375, Feb. 2011.

[9] J. P. Bons, R. Prenter, and S. Whitaker, "A Simple Physics-Based Model for Particle Rebound and Deposition in Turbomachinery," *J. Turbomach.*, vol. 139, no. 8, 2017.

[10] A. R. McFarland, H. Gong, A. Muyshondt, W. B. Wente, and N. K. Anand, "Aerosol Deposition in Bends with Turbulent Flow," *Enviromental Sci. Tecnhnology*, vol. 31, no. 12,

1997.

[11] J. B. Wu, Z Young, “The Deposition of Small Particles from a Turbulent Air Flow in a Curved Duct,” *Int. J. Multiph. Flow*, vol. 44, 2012.

[12] J. P. Engelbrecht and E. Derbyshire, “Airborne Mineral Dust,” *Elements*, vol. 6, no. 4, pp. 241–246, 2010.

[13] J. M. Delimont, M. K. Murdock, W. F. Ng, and S. V Ekkad, “Effect of Near Melting Temperatures on Microparticle Sand Rebound Characteristics at Constant Impact Velocity - Part I,” *ASME Turbo Expo 2014*, vol. 137, 2014.

[14] Tutco, “Jet Air Heater and Control Panel Operating Instructions,” Exeter, NH, 2017.

[15] “ISO12103-1 Road vehicles - Test dust for filter evaluation - Part 1: Arizona test dust,” 1997.

[16] S. Elghobashi, “On Predicting Particle-Laden Turbulent Flows,” *Appl. Sci. Res.*, vol. 52, pp. 309–329, 1994.

[17] S. Beal, “Experimental Investigation into Particle Deposition in a Rectangular Cross-Section S-Bend Channel Under Engine Representative Conditions,” University of Oxford, 2020.

[18] A. S. Berrouk and D. Laurence, “Stochastic Modelling of Aerosol Deposition for LES of 90° Bend Turbulent Flow,” *Int. J. Heat Fluid Flow*, vol. 29, no. 4, pp. 1010–1028, Aug. 2008.

[19] P. Forsyth, “High Temperature Particle Deposition with Gas Turbine Applications,” DPhil Thesis, University of Oxford, 2017.

[20] D. P. Healy and J. B. Young, “An Experimental and Theoretical Study of Particle Deposition Due to Thermophoresis and Turbulence in an Annular Flow,” *Int. J. Multiph. Flow*, vol. 36, no. 11–12, pp. 870–881, Nov. 2010.

[21] M. Breuer, H. Baytekin, and E. Matida, “Prediction of aerosol deposition in 90 degree bends using LES and an efficient Lagrangian tracking method,” *J. Aerosol Sci.*, vol. 37, pp. 1407–1428, 2006.

[22] A. K. Vester, “Turbulent Pipe Flow Past a Pipe Bend: Effects of Upstream Conditions and Curvature Ratio,” KTH, 2014.

4.3 Further Results from the Experiments

The paper in Section 4.2 presents half of the experimental data available, the remaining results are included here to provide an indication of the variation seen in experiments.

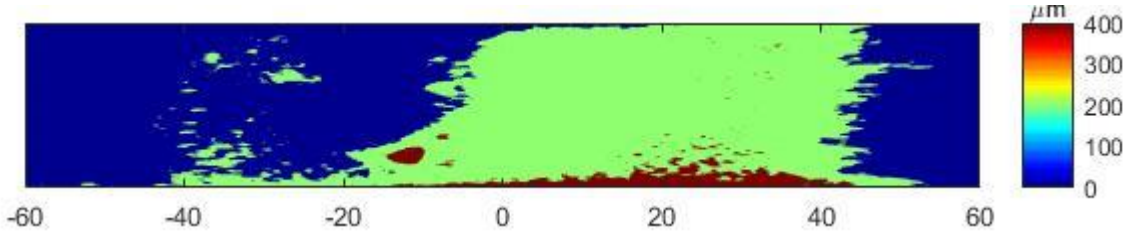

(a) Experiment 1. R_0 = 10, T_m = 1239 K, Re = 3442

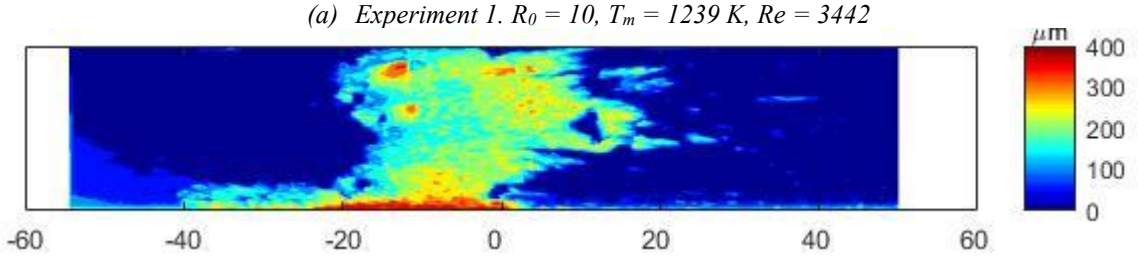

(b) Experiment 2. R0 = 20, T_m = 1237 K, Re = 3429

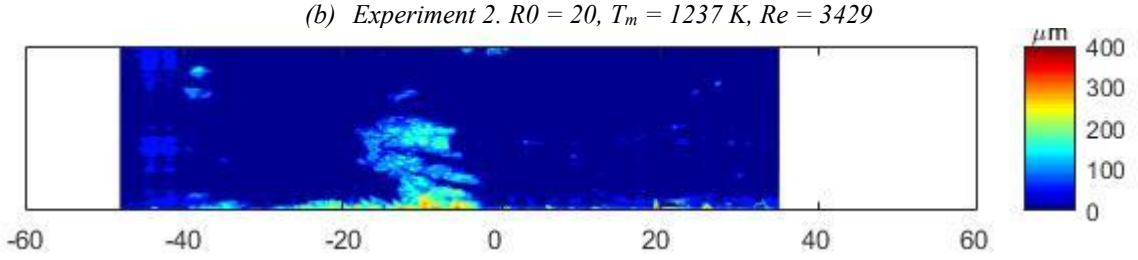

(c) *Experiment 3. R0 = 30, T_m = 1238 K Re = 3442*

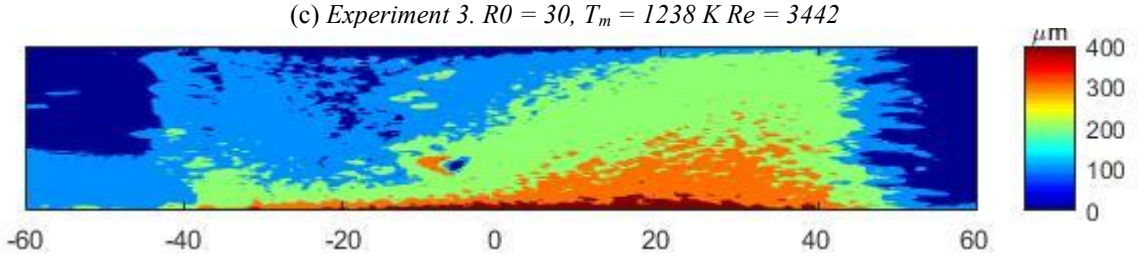

(d) Experiment 4. R0 = 10, T_m = 1225 K, Re = 4415

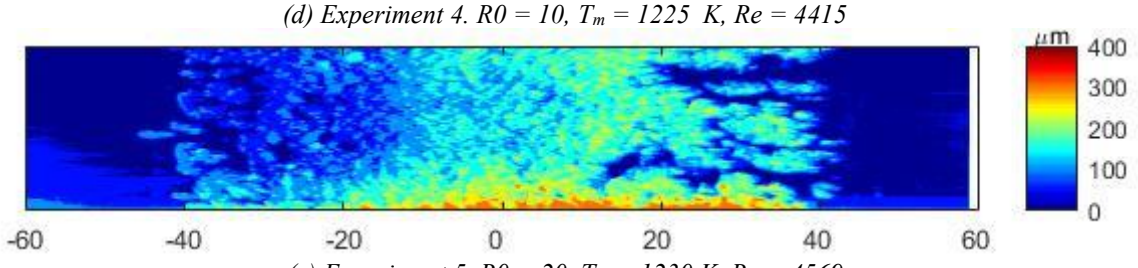

(e) Experiment 5. R0 = 20, T_m = 1230 K, Re = 4569

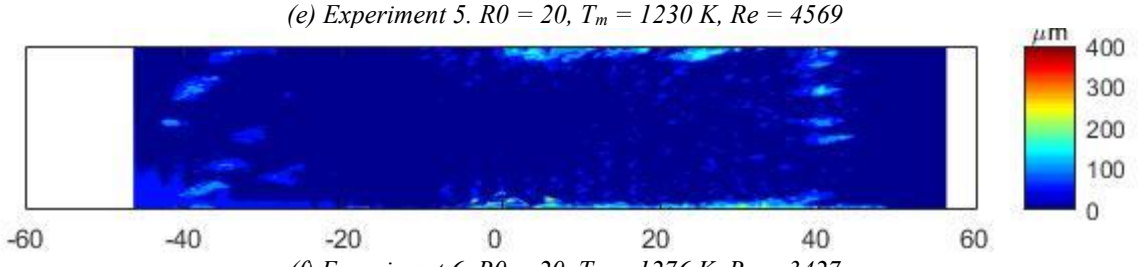

(f) Experiment 6. R0 = 20, T_m = 1276 K, Re = 3427

Figure 36 Deposition height (μm) on the first bend in experiments 1-6. Flow from left to right, with the middle of the bend corresponding to 0°. Y-axis is height of the wall.

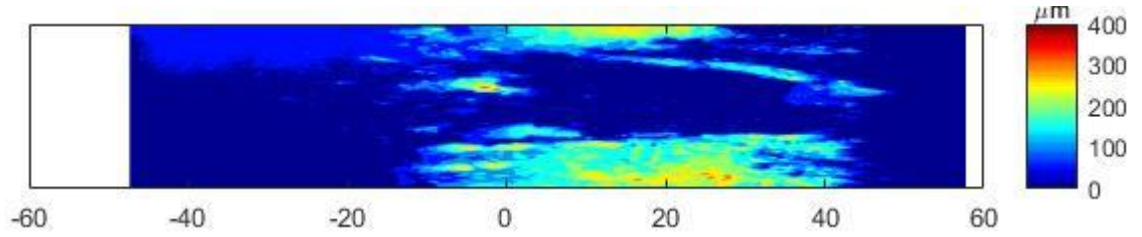

(a) Experiment 1. R0 = 10, T_m = 1239 K, Re = 3442

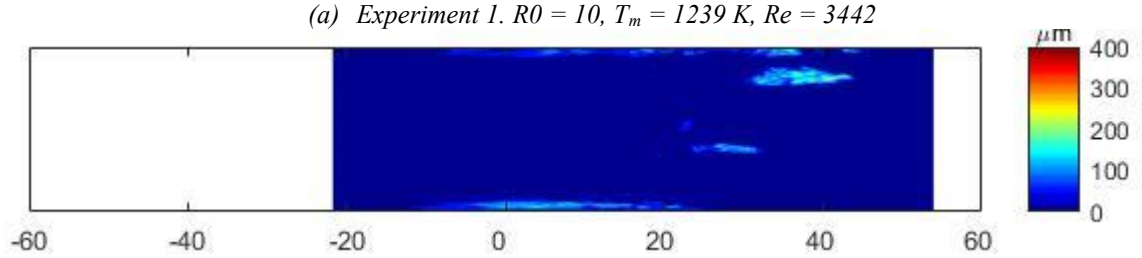

(b) Experiment 2. R0 = 20, T_m = 1237 K, Re = 3429

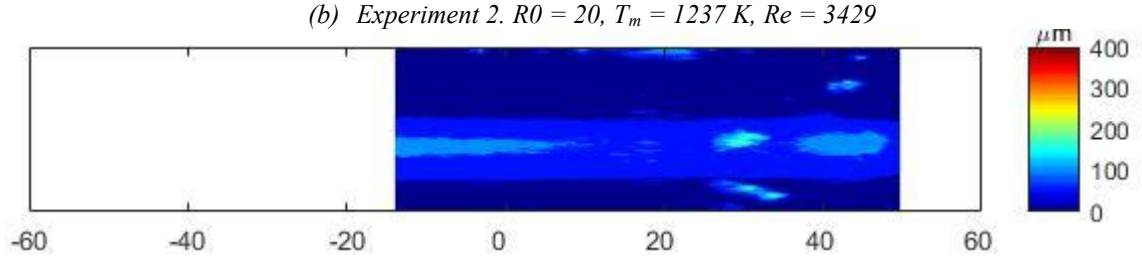

(c) Experiment 3. R0 = 30, T_m = 1238 K Re = 3442

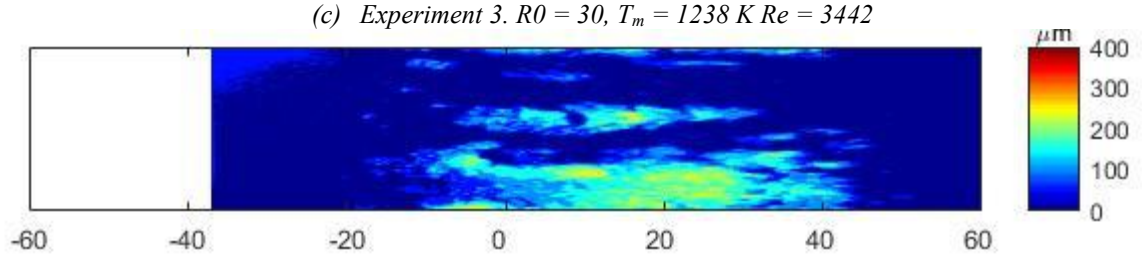

(d) Experiment 4. R0 = 10, T_m = 1225 K, Re = 4415

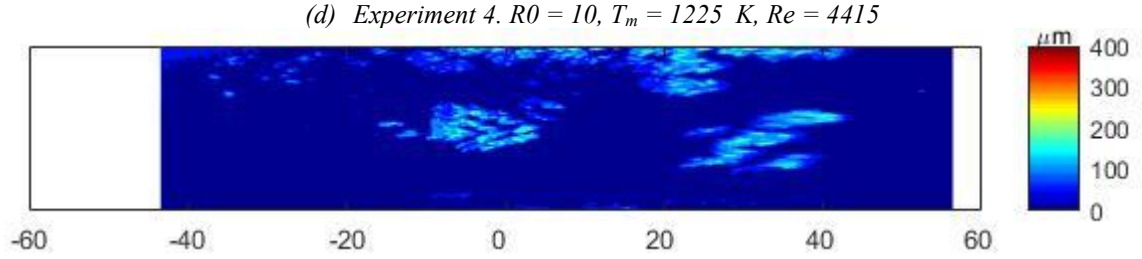

(e) Experiment 5. R0 = 20, T_m = 1230 K, Re = 4569

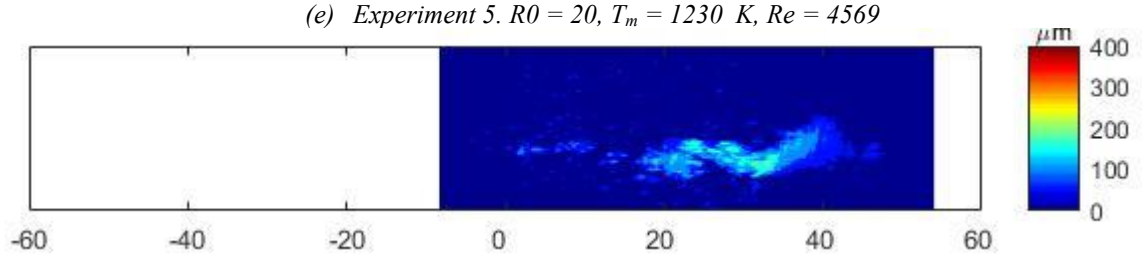

(f) Experiment 6. R0 = 20, T_m = 1276 K, Re = 3427

Figure 37 Deposition height (μm) on the second bend in experiments 1-6. Flow from left to right, with the middle of the bend corresponding to 0°. Y-axis is height of the wall.

5 Spatial Convergence of Numerical Simulations

In conventional numerical fluid dynamics studies numerical tests are applied to ensure the fluid solution is converged within a prescribed confidence interval. Convergence of the particle phase solution is similarly essential, but for the sparsely loaded flow of interest with random fluctuations affecting each particle trajectory the definition of convergence is complex, yet for a timely solution is essential. Typically, in multi-phase studies, integral values are monitored to establish convergence of the discrete phase: the most commonly used is the deposition fraction (the percentage of particles injected that impact on a surface). The validity of this was considered suspect, particularly in light of very different spatial distributions corresponding to similar integral depositions seen in the results section of the paper presented in chapter 3. Thus, before simulating the geometries described in Chapter 4, and comparing the predicted deposition to the experimental results, it was necessary to investigate the suitability of monitoring integral values as an indication of the convergence of spatially resolved quantities as reported in the paper below (Section 5.1). The paper shows that integral methods are wholly insufficient. Consequently, new methods to quantitatively measure differences between spatial deposition distributions from successive particle injections are tested to establish their suitability. A method for the use of these metrics to ensure convergence, in conjunction with turbophoresis models, and computational efficiency in mind, is established. This method is further applied in Chapter 6 to ensure that simulations are run efficiently (minimising the number of injections), and are converged such that comparisons are fair (the proposed spatial distribution metric varies by less than a prescribed value).

5.1 Paper: Convergence of Spatially Resolved Particle Deposition

The paper below describes the development of convergence metrics and the tests performed to assess their validity and robustness for the current application. In this paper, the thesis author is the primary author. Professors. McGilvray and Gillespie are the principal investigators on the project, Mr. Jonathan Connolly is a D.Phil. candidate at the OTI and provided feedback on the author's work by application to a separate particle deposition application. The thesis author generated all the material reported in the paper.

CONVERGENCE OF SPATIALLY RESOLVED PARTICLE DEPOSITION

N. Vadgama, J. Connolly, M. McGilvray, D. R. H. Gillespie

Department of Engineering Science, University of Oxford, Oxford, OX1 3UJ

ABSTRACT

Lagrangian stochastic models are frequently used to model the turbulent dispersion of particles and predict their deposition. While there are methods to calculate uncertainty for spatially resolved properties, there is no standard method to ensure these properties are converged. This paper presents a methodology for the application of distance metrics to achieve quantifiably converged maps of spatially resolved deposition in a computationally efficient way. The methodology is insensitive to the choice of distance metric, provided the metric is valid for null values. The number of particles tracked is increased by both increasing the spatial resolution of particles injected, and aggregating the results of repeated injections at a fixed resolution. Established distance metrics are used to compare evolving spatially resolved particle deposition distributions generated from each approach. It is shown that when an insufficiently high spatial particle density is injected, turbulent dispersion will not necessarily redistribute particles through the domain sufficiently to achieve converged maps of deposition. Further, it is shown that monitoring bulk deposition statistics is insufficient for the evaluation of spatial convergence. For the test case used, the minimum spatial particle injection density for convergence of spatially resolved statistics is higher than that required for integral statistics.

KEYWORDS

Particle Deposition, Turbophoresis, Turbulent flows, Convergence

NOMENCLATURE

d_p	Particle diameter
D_KL	Kullback-Leibler Distance
D_Hell	Hellinger Distance
D_h	Hydraulic Diameter (m)

N_S Number of samples

N_p Number of particles per sample

P Prior distribution

Q Posterior distribution

R_c Radius of Curvature (m)

s Sample number (m)

S Sample standard deviation

S Arc-length (m)

$t_{N_{S-1,\alpha}}$ T-multiplier with α confidence

U_g Bulk gas velocity (ms^{-1})

$\delta\eta$ Absolute percentage difference (%)

η_s Deposition fraction of sample number S (%)

$\bar{\eta}$ Mean deposition fraction (%)

μ_g Gas kinematic viscosity (m^2s^{-1})

ρ Density (Kg m^{-3})

Re Reynolds Number ($= \rho_g U_g D_h/\mu_g$)

R_0 Ratio of Curvature ($= 2R_c/D_h$)

Stk Stokes Number ($= \rho_p d_p^2 U_g/18\,\mu_g D_h$)

CI Confidence Interval

KL Kullback-Leibler

CRW Continuous Random Walk

I. INTRODUCTION

Particle modelling has proven to be important for multiple engineering fields, from oral drug delivery optimisation to gas turbine degradation prevention. An estimated 10 tonnes of dust pass through an engine's core during its lifetime, so the accumulation of even small impact fractions would be significant for its performance. Previous research (Vadgama *et al.*, 2020) shows that even

when modelled integral deposition values are comparable to experimental validation data the spatial distribution of particles can be strikingly different. Thus, for the validation of particle tracking models accurate spatially resolved results are essential. Therefore, a precise understanding of where this deposition occurs, including small deposition fractions, can be important.

Whilst it is common for studies to show that the results, such as the fraction deposited from those injected, have become independent of the number of particles tracked it is often not clear how the required number and spatial distribution of particles is established (Graham and Moyeed, 2002; Berrouk and Laurence, 2008). Typically, predictions using increasing numbers of injected particles are compared in a method, analogous to mesh sensitivity studies for the continuous phase based on the number of cells. However, detail of the spatial density of injection and the number of repeated samples are not commonly reported. Further, convergence in one quantity is typically employed as a proxy for general convergence. (Graham and Moyeed, 2002; Reynolds, 1997)

To conduct particle tracking, the particles' diameters, initial locations and velocities, and mass must be specified. For the particles' locations, it is unrealistic to know the exact initial distribution of particles, and hence a uniform injection distribution is often considered with the aim of understanding all potential deposition.

Due to the complexity of the flow fields, low particle concentrations, and limited computing power, one-way coupled particle models have proven popular. These allow the à priori generation of a Reynolds Averaged Navier Stokes flow solution of the continuous phase into which the particles are injected. Lagrangian particle tracking through this steady state flow field would be spatially deterministic. Thus, in turbulent flows, a further stochastic model is required to capture turbophoretic effects, which are particularly important for small particles. With stochastic models, that calculate and apply the fluctuating turbulent velocities, the trajectories of identical particles with the same initial conditions are different for each injection (Legg and Raupach, 1982; Bocksell and Loth, 2006; Vadgama *et al.*, 2020). Thus, multiple injections (N_s>1) of the same spatial particle distribution can be combined to provide a probabilistic distribution. This paper focuses on this more complex case of stochastic models, with the results being equally applicable to deterministic models.

To demonstrate these issues, a test case of flow through a 90-degree bend where turbophoresis has been shown to be influential on the spatial distribution (Vadgama *et al.*, 2020) is introduced. For this paper a bespoke particle turbulent transport model has been applied, however, the technique is equally valid when using industry standard models such as the Direct Random Walk. It is shown that evaluating changes in integral deposition statistics using existing error estimation methods is insufficient to ensure a representative spatial deposition distribution. Measures of distance are introduced to quantify the difference between spatial distributions, and their robustness is assessed. These are then used to investigate the role of increasing the number of particles, both via further samples and a higher spatial density of particles per injection. The results show that a minimum sufficient density of particles and number of injected samples are required for convergence of the spatial distribution. This leads to a clear practicable method for the generation of converged spatial distributions in an efficient way.

II. METHODS

In typical convergence strategies integral statistics are used, particle injection simulations are conducted using an arbitrary number of particles (N_p) on the injection plane. N_p is then increased until the mean impact fraction is found to be steady. In most cases this is confirmed using some user judgement (Pascal and Oesterlé, 2000; Graham and Moyeed, 2002). In such a process it is normal for a single injection ($N_s = 1$) of the particle location distribution to be computed, rather than multiple samples ($N_s > 1$). In the latter case, an average must be computed (Equation 1). Metrics used to monitor convergence are then the absolute percentage difference in impact fraction (Equation 2) and the confidence interval (CI, Equation 3). The user then sets two threshold criteria by which convergence is achieved: 1) the result is sufficiently close to the fully converged solution, $< criterion\ 1$; 2) that the uncertainty lies within acceptable limits, $CI < criterion\ 2$.

$$\bar{\eta} = \frac{1}{N_S} \sum_{s=1}^{N_S} \eta_s \tag{1}$$

$$\delta\eta = 100 \times \frac{\bar{\eta}_s - \overline{\eta_{s-1}}}{\bar{\eta}_s} \tag{2}$$

$$CI = 2t_{N_S-1,95}\, S/N_S \tag{3}$$

This study is focused on ensuring the computed spatial distribution of deposit is representative. To the authors' knowledge, no criterion has been proposed to assess the closeness of a spatially resolved result to the fully converged result in the existing open literature, thus this is the focus of this paper.

In order to compare the similarity of multi-dimensional data distributions, where new data are added to an existing set, there already exist a multitude of tests. Typically, they compare the prior distribution (P) and posterior distribution (Q), the former is the distribution before the current observed data are included and the latter after the newly observed data is included. In this study, the prior distribution (P) and posterior distribution (Q) are either different due to increased spatial density, or a further sample being used in the calculation of the posterior distribution.

One category of tests is distance or divergence metrics: a commonly used divergence measure being the Kullback-Leibler (KL) divergence (Equation 4). This, however, is unsuitable for the assessment of deposition as it fails when the probability changes from 0 in the prior to non-zero in the posterior, which is the most common change in probability state when little deposition occurs. An alternative measure is the Hellinger distance, Equation 5, which is more robust and thus is used in this remainder of this paper. The authors also propose Equation 6 as an alternative, with a form more similar to the familiar differencing formula used in Equation 2. The normalising factor, of ½, ensures this measure scales between 0 and 1 for true probability distribution functions (i.e. their integral is 1).

$$D_{\mathrm{KL}}(P||Q) = \sum_{x \in X} \sum_{y \in Y} P(x,y)\, log\left(\frac{P(x,y)}{Q(x,y)}\right), P(x,y), Q(x,y) > 0 \tag{4}$$

$$D_{\mathrm{Hell}}(P||Q) = \frac{1}{\sqrt{2}} \sqrt{\sum_{x \in X} \sum_{y \in Y} \left(\sqrt{P(x,y)} - \sqrt{Q(x,y)}\right)^2}, P(x,y), Q(x,y) \geq 0 \tag{5}$$

$$D(P||Q) = \frac{1}{2} \sum_{x \in X} \sum_{y \in Y} |P(x,y) - Q(x,y)|, P(x,y), Q(x,y) \geq 0 \tag{6}$$

An equivalent measure for the confidence interval can be calculated using the approach of Graham et al. (2002) who provide a method to characterise the uncertainty of spatially resolved results and estimate the number of particles required to meet the required confidence interval (Graham and Moyeed, 2002). They found that the uncertainty is only dependent on the total number of particles injected (N_s x N_p). Further, to increase the precision by an order of magnitude the number of particles must be increased by two orders of magnitude. Graham et al. (2002) suggest that in the region of interest the steps are:

1. Use a nominal number of particles (N_p) per sample and repeat the injection (i.e. increment N_s) until the maximum standard deviation at each location in the distribution of the aggregated results, $S(x,y)_{\max}$, becomes a good estimation of the population's maximum local standard deviation, σ_{max}, (i.e. $\sigma_{max} = S_{\max}$ when $N_s \to \infty$, hence $\sigma_{max} \approx S_{\max}$ when N_s is large). This indicates the number of samples (N_s) that need to be used.
2. Increase the number of particles per injection, each time taking N_s samples, until the trend in the injection location with highest standard deviation $S(x,y)_{\max}$ is proportional to $N_p^{-1/2}$.
3. Calculate the confidence interval using Equation 3 replacing the sample standard deviation (S) with the local maximum sample standard deviation ($S(x,y)_{\max}$). Decide on the precision required and use the trend identified to calculate the parameters needed to provide the required level of accuracy.

III. TEST CASE

To assess current approaches and the proposed approach, a simple but sufficiently complex case of interest is chosen. Pui et al. (1987) conducted experiments of deposition in a 90-degree bend of curvature ratio (R_0) 5.6-5.7 with a diameter of 8.51 mm. The flow characterised by ambient conditions and a Reynolds number (Re) of 6,000 - 10,000. Monodisperse liquid droplets of Uranine (ρ_g= 925 kg/m^3) with Stokes numbers (Stk) between 0.03 and 1.35 were dispersed in the flow. This

liquid allowed experimentalist to mimic an all-stick condition, which eliminates the need for particle bounce-stick modelling.

A domain (Figure 1) and validated mesh (Figure 2) from a previous study by Vadgama et al (2020) is used. A linear pressure-strain Reynolds stress model with wall reflection effects and enhanced wall treatment was used, with the maximum Y^+ below one. Fluent 19.2 and ICEM 19.2 were used for the flow solution and the mesh generation respectively. The CRW model, as in its final implementation, from Vadgama et al. (2020) is used to model turbulent dispersion. In this paper, it is shown that there is sufficient turbophoresis to influence particle trajectory for the particles studied. The simulations simulate 6.4 □m diameter particles in a flow with Reynolds number 10,000, these particles showed most variation due to turbophoresis.

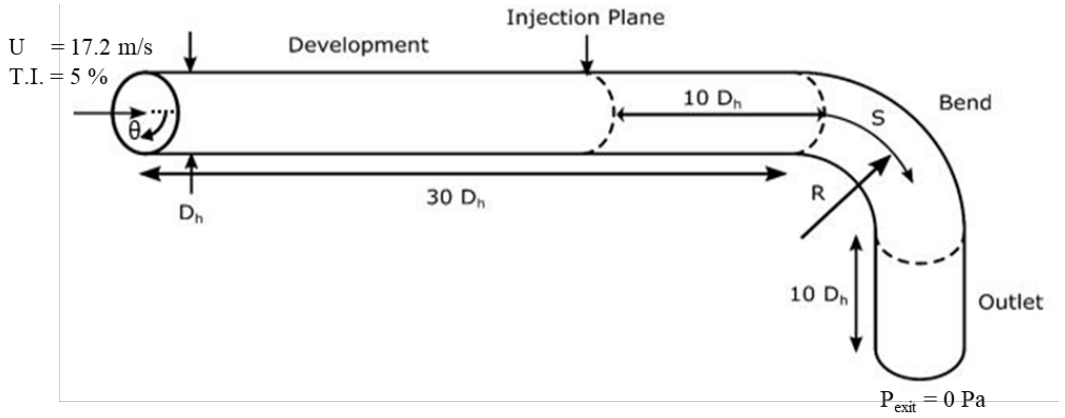

Figure 1 Simulated domain of the Pui et al. (1987) 90-degree pipe bend experiment. Entry and exit are labelled with boundary conditions.

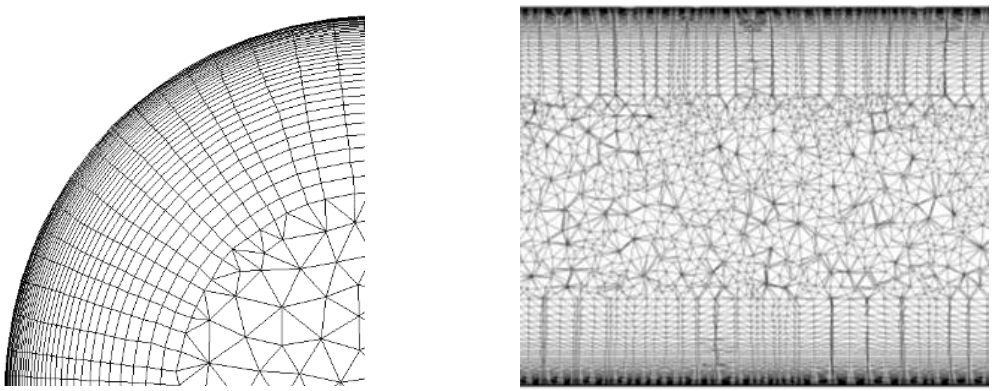

Figure 2 Cross-sections of mesh used. The mesh has a minimum cell quality of 0.29, and a maximum Y^+ of 0.51.

Injections using 10 different spatial densities of uniformly distributed particles are compared, all located at the injection plane. For this study, particles are injected ten diameters upstream of the bend entrance, Figure 1. The spatial density is approximately doubled between injections, and described by Table 1 and shown in Figure 3. Each of these injections, with the particles located at the same initial positions for each sample, were simulated 50 times to create 50 samples.

Table 1: Definition of the 10 different injections, with varying spatial density of particles.

Injection Reference	Density (# particles/m^2)	Spacing (m)
1	2.1E+06	6.86E-04
2	4.5E+06	4.71E-04
3	9.3E+06	3.28E-04
4	1.8E+07	2.36E-04
5	3.6E+07	1.68E-04
6	7.2E+07	1.18E-04
7	1.4E+08	8.38E-05
8	3.3E+08	5.50E-05
9	1.1E+09	2.96E-05
10	2.3E+09	2.09E-05

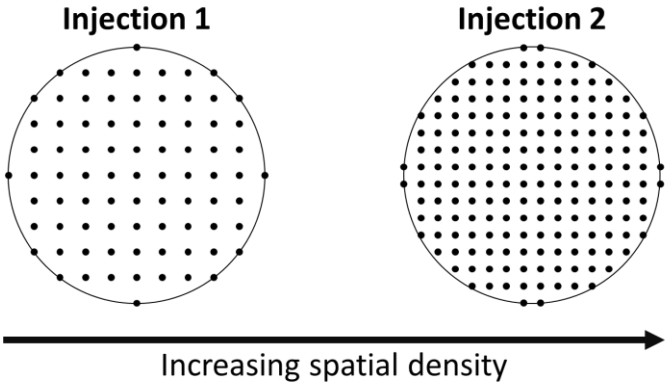

Figure 3 Initial positions of particles used in injections 1 and 2. Injection plane shown located as per Figure 1. Particle concentration was approximately doubled between each injection, Table 1.

The simulations investigate both the integral and spatial distribution in the bend. The deposition fraction is calculated as the number of particles hitting the wall of the 90-degree bend divided by the number of particles entering the 90-degree bend that are successfully tracked (either hit the wall or exit the domain). To generate a map of deposition fraction that can be easily presented, the bend wall is represented as a 2D surface with the two axes being the circumferential

angle and arc length (θ and S respectively in Figure 1). The local deposition fraction is plotted, its integral is equal to the total deposition fraction.

While judicious choice of a kernel function could result in a continuous distribution, and possibly reduce the number of particles required, this introduces further degrees of freedom because this function needs to be specified. For this study, discontinuous distributions are used with a resolution of 92 (arc-length-wise) by 46 (circumferentially) to be consistent with the study by Berrouk and Laurence (2008).

IV. Results & Discussion

Firstly, the impact fraction (equivalent to deposition fraction as all particles which impact also stick) of particles sticking on the bend wall is monitored. The mean impact fraction of 50 samples of is plotted in Figure 4. Injection 4 is seen to be sufficient to predict the percentage of particles impacting, with the mean of the highest density injection falling within the confidence interval. Further, Figure 5 shows that the absolute error by this point is, and remains, below ~1%.

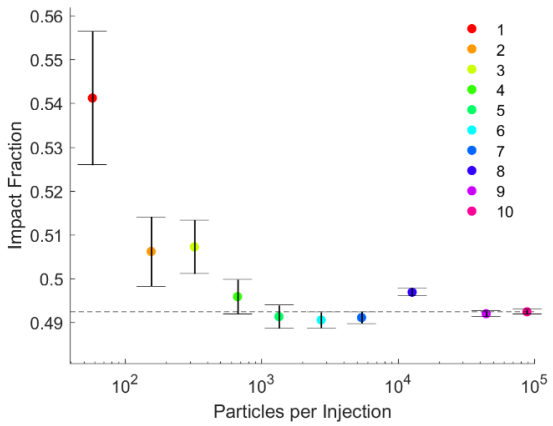

Figure 4 Average impact fraction from 50 samples with 95% confidence intervals. The horizontal line shows the mean impact fraction as per injection 10.

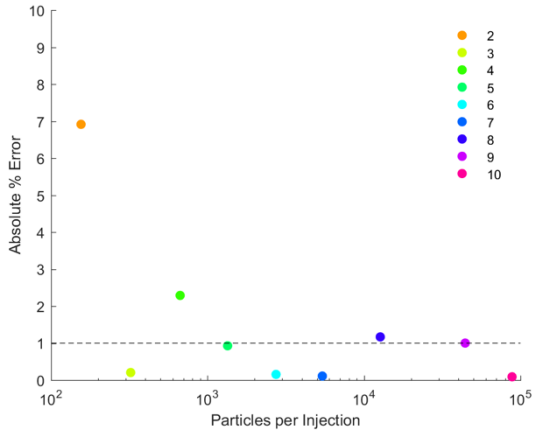

Figure 5 The absolute percentage error of impact fraction as calculated using Equation 2. The dotted horizontal line is at 1%, the chosen critical value.

To test that only the total number of particles injected matters, as per Graham and Moyeed (2002), the confidence interval of the resultant spatial distribution is investigated. Following step 1 in the procedure described above, it was found that 50 injections were sufficient for the samples' standard deviation (S) to become a good estimate of the population's standard deviation (σ). As per step 2, Figure 6 shows the error becomes proportional to $N_p^{-1/2}$ for injection number 3 (Table 1) and

above. Figure 7, as per Graham and Moyeed (2002), shows this error is only dependent on the total number of particles injected implying the calculation is correct. The 90% confidence interval using 50 samples of injection number 4 is 6.17×10^{-7}.

Figure 8 shows the spatial distributions for each of the injection cases. It is clear that the earlier injection cases are not converged for spatial distribution, with zero deposition in the lower density injection cases where there is significant deposition in the higher density injection cases. Figure 9 compares the spatial impact distribution from the lowest spatial density case that meets the criterion on integral deposition (injection 4) to the highest spatial density case (injection 10). It is shown that injection 10 does not fall within the distribution of injection 4 even after assuming a maximum deviation of the confidence interval. It is clear that the lack of particles is resulting in gaps in the distribution. Further calculations showed that even extremely low confidence intervals have the same results. This appears obvious once we consider that this comparison is equivalent to comparing the integral results using injection 10 to that of injection 1, as we have not checked that the distribution is converged.

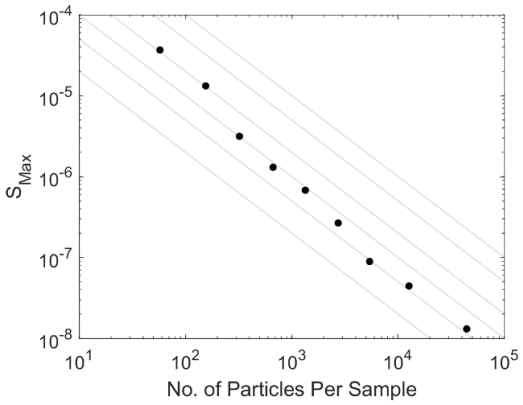

Figure 6 Maximum standard deviation (across the spatially resolved impact fraction distribution) with increasing density of particles on injection plane. N_s = 50. Lines $\propto N_p^{-1/2}$ are shown for comparison.

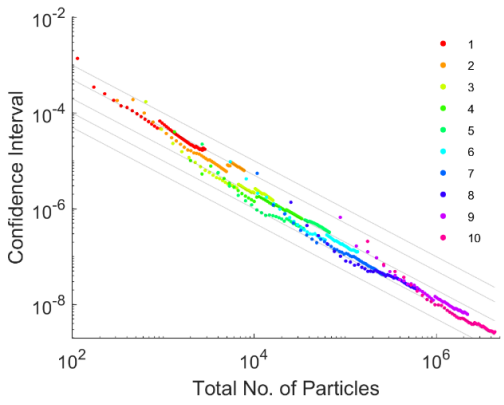

Figure 7 Confidence interval, using Equation 3, as a function of the total number of particles injected. Lines $\propto (N_p N_s)^{-1/2}$ are plotted for comparison.

Figure 10 shows the Hellinger distance between distributions calculated with an increasing density of particles. This is the equivalent of Figure 4, but for spatially resolved data. The number of samples used does not affect the ability to conclude when sufficient similarity has been established, therefore the required injection particle density can be found without conducting multiple samples. This is because, in this test case, turbophoresis is a second order effect compared

to the variation introduced by increasing the spatial density of particles at the injection plane. There is no guarantee this is the case in geometries where stochastic mechanisms are present. Figure 11 shows the Hellinger distance between distributions calculated with an increasing number of samples, where injections with less particles take longer to converge. Whilst these statistics do give an impression of the information gain, it is difficult for an engineer to contextualise these numbers.

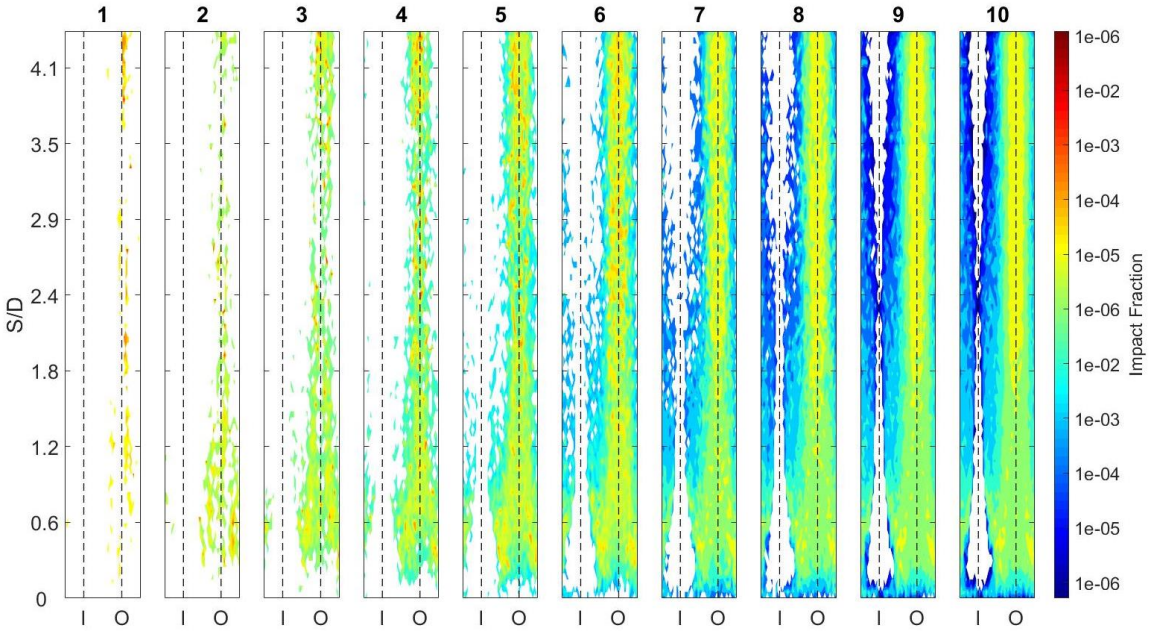

Figure 8 Spatially resolved impact fraction, I and O mark the inner and outer of the bend.

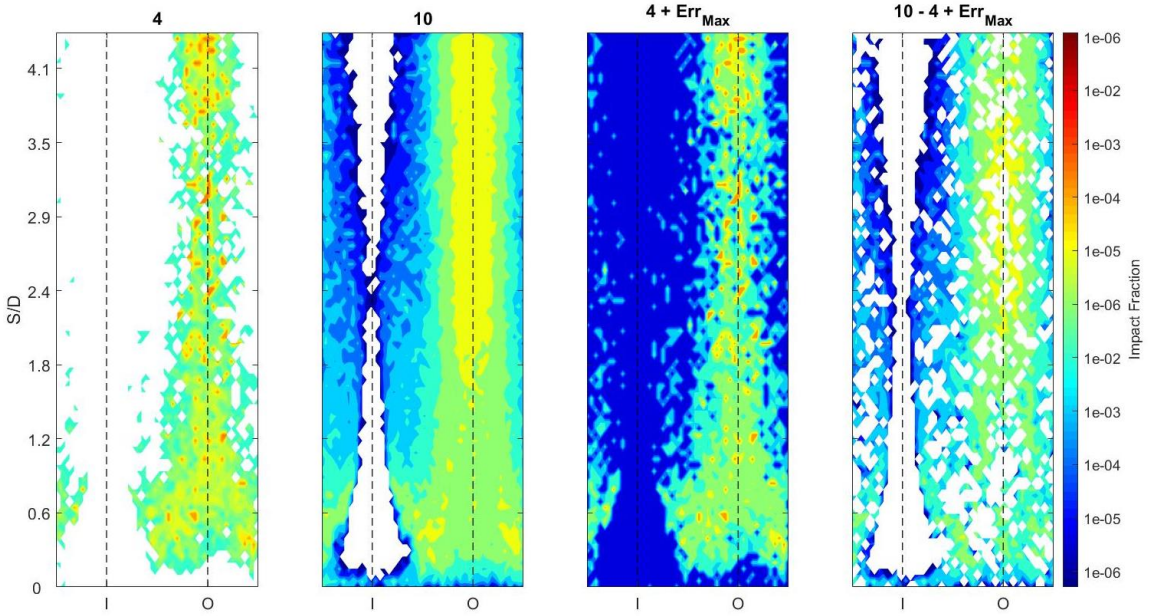

Figure 9 Comparison of spatially resolved deposition fraction resulting from injection 4 and 10, considering the estimated confidence interval. I and O mark the inner and outer of the bend.

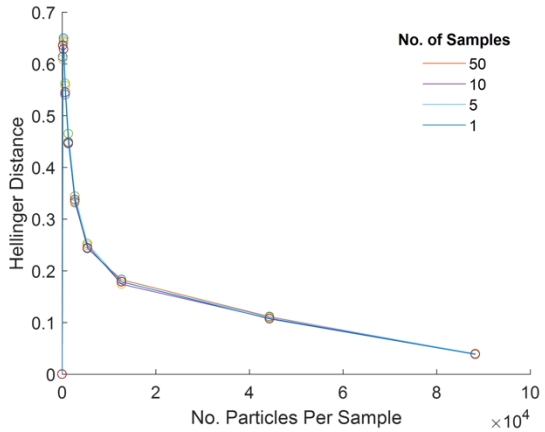

Figure 10 Hellinger distance (Equation 5) between deposition distributions, each injection is compared to the previous lower spatial injection density with an equal number of samples.

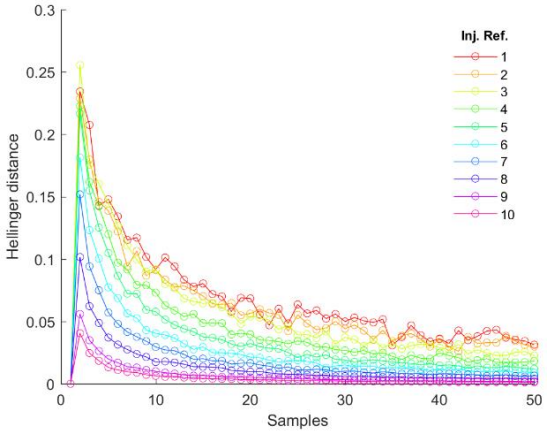

Figure 11 Hellinger distance (Equation 5) between distributions using n-1 and n samples of injections with the same particle density on their injection plane.

Figure 12 shows the use of Equation 6 to measure the distance between two distributions. Comparing with Figure 10, it is clear the choice of metric has had little effect on the implied convergence. By normalizing the distance by the integral deposition fraction, context for the magnitude of this result can be made (Figure 13). This normalization makes the result equal to the distance between distributions to the percentage of deposited particles at each location. This creates a universal (non-case-dependent) and interpretable threshold for convergence to be set (chosen here at 10%). It also provides a similar graph to Figure 5 for spatially resolved data. For this threshold, 10 injections of the highest density were enough to ensure an accurate representation of the spatial distribution had been generated.

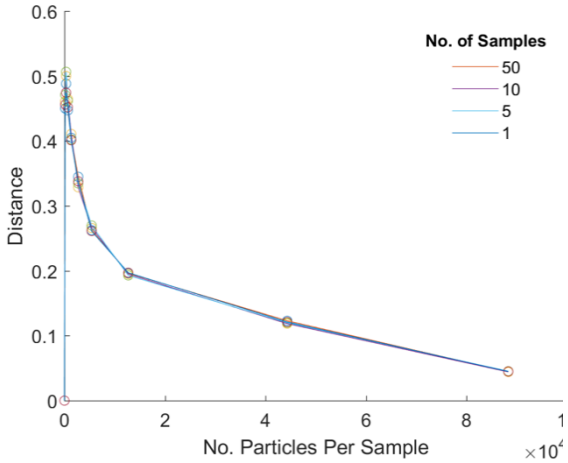

Figure 12 Distance (Equation 6) between deposition distributions, each injection is compared to the previous lower spatial injection density with an equal number of samples.

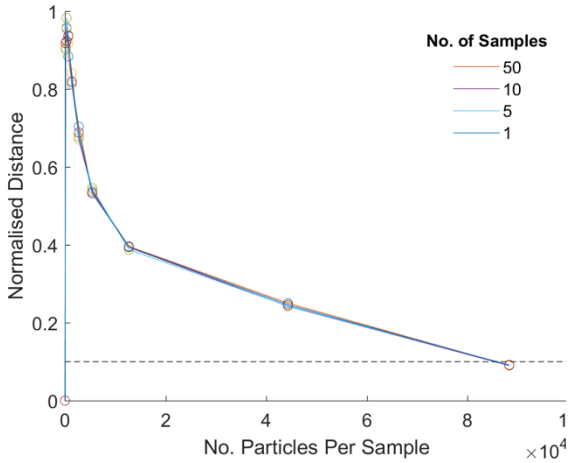

Figure 13 Normalised distance between deposition distributions as per Equation 6. Measure is normalized by the integral impact fraction. Each injection is compared to the previous lower density injection with an equal number of samples. Dotted line at 10%, used as the critical value.

The confidence interval can be calculated as per normal statistical techniques, as done by Graham and Moyeed (2002). To justify the number of particles per injection and the minimum number of samples when investigating spatially resolved quantities, where the stochastic effects are likely to be heavily influential, it is recommended that one should iteratively compare converged distributions of increasing N_p (using the required N_s for distance to fall within acceptable limits each time) until the distance between these converged distributions fall below a converged limit. Where turbophoresis is not modelled or it can be assumed a secondary effect, considerable time saving can be achieved by using this methodology:

1. Measure distance using increasing N_p with a single sample,
2. Measure distance using increased N_s with the required N_p from step 1

V. CONCLUSIONS

A measure of distance between particle deposition distributions is proposed, and a methodology for its use to ensure convergence is outlined. It is shown that in order to understand all potential deposition on a spatially resolved basis, a minimum spatial density of particle injection sites is required at the inlet, and that multiple repeated injection is insufficient to overcome the limitations imposed spatially. To achieve convergence this minimum density must first be increased while monitoring the distance metric until it lies beneath a maximum threshold. Further error measurement calculations can then be applied to repeated injections at this or higher particle densities. In this paper monodispersed particle injection has been used to establish the convergence procedure: the convergence criteria need not be updated in the event of injecting a size distribution, but the minimum number of repeated injections required to achieve a converged mass impact fraction distribution would increase.

This approach is applicable to turbomachinery components, the key challenge for more complex surfaces being the discretization of any deposition surface into sufficiently resolved sub-regions. It is likely that consideration of the requirement for the spatial distribution to be converged would increase the computational requirements, as significantly more particles must be tracked.

ACKNOWLEDGMENTS

Thanks go to Dr Rory Clarkson from Rolls-Royce for his support and openness to research direction, without which this work would not have been possible. The authors would also like to acknowledge the EPSRC via the Centre for Doctoral Training in Gas Turbine Aerodynamics studentship (EP/L015943/1) for their support.

REFERENCES

Berrouk, A. S. and Laurence, D. (2008) 'Stochastic Modelling of Aerosol Deposition for LES of 90° Bend Turbulent Flow', *International Journal of Heat and Fluid Flow*, 29(4), pp. 1010–1028.

Bocksell, T. L. L. and Loth, E. (2006) 'Stochastic modeling of particle diffusion in a turbulent boundary layer', *International Journal of Multiphase Flow*, 32(10–11), pp. 1234–1253.

Graham, D. I. and Moyeed, R. A. (2002) 'How many particles for my Lagrangian simulations?', *Powder Technology*, 125(2–3), pp. 179–186.

Legg, B. J. and Raupach, M. R. (1982) 'Markov-chain simulation of particle dispersion in inhomogeneous flows: The mean drift velocity induced by a gradient in Eulerian velocity variance', *Boundary-Layer Meteorology*, 24(1), pp. 3–13.

Pascal, P. and Oesterlé, B. (2000) 'On the dispersion of discrete particles moving in a turbulent shear flow', *International Journal of Multiphase Flow*, 26(2), pp. 293–325.

Pui, D., Romay-Novas, F. and Liu, B. (1987) 'Experimental Study of Particle Deposition in Bends of Circular Cross Section', *Aerosol Science and Technology*, 7(3), pp. 301–315.

Reynolds, A. M. (1997) 'A Lagrangian stochastic model for particle trajectories in non-Gaussian turbulent flows', *Fluid Dynamics Research*, 19(5), pp. 277–288.

Vadgama, N., Kapsis, M. , Forsyth, M. , McGilvray, M. and Gillespie, D. R. H. (2020) 'Development and Validation of a Continuous Random Walk For Particle Tracking In Accelerating Flows', *ASME Turbo Expo 2020, Turbomachinery Technical Conference and Exposition*, (GT2020-16026), pp. 1–14.

6 Deposition in Flow with Acceleration

In this chapter simulations of the experiments in Chapter 4 are conducted using the CRW model proposed in Chapter 3, according to the methodology established in Chapter 5. This demonstrates importance of each piece of work presented thus far, and provides insight for further development.

First, details of the numerical set-up and the mesh convergence study are presented. Following this, the structure of the flows in the different domains are explored, specifically in the context of particle motion. A detailed analysis of particle motion in the baseline case, including the effects of thermophoresis, turbophoresis, and gravity is presented. This analysis provides a platform to explore the trends identified in Chapter 4 using further numerical simulations. The experiments are referred to by the same naming convention used in the paper included in Chapter 4, Table 5. The effects of ratio of curvature and mass flow rate are investigated, but the effect of temperature is not. While temperature affects the flow field, which alone could change the deposition, it also impacts the particle-surface interaction. Due to the absence of a fully validated temperature dependant bounce-stick model, modelling a change of temperature would also introduce further uncertainty and complexity in the analysis of results. While the effect of temperature would be worthy of studying it was not investigated due to the additional cost of a wider parametric study.

	R_0	Re	T_g (K)
Experiment 1	5	3442	828
Experiment 2	10	3429	833
Experiment 4	5	4415	882

Table 5 Experimental conditions from the paper in Section 4.2 that were simulated for the work in this section.

6.1 Fluid Phase

6.1.1 Set-up and Solution

The numerical simulations conducted were conjugate simulations i.e. the solid material and fluid domain were coupled, Figure 38 shows the simulated domain and boundary conditions. The inlet mass flow rate and temperature is defined using the measurements from the experiment. The outlets are defined using the pressure measurements of the experiment. The conjugate simulation allows for the external metal temperature to be defined, a homogenous temperature is assumed on the

exterior. An exterior temperature of the oven's temperature resulted in a heat flux comparable to the oven's power, which supports the steady state conditions achieved.

As per the paper included in Chapter 3, a Reynolds stress model (with wall reflections) was used for turbulence modelling. This was found to best predict the important turbulent properties for the CRW model. The simulations were solved using a SIMPLE (Semi-Implicit Method for Pressure Linked Equations) pressure-velocity coupling. Third-order MUSCL (Monotone Upstream-Centred Schemes for Conservation Laws) were used for the spatial discretization as it has the potential to improve the spatial accuracy by reducing numerical diffusion in highly 3D flows like these [132]. Energy equation residuals were 1e-7, continuity 1e-9 and all others 1e-5. The gas was assumed to be an ideal gas that followed Sutherland's law. Gravity was turned on for all simulations unless explicitly otherwise indicated.

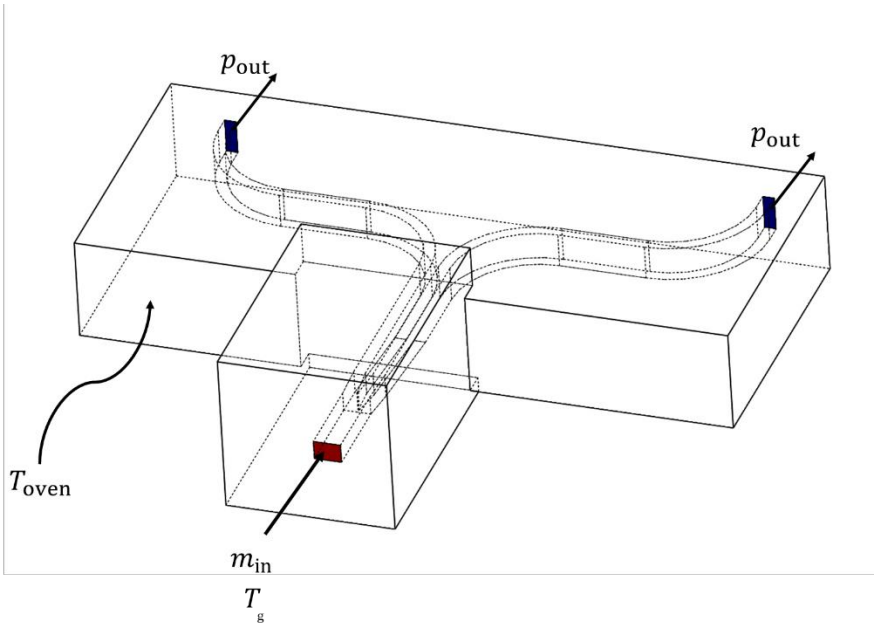

Figure 38 The domain used for conjugate simulation, the R_0=10 domain is shown. R_0=5 and 15 domains were identical apart from the internal channel which was adjusted accordingly.

6.1.2 Mesh Sensitivity and Convergence

An unstructured gird was used with mesh independency confirmed. The geometry and conditions used were based on experiment 4 which had the largest acceleration/tightest bend and highest Reynolds number. This ensured the same meshing parameters would result in a sufficiently resolved domain for all other simulations, without having to conduct further sensitivity studies.

Three meshes (Table 6) were solved using the numerical approach described above. Two fluid quantities were monitored to determine fluid convergence: tangential velocity at the exit (area averaged) and wall shear stress on the channel walls (area averaged). The first quantity was used as an indication of the fluid field's structure (strength of the induced secondary flows). The second ensures the near wall fluid structure is converged which has been shown to be critical for accurate deposition predictions, and is directly used by the CRW model. Figure 39 shows that results of the medium mesh fall within one percent of the large mesh, this mesh is used for all further work.

	Fluid Cells ($x10^{-6}$)	Solid Cells ($x10^{-6}$)	Total Cells ($x10^{-6}$)	Tangential Velocity @ Exit (ms^{-1})	Wall Shear Stress (Pa)
Small	0.9	0.6	1.6	0.657	14.1
Medium	3.3	2.0	5.6	0.589	14.2
Large	12	7.0	19	0.584	14.2

Table 6 Mesh sensitivity study results.

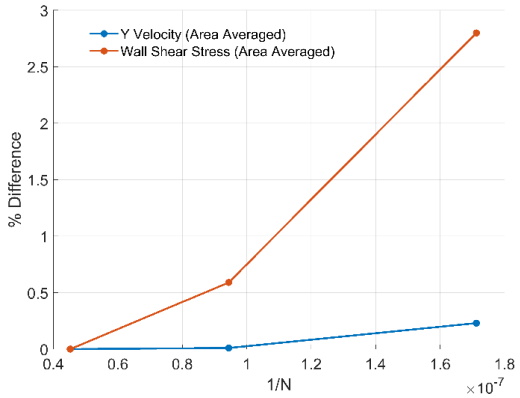

Figure 39 The convergence of wall shear stress and tangential velocity at the exit plane. The horizontal axis is the reciprocal of the total number of cells across both the fluid and solid domains.

6.1.3 Fluid Phase Description

An understanding of the fluid phase is required in order to analyse the motion of particles. Here the key aspects of the fluid phase are presented, and discussed in the context of particle motion.

The primary drivers of motion of the fluid through the bend are the axial pressure gradient and bend curvature. As seen in the 90 degree pipe flow, strong secondary flows, counter-rotating Dean vortices are induced as the fluid is accelerated around the bend. Figure 40a shows that the fluid initially accelerates towards the inner-wall, balancing the centripetal force it experiences. By 30 degrees around the bend, the Dean vortices are clearly present. The centre of rotation of the Dean

vortices varies throughout the sweep of the bend, initially the position is close to the upper and lower end-walls. While the vortices migrate toward the centreline slightly mid-way around the bend, they return to a similar position at the bend exit. Figure 41 shows the Dean vortices persist throughout the channel connecting the first and second bends: the vortices gradually move together to be approximately equidistant from the end walls and the centre of the passage. The second bend would induce identical but counter-rotating Dean vortices to the first bend, and, the resulting flow is the superposition of these potential fields. Figure 40b shows that this results in a more complex secondary motion. Figure 43 shows helicity in the passage. The generation of secondary corner cortices is clearly demonstrated. The primary Dean vortices from the first bend are observed to drift outwards towards the top and bottom walls in the transition passage between bends, but are strongly accelerated towards the centre of the passage when the counter rotating Dean vortices are induced by the second bend. These residual vortices are swept toward the middle of the outer bend and are clearly visible at the passage exit, forming additional flow feature unique to the second bend.

In addition to the steady pressure field, particles are affected by turbulence via turbophoresis. This is an effective force that results in the net movement of particles from regions of higher turbulence to lower turbulence. Differences in the unsteady flow are demonstrated in Figure 42 where the structure of turbulent kinetic energy is clearly different in the first and second bend. Whilst both show region of lower turbulence on the inner wall, in the first bend this is a unimodal and on the second bend this is bimodal. On the outer bend wall the region of higher turbulence is more concentrated on the second bend.

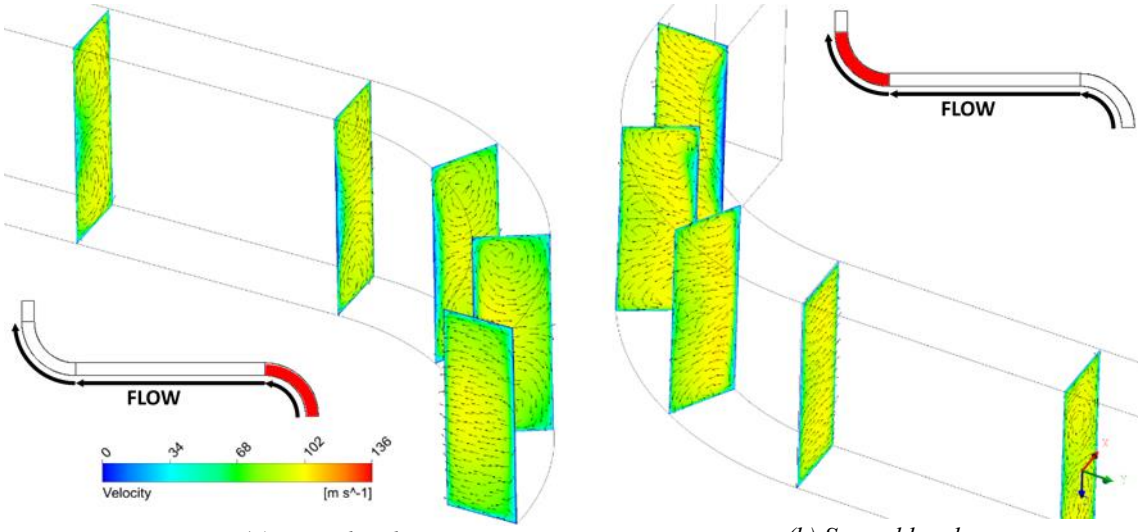

(a) First bend *(b) Second bend*

Figure 40 Contours of velocity around the bends in experiment 1. Vectors showing tangential projections of velocity. Flow into the page. Same colour scale applies to both figures.

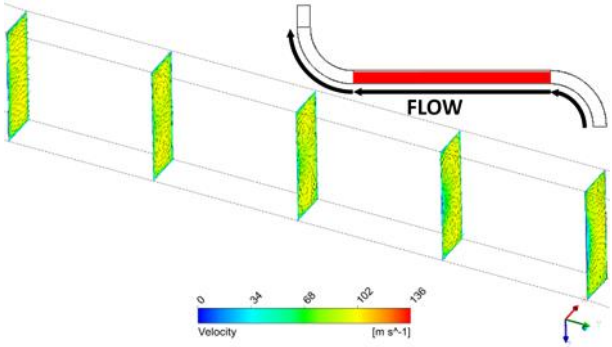

Figure 41 Contours of velocity in passage connecting the first and second bends in experiment 1. Vectors showing tangential projections of velocity. Flow from right to left.

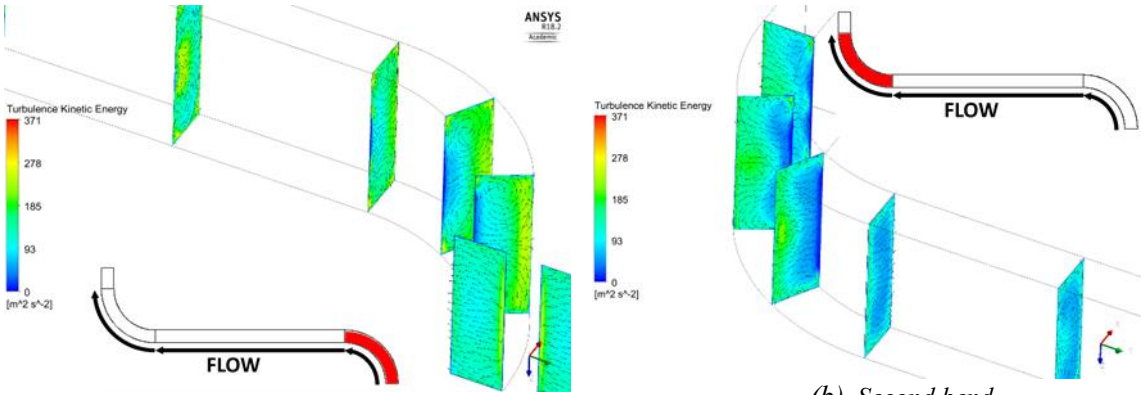

(a) First bend *(b) Second bend*

Figure 42 Contours of turbulent kinetic energy in in experiment 1. Vectors showing tangential projections of velocity.

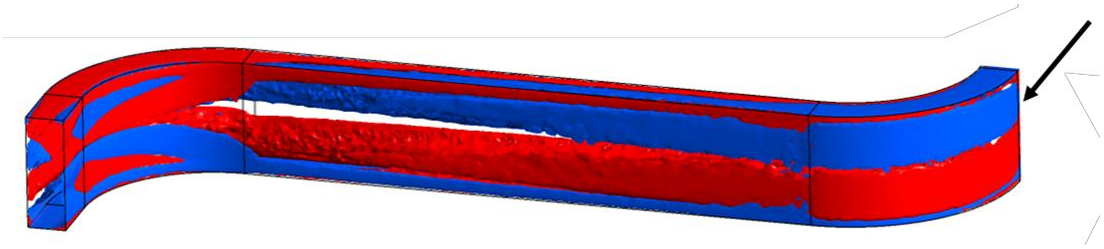

Figure 43 Isocontours of helicity, at +/-180000 ms^{-2}, in Experiment 1. Arrow shows flow direction.

Experiment 4 was conducted at a 33% higher flow rate, in the same geometry as experiment 1. There were no major changes in the flow structure induced by increasing the bulk flow velocity, Figure 44. On the first bend this is very similar, although the vortices stay close to the end-walls throughout. In the second bend, the vortices near the outer-wall and centre-line appear more coherent compared to experiment 1 (Figure 40b), especially early on in the bend (Figure 44b). This results in a more concentrated region of turbulent kinetic energy where the two vortices meet (Figure 45).

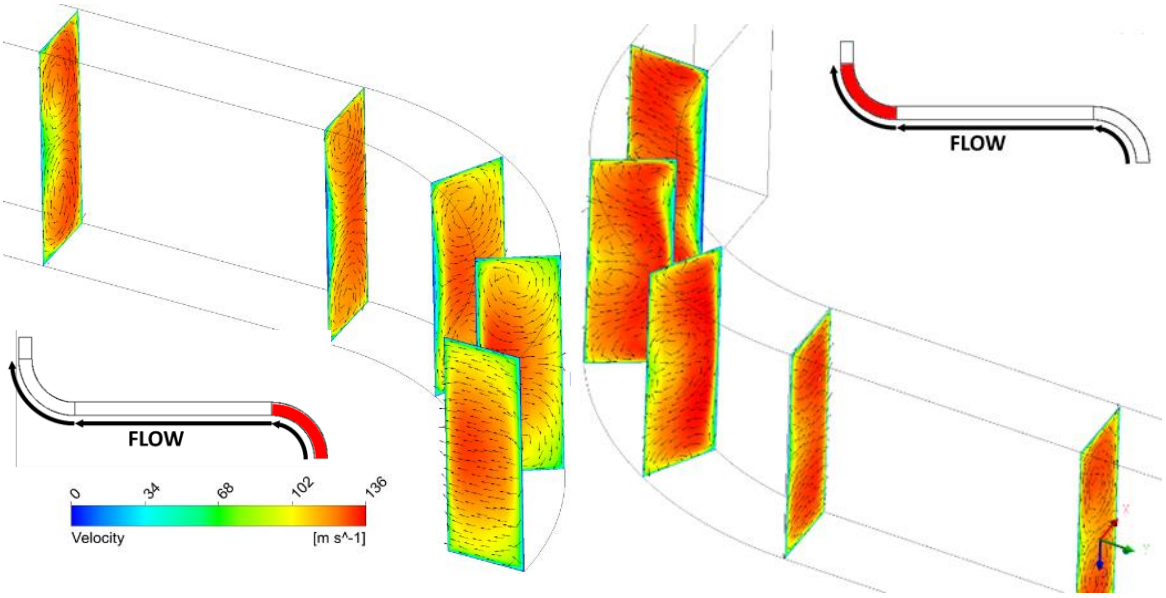

(b) Second bend

Figure 44 Contours of velocity around bends of in a simulation of experiment 4 (R_0 = 5, Re =4415, T_g= 882 K).

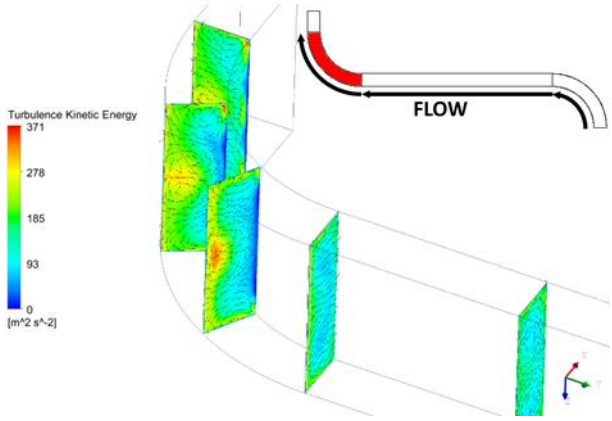

Figure 45 Contours of turbulent kinetic energy around the second bend of in a simulation of experiment 4 (R_0 = 5, Re =4415, T_g= 882 K)

As well as Reynolds number, the effect of ratio of curvature is investigated. This changes the strength of the Dean Vortices for a given average axial Reynolds number. Experiment 1 ($R_0 = 5$) has stronger vortices than experiment 2 ($R_0 = 10$). The effects of this are most notable looking at the second bend, with little difference observed on the first bend. Entering the second bend, the fluid maintains more of its vorticity, with evidence of the Dean vortices more apparent (Figure 46a). Secondly the Dean vortices resulting from the first bend are confined to a larger area than in the case of a tighter bend. Figure 46b shows that the turbulent kinetic energy is lower, and there is once again a higher concentration at the outer-wall at mid-height.

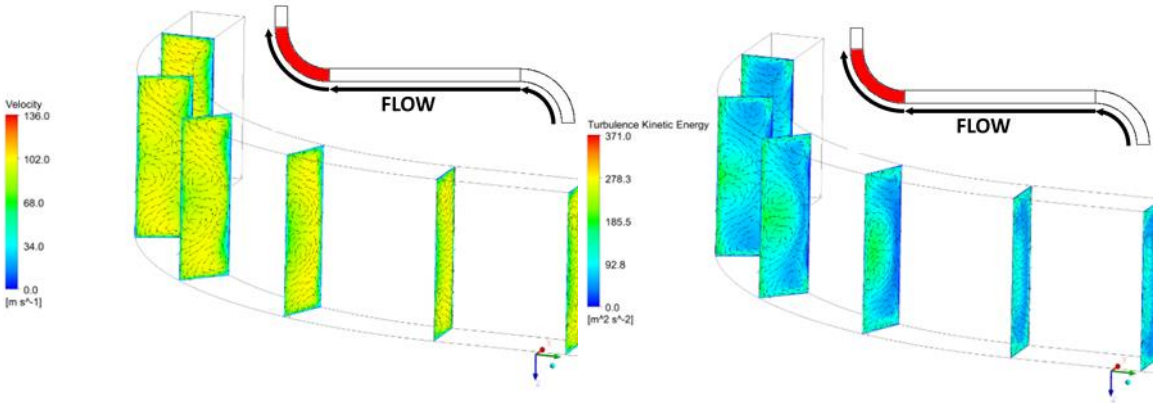

(a) Velocity *(b) Turbulent Kinetic Energy*

Figure 46 Second bend of in a simulation of experiment 2 (R_0 = 10, Re =3429, T_g= 833 K)

6.2 Discrete Phase Solution Set-Up

The particle trajectories are calculated using FLUENT's inbuilt particle tracking tools, for the steady Lagrangian element, with a user defined function (UDF) which implements the CRW (as described in Chapter 3), and an in-built model for thermophoresis [13]. The fluid domain (Figure 38) is

slightly asymmetric, and marginal differences in deposition were observed between the left and right S-bend passages. Thus, for computational efficiency, particle injection was limited to the uniform injection of particles into one leg of the flow domain at the point of flow bifurcation.

The development of a more robust high temperature bounce-stick model is the subject of further research at the OTI, and at present no reliable model was available for these flow conditions. To understand the range of results possible, tracking is therefore conducted both with all-stick and all-bounce conditions at the wall. It was found that during initial simulation the inlet region captured an unrealistic proportion of the particles when the all stick model was applied: this meant that insufficient particles continued into the main passage. To allow a meaningful distribution to be determined this region was assigned as an all bounce region and generated a realistic distribution of particles entering the first bend. To replicate the particle distribution of the Ultra-fine Arizona Road Dust used in experiments, a Rosin-Rammler distribution with 10 discrete particle diameters was used (Appendix C). The distribution has a minimum of 9.7×10^{-7} m, a maximum 2.2×10^{-5} m, and a median of 5.2×10^{-6} m. The heat capacity and thermal conductivity of this dust is not well reported, but the dust is primarily quartz for which data is available and were used here [130]. Material properties were set to ρ_{p} = 2650 kg/m^3 [133], c_p = 820 J/kg K, k_p = 1.85 W/m K [130].

A key premise of this thesis is that knowledge of spatially resolved deposition is critical to predict subsequent component performance. To allow this to be reliably predicted, the tracking has been conducted using the convergence criteria developed in chapter 4.3. These resulted in converged spatially resolved maps of deposition for comparison to experiment. The metric used to determine convergence is the normalised distance (D_2) reiterated in Equation 69, where M_1 and M_2 are 2D mass fraction distributions over the surface. In this M_2 is constructed by including additional particles injections (through a further repetition of injection from the same sites or using a higher density of particles on the injection plane). The normalised distance is reported at the highest number of particles injected/highest number of repeat injections. As a distribution of particle sizes was injected the spatially resolved mass fraction is compared, rather than the impact fraction. To illustrate this convergence test, and determine the number of injections required for all cases a

simulation of experiment 2 is considered. Here, a low flow rate and gentle curvature make the results most sensitive to turbophoresis compared to all other cases investigated. To ensure robust convergence, thermophoresis and gravity were switched off in this study to ensure maximum possible variation occurred because of turbophoresis. Thus the largest variation injection to injection should be observed in this case and hence an injection methodology sufficient for all cases presented here determined. The deposition on the bend walls can be discretised depending on the level of resolution required. In this case 15 degree arc-wise and 1.5mm high segments were used, creating a 6 by 6 grid over each surface. Figure 47a shows that at least ~1×10^6 particles are required per injection. Figure 47b shows that if a single repetition of such an injection is made, this ensures that enough particle trajectories are sampled to give a representative distribution. In both Figure 47a and Figure 47b the inside of the second bend requires the largest number of particles to reach a converged solution. This is due to the limited deposition that occurs on this face, and the importance of turbophoresis for this deposition to occur, and the limited remaining particles in the flow following deposition in the first bend.

$$D = \left(\frac{1}{2}\sum|M_1(x,y) - M_2(x,y)|\right) / \sum M_2(x,y) \qquad 69$$

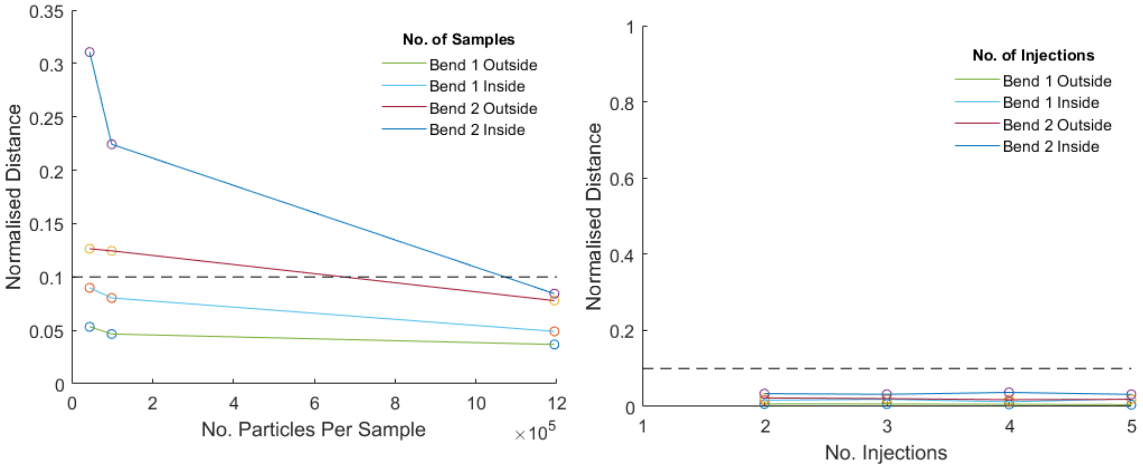

(a) Increasing the number of particles per sample (uniform spatial distribution, initially 2040 particles)

(b) Increasing the number of repeated sample injections whilst maintaining the same particle injection locations (uniform spatial distribution of 2040 particles).

Figure 47 The normalized distance between distributions of mass fraction. A critical value of 10% was chosen.

6.3 Results and Discussion

The numerical and experimental data of these test cases are compared. This is firstly done in the baseline case, with the effect of different forces and bounce-stick discussed. Whilst the use of a bounce-stick model would enable direct and quantitative comparison it also would introduce further uncertainty. Rather a qualitative comparison is made considering the impact locations, angles, and velocities. Trends noticed, from the baseline case, in the experimental data and associated hypothesis suggested in Section 4.2 are discussed using these numerical results.

6.3.1 Baseline Case

Experiment 1 displays most of the key features seen in all the hot deposition experiments conducted. The deposition, likely flow physics, and ability of the simulation to capture these are set our below.

In Figure 48, the experiemental deposition map of the outer wall of the first bend, shows distinct skewing of the depsoition towards the upper half of the wall. This is captured in bulk terms by the simulation, Figure 49b. The flow solution suggests that this is due to the distribution of particles entering the bend also being weighted towards the upper half of the passage (Figure 49a). A diverging passage was required upstream of the bend, to smoothly transition from the original inlet geometry to the cross section used in this study. This, appears responsible for this non-uniformity. The distribution is also found to be more strongly biased to the inside of the bend, Figure 49a, this is due to the bifurcation of the passage which was implemented to generate two simultaneous experiments at identical conditions.

6.3.1.1 First Bend

On the first bend, the experimental deposition is bimodal in form in the stream-wise direction, the first peak occurs at approximately -40 degrees, and is smaller and more defined than the second more wide spread region of high deposition at approximately +35 degrees, Figure 48. Without an accurate bounce-stick criterion the simulation results must be carefully considered. While a large range of particles impact the surface, those which arrive with low velocity and high angle (oblique) are most likely to stick. The all stick simulation results show that although there is

no apparent concentration of particles impacting at -40 degrees, Figure 49, a notably higher portion of these have a low velocity (<20 m/s, Figure 50) compared to the region from -20 to +20 degrees. These particles are most likely to stick despite their low impact angle (<10 degrees, Figure 53). The simulations predict a concentration of impacts, by mass fraction, at -10 degrees (Figure 49) but this is not seen in the experimental results. The all stick case, of course, identifies the particles' first impact, while the all bounce condition (*CoR* = 1) shows that these same particles would go on to impact again at the ~+40 degree with a high impact angle (~30 degrees, Figure 54). In reality, the particles would lose some energy (and there would be a distribution in energy lost) which correlates with experimental deposition occurring earlier and over a larger area.

Another experimental feature shows deposit along the bottom of the wall in the region between 0 and 40 degrees (Figure 48). This is attributed to the low impact velocities seen in Figure 50, and although these are glancing impacts, Figure 51 shows that even if these particle rebound they are confined to this region. The lack of deposition at a similar position on the top wall is likely an artifice of the experiment. The test rig must be separated in order to measure deposition and this results in loss of deposited material in this region, Section 4.2. The sharp corners between the sidewalls and end-walls result in small regions of recirculation, Figure 43, which these low velocity particles have insufficient inertia to exit.

Figure 52 shows that the impacts predicted using no turbophoresis model look quite different. There are no higher velocity impacts past 20 degrees, and there is clear patch of no particle impacts near the endwall.

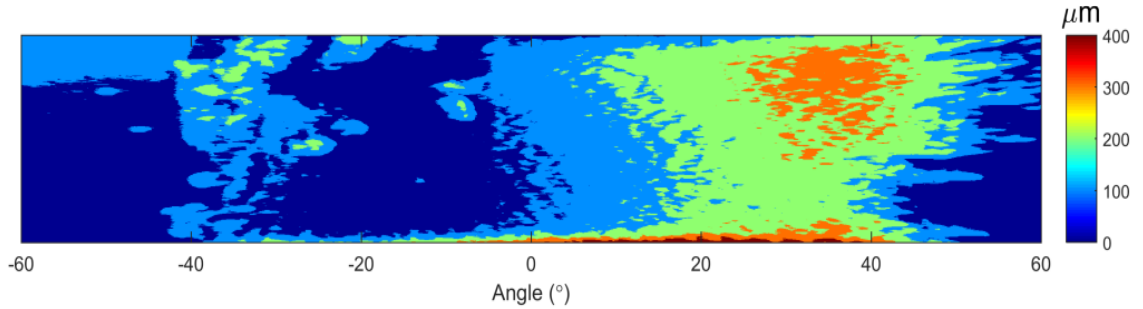

Figure 48 Deposition measured on the outside wall of the first bend after Experiment 1

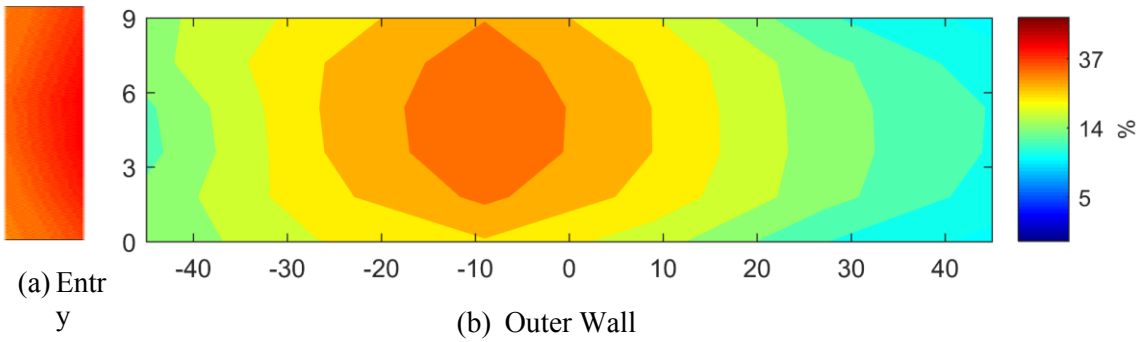

Figure 49 Mass fraction distribution, predicted by simulation with an all-stick boundary condition, on the outside wall of the first bend for Experiment 1.

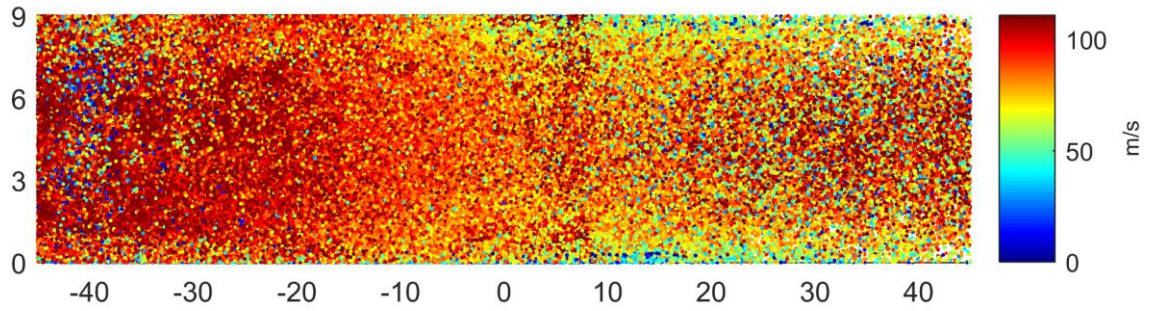

Figure 50 Impact velocities, predicted by simulation with an all stick boundary condition, on the outside wall of the first bend for Experiment 1. Colour bar up to 90th percentile of values.

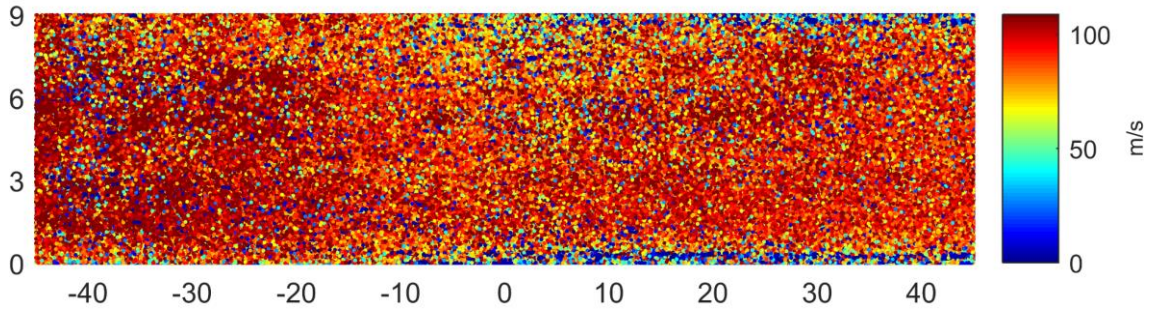

Figure 51 Impact velocities, predicted by simulation with an all bounce boundary condition, on the outside wall of the first bend for Experiment 1. Colour bar up to 90th percentile of values.

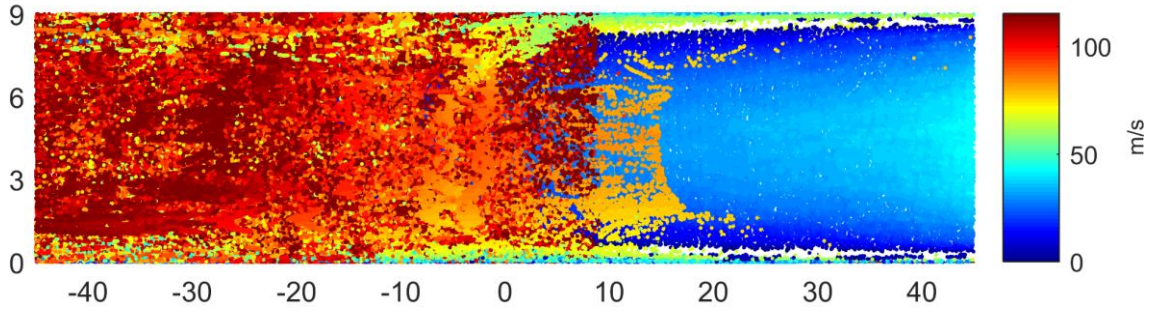

Figure 52 Impact velocities, predicted by a simulation with an all stick condition and no turbophoresis, on the outside wall of the first bend for Experiment 1. Colour bar up to 90th percentile of values.

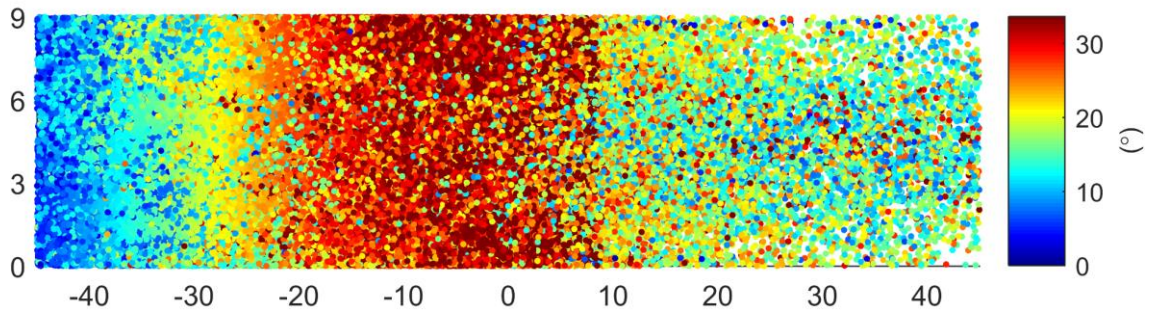

Figure 53 Impact angles, predicted by simulation with an all stick condition, on the outside wall of the first bend for Experiment 1. Colour bar up to 90th percentile of values.

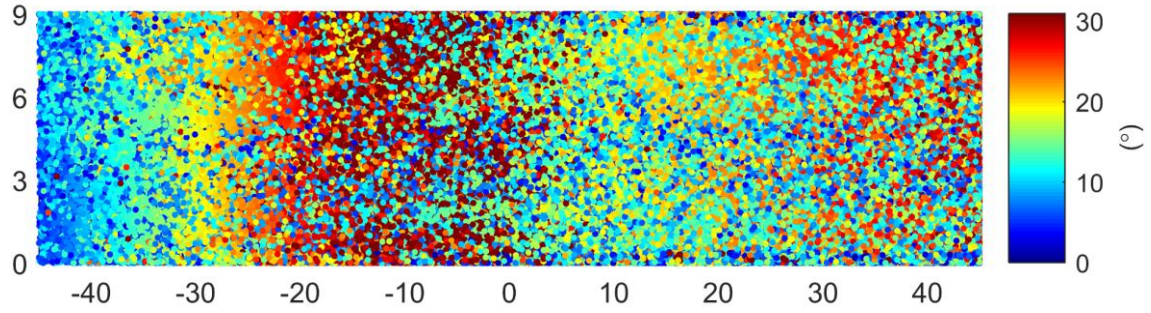

Figure 54 Impact angles, predicted by simulation with an all bounce condition, on the outside wall of the first bend for Experiment 1. Colour bar up to 90th percentile of values.

6.3.1.2 Second Bend

Deposition is higher on the lower half of the outer wall of the second bend (Figure 55). Nonetheless the shape of deposition is similar on the upper and lower walls. A near continuous streak occurs between 0 and 40 degrees in the stream wise direction, increasing in width in the stream wise direction up to 3 mm in each case. The all-stick simulations here show a very good match to the experimental pattern of deposition when the mass fraction is considered (Figure 56). These impacts are largely at angles above 15 degrees and of velocities faster than 75 m/s. When the all bounce condition is applied, many more particles arrive in the second bend. The additional impacts predicted by all bounce simulations (Figure 58), are seen to be more tangential and thus less likely to stick. Therefore, it seems that smaller particles, which are seen to impact during the all-stick simulation, stick on their first bounce to form the deposit seen in experiments.

The need and usefulness of an accurate turbophoresis model is made clear evaluation of two features of deposition predicted on the outer wall of the second bend.

The first trend supporting the need for accurate modelling of turbophoresis is introduced here for clarity, but best supported by the further two experiments. Experiment 1 showed deposition

at mid height of the passage, between 0-5 degrees. The all stick simulations (Figure 57) show a group particles impact at mid-height and ~0 degrees arc-wise, with low velocity. The all bounce simulations (Figure 58) show that these go on to make further impacts between 0 and 40 degrees arc-wise, at the same height. These subsequent impact also have low velocity (Figure 58), in reality sticking is likely to occur as particles continue to impact and lose energy. These initial impacts are not seen in the case where turbophoresis is not modelled. The high turbulence intensity caused by the Dean vortices colliding at the outer bend (Figure 42b), which then diminishes towards the wall, creates a gradient for particle to be transported by turbophoresis. Turbophoresis appears essential to capturing this deposition at mid-height.

Secondly, comparing all-stick simulations, with and without the CRW model. In all-stick simulations it is only the smaller particles which are able to follow the flow to the second bend, these are more affected by turbulent fluctuations. Without turbophoresis the particle impacts form a curved shape mirroring the extremities of the developing Dean vortices. There is an outline of very low speed impacts (<5 m/s), which one would expect to see in experiments but does not. Rather deposition is much more akin to that predicted by simulations that calculate turbophoresis.

Thermophoresis and gravity were seen to have no notable effects on simulation results. For gravity this is unsurprising, as the acceleration in the bend is substantially higher than the gravitational acceleration.

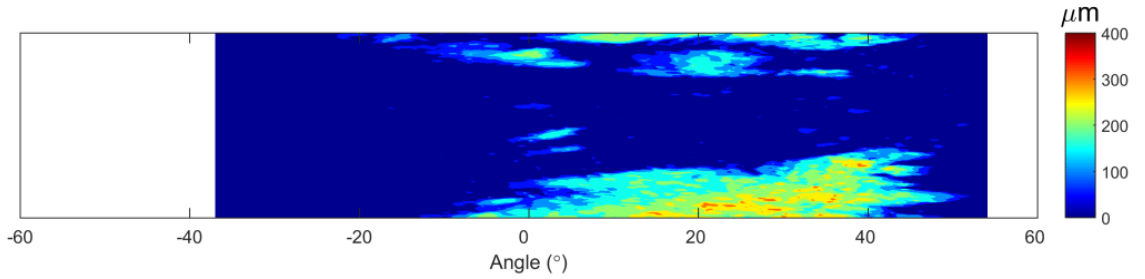

Figure 55 Deposition measured on the outside wall of the second bend after Experiment 1

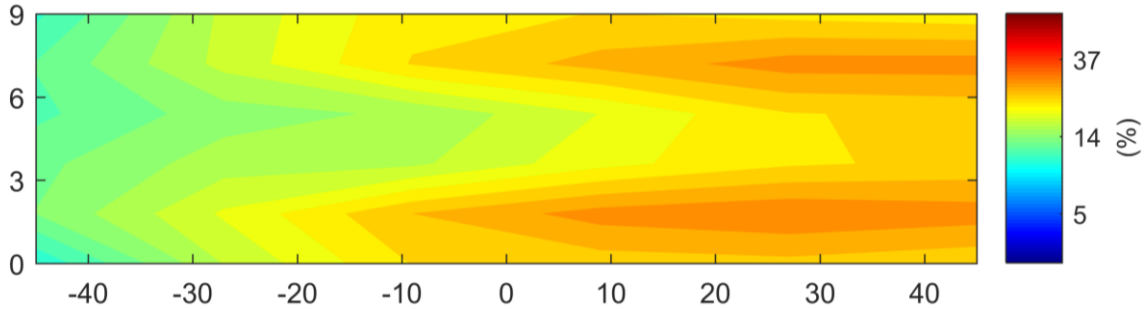

Figure 56 Mass fraction distribution, predicted by simulation with an all stick boundary condition, entering the second bend for Experiment 1.

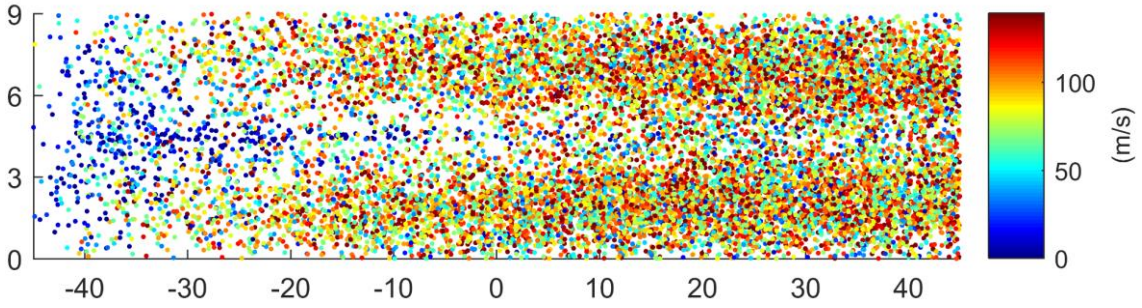

Figure 57 Impact velocities, predicted by simulation with an all stick boundary condition, on the outside wall of the second bend for Experiment 1. Colour bar up to 90th percentile of values.

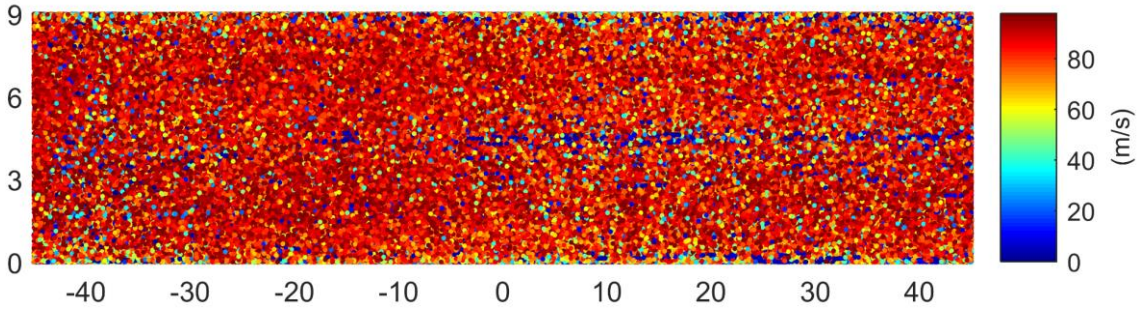

Figure 58 Impact velocities, predicted by simulation with an all bounce boundary condition, on the outside wall of the second bend for Experiment 1. Colour bar up to 90th percentile of values.

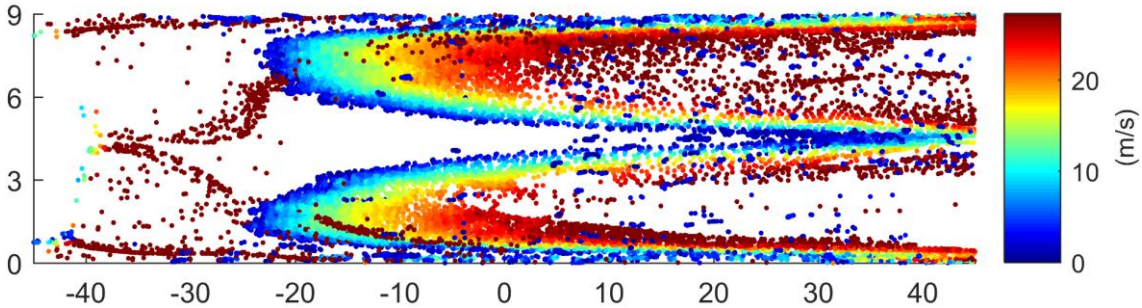

Figure 59 Impact velocities, predicted by simulation with an all stick boundary condition and no turbophoresis modelling, on the outside wall of the second bend for Experiment 1. Colour bar up to 90th percentile of values.

6.3.2 Ratio of Curvature

Experiment 2 was conducted at the same Reynolds number and temperatures as experiment 1 but with twice the ratio of curvature (Table 5). A number of trends in the location of deposition were identified during the analysis presented in Section 4.2. These trends are discussed here, with the numerical results used to test the physical hypothesis previously suggested.

The most apparent trend in experiments is that deposition is found further upstream, in a region from -20 to +20 degrees (Figure 60). This appears to be the result of higher impact angles (>20 degrees) occurring further upstream (Figure 62 compared with Figure 53). Similarly to the base case the deposit appears to take place after this initial contact, with simulations predicting a secondary region of high angle impacts further upstream than in the base case (Figure 63).

The second observation was that deposition is more even centred across the height of the passage as the bend was made gentler. It was initially suggested that this was due to a lack of impacts at the end-walls in tighter bends, or the impacts did occur but were more tangential as particles followed the Dean vortices. Figure 63 shows that the simulations predict a more centralised region of secondary, high angle, impacts compared to Figure 54 which appear to be responsible for the deposition.

Finally, a consistent patch of deposition at -40 degrees is formed in the experiments (Figure 60) with the simulations showing that it is likely low velocity impacts that enable this once again (Figure 64).

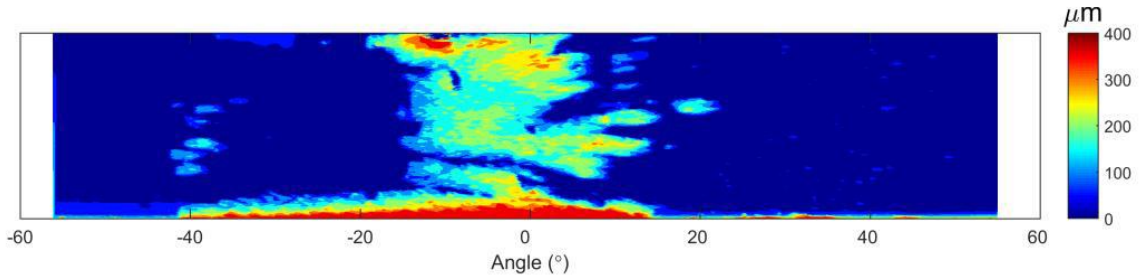

Figure 60 Deposition measured on the outside wall of the first bend after Experiment 2

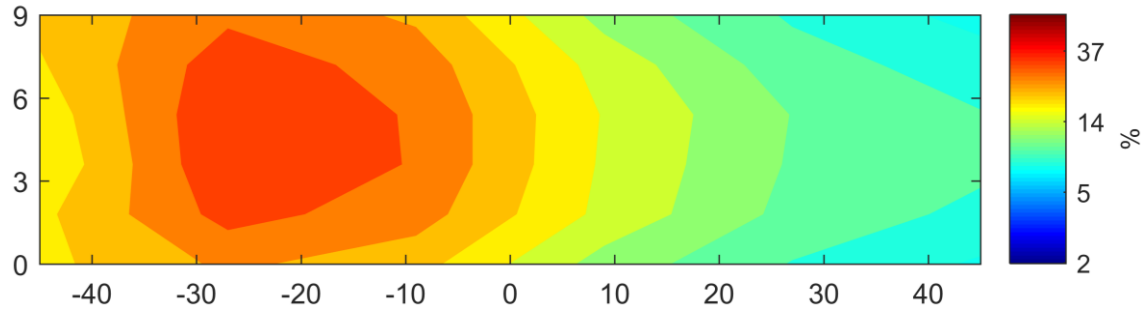

Figure 61 Mass fraction distribution, predicted by simulation with an all stick boundary condition , on the outside wall of the first bend for Experiment 2

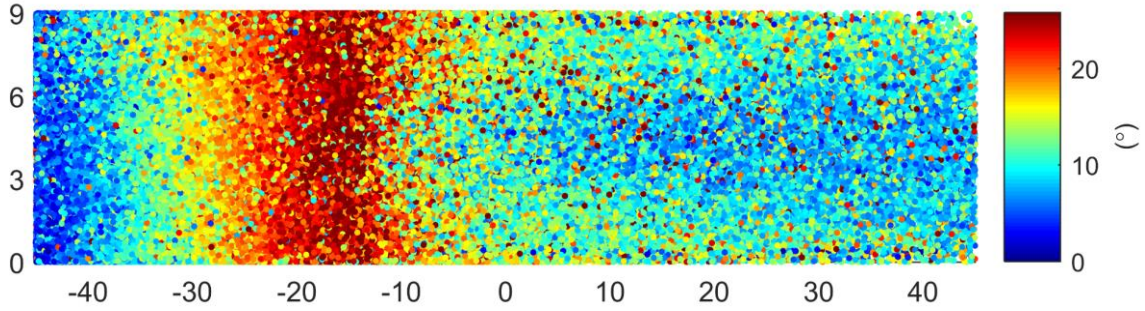

Figure 62 Impact angles, predicted by simulation with an all stick boundary condition, entering the first bend for Experiment 2. Colour bar up to 90th percentile of values.

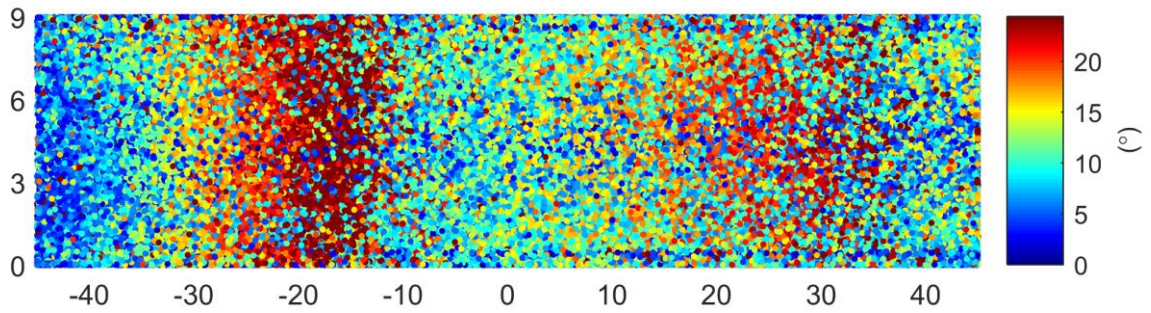

Figure 63 Impact angles, predicted by simulation with an all bounce boundary condition, entering the first bend for Experiment 2. Colour bar up to 90th percentile of values.

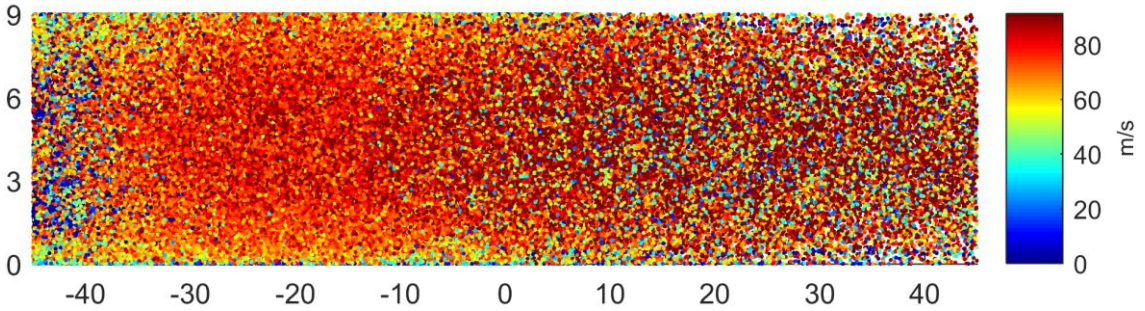

Figure 64 Impact velocity distribution, predicted by simulation with an all stick boundary condition, entering the second bend for Experiment 2. Colour bar up to 90th percentile of values.

On the second bend the main effect of an increased ratio of curvature was higher deposition at the mid height of the bend. As per the baseline case, this deposit appears to be the result of turbophoresis of particle impacts upstream at a shallow angle which then stay near the wall and continue to make low velocity and low angle impacts where deposit is seen. Figure 66 shows simulations predict these same impacts upstream, while Figure 67 and Figure 68 show the downstream impacts that likely result in deposition. As set out in Section 4.2 the Dean vortices are likely to have a comparatively larger effect compared to centrifugal forces for larger bend radii. Figure 46 shows that the Dean vortices which appear essential to this deposition are larger compared to the baseline case. Further, despite the peak in turbulent kinetic energy, at the outer wall where the newly formed vortices meet, being lower than the baseline case (Figure 45) this affect is more pronounced.

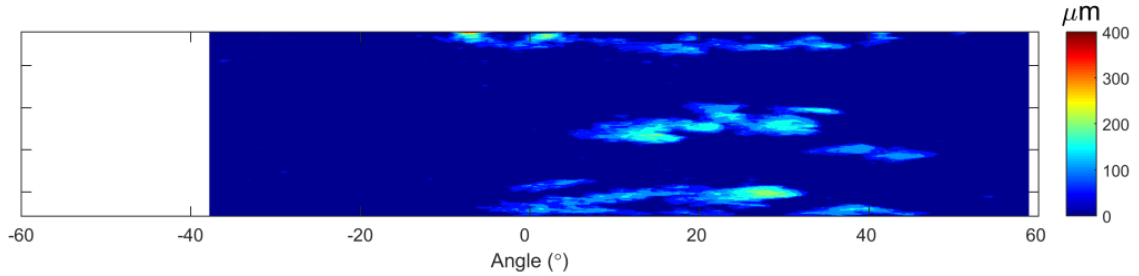

Figure 65 Deposition measured on the outside wall of the second bend after Experiment 2

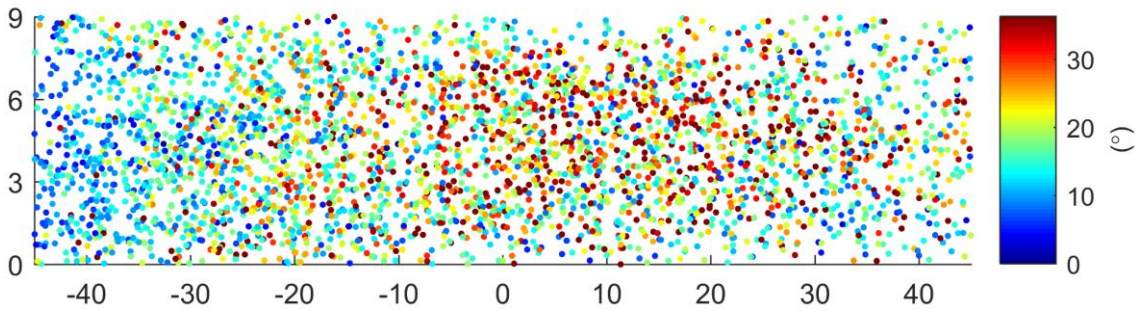

Figure 66 Impact angles, predicted by simulation with an all stick boundary condition, entering the second bend for Experiment 2. Colour bar up to 90th percentile of values.

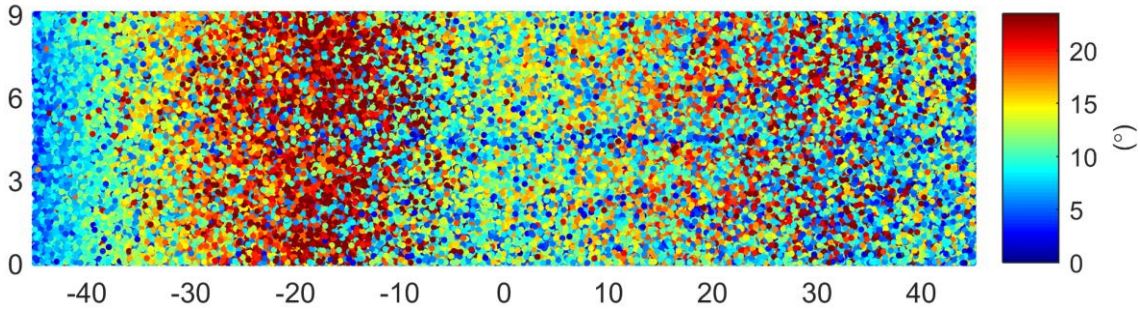

Figure 67 Impact angles, predicted by simulation with an all bounce boundary condition, entering the second bend for Experiment 2. Colour bar up to 90th percentile of values.

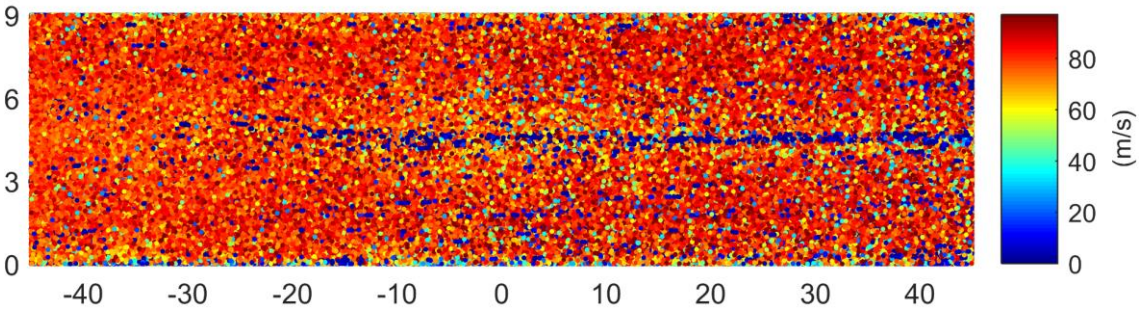

Figure 68 Impact velocities, predicted by simulation with an all bounce boundary condition, entering the second bend for Experiment 2. Colour bar up to 90th percentile of values.

6.3.3 Flow Rate

In the experimental campaign a dependence between surface temperature changes and changes in the flow field appeared critical to the trends in deposition fraction. Comparing Figure 69 and Figure 48 shows that little difference in the deposition was witnessed. Simulations of experiment 4 showed deposition behaviour remained similar to experiment 1, described in Section 6.3.1. The increased impact angles would act to increase deposition (Figure 70 and Figure 73), whilst the increased impact velocities would act to reduce deposition (Figure 71 and Figure 74). Further, the increase in flow speed at a constant temperature acts to reduce metal temperatures which would reduce sticking.

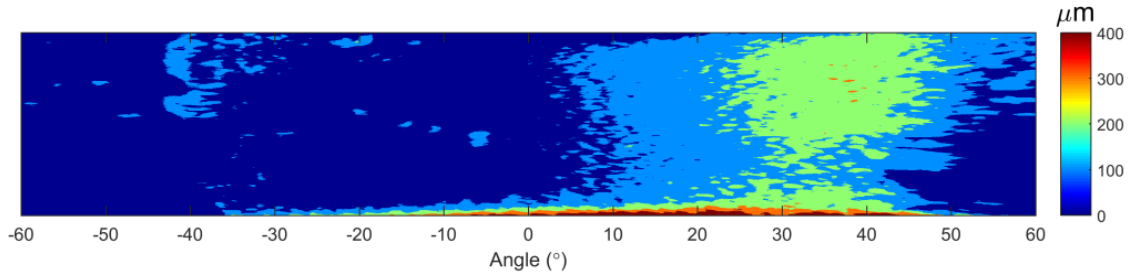

Figure 69 Deposition measured on the outside wall of the first bend after Experiment 4

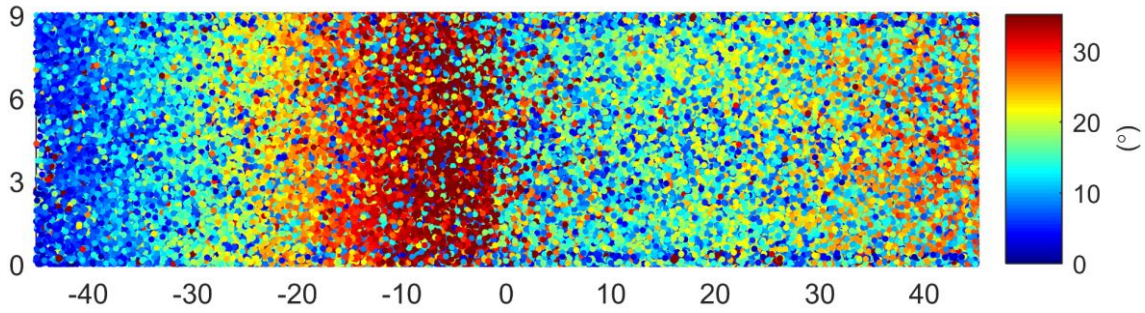

Figure 70 Impact angles, predicted by simulation with an all bounce boundary condition, on the first bend for Experiment 4. Colour bar up to 90th percentile of values.

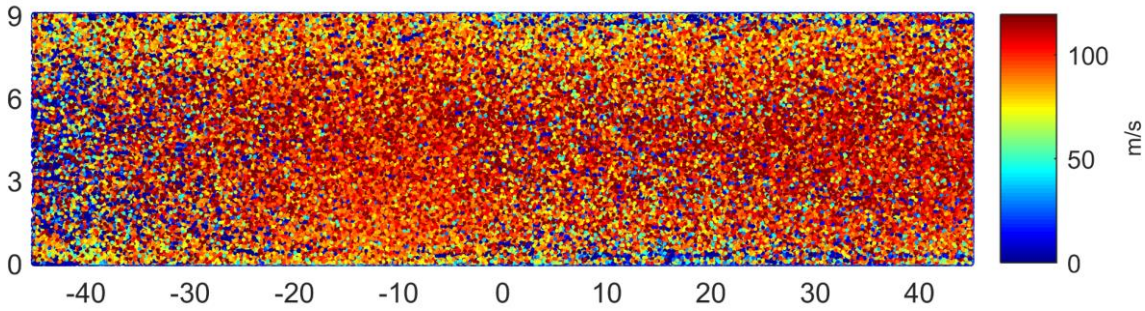

Figure 71 Impact velocities, predicted by simulation with an all bounce boundary condition, on the first bend for Experiment 4. Colour bar up to 90th percentile of values.

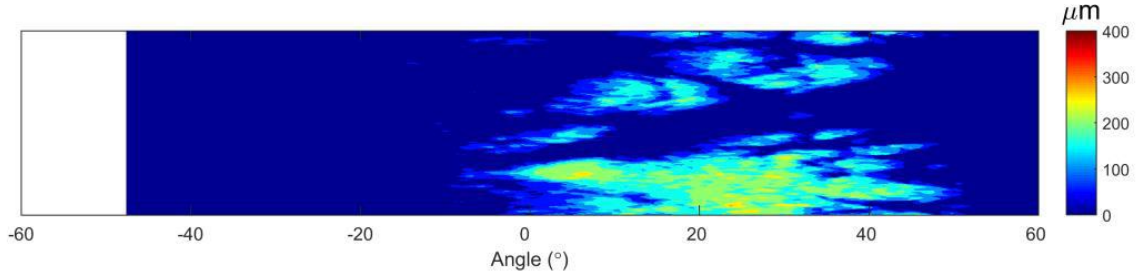

Figure 72 Deposition measured on the outside wall of the second bend after Experiment 4

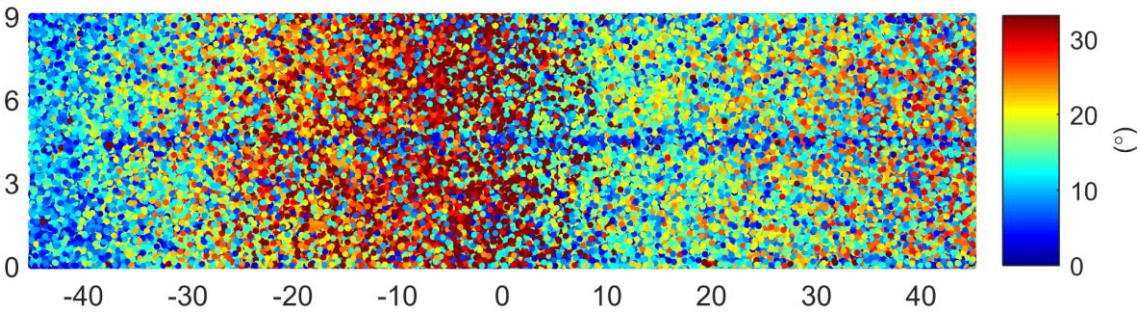

Figure 73 Impact angles, predicted by simulation with an all bounce boundary condition, on the second bend for Experiment 4

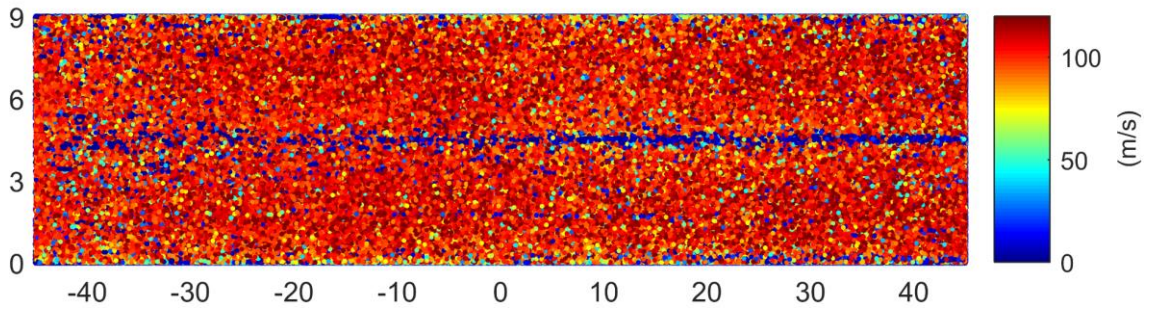

Figure 74 Impact velocities, predicted by simulation with an all bounce boundary condition, on the second bend for Experiment 4

6.4 Summary and Conclusions

Conjugate simulations of three experimental conditions were conducted using the RSM model previously deemed most appropriate for use with the proposed CRW model. The conditions were chosen to test the model's capability of capturing the effects of higher flow rates and more gentle curvature than the base case selected. The CRW model was run assuming all-stick and all-bounce conditions in order to bound the deposition.

The results showed that thermophoresis and gravity played little role in the impacts simulated. There is strong evidence that accurately capturing turbophoresis was critical to predicting some of the experimental deposit seen. In particular, that at mid-height of the second bend.

For future work, more care should be given to generating a uniform distribution of particles to the geometry. This could be done by maintaining a constant cross section for longer, and would remove the need for models to accurately model the inlet distribution.

It is clear from these simulations that an accurate bounce stick model is required to make a quantitative comparison. During experiments it was not clear if particles were impacting regions without deposit, but not sticking, or not impact these regions. Simulations make clear that particles are able to impact almost every location on the outer bends walls depending on their interaction with the wall. But the conditions, which were representative of a gas turbine, led to a high dependency on bouncing behaviour and this appear critical to accurately predicting the deposit seen.

7 Conclusions and Further Work

7.1 Conclusions

This thesis has developed a robust turbulent transport model with the capability of accurately tracking particles with sizes typically encountered in gas turbine secondary air systems. The model is tailored for implementation with computational fluid dynamic codes which can be used to characterise full engine performance during the engine design process. It is likely to have a major impact in allowing component design to avoid and or tolerate deposition and therefore reduce the cost of ownership of the jet engine. The most significant contribution is the development and implementation of a model for turbophoresis in gas turbine representative flows, alongside a robust toolset to ensure fully converged solutions can be achieved in a timely manner.

The problem of particle deposition is broad and requires accurate modelling of the particles, their transport, and mechanical interaction with the wall or pre-existing deposit. While all elements require further development, the work here is focused on particle transport as it is foundational to the problem. Only if particle arrival at a wall is accurately predicted could there be any hope that a bounce-stick model would be accurate or useful in predicting deposition build up. The tools developed are applicable to any particle shape, and other work has shown that the characterisation of particle shape is a second order effect for particle trajectory models.

Current computational capabilities make RANS solutions the most commonly applied, both for industrial design and academic investigations. The low particle dosing generally encountered means that full coupling of the fluid and particles is neither common nor necessary. Hence, Lagrangian solid phase particle tracking, applied to an independently converged fluid solution, can be used as the basis of a particle tracking simulation.

The Langevin equation is a stochastic differential equation that describes a change in velocity as the sum of a damping term and random fluctuations. Over the last 100 years it has been built upon to generate the continuous random walk (CRW) model, which is of interest to the current research. This calculates the fluctuating velocity that a particle experiences in the particle's Lagrangian frame of reference and enables turbulent dispersion to be accounted for. The revised

CRW was developed such that it could be applied to any geometry without limiting assumptions regarding the form of turbulence. To date, CRW models have required external statistics in order to achieve accurate results - even in simple flows such as channels and pipes. As these external statistics cannot be generated in a similar manner for realistic gas turbine flows, an approach independent of this was required. Previous modelling also required the segregation of the flow into regions of isotropic and anisotropic turbulence, and this was eliminated. The proposed model was demonstrated to be equally as accurate as existing models in a pipe flow, across the relevant range of particle sizes. Whilst there was equivalence based on non-dimensional deposition velocity in pipe flows, it was apparent that previous models predicted deposition distribution very differently in accelerating flows.

To demonstrate utility in the gas turbine environment, sets of spatially resolved data were generated for the deposition of particles at gas turbine relevant conditions. This required a new experimental rig to be designed, built, and run. Specifically, a rectangular cross-section double 90 degree bend passage was tested at HP turbine blade representative conditions. In order to present and record spatially resolved data a unique methodology was adopted, this is critical in enabling future use of this data set. Analysis of the results showed several trends, at both the integral and spatial levels. It was seen that metal temperature was as critical to deposition as the geometry and flow conditions, within the representative range tested. Further, it was clear that the comparative strength of the secondary and primary fluid motions had substantial effects on particle deposition.

In order to use the spatially resolved experimental data, as validation data, it was critical that the stochastic simulations were run rigorously. The CRW model applies a different series of instantaneous fluctuations for each particle injected, hence a repeated calculation would result in a different trajectory. Unsurprisingly the rate of integral and locally resolved deposition showed are substantially different. Measures of distance between local distributions were compared to generate a set rules to ensure converged particle surface distributions were calculated in a computationally efficient manner.

Finally, the proposed CRW model was applied, using the aforementioned methodology developed, to simulations of the experiment. A comparison showed that the CRW model was critical

in capturing multiple features of deposition seen in experiments. Further, trends that resulted from changing the flow rate and ratio of curvature were well supported by the simulations, though much of the interpretation of the outcome was necessarily qualitative.

7.2 Further Work

As noted in the abstract of this thesis, the problem of particle deposition may be segregated into the transport of particles to a surface followed by what occurs on arrival. A similar advance in the modelling of bounce-stick is required to reliably model deposition under gas-turbine engine realistic conditions. This is highlighted by the qualitative nature of validation possible from the well resolved deposition distributions in Chapter 6 of the thesis.

7.2.1 Short-term

7.2.1.1 Model

Nonetheless, there is great opportunity to further improve particle transport modelling, a multi-dimensional problem with high uncertainty associated with stochastic turbulent events.

- The CRW model developed was applied with gas turbine modelling applications in mind, and the minimum required resolution of flow features was identified to allow accurate particle tracking. This results in fine near wall resolution where the Lagrangian time scale is capped when $Y^+ \leq 5$. While this is reasonable, where this region corresponds to the laminar sub-layer, modification may be required in the case of accelerating and decelerating flows.
- A major focus of the thesis was to generate a fit for purpose turbulent transport model for RANS simulations. It is clear that in some regions of the jet engine a steady solution is not available, and the extension of the model's application to URANS simulations would confirm its value. Here it is clearly impossible to match the time stepping between the URANS and particle tracking processes (arguably the time-stepping in URANS is in many cases meaningless), so a method of ensemble averaging results from a periodic unsteady set of solutions would be required.

- A further extension of the work is to generalise its implementation outside the commercial solver environment used for this work. The necessary methodology is captured in the papers already published, and the model as coded in the ANSYS environment is not dependent on bespoke functions of the commercial solver.
- Within the wider research community, an agreed, and shared, set of basic validation cases which code outputs could be compared against would allow the usefulness of further code development to be easily assessed. Some of these test cases may be DNS or LES studies while others should be experimental validation cases with complementary geometries.

7.2.1.2 Experiment and Validation

A robust set of validation data sets for transport models is still unavailable for code developers. In particular data are lacking in flows with substantial acceleration, including rotation. A number of short term improvements could be made to the test rig used in this research, but it is likely that this would increase throughput of test cases, and at a high level show the vulnerability of particular designs to deposition, rather than allow codes to be rigorously validated.

As highlighted by the validation campaign started in this thesis, the uncoupling of transport and bounce stick in validation tests would be extremely useful. Test methods using liquid particles have previously been employed for this purpose, though previous workers have not reported full surface deposition distributions. In order to reduce the sources of uncertainty in the experiments conducted the use of mono-mineral and mono-disperse particles with well-known material properties, and variation with temperature, could be used. Other workers have employed particles to stick at low temperatures, which removes the need to understand the particle material's dependence on temperature. However, other material properties appear to still be insufficiently understood to provide data which can be used for validation in the existing open data. Further work is required to exploit such techniques for test cases where very highly resolved fluid solutions are well known and can be used as the basis for the underlying Lagrangian tracking.

Finally, in addition to the validation of particle arrival, the near wall particle velocity and impact angle would be beneficial for the simultaneous validation of bounce stick models, and promising work is being developed at Oxford to allow this.

7.2.2 Long-term

In addition to the developments of the CRW, it would be a clear next step to integrate this model with the many others required to cover the predominant physics of deposition. These include a bounce-stick model, an erosion model, and a shatter model. Numerical codes which incorporate mesh-morphing may then be employed to dynamically model particle build up. While each of these involve substantial development work and validation in their own right, incorporation of these models together would allow more comprehensive studies on deposition, and a true comparison to the data generated in representative experiments.

Initially, the integration of these models would enable existing engines and relevant damage mechanisms to be better understood. This couldn inform a generic, non-engine-to-engine specific, understanding of how damage can be mitigated, and when maintenance may be required. Building on this, the integrated model should be used to create a digital twin of the engine that drives the optimal maintenance of each specific engine within a fleet. A digital twin would likely compromise of low order models of non-critical components, and more detailed computationally intense simulations for high-risk components where spatially resolved deposition is important. The digital twin should then be coupled with real-world flight path and atmospheric data, to provide an understanding of each engine's condition. Using this digital twin an engine-to-engine specific maintenance schedule, that reduces cost-of-ownership and risk, can be pursued. This digital twin can also be used to inform engine-to-engine specific damage mitigation strategies.

Finally, the research should be developed to enable design tools such that individual components, and the whole engine, can be optimised to be more tolerant of particulate matter during the design phase.

8 Appendices

8.1 Appendix A: Derivation of the Continuous Random Walk

A full derivation of the governing equation for the CRW is provided below. The Stepwise derivation allows the mathematical manipulations to be easily understood, rather than providing a compact form for record.

The Langevin equation is a stochastic differential equation that describes the change in velocity (V) as the sum of a damping term and random fluctuations. ξ is a stochastic term, and α & λ are constants [90].

$$\frac{dV}{dt} = -\alpha V + \lambda\xi(t) \tag{70}$$

Solving the homogenous part of Equation 70 (ignoring the stochastic term) [90], substituting a time varying form back into the full equation, and setting the initial time to be 0, provides a general solution (Equation 80).

$$\begin{aligned} \int \frac{1}{V}\, dV &= \int -\alpha \, \mathrm{d}t \\ V &= e^{-\alpha t + C_1} \\ V &= C_2 e^{-\alpha t} \end{aligned} \tag{71}$$

To capture the time-varying behaviour, C_2 is now made to time dependent.

$$V(t) = C_2(t)e^{-\alpha t} \tag{72}$$

$$\frac{d}{dt}(C_2(t)e^{-\alpha t}) = -\alpha(C_2(t)e^{-\alpha t}) + \lambda\,\xi(t) \tag{73}$$

$$\frac{d}{dt}C_2(t) = e^{\alpha t}\lambda\xi(t) \tag{74}$$

$$C_2(t) = \int_0^t e^{\alpha\tau}\lambda\xi(\tau)\, d\tau \tag{75}$$

$$C_2(t) = C_0 + \int_{t_0}^t e^{\alpha\tau}\lambda\xi(\tau)\, \mathrm{d}\tau \tag{76}$$

$$V(t)e^{\alpha t} = V_0 e^{\alpha t_0} + \int_{t_0}^t e^{\alpha\tau}\lambda\xi(\tau)\, \mathrm{d}\tau \tag{77}$$

$$V(t) = V_0 e^{-\alpha(t-t_0)} + e^{-\alpha t} \int_{t_0}^{t} e^{\alpha\tau} \lambda \xi(\tau)\, \mathrm{d}\tau \quad 78$$

$$V(t) = V_0 e^{-\alpha(t-t_0)} + \lambda \int_{t_0}^{t} e^{\alpha(\tau-t)} \xi(\tau)\, \mathrm{d}\tau \quad 79$$

$$V(t) = V_0 e^{-\alpha t} + \lambda \int_{0}^{t} e^{\alpha(\tau-t)} \xi(\tau)\, \mathrm{d}\tau \quad 80$$

Taking the ensemble average the second term on the RHS goes to 0, so $\bar{V} = \bar{V} e^{-\alpha t}$. Hence, the equation for velocity can be reduced into an equation for velocity fluctuations (V').

$$V'(t) = V'_0 e^{-\alpha t} + \lambda \int_{0}^{t} e^{\alpha(\tau-t)} \xi(\tau)\, \mathrm{d}\tau \quad 81$$

In order to use this equation we must express the coefficients (α & λ) in terms of known turbulent quantities, the Reynolds stress (σ^2) and the Lagrangian time scale (τ_L, Equation 82) [90]. Comparing the definition of the Lagrangian timescale (Equation 82) with the covariance of Equation 81 (Equation 83) shows that α must be defined by Equation 84 [90].

$$\tau_\mathrm{L} = \frac{1}{\overline{V'^2(0)}} \int_0^\infty \overline{V'(0)V'(t)}\, \mathrm{d}t \quad 82$$

$$\overline{V'(0)V'(t)} = \overline{V'(0)} e^{-\alpha t} \quad 83$$

$$\alpha = \frac{1}{\tau_L} \quad 84$$

The variance of Equation 81 is given by Equation 85. As the random process is uncorrelated ($\overline{\xi(s)\xi(u)} = \delta(t-s)$) and $\sigma^2 = \overline{v'(t)^2} = \overline{v'(0)^2}$, this simplifies to Equation 86. Rearranging Equation 86 provides an expression for λ, Equation 87 [90].

$$\overline{V'(t)^2} = \overline{V'_0} e^{-2\alpha t} + \lambda^2 \iint_0^t e^{\alpha(s-t)}\, e^{\alpha(u-t)} \xi(s)\xi(u)\, \mathrm{d}s\, \mathrm{d}u \quad 85$$

$$\begin{aligned} \overline{v'(0)^2} &= \overline{V'_0} e^{-2\alpha t} + \lambda^2 \iint_0^t e^{2\alpha(s-t)}\, \mathrm{d}s \\ \sigma^2 &= \sigma^2 e^{-2\alpha t} + \frac{\lambda^2}{2\alpha}(1 - e^{-2\alpha t}) \end{aligned} \quad 86$$

$$\lambda = \sigma \sqrt{2/\tau_L} \quad 87$$

The Markov sequence is described by Equation 88. Comparing this with equation 80 defines a, and with equation 86 defines b. The Langevin equation can now be written as Equation 89 [90].

$$v_{t+dt} = av_t + b\sigma\xi(t) \quad 88$$

$$\frac{dV'}{dt} = -\frac{1}{\tau_L}V' + \sigma\sqrt{\frac{2}{\tau_L}}\xi(t) \quad 89$$

In order to use this equation for finite inertia particles the decoupling of the particle and fluid must be considered also. Mathematically, this is the total derivative of the change in fluid velocity along the path (Equation 90). The first term on the RHS is given by sampling the fluid velocity along the particle trajectory. The second is responsible for particle drift [91].

$$\overline{\frac{\mathrm{D}v_f}{\mathrm{D}t}} = \overline{\frac{\partial \overline{v_f}}{\partial \mathrm{t}}} + \overline{v_p \frac{\partial \mathrm{v}_\mathrm{f}'}{\partial \mathrm{x}}} \quad 90$$

An equation for the second term, as a function of fluid velocity and particle characteristics, can be derived using the particle equation of motion (Equations 91-93) [91].

$$m_\mathrm{p}\frac{\mathrm{d}u_\mathrm{p}}{\mathrm{d}t} = 3\pi\mu d_\mathrm{p}\left(U_\mathrm{f} - U_\mathrm{p}\right) + m_\mathrm{p}g \quad 91$$

$$\frac{\mathrm{d}u_\mathrm{p}}{\mathrm{d}t} = \frac{U_\mathrm{f} - U_\mathrm{p}}{\tau_\mathrm{p}} + g \quad 92$$

$$\frac{\mathrm{d}u_\mathrm{p}}{\mathrm{d}t} + \frac{u_\mathrm{p}}{\tau_\mathrm{p}} = \frac{u'_\mathrm{f}}{\tau_\mathrm{p}} + \frac{\overline{u}_\mathrm{f}}{\tau_\mathrm{p}} + g \quad 93$$

The particle's equation of motion can be solved using Laplace transforms (Equation 95), and multiplying the result by $\partial \mathrm{u}_\mathrm{f}'(t)/\partial \mathrm{x}$, and time-averaging (Equation 96). Assuming that the turbulence is locally homogenous then the last time-averaged term in Equation 96 can be written as per Equation 97. Integrating Equation 96 provides the drift correction, Equation 98 [91].

$$u_\mathrm{p}(s)\left(s + \frac{1}{\tau_\mathrm{p}}\right) = u_\mathrm{p}(0) + \frac{1}{\tau_\mathrm{p}}u_\mathrm{f}'(s) + \frac{1}{s}\left(\frac{\overline{u}_\mathrm{f}}{\tau_\mathrm{p}} + g\right) \quad 94$$

$$u_{\mathrm{p}}(t) = u_{\mathrm{p}}(0)\exp\left(-\frac{t}{\tau_{\mathrm{p}}}\right) + \frac{1}{\tau_{\mathrm{p}}}\int_0^t exp\left(\frac{r-t}{\tau_{\mathrm{p}}}\right)u_{\mathrm{f}}'(r)\,\mathrm{d}r + (\bar{u}_{\mathrm{f}} + \tau_{\mathrm{p}}g)\left[1 - exp\left(-\frac{t}{\tau_{\mathrm{p}}}\right)\right] \quad 95$$

$$\overline{u_{\mathrm{p}}(t)\frac{\partial \mathrm{u}_{\mathrm{f}}'(t)}{\partial \mathrm{x}}} = \overline{u_{\mathrm{p}}(0)\frac{\partial \mathrm{u}_{\mathrm{f}}'(t)}{\partial \mathrm{x}}}\exp\left(-\frac{1}{\tau_{\mathrm{p}}}\right) + \frac{1}{\tau_{\mathrm{p}}}\int_0^t exp\left(\frac{r-t}{\tau_{\mathrm{p}}}\right)\overline{u_{\mathrm{f}}(r)\frac{\partial \mathrm{u}_{\mathrm{f}}'(t)}{\partial \mathrm{x}}}\,\mathrm{d}r \quad 96$$

$$\overline{u_{\mathrm{f}}(s)\frac{\partial \mathrm{u}_{\mathrm{f}}'(t)}{\partial \mathrm{x}}}\,\mathrm{d}r = \overline{u_{\mathrm{f}}(t)\frac{\partial \mathrm{u}_{\mathrm{f}}'(t)}{\partial \mathrm{x}}}\,exp\left(\frac{s-t}{\tau_{\mathrm{L}}}\right) \quad 97$$

$$\overline{u_{\mathrm{p}}\frac{\partial \mathrm{u}_{\mathrm{f}}'}{\partial \mathrm{x}}} = \overline{u_{\mathrm{f}}\frac{\partial \mathrm{u}_{\mathrm{f}}'}{\partial \mathrm{x}}}\,\frac{1}{1+\mathrm{Stk}} \quad 98$$

Combining Equations 89 and 98 given the continuous random walk equation, using velocity as the transported variable (Equation 99). Similar analysis to the above has been completed to derive the normalized continuous random walk (Equation 100).

$$\frac{\mathrm{d}V'}{\mathrm{d}t} = -\frac{1}{\tau_{\mathrm{L}}}V' + \sigma\sqrt{\frac{2}{\tau_{\mathrm{L}}}}\xi(t) + \overline{u'_{\mathrm{f}}\frac{\partial \mathrm{u}_{\mathrm{f}}'}{\partial \mathrm{x}}}\,\frac{1}{1+\mathrm{Stk}} \quad 99$$

$$\frac{\mathrm{d}(V'/\sigma)}{\mathrm{d}t} = -\frac{1}{\tau_{\mathrm{L}}}\left(\frac{V'}{\sigma}\right) + \sqrt{\frac{2}{\tau_{\mathrm{L}}}}\xi(t) + \overline{u'_{\mathrm{f}}\frac{\partial(\mathrm{u}_{\mathrm{f}}'/\sigma)}{\partial \mathrm{x}}}\,\frac{1}{1+\mathrm{Stk}} \quad 100$$

The drift correction term here can be expressed in measurable fluid statistics assuming that cross terms can be ignored and using the chain rule, Equation 101 [19].

$$\overline{u'_{\mathrm{f},\iota}\frac{\partial(\mathrm{u}_{\mathrm{f},J}'/\sigma)}{\partial \mathrm{x}}} = \overline{\frac{\partial(\mathrm{u}_{\mathrm{f,J}}'\mathrm{u}_{\mathrm{f},J}'/\sigma)}{\partial \mathrm{x}}} = \frac{\partial \sigma}{\partial \mathrm{x}} = \overline{\frac{1}{2\sigma}\frac{\partial \sigma^2}{\partial \mathrm{x}}} \quad 101$$

Integrating Equation 100 , to solve for the normalized fluctuating velocity [94].

$$\frac{V'_{t+\Delta t}}{\sigma_{t+\Delta t}} = \left(\frac{V'_t}{\sigma_t}\right)\exp\left(-\frac{\Delta t}{\tau_{\mathrm{L}}}\right) + \xi\sqrt{1 - \exp\left(\frac{-2\Delta t}{\tau_{\mathrm{L}}}\right)} + \frac{1}{2\sigma_t}\frac{\partial \sigma_t^2}{\partial \mathrm{x}}\frac{1}{1+\mathrm{Stk}}\Delta t \quad 102$$

8.2 Appendix B: Experimental Facility

8.2.1 Orifice Plates

ISO 5167:2003 covers the design and operation of orifice plates between 50 and 100 millimetres. The natural pipe size to use at the exit was 3/4" (19.05 mm) so calibrated orifice plates were required, this calibration also negated any concerns raised by there being a bend upstream of the orifice plates. A 12 mm sharp-edged orifice (β = 0.63), with 45 degree chamfers, was used with pressure and temperature measurements one diameter upstream and a pressure measurement half a diameter downstream. There were twenty diameters and ten diameters lengths of straight pipe before and after the orifices respectively. The discharge coefficient is calculated using Equation 103.

$$C_{\text{discharge}} = \frac{q_{\text{m}}\sqrt{1-\beta^4}}{\epsilon\sqrt{2\rho_{\text{in}}\Delta p}} \frac{4}{\pi d_{\text{orifice}}^2} \qquad 103$$

During the operation of the rig the maximum dilution flow is fed (1000 SLPM) into both exits, hence this is the minimum mass flow expected through the orifices. In Figure 75 the cold runs are done at ambient conditions, and the hot tests are done with the largest flow rate of hot gas we can expect (100 SLPM) at 300 K (the highest the filters could safely support at this flow rate). Figure 75 shows that the orifices are not dependent on temperature of the gas or momentum ratio of exit and dilution flow. Further, although there is variation between the orifices their respective discharge coefficients can be considered constant over the operating range. Orifices 1 and 2 had discharge coefficient (C_{d}) of 0.832 and 0.870 respectively.

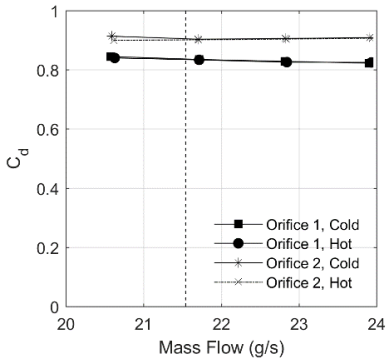

Figure 75 Discharge coefficient of the orifice plates used. Sensitivity to mass flow rate and temperature were investigated.

8.2.2 Packing density calibration

In order to know the mass entering the system two approaches were trialled: calibration of the packing density and transmission efficiency; and weighing each part along the particle laden gas path.

Particles are delivered using the Palas RB1000 IGD, in which a piston packed with powder is fed towards a rotating brush which has air flowing over it. The uncertainty of both the packed powder and delivered mass was investigated using Ultrafine A1 Arizona Road Dust, which is used for experiments. To calculate the packed density the piston was filled to 30mm and incrementally emptied. Figure 76 shows the variation across the filled piston. The quoted bulk density of this dust is 500 kg/m^3, a packed density of 969 (±56.9) kg/m^3 was calculated. The uncertainty in dosage delivered by the machine is also investigated, with a dependency on the pipe work length found. A 62 mm long pipe with a mean delivery of 73.55% (± 5.3) was used.

When this approach was compared with that of weighing each part along the particle-laden gas path it was found to be unfavourable. For the analysis carried out in the paper calculated the percentage deposited using the latter approach.

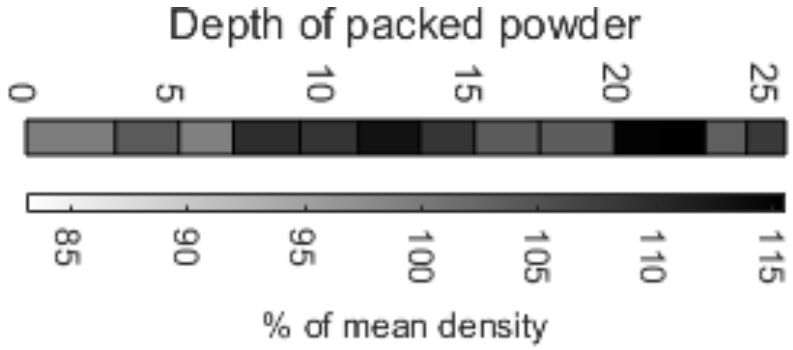

Figure 76 Variation of packed powder density in a sample piston. The ultrafine ARD had a packed density of 969 (±56.9) kg/m^3.

8.2.3 Experimental Method

For each experiment the same experimental procedure was followed, starting from fully disassembled and cleaned parts. This experiment took 6 hours end-to-end, excluding the cooling down phase which occurred overnight, after this, post processing took approximately 2 hours per specimen.

Step	Description	Time
1	Pack the dust delivery piston, to be inserted into the Palas RBG1000. Incrementally fill the powder into the piston, in increments of ~1 mm. Pack the powder down and then ensure the piston moves freely. In the case that the piston becomes stuck it was found best to restart the whole process, this would result from over-packing. Repeat until the piston is fully filled and insert into the particle dispenser.	15 minutes
2	Connect the air supply to the particle dispenser and dispense 5mm of height to ensure the internal brush is loaded and dust is being dispensed consistently.	5 minutes
3	Assemble the full gas-path and cover the oven using custom front plates	15 minutes
4	Turn on gas supply and use mass flow controllers (controlled via LabView VI) to set desired flow rates. Ensure the dilution flow is sufficient to dilute the hot gas below their maximum operating temperature (70°C). Ensure that a sufficient quantity of gas is flowing through the heater to prevent element overheating.	5 minutes
5	Switch on power to the oven and heater. Turn on the oven and air heater, setting the thermostats to maximum safe working temperatures.	5 minutes
6	Once metal is at above target temperature, reduce both oven and gas heater thermostats to the desired experimental conditions.	3 hours
7	Wait ten minutes at desired steady-state conditions	10 minutes
8	Begin the test by setting the piston speed correctly	10 minutes
9	Stop the piston once the desired amount of dust has been dispensed. Turn off the oven and gas heater, then turn off the gas.	5 minutes
10	Allow the test piece to cool down, then dismantle the gas path.	Overnight
11	Weigh each component before and after the test. Use the Alicona InfiniteFocus machine to measure the spatial deposition along both side-walls where is it visible to the naked eye. Take desired photos.	2 hours
12	Wash the test pieces using compressed air and deionised water.	30 minutes

8.3 Appendix C: Validation of Size Distribution used for Numerical Simulation of Experiments

In order to replicate the range of particles seen in ARD dust, used in experiments, a Rosin-Rammler distribution was used, Equation 104. Definition of this distribution requires a minimum (9.7×10^{-7} m), maximum (2.2×10^{-5} m), and median (5.2×10^{-6} m) particle size. In addition to this a spread parameter must be defined, it was found a spread parameter of 1.83 gave the best fit. Ten discrete particles were used for the simulations. Figure 77 shows a comparison of true distribution and that created using the Rosin-Rammler distribution.

$$MF = 1 - \exp\left(-(d/\bar{d})^{\beta}\right) \qquad 104$$

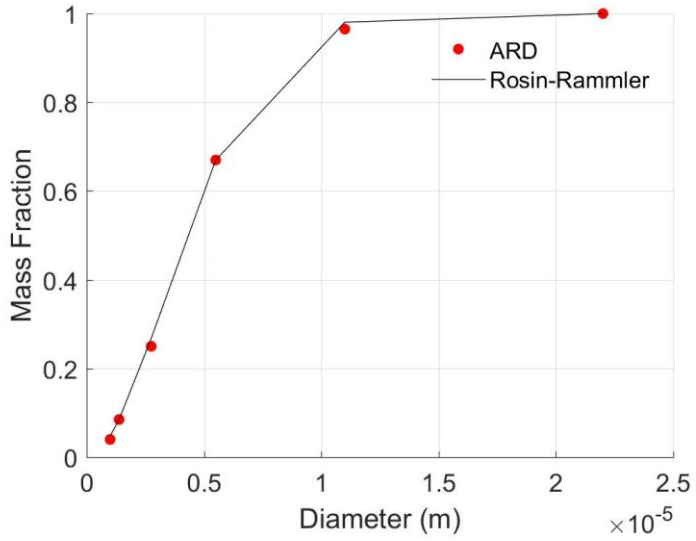

Figure 77 Comparison of the cumulative mass fraction distribution used in CFD simulations of the experiments (line) to the specified distribution on material data sheet from manufacturer (dots) [133] .

9 References

[1] A. H. Epstein, “Aeropropulsion for commercial aviation in the twenty-first century and research directions needed,” *AIAA J.*, vol. 52, no. 5, pp. 901–911, 2014 DOI:10.2514/1.J052713.

[2] National Academies of Sciences Engineering and Medicine, *Commercial Aircraft Propulsion and Energy Systems Research: Reducing Global Carbon Emissions*. Washington, DC: The National Academies Press, 2016 DOI:10.17226/23490.

[3] “GEnx Datasheet.” GE Aviation, pp. 1–2, 2004.

[4] R. Reed, *The Superalloys Fundamentals and Applications*. Cambridge: Cambridge University Press, 2006.

[5] B. Lakshminarayana, *Fluid Dynamics and Heat Transfer of Turbomachinery*, 1st ed. Wiley-Interscience, 1996.

[6] W. S. S. Walsh, K. A. A. Thole, and C. Joe, “Effects of Sand Ingestion on the Blockage of Film-Cooling Holes,” *Vol. 3 Heat Transf. Parts A B*, vol. 2006, pp. 81–90, 2006 DOI:10.1115/GT2006-90067.

[7] J. M. Delimont, W. F. Ng, S. V Ekkad, D. K. Tafti, T. Lowe, and G. R. Pickrell, “Experimental Investigation of Temperature Effects on Microparticle Sand Rebound Characteristics at Gas Turbine Representative Conditions,” p. 186, 2014.

[8] M. Darecki *et al.*, “Flightpath 2050 Europe’s vision for aviation: Report of the High Level Group on Aviation Research.,” EU, 2011, http://ec.europa.eu/transport/modes/air/doc/flightpath2050.pdf DOI:10.2777/50266.

[9] R. J. Clarkson, E. J. E. Majewicz, and P. Mack, “A re-evaluation of the 2010 quantitative understanding of the effects volcanic ash has on gas turbine engines,” *Proc. Inst. Mech. Eng. Part G J. Aerosp. Eng.*, vol. 230, no. 12, pp. 2274–2291, 2016 DOI:10.1177/0954410015623372.

[10] N. Bojdo, A. Filippone, B. Parkes, and R. Clarkson, “Aircraft engine dust ingestion

following sand storms," *Aerosp. Sci. Technol.*, vol. 106, p. 106072, 2020 DOI:10.1016/j.ast.2020.106072.

[11] R. Clarkson and H. Simpson, "Maximising Airspace Use During Volcanic Eruptions : Matching Engine Durability against Ash Cloud Occurrence (STO-MP-AVT-272)," NATO, 2017, https://www.wmo.int/aemp/sites/default/files/Matching_Engine_Durability_Against_Ash_Cloud_Occurrence_Rolls_Royce.pdf.

[12] G. Shepherd, U. K. E. Terradellas, A. Baklanov, S. N. W. A. Sprigg, and A. A.-D. A. D. Boloorani, *Global Assessment of Sand and Dust Storms*. 2016.

[13] P. Forsyth, "High Temperature Particle Deposition with Gas Turbine Applications," DPhil Thesis, University of Oxford, 2017.

[14] B. Reed, "Under The Ash Cloud," *Aerospace International*, 2011.

[15] S. Nathan, "Rolls-Royce explains problem with Trent 1000," *The Engineer*, 2019. [Online]. Available: https://www.theengineer.co.uk/rolls-royce-problems-trent-1000/.

[16] J. Kim, M. G. Dunn, A. J. Baran, D. P. Wade, and E. L. Tremba, "Deposition of Volcanic Materials in the Hot Sections of Two Gas Turbine Engines," *J. Eng. Gas Turbines Power*, vol. 115, no. 3, p. 641, Jul. 1993 DOI:10.1115/1.2906754.

[17] H. Tang *et al.*, "Effect of Ingress on Flow and Heat Transfer Upstream and Downstream of a Rotating Turbine Disc," *Aerospace*, vol. 6, no. 5, 2019 DOI:10.3390/aerospace6050049.

[18] Y. Il Kim and S. J. Song, "Unsteady measurement of core penetration flow caused by rotating geometric non-axisymmetry in a turbine rotor-stator disc cavity," *Exp. Therm. Fluid Sci.*, vol. 107, no. March, pp. 118–129, 2019 DOI:https://doi.org/10.1016/j.expthermflusci.2019.05.017.

[19] A. Dehbi, "Turbulent Particle Dispersion in Arbitrary Wall-bounded Geometries: A coupled CFD-Langevin-equation based Approach," *Int. J. Multiph. Flow*, vol. 34, no. 9, pp. 819–828, Sep. 2008 DOI:10.1016/J.IJMULTIPHASEFLOW.2008.03.001.

[20] J. P. Engelbrecht and E. Derbyshire, "Airborne Mineral Dust," *Elements*, vol. 6, no. 4, pp. 241–246, 2010 DOI:10.2113/gselements.6.4.241.

[21] R. Gieré and X. Querol, “Solid Particulate Matter in the Atmosphere,” *Elements*, vol. 6, no. 4, pp. 215–222, 2010 DOI:10.2113/gselements.6.4.215.

[22] R. Clarkson, “Characterisation of Atmospheric Sand and Dust, Including Engine Test Options (Rolls-Royce internal presentation),” 2017.

[23] G. Y. Lai, “Hot Corrosion in Gas Turbines,” in *High Temperature Corrosion and Materials Application*, ASME International, 2007, pp. 249–258 DOI:10.1361/hcma2007p249.

[24] B. Langmann, “Volcanic Ash versus Mineral Dust: Atmospheric Processing and Environmental and Climate Impacts,” *ISRN Atmos. Sci.*, pp. 1–17, 2013 DOI:10.1155/2013/245076.

[25] C. Chou *et al.*, “Size Distribution, Shape, and Composition of Mineral Dust Aerosols Collected During the African Monsoon Multidisciplinary Analysis Special Observation Period 0: Dust and Biomass-Burning Experiment Field Campaign in Niger, January 2006,” *J. Geophys. Res. Atmos.*, vol. 113, no. 23, pp. 1–17, 2008 DOI:10.1029/2008JD009897.

[26] N. Eliaz, G. Shemesh, and R. M. Latanision, “Hot Corrosion in Gas Turbine Components,” *Eng. Fail. Anal.*, vol. 9, pp. 31–43, 2002.

[27] R. Gier and X. Querol, “Solid Particulate Matter in the Atmosphere,” *Elements*, vol. 6, no. 4, pp. 215–222, 2010 DOI:10.2113/gselements.6.4.215.

[28] U. Kueppers, C. Cimarelli, K. Hess, J. Taddeucci, F. Wadsworth, and D. Dingwell, “The Thermal Stability of Eyjafjallajökull Ash Versus Turbine Ingestion Test Sands,” *J. Appl. Volcanol.*, vol. 3, no. 1, p. 4, 2014 DOI:10.1186/2191-5040-3-4.

[29] A. Filippone, N. Bojdo, and A. Filippone, “Effect of Desert Particulate Composition on Helicopter Engine Degradation Rate,” in *40th European Rotorcraft Forum*, 2014 DOI:10.13140/2.1.2959.8086.

[30] K. Yu and D. Tafti, “Size and Temperature Dependent Deposition Model of Micro-sized Sand Particles,” *ASME Turbo Expo 2017, Turbomach. Tech. Conf. Expo.*, pp. 1–8, 2017.

[31] K. Chow, “Ash Deposition in Turbine Cooling Holes,” Maters Thesis, University of Oxford, 2017.

[32] B. Aïssa, R. Isaifan, V. Madhavan, and A. Abdallah, “Structural and Physical Properties of the Dust Particles in Qatar and their Influence on the PV Panel Performance,” *Sci. Rep.*, vol. 6, no. 1, p. 31467, 2016 DOI:10.1038/srep31467.

[33] R. Clift, J. Grace, and M. Weber, *Bubbles, Drops and Particles*. Dover Publications, 1978 DOI:10.1017/s0022112079221290.

[34] P. Formenti *et al.*, “Recent Progress in Understanding Physical and Chemical Properties of African and Asian Mineral Dust,” *Atmos. Chem. Phys.*, vol. 11, no. 16, pp. 8231–8256, 2011 DOI:10.5194/acp-11-8231-2011.

[35] A. Szczepankowski, J. Szymczak, and R. Przysowa, “The Effect of a Dusty Environment Upon Performance and Operating Parameters of Aircraft Gas Turbine Engines,” NATO, 2017 DOI:10.14339/STO-MP-AVT-272-06.

[36] P. Venturini, D. Borello, K. Hanjali, and F. Rispoli, “Modelling of Particle Deposition in an Environment Relevant to Solid Fuel Boilers,” in *Applied Thermal Engineering*, 2012, vol. 49, pp. 131–138 DOI:10.1016/j.applthermaleng.2011.08.030.

[37] M. K. Parmar, “Unsteady Forces On a Particle In Compressible Flows,” PhD Thesis, University of Florida, 2010.

[38] J. H. E. Cartwright, U. Feudel, G. Károlyi, A. de Moura, O. Piro, and T. Tél, “Dynamics of Finite-Size Particles in Chaotic Fluid Flows,” in *Nonlinear Dynamics and Chaos: Advances and Perspectives*, M. Thiel, J. Kurths, M. C. Romano, G. Károlyi, and A. Moura, Eds. Berlin, Heidelberg: Springer Berlin Heidelberg, 2010, pp. 51–87 DOI:10.1007/978-3-642-04629-2_4.

[39] C. Crowe, M. Sommerfeld, and Y. Tsuji, “Multiphase Flow with Droplets and Particles,” *CRC Press. Florida, USA.*, 1998.

[40] M. Sommerfeld, “Forces on Particles and Bubbles,” in *Particles in Flows: Summer School and Workshop*, 2014, p. 48.

[41] C. T. Crowe, *Multiphase Flow Handbook*. CRC Press, 2006.

[42] NASA, “Drag-Sphere.” [Online]. Available: https://www.grc.nasa.gov/www/k-12/airplane/dragsphere.html.

[43] D. Borello *et al.*, “Modelling of Particle Transport, Erosion and Deposion in Power Plant Gas Paths,” in *ASME Turbo Expo 2016: Turbomachinery Technical Conference and Exposition*, 2016 DOI:10.1115/GT2016-57984.

[44] H. El-batsh, “Effect Of Particle Deposition on the Performance of Turbine Blades,” Vienna, Austria, 2001.

[45] J. A. C. Humphrey, “Fundamentals of Fluid Motion in Erosion by Solid Particle Impact,” *Int. J. Heat Fluid Flow*, vol. 11, no. 3, pp. 170–195, 1990 DOI:10.1016/0142-727X(90)90036-B.

[46] J. Gaskell, N. Vadgama, M. McGilvray, D. R. H. Gillespie, and R. J. Clarkson, “Collision-Induced Rotation and the Magnus Force on Particulates,” in *AIAA Aviation 2020 Forum*, 2020 DOI:10.2514/6.2020-2820.

[47] P. Forsyth, “High Temperature Particle Deposition with Gas Turbine Applications,” University of Oxford, 2017.

[48] J. Valentin and P. J. Smith, “Numerical Predictions of Deposition with a Particle Cloud Tracking Technique,” *Report, Dep. Chem. Fuels Eng. Univ. Utah, Salt Lake City, UT*, 1998.

[49] J. B. Young, “Thermophoresis of a spherical particle: Reassessment, clarification, and new analysis,” *Aerosol Sci. Technol.*, vol. 45, no. 8, pp. 927–948, 2011 DOI:10.1080/02786826.2011.569777.

[50] Y. Sone, “Flow induced by thermal stress in rarefied gas,” *Phys. Fluids*, vol. 15, no. 8, pp. 1418–1423, 1972 DOI:10.1063/1.1694102.

[51] A. Soldati and C. Marchioli, “Physics and modelling of turbulent particle deposition and entrainment: Review of a systematic study,” *Int. J. Multiph. Flow*, vol. 35, no. 9, pp. 827–839, 2009 DOI:10.1016/j.ijmultiphaseflow.2009.02.016.

[52] C. Marchioli, “Non-Spherical Particles in Turbulence: Numerical Modelling and Computation,” in *CISM-AIMETA Summer School on Anisotropic Particles in Viscous and Turbulent Flows*, 2019, pp. 1–66.

[53] J. Young and A. Leeming, “A Theory of Particle Deposition in Turbulent Pipe Flow,” *J.*

Fluid Mech., vol. 340, 1997 DOI:10.1017/S0022112097005284.

[54] P. Forsyth, D. R. H. Gillespie, M. Mcgilvray, and V. Galoul, "Validation and Assessment of the Continuous Random Walk Model For Particle Deposition In Gas Turbine Engines," *ASME Turbo Expo 2016 Turbomach. Tech. Conf. Expo.*, vol. GT2016-573, pp. 1–13, 2016 DOI:10.1115/GT2016-57332.

[55] J. B. Wu, Z Young, "The Deposition of Small Particles from a Turbulent Air Flow in a Curved Duct," *Int. J. Multiph. Flow*, vol. 44, 2012 DOI:10.1016/j.ijmultiphaseflow.2012.03.011.

[56] R. Brach and P. Dunn, "A Mathematical Model of the Impact and Adhesion of Microspheres," *Aerosol Sci. Technol.*, vol. 16, no. 1, pp. 51–64, 1992 DOI:10.1080/02786829208959537.

[57] G. G. Adams, "The Mechanics of Adhesion: A Tutorial," *STLE/ASME 2008 Int. Jt. Tribol. Conf.*, pp. 87–89, 2008 DOI:10.1115/IJTC2008-71247.

[58] G. Agati, D. Borello, F. Rispoli, and P. Venturini, "An Innovative Approach To Model Temperature Influence on Particle Deposition in Gas Turbines," *ASME Turbo Expo 2016, Turbomach. Tech. Conf. Expo.*, pp. 1–10, Jun. 2016 DOI:10.1115/GT2016-57997.

[59] K. L. Johnson, K. Kendall, and A. D. Roberts, "Surface Energy and the Contact of Elastic Solids," *Proc. R. Soc. A Math. Phys. Eng. Sci.*, vol. 324, no. 1558, pp. 301–313, 1971 DOI:10.1098/rspa.1971.0141.

[60] K. Johnson and J. Greenwood, "An Adhesion Map for the Contact of Elastic Spheres," *J. Colloid Interface Sci.*, vol. 192, pp. 326–333, 1997.

[61] S. Alvo, P. Lambert, M. Gauthier, and S. Régnier, "A van der Waals Force-Based Adhesion Model for Micromanipulation," *J. Adhes. Sci. Technol.*, vol. 24, no. 15–16, pp. 2415–2428, 2010 DOI:10.1163/016942410X508334.

[62] J. A. Zukas, *High Velocity Impact Dynamics*, vol. 59, no. 3. Wiley, 1990 DOI:10.1016/j.ces.2003.09.037.

[63] C. Thornton and Z. Ning, "A theoretical model for the stick/bounce behaviour of adhesive, elastic- plastic spheres," *Powder Technol.*, vol. 99, no. 2, pp. 154–162, 1998

DOI:10.1016/S0032-5910(98)00099-0.

[64] J. P. Bons, R. Prenter, and S. Whitaker, “A Simple Physics-Based Model for Particle Rebound and Deposition in Turbomachinery,” *J. Turbomach.*, vol. 139, no. 8, 2017 DOI:10.1115/1.4035921.

[65] M. Sommerfeld, “Modelling of Particle-wall Collisions in Confined Gas-particle Flows,” *Int. J. Multiph. Flow*, vol. 18, no. 6, pp. 905–926, 1992 DOI:10.1016/0301-9322(92)90067-Q.

[66] O. V Kim and P. F. Dunn, “A Microsphere-surface Impact Model for Implementation in Computational Fluid Dynamics,” *J. Aerosol Sci.*, vol. 38, no. 5, pp. 532–549, 2007 DOI:10.1016/j.jaerosci.2007.03.006.

[67] S. Singh and D. Tafti, “Predicting the Coefficient of Restitution for Particle Wall Collisions in Gas Turbine Components,” *ASME Turbo Expo 2013, Vol. 6B Turbomach.*, p. V06BT37A041, 2013 DOI:10.1115/GT2013-95623.

[68] W. Ai and T. Fletcher, “Computational Analysis of Conjugate Heat Transfer and Particulate Deposition on a HP Turbine Vane,” *J. Turbomach.*, vol. 134, no. 4, 2012 DOI:10.1115/1.4003716.

[69] P. M. Walsh, A. N. Sayre, D. O. Loehden, L. S. Monroe, J. M. Beer, and A. F. Sarofim, “Deposition of Bituminous Coal Ash on an Isolated Heat Exchanger Tube: Effects of Coal Properties on Deposit Growth,” *Prog. Energy Combust.*, vol. 16, no. 4, pp. 327–345, 1990 DOI:10.1016/0360-1285(90)90042-2.

[70] N. Maw, J. R. Barber, and J. N. Fawcett, “The Oblique Impact of Elastic Spheres,” *Wear*, vol. 38, no. 1, pp. 101–114, 1976 DOI:10.1016/0043-1648(76)90201-5.

[71] N. Casari, M. Pinelli, A. Suman, L. di Mare, and F. Montomoli, “An Energy-Based Fouling Model for Gas Turbines: EBFOG,” *J. Turbomach.*, vol. 139, no. 2, p. 021002, 2016 DOI:10.1115/1.4034554.

[72] J. Altmeppen, H. Sommerfeld, C. Koch, and S. Staudacher, “An Analytical Approach to Estimate the Effect of Surface Roughness on Particle Rebound,” *J. Glob. Power Propuls. Soc.*, vol. 4, pp. 27–37, 2020 DOI:10.33737/jgpps/118624.

[73] X. Weiwei, Z. Konghao, W. Jianjun, L. Yajun, and L. Qiang, “Modeling and numerical analysis of the effect of blade roughness on particle deposition in a flue gas turbine,” *Powder Technol.*, vol. 347, pp. 59–65, 2019 DOI:10.1016/j.powtec.2019.02.033.

[74] S. M. Whitaker and J. P. Bons, “Evaluation of Elastic-Plastic Rebound Properties of Coal Fly Ash Particles for Use in a Universal Turbine Deposition Model,” *Vol. 1 Aircr. Engine; Fans Blowers; Mar.*, pp. 1–17, Jun. 2015 DOI:10.1115/GT2015-43765.

[75] H. El-Batsh, “Modeling Particle Deposition on Compressor and Turbine Blade Surfaces Modeling Particle Deposition on Compressor and Turbine Blade Surfaces,” PhD Thesis, Institute of Thermal Turbomachines and Powerplants, Vienna University of Technology, 2001.

[76] R. . Smith, C. Brown, R. Martinez-Botas, P. Reading, S. Tetlow, and P. Watson, “Volcanic Ash: To Fly or Not to Fly?,” 2010, https://www.imeche.org/policy-and-press/reports/detail/volcanic-ash-to-fly-or-not-to-fly.

[77] A. Castorrini, A. Corsini, F. Morabito, F. Rispoli, I. Meccanica, and S. Università, “Numerical Simulation With Adaptive Boundary Method for Predicting Time Evolution of Erosion Processes,” *ASME Turbo Expo 2017, Turbomach. Tech. Conf. Expo.*, pp. 1–10, 2017.

[78] H. El-Batsh and H. Haselbacher, “Numerical Investigation of the Effect of Ash Particle Deposition on the Flow Field Through Turbine Cascades,” in *ASME Turbo Expo 2002: Power for Land, Sea, and Air*, 2002, pp. 1035–1043 DOI:10.1115/GT2002-30600.

[79] F. Greifzu, C. Kratzsch, T. Forgber, F. Lindner, and R. Schwarz, “Assessment of Particle-tracking Models for Dispersed Particle-laden Flows Implemented in OpenFOAM and ANSYS FLUENT,” *Eng. Appl. Comput. Fluid Mech.*, 2016 DOI:10.1080/19942060.2015.1104266.

[80] E. Cunningham, “On the Velocity of Steady Fall of Spherical Particles through Fluid Medium,” *Proc. R. Soc. A Math. Phys. Eng. Sci.*, vol. 83, no. 563, pp. 357–365, 1910 DOI:10.1098/rspa.1910.0024.

[81] ANSYS, “Fluent User Guide Chapter 19: Discrete Phase Models,” 2001,

http://www.afs.enea.it/fluent/Public/Fluent-Doc/PDF/chp19.pdf.

[82] A. Haider and O. Levenspiel, "Drag Coefficient and Terminal Velocity of Spherical and Nonspherical Particles," *Powder Technol.*, vol. 58, pp. 63–70, 1989 DOI:10.1021/ie50688a011.

[83] B. Oesterle and T. Bui Dinh, "Experiments on the lift of a spinning sphere in a range of intermediate Reynolds numbers," *Exp. Fluids*, vol. 25, no. 1, pp. 16–22, 1998 DOI:10.1007/s003480050203.

[84] A. Li and G. Ahmadi, "Dispersion and deposition of spherical particles from point sources in a turbulent channel flow," *Aerosol Sci. Technol.*, vol. 16, no. 4, pp. 209–226, 1992 DOI:10.1080/02786829208959550.

[85] L. Talbot, R. K. Cheng, R. W. Schefer, and D. R. Willis, "Thermophoresis of Particles in a Heated Boundary Layer," *J. Fluid Mech.*, vol. 101, no. 04, p. 737, Dec. 1980 DOI:10.1017/S0022112080001905.

[86] D. P. Healy and J. B. Young, "An Experimental and Theoretical Study of Particle Deposition Due to Thermophoresis and Turbulence in an Annular Flow," *Int. J. Multiph. Flow*, vol. 36, no. 11–12, pp. 870–881, Nov. 2010 DOI:10.1016/j.ijmultiphaseflow.2010.07.006.

[87] C. Jin, I. Potts, and M. W. Reeks, "A simple stochastic quadrant model for the transport and deposition of particles in turbulent boundary layers," arXiv:1406.0153v2, 2016, https://arxiv.org/pdf/1406.0153.pdf.

[88] E. Krasnoff and R. Peskin, "The langevin model for turbulent diffusion of marked particles," Livermore, California, United States, 1994 DOI:10.1080/03091927108236054.

[89] S. R. Wilson, Y. Liu, E. A. Matida, and M. R. Johnson, "Aerosol Deposition Measurements as a Function of Reynolds Number for Turbulent Flow in a Ninety-Degree Pipe Bend," *Aerosol Sci. Technol.*, vol. 45, no. 3, pp. 364–375, Feb. 2011 DOI:10.1080/02786826.2010.538092.

[90] B. J. Legg and M. R. Raupach, "Markov-chain simulation of particle dispersion in inhomogeneous flows: The mean drift velocity induced by a gradient in Eulerian velocity

variance," *Boundary-Layer Meteorol.*, vol. 24, no. 1, pp. 3–13, Sep. 1982 DOI:10.1007/BF00121796.

[91] T. L. Bocksell and E. Loth, "Random Walk Models for Particle Diffusion in Free-Shear Flows," *AIAA J.*, vol. 39, no. 6, pp. 1086–1096, Jun. 2001 DOI:10.2514/2.1421.

[92] J. D. Wilson, B. J. Legg, and D. J. Thomson, "Calculation of particle trajectories in the presence of a gradient in turbulent-velocity variance," *Boundary-Layer Meteorol.*, vol. 27, no. 2, pp. 163–169, 1983 DOI:10.1007/BF00239612.

[93] J. D. Wilson, G. W. Thurtell, and G. E. Kidd, "Numerical simulation of particle trajectories in inhomogeneous turbulence, II: Systems with variable turbulent velocity scale," *Boundary-Layer Meteorol.*, vol. 21, no. 4, pp. 423–441, 1981 DOI:10.1007/BF02033592.

[94] T. L. L. Bocksell and E. Loth, "Stochastic modeling of particle diffusion in a turbulent boundary layer," *Int. J. Multiph. Flow*, vol. 32, no. 10–11, pp. 1234–1253, Oct. 2006 DOI:10.1016/j.ijmultiphaseflow.2006.05.013.

[95] A. Tanière and B. Arcen, "Prediction of a particle-laden turbulent channel flow: Examination of two classes of stochastic dispersion models," *Int. J. Multiph. Flow*, vol. 60, pp. 1–10, 2014 DOI:10.1016/j.ijmultiphaseflow.2013.11.005.

[96] R. Ouchene *et al.*, "Numerical simulation and modelling of the forces acting on single and multiple non-spherical particles," in *American Society of Mechanical Engineers, Fluids Engineering Division (Publication) FEDSM*, 2014, vol. 2 DOI:10.1115/FEDSM2014-22244.

[97] Y. Mito and T. J. Hanratty, "Use of a Modified Langevin Equation to Describe Turbulent Dispersion of Fluid Particles in a Channel Flow," *Flow, Turbul. Combust.*, vol. 68, pp. 1–26, 2002.

[98] G. A. Kallio and M. . Reeks, "A Numerical Simulation of Particle Deposition In Turbulent Boundary Layers," vol. 15, no. 3, pp. 433–446, 1988.

[99] L. Tian and G. Ahmadi, "Particle deposition in turbulent duct flows-comparisons of different model predictions," *Aerosol Sci.*, vol. 38, pp. 377–397, 2007

DOI:10.1016/j.jaerosci.2006.12.003.

[100] A. Dehbi, "A CFD Model for Particle Dispersion in Turbulent Boundary Layer Flows," *Nucl. Eng. Des.*, vol. 238, no. 3, pp. 707–715, 2008 DOI:10.1016/j.nucengdes.2007.02.055.

[101] A. Noorani, G. Sardina, L. Brandt, and P. Schlatter, "Particle transport in turbulent curved pipe flow," *J. Fluid Mech*, vol. 793, pp. 248–279, 2016 DOI:10.1017/jfm.2016.136.

[102] X. Huang and P. A. Durbin, "Particulate mixing in a turbulent serpentine duct," *Phys. Fluids*, vol. 24, no. 1, pp. 1–14, 2012 DOI:10.1063/1.3673610.

[103] D. Pui, F. Romay-Novas, and B. Liu, "Experimental Study of Particle Deposition in Bends of Circular Cross Section," *Aerosol Sci. Technol.*, vol. 7, no. 3, pp. 301–315, 1987 DOI:10.1080/02786828708959166org/10.1080/02786828708959166.

[104] M. Breuer, H. Baytekin, and E. Matida, "Prediction of aerosol deposition in 90 degree bends using LES and an efficient Lagrangian tracking method," *J. Aerosol Sci.*, vol. 37, pp. 1407–1428, 2006.

[105] A. S. Berrouk and D. Laurence, "Stochastic Modelling of Aerosol Deposition for LES of 90° Bend Turbulent Flow," *Int. J. Heat Fluid Flow*, vol. 29, no. 4, pp. 1010–1028, Aug. 2008 DOI:10.1016/J.IJHEATFLUIDFLOW.2008.02.010.

[106] A. Arsalanloo and M. Abbasalizadeh, "Numerical study on deposition of particles in a 90° bend in the presence of swirling flow using Eulerian-Lagrangian method," *Powder Technol.*, vol. 320, 2017 DOI:10.1016/j.powtec.2017.07.050.

[107] E. Ghahramani, O. Abouali, H. Emdad, and G. Ahmadi, "Numerical analysis of stochastic dispersion of micro-particles in turbulent flows in a realistic model of human nasal/upper airway," *J. Aerosol Sci.*, vol. 67, pp. 188–206, 2014 DOI:10.1016/j.jaerosci.2013.09.004.

[108] A. Suman *et al.*, "Estimation of the Particle Deposition on a Subsonic Axial Compressor Blade," in *ASME Turbo Expo 2016, Turbomachinery Technical Conference*, 2016, vol. 1, no. 1, pp. 1–12 DOI:10.1115/GT2016-57340.

[109] A. Suman *et al.*, "Quantitative Computational Fluid Dynamics Analyses of Particle Deposition on a Subsonic Axial Compressor Blade," *J. Eng. Gas Turbines Power*, vol.

138, no. 1, pp. 1–14, 2016 DOI:10.1115/1.4031205.

[110] S. M. Whitaker, R. Prenter, and J. P. Bons, “The effect of freestream turbulence on deposition for nozzle guide vanes,” *J. Turbomach.*, vol. 137, no. 12, pp. 1–9, 2015 DOI:10.1115/1.4031447.

[111] R. Prenter, A. A. Ameri, and J. P. Bons, “Computational Simulation of Deposition in a Cooled High-Pressure Turbine Stage With Hot Streaks,” in *ASME Turbo Expo 2016, Turbomachinery Technical Conference and Exposition*, 2016, vol. 1, no. Turbomachinery, pp. 1–13 DOI:10.1115/GT2016-57815.

[112] B. Casaday, C. Clum, and J. P. Bons, “Particle Deposition in Internal Cooling Caviities of a Nozle Guide Vane - Part ii: Analytical and Computational Modelling,” in *Proceedings of ASME Turbo Expo 2014: Turbine Technical Conference and Exposition*, 2014, pp. 1–13 DOI:10.1115/GT2014-27155.

[113] S. S. Sreedharan and D. K. Tafti, “Three-Row Leading Edge Film Cooling Geometry Using Large Eddy,” in *ASME Turbo Expo 2009: Power for Land, Sea and Air*, 2009, pp. 1–15.

[114] S. Wylie, A. Bucknell, P. Forsyth, M. McGilvray, and D. R. H. Gillespie, “Reduction in Flow Parameter Resulting From Volcanic Ash Deposition in Engine Representative Cooling Passages,” in *ASME Turbo Expo 2016: Turbomachinery Technical Conference and Exposition*, 2016, pp. 1–15 DOI:10.1115/1.4034939.

[115] B. Y. . Liu and J. . Agarwal, “Experimental observation of aerosol deposition in turbulent flow,” *J. Aerosol Sci.*, vol. 5, no. 2, pp. 145–155, Mar. 1974 DOI:10.1016/0021-8502(74)90046-9.

[116] P. Forsyth, D. R. H. Gillespie, and M. McGilvray, “Experimental deposition of NaCl particles from turbulent flows at gas turbine temperatures,” *Int. Symp. Transp. Phenom. Dyn. Rotating Mach.*, 2017.

[117] T. L. Montgomery and M. Corn, “Aerosol deposition in a pipe with turbulent airflow,” *J. Aerosol Sci.*, vol. 1, no. 3, 1970 DOI:10.1016/0021-8502(70)90034-0.

[118] M. R. Sippola and W. W. Nazaroff, “Experiments Measuring Particle Deposition from

Fully Developed Turbulent Flow in Ventilation Ducts," *Aerosol Sci. Technol.*, vol. 38, no. 9, pp. 914–925, 2004 DOI:10.1080/027868290507213.

[119] R. Lundgreen, C. Sacco, R. Prenter, and J. P. Bons, "Temperature Effects on Nozzle Guide Vane Deposition in a New Turbine Cascade Rig," in *ASME Turbo Expo 2016, Turbomachinery Technical Conference and Exposition*, 2016, pp. 1–11 DOI:10.1115/GT2016-57560.

[120] J. P. Bons, "A Comparison of Techniques for Particle Rebound Measurement in Gas Turbine Applications," in *Proceedings of ASME Turbo Expo 2015: Turbine Technical Conference and Exposition*, 2015, pp. 1–11 DOI:10.1115/GT2015-43766.

[121] T. Wolff, C. Bowen, and J. P. Bons, "The Effect of Particle Size on Deposition in an Effusion Cooling Geometry," in *ASME Turbo Expo 2016: Turbomachinery Technical Conference and Exposition*, 2016, pp. 1–14 DOI:10.2514/6.2018-0391.

[122] C. J. Reagle, J. M. Delimont, W. F. Ng, and S. V. Ekkad, "Study of Microparticle Rebound Characteristics Under High Temperature Conditions," *J. Eng. Gas Turbines Power*, vol. 136, no. 1, pp. 011501–011501, 2013 DOI:10.1115/1.4025346.

[123] B. J. Barker, K. Hsu, B. Varney, A. Boulanger, J. Hutchinson, and W. F. Ng, "An Experiment-Based Sticking Model for Heated Sand," in *ASME Turbo Expo 2017: Turbomachinery Technical Conference and Exposition*, 2017, pp. 1–11 DOI:10.1115/GT2017-64421.

[124] A. Hamed, W. C. Tabakoff, and R. V. Wenglarz, "Erosion and Deposition in Turbomachinery," *J. Propuls. Power*, vol. 22, no. 2, pp. 350–360, 2006 DOI:10.2514/1.18462.

[125] J. Yoon and Y. Yoon, "Comparative Study of Mixing Characteristics of Particle-Laden Shear and Swirl Coaxial Jets," *J. Propuls. Power*, vol. 33, no. 5, pp. 1–9, 2016 DOI:10.2514/1.B36326.

[126] P. Hedman and D. Smoot, "Particle-Gas Dispersion Effects in Confined Coaxial Jets," *Am. Inst. Chem. Eng.*, vol. 21, no. 2, pp. 372–279, 1975.

[127] L. Smoot, "Particle-Gas Mixing in Confined Nonparallel Coaxial Jets," *AIAA J.*, vol. 13,

no. 6, pp. 1–2, 1975 DOI:10.2514/3.60426.

[128] Z. Duan, B. He, and Y. Duan, “Sphere Drag and Heat Transfer,” *Sci. Rep.*, vol. 5, pp. 1–7, 2015 DOI:10.1038/srep12304.

[129] E. C. Robertson, “Thermal Properties of Rocks (Report 88-441),” Reston, Virginia, 1988, https://pubs.usgs.gov/of/1988/0441/report.pdf.

[130] I. Abdulagatov, S. Emirov, T. Tsomaeva, K. Gairbekov, S. Askerov, and N. Magomedova, “Thermal conductivity of fused quartz and quartz ceramic at high temperatures and high pressures,” *J. Phys. Chem. Solids*, vol. 61, pp. 779–787, 1999.

[131] J. M. Delimont, M. K. Murdock, W. F. Ng, and S. V. Ekkad, “Effect of near melting temperatures on microparticle sand rebound characteristics at constant impact velocity,” in *Proceedings of the ASME Turbo Expo*, 2014, vol. 1A DOI:10.1115/GT2014-25686.

[132] FLUENT, “ANSYS Fluent 12.0 Theory Guide - 18.3.1 Spatial Discretization.” 2009.

[133] “Arizona Test Dust Material Safety Data Sheet.” Powder Technology, Minnesota, USA, pp. 1–5, 2014.